Science

$15
13 JANUARY 2023
science.org

AAAS

THE MAZE OF
HAZE

Labmade aerosols
help make sense of alien
atmospheres p. 130

CONTENTS

13 JANUARY 2023
VOLUME 379
ISSUE 6628

124

Miners in the Democratic Republic of the Congo search for cassiterite, the principal source of tin. Satellites have revealed a surge in ecologically damaging river mining.

NEWS

140

INSIGHTS

YOUR RESEARCH HAS ITS REWARDS.

Submit an essay by 3/15/23 to enter to win $25K.

The prestigious international *Science* & PINS Prize is awarded annually to outstanding early-career researchers in the emerging field of neuromodulation. Findings already show improved outcomes in several neurological disorders. To enter, just write a 1000-word essay about your research performed in the last three years. The Grand Prize winner will be presented a US$25,000 award, as well as have their essay published in *Science* magazine and on *Science* Online. A runner-up will have their essay published online. For additional inquiries, email SciencePINSPrize@aaas.org.

SCIENCE.ORG/PINS

RESEARCH

154
Cross-species signaling influences tick immunity and development.

ON THE COVER

In this artist's conception, light from a star 700 light-years from Earth glints off the soupy cloud tops of WASP-39b, a water-rich gas giant. In November 2022, astronomers using JWST, NASA's giant space telescope, reported detecting sulfur dioxide—a contributor to smog—in WASP-39b's skies. Hazes can obscure a planet's atmosphere, but recreating them in the laboratory could help unlock their secrets. See page 130. *Credit: NASA; ESA; CSA; Joseph Olmsted (STScI)*

PHOTO: VIPIN SINGH RANA, MOLLY THOMPSON AND UTPAL PAL

Science

AAAS

Science in postwar Ukraine

Next month will mark 1 year since Russia escalated its war on Ukraine. The senseless casualties and destruction have been met with stunning resilience by Ukraine and international opposition to Russia. Although the war continues, there is hope that Ukraine will emerge as an open and free democracy, which would include rebuilding its scientific enterprise with new infrastructure and laws.

Transforming the scientific system in Ukraine, which includes education, research, and technological development, began after the country gained independence in 1991. Although progress in moving away from research agendas and programs dictated by the Soviet Union has been slow and inefficient, the unprovoked war that started in 2014 stoked the destruction of educational and scientific institutions by Russian troops. Escalation to full-scale war in 2022 has destroyed at least 15% of Ukraine's research infrastructure, including an atomic physics laboratory and Karazin National University in Kharkiv, a chemical laboratory at Chernobyl, and the Ministry of Education and Science of Ukraine in Kyiv. The damage has created economic and political rifts that have affected research in physics, space science, climate, food security, and energy on a global scale. This includes international projects such as ExoMars and Arctic PASSION, which have stimulated discussions about how to best restructure global scientific cooperation models.

The European Union will help assess the physical damage to scientific and educational infrastructure. However, damage to human capital will be more difficult to evaluate. More than 200,000 students and scientists have left the country and may never return unless post-war Ukraine shows signs of new potential.

Should the end of the war create an opportunity to leapfrog the existing Ukrainian scientific system, what could the new structure look like and how might it be achieved? Ideally, there should be a new funding system to attract the best scientists and personnel. The money for this would come from frozen €19 billion of assets belonging to Russian oligarchs and €300 billion of Russian Central Bank reserves that are blocked in the European Union and other G7 partners. Another improvement would be to consolidate the state-owned higher education network that operates according to a decentralized management model in which each administrative region has at least one public traditional and one public technical research university. This would be supported by regional hybrid financial mechanisms involving state budget and local business in partnership. National academies could maintain the status of nonprofit professional organizations with a focus on scholarly publishing and providing high-level expertise to public and private organizations. Another strategy would be to establish institutions that focus on fundamental research and those that support applied research and production. Here, the government could be guided by recommendations of the Organization for Economic Cooperation and Development (called the Frascati guidelines) to construct, fund, and monitor complex research and development programs.

> "...scientists...may never return unless post-war Ukraine shows signs of new potential."

In 2018, Ukraine's Ministry of Education and Science established the New Ukrainian School, a reform of primary school in which students gained knowledge and skills through more practical activity and engagement with teachers and others. The success of this program suggested a continuation of this approach at the next levels of education. This will require new training for teachers and new curricula.

The world's scientific and educational community has formed ad hoc groups to help save Ukrainian scientists that have left the country. In September 2022, an international workshop (Rebuilding Research, Education and Innovation in Ukraine) organized by the US National Academy of Sciences, Engineering, and Medicine recognized that the future of Ukrainian science must be based on global research networks, paired with global higher education systems and training programs for decision-makers and scientific managers. Other international efforts committed to rebuilding Ukrainian science include the European Commission, which is working on a plan to help Ukraine prepare for its eventual reconstruction.

It will be a challenge to bring people back to Ukraine to rebuild. Hopefully, those elected to lead Ukraine will understand that supporting education and science is not an unnecessary cost, but rather an invaluable investment in human capital and the future of the country. But the war must end first.

–Nataliya Shulga

Nataliya Shulga
is a director at Ukrainian Science Club, Kyiv, Ukraine.
n.i.shulga@gmail.com

NEWS

IN BRIEF

Edited by **Jeffrey Brainard**

People walk in a part of the Great Salt Lake that was underwater.

ENVIRONMENT

Utah's Great Salt Lake may dry up within 5 years

North America's largest saline lake could be gone by 2028 if water inflows are not restored, researchers warned last week. The Great Salt Lake in Utah has lost nearly three-quarters of its water and 60% of its surface area since 1950, a report from 32 scientists at multiple institutions concludes, and a recent drought has accelerated the losses. To restore the lake, farmers, homeowners, and others will need to reduce the amount of water they take from feeder streams by 30% to 50%. If they don't, the continent could lose a key habitat for some 10 million migratory birds and the dry lakebed could become a major source of dangerous dust pollution. "Most Utahns do not realize the urgency of this crisis," the researchers wrote, adding that the state's governor and legislature should immediately launch "a watershed-wide emergency rescue" that includes more funding for water conservation efforts. In 2022, Utah enacted new policies that allow those permitted to withdraw water to limit their take without losing their rights. But the amount conserved that year was less than one-tenth the average annual rate of loss, the report says.

Ebola outbreak nears official end

INFECTIOUS DISEASES | An Ebola outbreak in Uganda that surfaced in September 2022 and led to 77 probable and confirmed deaths was expected to be declared over on 12 January, 2 days after *Science* went to press and 42 days after the last known case. That interval, twice the maximum known incubation period, is considered long enough for health authorities to proclaim victory over Ebola. An approved vaccine exists for the Zaire ebolavirus but not for the distantly related Sudan species that surfaced in Uganda. The country instead curbed the outbreak by isolating people with confirmed cases, testing their contacts, and improving sanitation. The dwindling case numbers led Ugandan officials and international partners to call off a planned efficacy trial of three experimental Sudan vaccines. But the country may still test the safety of the vaccines and the immune responses they trigger, which could speed their eventual approval by regulators and help prepare Uganda for a future return of the virus.

Lander to head science 'incubator'

| Eric Lander, who resigned as President Joe Biden's top science adviser in February 2022 after an investigation found he bullied subordinates, has a new job. He will be chief scientist at Science for America, a new nonprofit that aims to become a "solutions incubator" to help address big global problems, including climate change and pandemics. Its board boasts leading scientists in multiple fields (including Gilda Barabino, president of AAAS, which publishes *Science*). The group has collected commitments of $30 million over 2 years from nine philanthropies, including Bloomberg Philanthropies, the Ford Foundation, and Gates Ventures. Science for America announced Lander's role in a blog post in July 2022 that did not receive wide attention; *STAT* reported the news in December 2022. Lander is on leaves of absence from faculty positions at Harvard University and the Massachusetts Institute of Technology, *STAT* reported.

Florida vaccine warning criticized

COVID-19 | Florida's surgeon general, a professor of medicine at the University of Florida, may have violated the institution's research integrity rules when he advised young men not to receive messenger RNA vaccines against COVID-19, a panel of UF faculty public health experts concluded recently. However, the university said last week that Joseph Ladapo was not acting in his academic capacity in October 2022 when he offered the advice, claiming the vaccines produced a high risk of cardiac-related death. In an evaluation first reported by *The Washington Post*, the faculty panel said Ladapo cherry-picked evidence to support that view, ignoring evidence that the risk of death is low and the vaccines' benefits are significant. Ladapo joined UF in 2021, the year he was appointed surgeon general by Governor Ron DeSantis (R), a COVID-19 vaccine skeptic.

UCSF contrite on prisoner studies

RESEARCH ETHICS | The University of California, San Francisco (UCSF), last month apologized for "past harms" by two faculty members who conducted experiments on prisoners in the 1960s and '70s. The work was done in most cases without their informed consent, even though UCSF and the federal government required it. The university described the research, in which prisoners volunteered to participate and were paid, in a preliminary report about an internal review it is conducting. One

FIREARMS RESEARCH
Keeping guns from children reduces deaths

Two types of gun policies in the United States produce starkly different results for public safety, a study has found. "Safe storage" laws, aimed at preventing children from accessing firearms, reduce deaths; laws that strengthen concealed-carry and stand-your-ground protections tend to increase them, according to the study, issued this week by the nonprofit RAND Corporation. Americans privately own as many as 393 million guns, and more than 45,000 die annually from both deliberate and unintentional gun injuries. Just over half the deaths are suicides. In 2020, firearm-related injuries surpassed motor vehicle crashes as the leading cause of death among U.S. children and adolescents ages 1 to 19. Authors of the study, a meta-analysis, examined evidence from 152 studies covering 18 areas of federal and state gun control policies.

To protect kids, "safe storage" laws require ammunition to be stored locked and separate from guns.

study dosed the prisoners with pesticides and herbicides. One of the researchers, Howard Maibach, remains on the faculty. In a letter to colleagues, Maibach said that "the work I did," which involved more than 2600 prisoners, "was considered by many to be appropriate by the standards of the day," but given today's mores, "I have sincere remorse." He and a colleague, the late William Epstein, undertook the UCSF experiments after being trained by the late Albert Kligman, a dermatologist at the University of Pennsylvania, whose research on that state's prisoners triggered a similar apology by that institution. The UCSF studies continued until 1977, when California halted human subject research in state prisons.

A dragnet for respiratory bugs

PUBLIC HEALTH | The Wellcome Sanger Institute this week announced a project to collect and sequence millions of genomes of common respiratory pathogens, such as adenovirus, rhinovirus, and respiratory syncytial virus. The goal for these pathogens is to emulate the massive effort to monitor SARS-CoV-2. Using hundreds of thousands of swab samples collected in the United Kingdom since the pandemic started, researchers hope to develop a method to sequence all known respiratory viruses from a single sample. The pioneering plan could eventually be expanded to detect a wide range of bacteria and fungi, including benign ones naturally present as part of the human microbiome. The Respiratory Virus and Microbiome Initiative should help answer scientific questions about the evolution and transmission of the pathogens, says microbiologist Ewan Harrison, who leads the initiative. It could also give doctors and policymakers a snapshot of their activity almost in real time, perhaps starting as soon as 1 year from now, he

says—which may allow public health workers to focus their response efforts.

Journals widen free open access

PUBLISHING | Paywalled journals in the *Science* and JAMA families this month started to allow all research articles to be free to read immediately when published, without authors paying a fee. The arrangement, known as "green" open access, permits authors to deposit near-final, peer-reviewed versions of papers accepted by the journals in publicly accessible repositories. Supporters of open access have long argued that immediate access will accelerate scientific discovery, and some supporters hail green open access as an alternative to "gold" open access, which requires authors to pay a fee unless journals waive it. Since January 2021, *Science* has offered the green approach for authors whose research was funded by Coalition S, a group of mostly European funders that require open access. The new policy for *Science* and four other paywalled journals in its family extends the approach to all research articles regardless of the authors' funding source and allows use of repositories outside the authors' institution. The 14 journals in the JAMA Network adopted a similar policy. Questions persist about whether the green model is financially sustainable, because institutions might drop subscriptions to journals supporting it. In a statement, AAAS, which publishes the *Science* journals, says that hasn't happened.

New role for viruses: dinner

BIOLOGY | Scientists have long viewed viruses only as predators, but a new study calls them something else: food. It found that microbes called ciliates can survive and thrive on a virus-only diet. A research team placed *Halteria* ciliates—a type of protozoan with hairlike organelles found in freshwater worldwide—in a petri dish with only chloroviruses, which infect green algae. The ciliates multiplied, and the researchers found they ingested a green dye the team had used to tag the viruses, the team reported in the 27 December 2022 issue of the *Proceedings of the National Academy of Sciences* (*PNAS*). Without the viral feedstock, the ciliates' population remained stable. Virus particles are "made up of really good stuff: nucleic acids, a lot of nitrogen and phosphorus—everything should want to eat them," says co-author John DeLong of the University of Nebraska, Lincoln, in a news release about the study. One ciliate can consume up to 1 million virus particles a day, he and his colleagues wrote in *PNAS*. Because Earth's viruses are vastly abundant and ciliates are themselves eaten by larger organisms, the new finding may lead to a better understanding of food webs and other ecosystem dynamics, the authors said.

AI meeting bans AI text

MACHINE LEARNING | In a sign of the growing worries about text generated by algorithms, organizers of this year's International Conference on Machine Learning have banned presenters from submitting papers containing text produced by "large-scale language models," such as OpenAI's ChatGPT, launched in November 2022. Organizers of the conference, to be held in July, exempted text presented in a scholarly article's experimental analysis. The wording produced by such algorithms can contain factual errors and be difficult to distinguish from human-generated text, which has raised concerns that they may fuel plagiarism and shoddy papers in laboratories and classrooms. The ban, announced last week, only applies to this year's conference; conference organizers said they will review the models' pros and cons.

To stop the spread of American foulbrood disease, beekeepers burn infected hives.

ENTOMOLOGY
First honey bee vaccine approved

American foulbrood disease is one of the worst diagnoses a beekeeper's brood can get. The bacteria that cause it are deadly to honey bee larvae, extremely contagious, and rarely treatable. Now, the U.S. Department of Agriculture has granted preliminary approval for a vaccine, the first intended for honey bees, the vaccine's developer said last week. After spores of the bacteria (*Paenibacillus larvae*) enter a honey bee hive, worker bees unintentionally spread them to larvae. When workers clean out the remains of the dead larvae, the spores are spread to those still alive. Many beekeepers must incinerate infected colonies, bees and all. Dalan Animal Health created the vaccine from killed bacteria. Beekeepers add it to food that worker bees include in the "royal jelly" they feed to the queen. Eggs in her ovaries are exposed to the vaccine, and the larvae that develop from those eggs are immune to the bacteria.

S SCIENCE.ORG/NEWS
Read more news from *Science* online.

PHOTO: ISTOCK.COM/BEEKEEPX
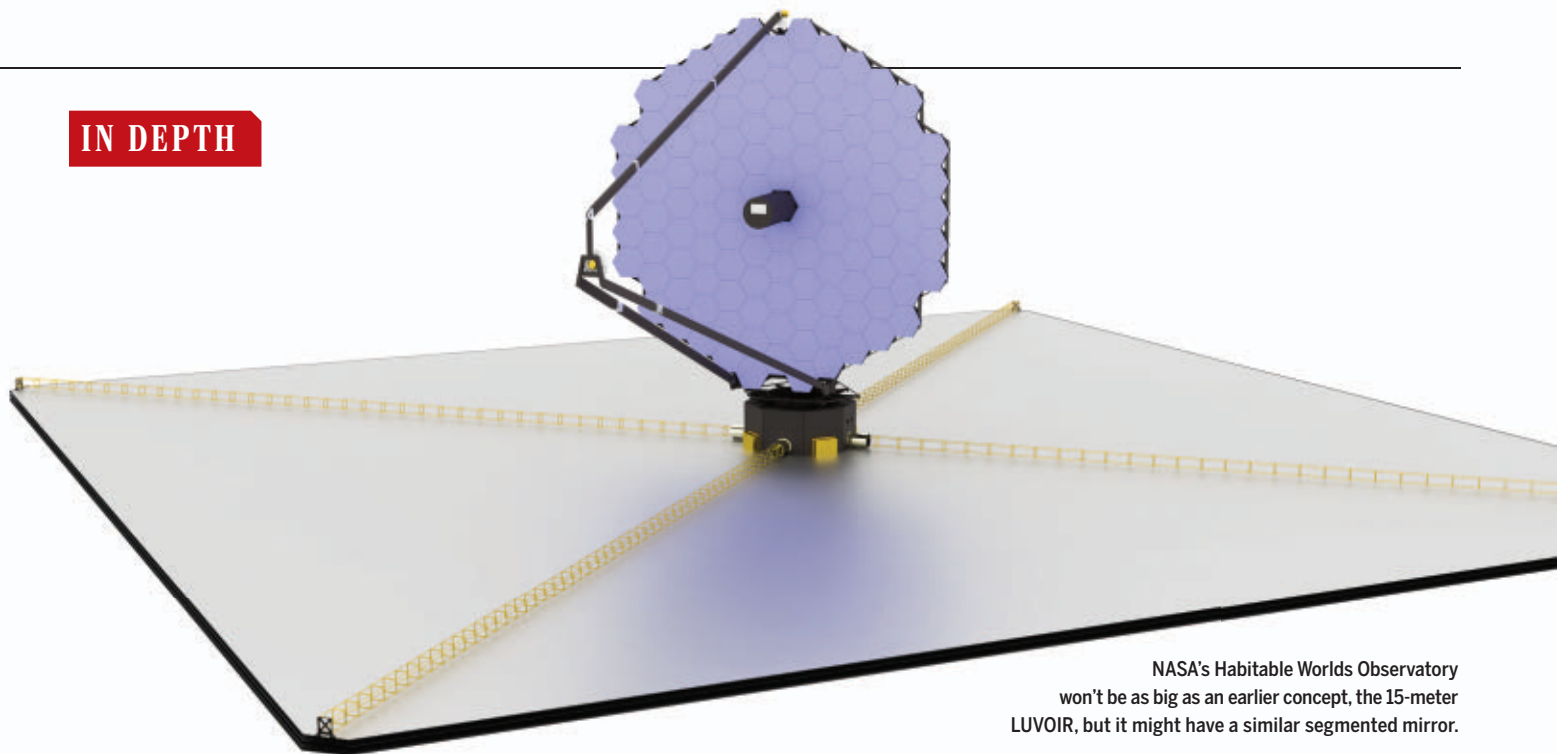
NASA's Habitable Worlds Observatory won't be as big as an earlier concept, the 15-meter LUVOIR, but it might have a similar segmented mirror.

ASTRONOMY

Future NASA scope would find life on alien worlds

Agency lays out initial plan for multibillion-dollar Habitable Worlds Observatory

By **Daniel Clery**

Astronomers are always looking to the next big thing. This week, at a meeting of the American Astronomical Society, researchers packed into a standing-room-only conference room to hear about a successor to JWST, the 6.5-meter space telescope that began operations last year. Flush with JWST's success, NASA is now planning an optical telescope that would be just as big as JWST and have a grand new goal: looking for signs of life on Earth-like planets, perhaps by the early 2040s.

Mark Clampin, NASA's astrophysics division director, told the audience that little about the telescope has been settled. But what he did say tantalized them: The telescope will, like JWST, be perched at L2, a gravitational balance point 1.5 million kilometers from Earth. Unlike JWST, it will be designed for robotic servicing and upgrades, which could enable it to operate for decades, getting better with age. Without a dedicated budget, Clampin says he can't yet make much headway on the design and technology. But he does have a working name for the telescope: the Habitable Worlds Observatory (HWO).

"I'm really, really excited to see it actually happening," says John O'Meara, chief scientist of the W.M. Keck Observatory. "Serviceability will be huge," says Aki Roberge of NASA's Goddard Space Flight Center. It essentially creates a "mountaintop observatory at L2," she says. Like a telescope on Earth, the mirrors and structure can remain while increasingly sophisticated instruments are swapped in. "It's the instruments that make a difference," she says.

The HWO won't be NASA's next flagship space telescope after JWST. The agency plans in 2027 to launch the Nancy Grace Roman Observatory, a 2.4-meter survey telescope that will hunt for dark energy and exoplanets. But with the HWO, NASA is following through on the top priority of astronomy's decadal survey, a community-led wish list that guides funding agencies and lawmakers.

The survey's final report, published in November 2021, called for NASA to resurrect its Great Observatories program, which launched the Hubble Space Telescope and several others in the 1990s and early 2000s. The report said an $11 billion, 6-meter telescope sensitive to ultraviolet, optical, and near-infrared wavelengths should kick off a new Great Observatories program. It specified that the telescope, in addition to doing general astrophysics, must be capable of detecting signs of life on 25 nearby Earth-like exoplanets—the minimum needed to confirm statistically whether life is common in the Galaxy.

NASA suggested several options for this next big thing in space, but the decadal report called for something between two of NASA's proposals, HabEx and LUVOIR. HabEx would have relied on a 4-meter monolithic mirror, as well as a robotic starshade, floating more than 100,000 kilometers away, to screen out the light of an exoplanet's star so the planet could be seen. LUVOIR, as big as 15 meters across in one configuration, was designed more as a multipurpose observatory, and would build on JWST's segmented mirror technology. Although segmented mirrors can't produce images quite as crisp as those from monolithic mirrors, they can be folded up, making it possible to pack a far bigger telescope into a rocket. As described, the HWO "contains no technology that has not already been thought about for HabEx or LUVOIR," says Scott Gaudi of Ohio State University, Columbus, one of the designers of HabEx.

Clampin says the agency will take a conservative approach to the HWO, to avoid the cost overruns and delays that plagued JWST. That project required many unproven technologies, which took longer to refine than expected. For the new

telescope, NASA will take advantage of technologies already developed or in development, including segmented mirrors such as the one used in JWST and the Roman observatory's coronagraph, an optical device that, like a distant starshade, blocks starlight but is built into the telescope. It will also set up a Great Observatories Technology Maturation Program (GOMaP) to refine those technologies for the HWO and do similar prep work for subsequent great observatories.

For example, because the HWO will work with optical light, which has shorter wavelengths than the infrared light JWST captures, the HWO will need much tighter control over the shape of the mirror. It will need to be perfectly shaped down to a level of 1 picometer—one-millionth of one-millionth of 1 meter—1000 times the

The HabEx telescope concept included a free-floating starshade to help it screen out all but a planet's light, but the Habitable Worlds Observatory may only include an internal starlight blocker called a coronagraph.

precision required for JWST. The HWO will also have to improve on the Roman telescope's coronagraph, which can block out the light of a star 100 million times brighter than its planet. The HWO's coronagraph will need to cope with stars that are 10 billion times brighter. One key will be suppressing stray light, which may require a cylindrical baffle around the HWO, similar to the one surrounding the Hubble telescope. That would protect its mirror from micrometeorites of the sort that have already struck JWST. Every pit in the mirror from a micrometeorite causes stray light.

Some astronomers argue that a monolithic mirror, which has fewer edges than a segmented one, would scatter less light—which might push NASA toward a design more like HabEx. But Clampin says recent research suggests coronagraphs can also work with segmented mirrors. "None of these are impossible problems,"

says O'Meara, who was a member of the LUVOIR team. He prefers a segmented design, which allows engineers to make the mirror bigger if the science requires it, without running into the space constraints of a rocket fairing.

Making it possible to send service and repair missions to a flagship telescope also marks a change for NASA. The Hubble telescope was serviceable—at huge expense—by space shuttle astronauts in low-Earth orbit. Future missions, Clampin says, will exploit the wealth of private companies that are developing robots to help service NASA's Artemis program of lunar exploration. "Robotic servicing is part of the architecture and philosophy" of the HWO, he says, adding that the extra distance of L2 "is not a great challenge." As well as extending the life of a mission by installing new instruments—as was done for Hubble—servicing also allows flexibility in development. If, say, one instrument proved tricky to get ready for launch, it could be added later. Extending the life of a mission also looks good to funders. "It makes it more palatable to Congress," O'Meara says.

Congress is perhaps Clampin's first big challenge. Last month, lawmakers allocated $1.51 billion to NASA astrophysics for this year, a decline of 4% from the previous year. Astrophysics was the only one of NASA's four science divisions to lose funding. Without funds to start GOMaP, Clampin is repurposing some existing tech development funding to support small studies of the trade-offs of different designs. After that, he says, he will "work with stakeholders to align funding." That's a polite way of saying that for the HWO to succeed, NASA—and the astronomical community—needs to get Congress onboard with the idea. ∎

Surge in illegal river mining revealed in global survey

Satellites show how mining has muddied waters in 173 tropical rivers

By **Paul Voosen**

A mighty river is an efficient miner. Year after year, its waters erode and sluice rock away from mountains, liberating precious metals and whisking them to lowlands, where they are deposited among sediments in riverbeds and floodplains. No need to move mountains; the mountain moves to you.

But the process also draws human miners, especially in the tropics, where homespun operations to extract gold and other riches from river sediments are poisoning waters and drowning aquatic life in sediment. The destruction wrought in places such as Peru, Ghana, and Sumatra has captured headlines. But the true global extent of the crisis has been obscured by verdant forest canopies, venal companies, and indifferent governments.

Now, a comprehensive satellite survey spanning 4 decades shows river mining has surged over the past 20 years and today affects 173 large rivers in 49 countries. The work, presented last month at a meeting of the American Geophysical Union, shows levels of suspended sediment have doubled, compared with premining levels, in some 80% of the rivers. In total, almost 7% of all large tropical river stretches are now cloudy with mining debris. "It's completely flown under the radar," says Miles Silman, a forest ecologist at Wake Forest University and coauthor of the study. "The pervasiveness was really shocking to me. It's just nuts."

The survey grew out of work by Bowdoin College geomorphologist Evan Dethier in the Peruvian Amazon. He and others have studied the growth of mining in Madre de Dios, a province bordering Brazil, sparked by a spike in gold's price during the 2008 financial crisis. The region's miners use small-scale techniques not unlike those in 19th century gold rushes. They dredge sedi-

Miners sift for gold in the riverbeds of the Peruvian Amazon. The global extent of river mining, which emits toxic mercury and stirs up sediment, is coming into focus.

ments from the beds and banks of the Amazon tributaries, then add mercury, a cheap and toxic liquid metal, to the watery slurry. It selectively binds to several precious metals, including gold, creating heavier nuggets that fall out of the slurry. After the nuggets are collected, the sediment "tailings" are dumped back into the river.

Up to $3 billion in gold is thought to be exported each year from Madre de Dios alone. Although a 2019 military crackdown pushed mining out of protected regions, the work has simply moved to other parts of the watershed, says Enrique Ortiz, a tropical ecologist at the Andes Amazon Fund. "In the general picture, it has gotten worse by the day."

Researchers have typically focused on the dangers of the mercury, which is burned off as a vapor. It settles in the surrounding ecosystem and can poison the miners themselves. But Dethier was shocked to see how muddy the mining had made the rivers in Madre de Dios. He wondered whether that increased muddiness could be seen on a global scale in Landsat satellite imagery since the 1980s. Dethier and his colleagues found the mud stood out in parts of the spectrum that Landsat is sensitive to, and they verified the observations by comparing them with on-the-ground measurements. That led to a paper last year documenting a global increase in suspended sediments in the tropics (*Science*, 24 June 2022, p. 1447).

The new work goes a step further. Combing through tens of thousands of river images by hand, Dethier and colleagues pinpointed where sediment loads begin to rise along each watercourse. They cross-checked those locations with high-resolution imagery from private satellite companies and scoured news and social media for any clues to the cause of the increased muddiness. Some was due to oil palm plantations, but mining was by far the dominant cause, Dethier says. In all, 381 sites showed a surge in muddiness because of mining.

The work "is incredibly powerful and something the community has needed for a while," says Jackie Gerson, a biogeochemist at the University of Colorado, Boulder, who has studied mercury pollution from mining in Peru and Senegal. Although environmentalists and activists have drawn attention to individual watersheds, the study shows how river mining is a global issue, in need of more attention and action, she says.

The study comes at a critical time, when "artisanal" mining operations are growing more sophisticated—and even more destructive, says Sara Geenen, a social scientist at the University of Antwerp. "You see all over the world a scaling up of activities." Miners who once used shovels and pans are now wielding backhoes and dredgers supplied by shady mining concerns, from China and elsewhere, says Bossissi Nkuba, a natural resources researcher at the Catholic University of Bukavu in the Democratic Republic of the Congo who has documented a scale-up in mining in the eastern part of the country. "It is really a larger endeavor."

Gold mining is now the world's top source of mercury pollution, emitting more than coal-fired power stations. A 2022 study led by Gerson found trees and birds in Madre de Dios contained mercury at levels resembling contaminated industrial regions in China. What all this mercury pollution is doing to residents, including nearby Indigenous tribes, is far less clear, Ortiz says. "We know more about the impact of mercury on wildlife than people."

The mud is likely taking an environmental toll, too. Much mining is in headwaters, where fish come to spawn, Ortiz says. In the cloudy water, "There's trouble seeing, and trouble breathing in the water," Bossissi says. The mud also degrades drinking water. That's not simply a local problem, Dethier adds: Some of this dirt washes as far as 1000 kilometers downstream.

There are no easy ways to reduce this damage. As long as the price of gold stays high and the cost of illegality is low, "it's worth the risk," Ortiz says. "If you're looking for quick cash, that's a way to go." It's important not to vilify the miners themselves, many of whom are simply trying to make a living, Geenen says. "The workers are victims." The real culprits, she adds, are the buyers and owners behind this work. So far, the gold industry has avoided the reputational tarnish that diamond companies had to reckon with for their "blood" diamonds, Gerson says. "It's superhard to trace where gold comes from."

However, the growing industrialization of the mining operations also presents a regulatory opportunity, Ortiz adds. Heavy machinery—and the fuel it needs—can be tracked and controlled, if the will is there. But too often, it is not, Ortiz says. A few months ago, he visited a part of Madre de Dios that was thought to have little potential for gold mining. But day in and day out, up and down the river, he ran into two- to three-person mining operations, all illegal, he says. "There were operations, one after another." ∎

A new antibody drug aims to slow the cognitive decline of Alzheimer's disease, a fatal disorder that has caused this patient's brain to atrophy.
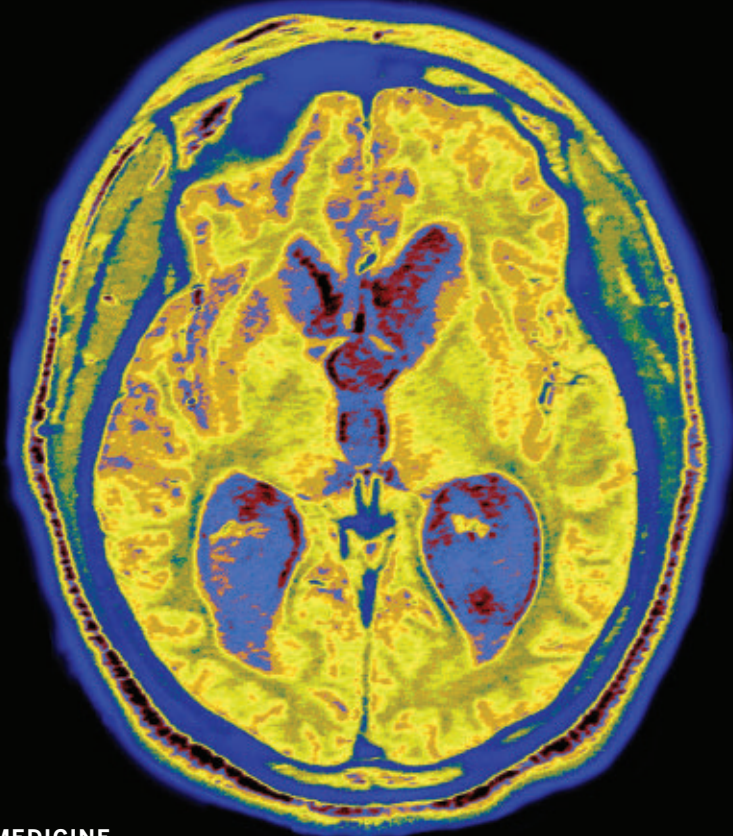
BIOMEDICINE

Alzheimer's drug approval gets a mixed reception

FDA allows use of antibody despite ongoing debates over its benefits and dangers

By **Jennifer Couzin-Frankel**

L ast week's Food and Drug Administration (FDA) approval of the first Alzheimer's drug to clearly slow the disease's cognitive decline prompted cheers in many quarters, but consternation in others. The benefits of the drug, an antibody called lecanemab, appear modest and have only been shown in people with early Alzheimer's. It also comes with serious side effects including brain swelling and bleeding.

Still, the prospect of finally having something to offer people with a ruinous neurodegenerative disease has won over many scientists and physicians. "I'm on the side that it's not perfect, but it's a step in the right direction," says Joy Snider, a neurologist at Washington University School of Medicine in St. Louis who was part of the recent phase 3 trial that demonstrated the drug's efficacy—but also highlighted its potentially grave risks.

Now, a second U.S. regulatory agency must decide whether to reverse a controversial stance that would preclude federal reimbursement for the drug outside of clinical trials. The treatment, which must be given intravenously every other week, requires close monitoring and is likely to cost tens of thousands of dollars a year.

Hospitals and medical groups are now weighing guidance on which people should be offered the antibody. Sam Gandy, a neurologist at the Icahn School of Medicine at Mount Sinai, is on a committee there that's developing guidance for its hospital. He believes that "it's a fairly small minority of patients" that will qualify, about 20% of those with early Alzheimer's. One reason is that Gandy prefers not to go beyond the profile of participants in the phase 3 trial, which excluded people with various preexisting conditions such as a history of stroke.

Another is the side effects that emerged during the nearly 1800-person clinical trial. The antibody is designed to clear or prevent the creation of amyloid plaques, protein deposits in the brain that are thought to pro-

pel cognitive decline and other symptoms of Alzheimer's disease. But such drugs can put patients at risk for the mix of brain bleeds and swelling known as ARIA, which stands for amyloid-related imaging abnormalities, perhaps because the antibodies also strip amyloid deposits in blood vessel walls, weakening them.

In the phase 3 lecanemab trial, the danger of ARIA appeared greater for patients also taking drugs that prevent or dissolve blood clots. Two people given those drugs while taking lecanemab as part of an extension of the trial died after brain bleeds or swelling, *Science* and *STAT* have reported, and some others had serious brain injuries.

Data from the phase 3 trial haven't yet been submitted to FDA, which made its decision based on earlier, smaller trials. But the agency was also familiar with basic findings of the large trial, which were published in November 2022. In a 54-page summary report describing its reviewers' analyses, FDA said it can't pin any of the trial deaths on lecanemab. The drug's main developer, the Japanese biotech Eisai, and its U.S. partner Biogen have taken the same position.

Yet in approving the drug, FDA recommended "additional caution" in prescribing it to people taking blood thinners. And *Science* learned that in July, Eisai distributed a revised consent form alerting trial participants that the risk of a major brain bleed in people on both the antibody and blood thinners "is estimated to be more than 1 in 100 people, but less than 5 in 100 people." The form noted that bleeding "can be serious and can even lead to death." Gandy says he would advise "virtually all" patients on anticoagulants "not to proceed" with lecanemab treatment.

People with two copies of *APOE4*, a gene variant that increases risk for Alzheimer's, also seem at higher risk of ARIA. For example, 9.2% of people with two copies of the variant had symptomatic brain swelling in the pivotal lecanemab trial, compared with 1.4% with no copies. And a third death in the lecanemab trial, which *Science* recently described, involved a 79-year-old woman who had two copies of *APOE4*. She died in mid-September, days after experiencing what looked like a stroke at a restaurant; doctors who treated her at a hospital found extensive brain swelling and bleeding.

Several neurologists who reviewed the woman's case for *Science* said lecanemab was likely the culprit in her death. FDA noted that it has requested MRI images and the autopsy report on the woman, but "the applicant has not been able to obtain additional

information as of January 3. … The available information does not change the risk-benefit assessment for this review."

People with Alzheimer's disease aren't routinely tested for *APOE4* because it hasn't so far guided diagnosis and treatment. Although some scientists had hoped FDA would rule against giving lecanemab to people with two copies of *APOE4*, the agency instead suggested people "consider testing" for *APOE4* status "to inform the risk of developing ARIA when deciding to initiate treatment." Gandy's hospital expects to offer testing for *APOE4* to those interested in lecanemab, to help them better gauge their risk from the therapy.

The drug label approved by FDA also recommends that anyone taking lecanemab have three MRIs over roughly the first 6 months of treatment to watch for side effects, as well as an MRI before beginning treatment. Some scientists had hoped the agency would require that lecanemab be enrolled in FDA's Risk Evaluation and Mitigation Strategies (REMS) program for medications with "serious safety concerns." REMS can require that physicians prescribing a new drug report side effects to FDA, that the drug be administered in qualified health care settings, and that doctors get training about which patients may be at highest risk of dangerous side effects.

FDA did note that it's requesting "expedited reporting" of any deaths in ongoing trials and deaths from significant brain hemorrhages in people who take lecanemab postapproval. University of Cincinnati neurologist Alberto Espay also worries about recipients of the antibody who may develop less severe ARIA. For at least some of them, he says, "I cannot imagine it's irrelevant or inconsequential."

Discussion of these safety concerns comes amid continued debate over lecanemab's benefits. On an 18-point cognition scale, those getting the drug on average declined 0.45 points less than those getting placebo after 18 months. Neurologists disagree over whether patients and caregivers would perceive this difference. "It's really on the edge" of what's meaningful, says Lon Schneider, a geriatric psychiatrist at the University of Southern California Keck School of Medicine. The drug is "approvable, but like many medications that are approved it leaves much to be desired."

Others, such as Snider, say the benefits may well be noticeable. On the part of the scale that assesses orientation, she notes, an individual who scores 0.5 "can still drive" and

> **"Like many medications that are approved, it leaves much to be desired."**
> **Lon Schneider**, University of Southern California Keck School of Medicine

get around independently. "If you go to a one, you're going to start getting lost."

The Alzheimer's Association, which has come out in favor of lecanemab, celebrated FDA's thumbs-up. And in the lead-up to the agency's decision, more than 200 researchers and physicians signed an open letter that endorsed the drug. Nearly half are recent consultants or grant recipients of Eisai or Biogen, *Science* has found.

Espay, however, argues FDA had painted itself into a corner with an earlier decision. He says officials "are victims of an artificially low bar" they set in 2021 when they approved another anti-amyloid antibody, aducanumab, even though FDA's advisory committee had voted against approval and the evidence that the drug worked was weak. (Last month, a congressional report described that approval process as "rife with irregularities.")

Both drugs were approved under FDA's accelerated approval pathway, which allows for decisions based on "surrogate endpoints," biological measures thought to predict clinical benefits to patients. In May 2022, Eisai had asked FDA to approve lecanemab based on evidence that it is highly effective at clearing the brain of amyloid plaques, the same surrogate endpoint cited in the aducanumab approval.

Many of the same FDA officials reviewed both drugs, and in both cases, the lead biostatistician, Tristan Massie, expressed hesitations. In the summary report for lecanemab, Massie questioned whether the surrogate endpoint "is reasonably likely to predict change on the clinical outcome." His colleagues didn't agree. "The Division notes the issues that Dr. Massie has raised but, overall, the findings" on amyloid plaques "appear robust and persuasive," they wrote.

But it's unclear whether the Centers for Medicare & Medicaid Services (CMS), the federal agency that pays for many treatments for older Americans, will reimburse for lecanemab. In April 2022, CMS announced it would decline to reimburse for aducanumab, except in certain clinical trials, tanking its commercial prospects. CMS also said it would only consider covering such anti-amyloid antibodies after full FDA approval.

In a statement after FDA approved lecanemab, the Alzheimer's Association called that stance "harmful and unfair" and called on CMS to reverse its position. ∎

FDA no longer has to require animal testing for new drugs

Agency can rely on animal-free alternatives before human trials

By **Meredith Wadman**

New medicines need not be tested in animals to receive U.S. Food and Drug Administration (FDA) approval, according to legislation signed by President Joe Biden in late December 2022. The change—long sought by animal welfare organizations—could signal a major shift away from animal use after more than 80 years of drug safety regulation.

"This is huge," says Tamara Drake, director of research and regulatory policy at the Center for a Humane Economy, a nonprofit animal welfare organization and key driver of the legislation. "It's a win for industry. It's a win for patients in need of cures."

In place of the 1938 stipulation that potential drugs be tested for safety and efficacy in animals, the law allows FDA to promote a drug or biologic—a larger molecule such as an antibody—to human trials after either animal or nonanimal tests. Drake's group and the nonprofit Animal Wellness Action, among others that pushed for changes, argue that in clearing drugs for human trials the agency should rely more heavily on computer modeling, "organ chips," and other nonanimal methods that have been developed over the past 10 to 15 years.

But pro-research groups are downplaying the law, saying it signals a slow turning of the tide—not a tsunami that will remake the drug approval process overnight. Jim Newman, communications director at Americans for Medical Progress, which advocates for animal research, argues nonanimal technologies are still "in their infancy" and won't be able to replace animal models for "many, many years." FDA still retains tremendous discretion to require animal tests, he notes, and he doesn't expect the agency to change tack anytime soon.

In order for a drug to be approved in the United States, FDA typically requires toxicity tests on one rodent species such as a mouse or rat and one nonrodent species such as a monkey or dog. Companies use tens of thousands of animals for such tests each year. Yet more than nine in 10 drugs that enter human clinical trials fail because they are unsafe or ineffective, providing grist to those who argue that animal experiments are a waste of time, money, and lives.

"Animal models are wrong more often than they are right," says Don Ingber, a Harvard University bioengineer whose lab developed organ chip technology now being commercialized by the company Emulate, where he sits on the board and owns stock.

Such chips typically consist of hollow channels embedded in silicone-based polymers about the size of a computer thumb drive. The channels are lined with living cells and tissues from organs such as the brain, liver, lung, and kidney. Fluids flow through them to mimic blood flowing through tiny vessels and fluid tracking through tissues, as it does in living organs. In the body, drug damage often shows up in the liver because it breaks down drugs for excretion. A human liver chip can warn of such toxicity when an experimental drug pumped through it damages the cells.

Last month, Lorna Ewart, chief scientific officer at Emulate, Ingber, and colleagues published a study highlighting the potential of this technology. The company's liver chips correctly identified 87% of a variety of drugs that were moved into humans after animal studies, but then either failed in clinical trials because they were toxic to the liver or were approved for market but then withdrawn or scaled back because of liver damage. The chips didn't falsely flag any nontoxic drugs.

Other animal alternatives include organoids—hollow, 3D clusters of cells that are derived from stem cells and mimic specific tissues. They have shown promise in predicting liver and cardiac toxicities. Proponents also tout the potential of digital artificial neural networks for rapidly identifying the toxic effects of drugs.

Some drug companies have chafed at FDA's animal testing requirement, arguing that animal studies cost them millions of dollars, slowing drug development and making the medicines

Tens of thousands of rodents are used by companies for drug toxicity testing each year.

that do reach the market far more expensive. In 2019, Vanda Pharmaceuticals sued the agency, charging that its requirement of additional toxicity testing of an antinausea drug in dogs was unreasonable. A U.S. judge ruled against the company in 2020, citing the animal testing requirement in what was then the law governing FDA's drug assessments.

Now, that requirement is gone. In eliminating it, Congress seems to have responded to the emergence of nonanimal methods and growing public sentiment against animal research. Senator Rand Paul (R–KY) and Senator Cory Booker (D–NJ), who both call animal research inefficient and inhumane, introduced the changes, which the Senate passed by unanimous consent in September 2022. In December, Biden signed them into law as part of the Consolidated Appropriations Act, which funds the government through this fiscal year.

Wendy Jarrett, CEO of Understanding Animal Research, an animal research advocacy group based in the United Kingdom, doesn't share animal advocates' delight at the changes. She says nonanimal methods can't capture all the ways a drug might put human trial participants at risk. "We can drop a new [candidate

A liver chip made by Emulate contains cells and fluids found in the human liver.

drug] onto a bunch of liver cells. And we can see that it doesn't damage them," she says. "But what we don't know is whether it's going to make the person cough, whether it's going to damage their intestines or their brain."

FDA's chief scientist says the agency is in favor of trying to move away from animal testing—when other approaches are ready. "We support alternative methods that are backed by science and provide the necessary data showing whether products are safe and effective," Namandjé Bumpus says. "We continue to encourage developers working on alternative methods to present their work to the FDA." She also notes that the agency requested and received $5 million this year to launch an FDA-wide program to develop methods to replace, reduce, and refine animal testing.

Still, it remains unclear just how much the new law will change things at FDA. Although the legislation *allows* the agency to clear a drug for human trials without animal testing, it doesn't *require* that it do so. What's more, FDA's toxicologists are famously conservative, preferring animal tests in part because they allow examination of a potential drug's toxic effects in every organ after the animal is euthanized.

The main impact of the new law is that it opens the way for FDA and a company to have a serious discussion about whether alternatives are adequate, says Steven Grossman, a former deputy assistant secretary of health who advises companies on their FDA applications. "It provides a little additional authority. It says in law: 'Congress is cool that these discussions are going on.'" ■

Mutations help genes emerge from aimless DNA

By allowing genetic messages to make proteins, the changes led to key brain genes

*By **Elizabeth Pennisi***

Biologists have shone a light on an evolutionary mystery: how stretches of seemingly useless DNA can become meaningful, protein-coding genes. New genes are known to arise when existing ones are accidentally duplicated, freeing one copy to evolve novel or additional functions. But some genes seem to evolve from stretches of DNA once disparaged as "junk."

Now, a study has identified mutations that play a key part in this process: They enable RNA encoded by this DNA to slip out of the cell nucleus into the cell cytoplasm, where it can be translated into a protein. The study highlights 74 human protein genes that appear to have evolved this way, including some that may have helped drive the evolution of our large and complex brains.

"This work is a big advance," says Anne-Ruxandra Carvunis, an evolutionary biologist at the University of Pittsburgh who was not involved with the research, which was reported last week in *Nature Ecology & Evolution*. It "suggests that de novo gene birth may have played a role in human brain evolution." Manyuan Long, an evolutionary biologist at the University of Chicago, calls the new study "a breakthrough in the understanding of the molecular evolutionary processes that generate [new] genes."

A decade ago, Chuan-Yun Li, an evolutionary biologist at Peking University, and colleagues discovered that some human protein genes bear a striking resemblance to DNA sequences in rhesus monkeys that get transcribed into long noncoding RNAs (lncRNAs), which don't make proteins or usually have any other purpose. How those stretches of monkey DNA could have become true protein-coding genes was a mystery, but Li's postdoc, Ni A. An, discovered a clue.

Many lncRNAs, An found, have a hard time exiting the nucleus and traveling to ribosomes, the organelles that translate messenger RNA (mRNA) into proteins. The researchers then searched for differences between protein-coding genes whose mRNA got out of the nucleus and DNA sequences whose RNAs did not. Stretches of DNA known as U1 elements seemed to be the key: When transcribed into RNA they make the strand too sticky to escape. In protein-coding genes, mutations have altered or eliminated the U1 elements to make the RNA less sticky.

"This makes perfect sense because for an RNA to be translated, it needs to go the cytoplasm [where ribosomes are found] first," says Maria Del Mar Albà, an evolutionary biologist at Hospital del Mar Medical Research Institute in Barcelona.

In search of genes that originated this way, Li's team scoured the human and chimpanzee genomes for protein-coding genes that had lncRNA counterparts in rhesus monkeys, as well as the crucial U1

Scientists have traced the birth of dozens of human-specific genes, including some that may have expanded our brains beyond the size of other primates, from DNA sequences that once only made RNA.

element mutations. Dozens fit the bill, including nine that are active in the human brain. To learn what they do, Li's collaborator Baoyang Hu, a neuroscientist from the Chinese Academy of Sciences Institute of Zoology, grew clumps of human brain tissue called cortical organoids with and without each of these genes. Two of them made the organoids grow slightly bigger than normal.

When Hu introduced the genes into mice, their brains also grew larger and developed a bigger cortex, the wrinkly outer layer of the mammalian brain that in humans is responsible for high-level functions such as reasoning and language. One of the genes also caused the animals' brains to develop more humanlike ridges and grooves, and mice that carried it performed better on tests of cognitive function and memory than mice lacking this gene. Li and Hu's team says it will soon report these findings in *Advanced Science*.

Xiaohua Shen, a molecular biologist at the Tsinghua University School of Medicine, says she wishes the authors had studied a larger sample of mice to be sure the differences in brain size couldn't be explained by natural variation. Long adds other reasons to be cautious about concluding the genes had a role in human brain expansion: Organoids are far simpler tissues than the brain itself, he notes, and human and mouse brains have evolved along very different paths.

But Long doesn't doubt that many key genes do emerge from noncoding sequences. His own group has found that most of the recognizable de novo genes in rice were once lncRNAs, and that lncRNAs also helped form new genes in bamboo.

Carvunis says there's still much to be learned about how DNA sequences eventually become true genes after their RNAs gain the ability to escape from the nucleus. "There are a lot of barriers to gene birth," she says. "I hope this work will contribute to inspiring more research towards understanding what these barriers are and how emerging genes can overcome them." ∎

LIFTING THE VEIL

Alien planets are shrouded in hazes that hide clues to their makeup. Lab experiments could help clear the view *By* **Zack Savitsky**

n 2013, from a windowless office at the University of Chicago, Laura Kreidberg peered into the sky of a distant planet. Kreidberg, then an astronomy graduate student, parsed data from the Hubble Space Telescope, its gaze set on the exoplanet GJ1214b, roughly three times the size of Earth. GJ1214b is a popular target for astronomers seeking clues to the nature of alien worlds, and not only because it's relatively close, a mere 48 light-years away. It also orbits its star every 1.5 days, and each lap exposes its atmosphere to inspection.

On every pass, the planet briefly eclipses a portion of the star's face. A fraction of the star's light filters through the planet's atmosphere, where different molecules absorb the light at characteristic wavelengths. By layering Hubble observations of 15 eclipses, Kreidberg hoped to see how GJ1214b's atmosphere gobbled up parts of the rainbow, creating distinctive dips in the light. Markers for water vapor would hint at the presence of oceans, whereas sulfur signatures could indicate volcanoes.

But to her disappointment, "the spectrum got flatter and flatter and flatter," says Kreidberg, now at the Max Planck Institute for Astronomy. Light just wasn't getting through. The planet's impenetrable atmosphere could only indicate one thing, she concluded: A layer of aerosols high in the atmosphere was blocking the light. The chemical richness she wanted to capture was hidden beneath mysterious clouds or hazes.

Frustrated, she wrote up her results. The paper, published in *Nature* in 2014, sparked a reckoning for exoplanet astronomers. They had spent decades preparing to dissect exoplanet atmospheres with JWST, the massive new space telescope that began operations last year with six times the light-gathering power of Hubble. With its superior resolution and a wavelength range extending into the infrared, they hoped to detect potential exoplanet biosignatures: molecules that indicate life, such as oxygen or a combination of carbon dioxide and methane.

But they had mostly ignored the possibility that JWST's view would be obstructed by suspended aerosols—either cloud droplets, formed when gases condense, or haze particles, formed through light-driven chemical reactions. Thanks to observations of GJ1214b and a handful of similarly muted exoplanets, astronomers now acknowledge that hazes and clouds are likely to veil most of JWST's exoplanet targets—as they do every planet and moon with an atmosphere in the Solar System.

"What we don't want is to spend all our efforts building enormous, billion-dollar telescopes to get data we don't understand," says planetary scientist Peter Gao of the Carnegie Institution for Science. Researchers have a decent understanding of how a handful of common planetary gases interact and condense into clouds. But hazes—which can be made up of any number of tens of thousands of complex molecules—are more mysterious. Without laboratory experiments to show how they arise, what they are, and how they interact with light, Gao says, "it's like putting together a puzzle, but you're missing a piece."

Thankfully, a handful of haze researchers are prepared to supply that missing piece. One is Sarah Hörst, a planetary scientist at Johns Hopkins University who has spent years trying to understand methane-based hazes on Titan, an icy moon of Saturn, by re-creating them in the lab. Prompted by the wake-up call from the GJ1214b spectrum—what she calls "the most expensive flat line in the history of science"—Hörst modified her setup to create haze particles in warmer exoplanet conditions. At the behest of anxious

> ## "What we don't want is to spend all our efforts building enormous, billion-dollar telescopes to get data we don't understand."
>
> **Peter Gao**, Carnegie Institution for Science

JWST observers, Hörst and her colleagues this week released long-awaited measurements of how the particles absorb and scatter light—providing a critical update to outdated models and a guide to help observers make sense of spectra flattened and distorted by alien hazes. "We have to go to the laboratory to reproduce the conditions," Kreidberg says. "That is really the key to solving this problem."

THE EFFORT to simulate photochemistry in the lab traces back to the famed Miller-Urey experiment in 1952, which attempted to re-create prebiotic chemistry on early Earth. In the 1970s, Carl Sagan and Bishun Khare, planetary scientists at Cornell University, extended this work to other bodies in the Solar System. By subjecting nitrogen and methane gases to light and radiation, they produced sticky grains made up of long-chain carbon-based molecules. They called them "tholins," after the Greek word for "muddy." (The runner-up name was "star tar.") These particles helped explain the diffuse blue glow around Pluto that NASA's New Horizons mission captured in 2015, and their organic complexity helped motivate the search for life on Titan.

The scientists also used an array of instruments to study how the particles block light across a wide range of wavelengths—from x-rays all the way to microwaves. The work was "maybe a little too meticulous," recalls Gene McDonald, then a postdoc in Sagan's lab who's now a biochemist at the University of Texas (UT), Austin. But because it was so thorough, the data remain valuable half a century later.

Sagan and Khare showed how the haze particles scatter light in different directions, which would erode many of the distinctive absorption features in starlight passing through a planet's atmosphere. But they found this effect depends on the size and composition of the particles. For example, Earth's sky is blue because small nitrogen and oxygen molecules in the atmosphere preferentially scatter shorter, blueish wavelengths of light, whereas clouds appear white because their much larger water droplets scatter sunlight evenly.

Besides scattering light, tholins also absorb it at certain wavelengths, with each molecular bond soaking up a sliver of the spectrum, the researchers found. Even though an exoplanet haze might stomp out signs of atmospheric gases, a tholin's own absorption signature offers clues. If it is one that has been studied in a lab, the atmospheric composition can be inferred based on the gases used in the experiment.

"Most of the time, people treat these particles as nuisances," says Lia Corrales, an astronomer at the University of Michigan, Ann Arbor. In a paper posted this month to the preprint server arXiv, Corrales and colleagues show how even slight changes to experimental conditions can produce tholins with distinct optical properties. "Aerosols themselves have some of that [compositional] information because they have spectral shapes," she says.

To glean that information from the spectra they observe, astronomers need to have a point of comparison: a predicted spectrum for a given mixture of gases, clouds, and haze. Scientists spin out forecasts for hypothetical atmospheres using computer programs such as the Planetary Spectrum Generator, which sometimes draws more than 1 million hits a month, according to its developer, Geronimo Villanueva at NASA's Goddard Space Flight Center (GSFC). In addition to varying the atmospheric composition, users of the program can account for hazes or clouds by entering their optical properties.

The trick is knowing those properties. Databases exist for clouds, but not for different hazes. In fact, most modelers still rely on tholin properties from the Sagan-Khare experiments 40 years ago—which were

NASA's New Horizons mission captured the blue glow from Pluto's haze in 2015.

designed for Titan, an environment that's nothing like most exoplanet atmospheres. Some instead opt to use data for ordinary soot, which has well-studied properties but is also unlikely to be found on an exoplanet. "We basically have a menu of two to choose from, and beyond that, we just make things up—we guess," says Eliza Kempton, an astronomer at the University of Maryland, College Park. A wrong guess could mean misinterpreting the atmosphere's makeup. The knowledge gap about exoplanet-relevant hazes has been "the elephant in the room" for years, Villanueva says.

NIKOLE LEWIS, an astronomer at Cornell, says efforts to fill the gap have been slowed by a disconnect between exoplanet and planetary science. Because of the way NASA funding is siloed, "the same infrastructure that we use to explore planets in our own Solar System is not immediately transferable to exoplanets," she says. "We just had to basically grow the momentum to be able to do these types of experiments."

And so, Lewis grew it herself. As disappointingly flat exoplanet spectra trickled in, Lewis turned to Hörst, a close friend from graduate school who had just started to build her own tholin chamber for studies of Titan. Over the course of a year, Lewis worked to sell Hörst on modifying her setup to use the different gas mixtures and higher temperatures expected for looming exoplanet targets. Finally, in 2016, the team received funding from a new NASA exoplanet research program. They were ready to make some exo–star tar. "We knew how hard these experiments were going to be, and there was a little bit of buyer's remorse there," Hörst says with a chuckle. "The things we do for the exoplanet people."

The first challenge was figuring out the ingredients of atmospheres that haven't yet been observed. To start off, Hörst and Lewis narrowed their scope to super-Earths, exoplanets two to 10 times the mass of our planet. (As the most common type of planet in the Milky Way, super-Earths are a primary target for JWST.) Then, they ran models to predict the atmospheric gases that might be present for a range of temperatures and bulk compositions. They were left with 12 archetypes—hypothetical combinations of gases such as hydrogen, water vapor, and carbon dioxide that should represent genuine exoplanet conditions.

Then came the experimental hurdles. First, they had to rig up a way to simultaneously mix eight or nine gases—many of which are toxic, flammable, or otherwise hard to handle. Next, rather than cooling the gases down as for Titan, they had to be able to heat the mixture to more than 520°C. Worst of all were the water-rich planets. They might be sanctuaries for life, but they are a pain for postdoctoral student Chao He, who treks to the lab repeatedly through the night to replace stashes of dry ice. The cold helps the water vaporize into the chamber at the right pressures. "I have to babysit the experiment," He says. "It's not pleasant."

When He flips a valve, the gas mixture races down pipes, twirls around a heating coil, and flows through a stainless steel chamber the size of a water bottle. There, the gas is held at light pressures meant to simulate the thin air at the top of an atmosphere. He floods the chamber with ultraviolet (UV) light, to replicate starlight, or radiation from a plasma discharge source, to mimic solar storms and cosmic rays. After 3 to 5 days, he pumps out the gas and cracks open the chamber within a glovebox. With a spoon, He scrapes tholins off the walls into a vial or dish.

The team was concerned the modifications might not yield enough hazes to study—or that they would destroy the setup entirely. "This was a giant leap of faith on Sarah's part," Lewis says. "And it paid off."

Using microscopes, spectrometers, and other instruments, the researchers measured the size, optical properties, and density of the particles. It was immediately obvious that the samples, gold and olive green in color, were radically different from Sagan and Khare's brownish Titan tholins. Some experiments generated haze without adding

Dissecting alien worlds

When an exoplanet eclipses its star, a portion of the starlight filters through the planet's atmosphere. Space telescopes such as JWST can capture the light and identify gases based on how they absorb specific wavelengths. But hazes and clouds sometimes get in the way.
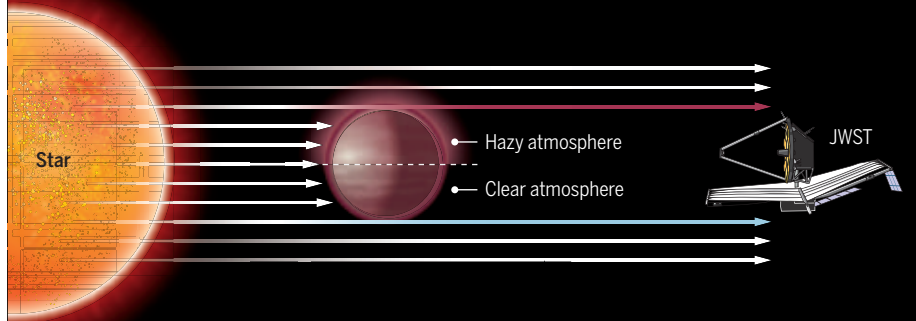
Reading the haze

Hazes can mute some absorption features by scattering starlight. However, they can encode clues of their own in the way they absorb certain wavelengths of light.

The slope of a smooth spectrum is affected by the light-scattering properties of the haze.

Some hazes have unique absorption features, which can help reveal their composition.

● Hazy atmosphere   ● Clear atmosphere

Wavelength of light (micrometers)
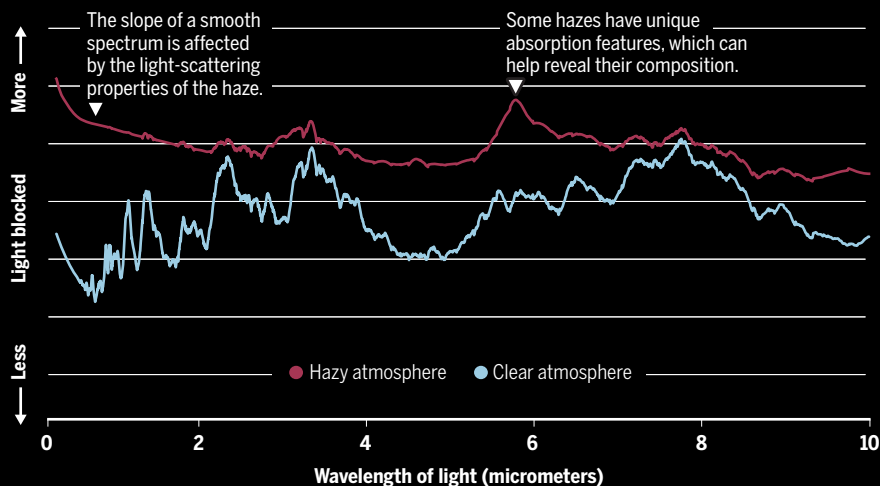
Note: Chart shows computer-generated spectra for the exoplanet GJ1214b. Rather than looking for dips in the light, astronomers typically flip the Y axis and look for absorption peaks.

Researchers at Johns Hopkins University create hazes by irradiating gases in a steel chamber. The color of the haze particles offers clues to their composition.

methane, long thought to be an essential ingredient for these large organic molecules. Another surprise came after Sarah Moran, then Hörst's graduate student who's now an astronomer at the University of Arizona, brought samples to the Institute for Planetary Sciences and Astrophysics in Grenoble, France. (She prayed she wouldn't get stopped by customs for the "weird, strangely colored powders" in her suitcase.) There, Moran found that the tholins appeared to contain amino acids and nucleobases—primary building blocks of life.

That may be no coincidence—some researchers believe hazes could be critical to kick-starting life. In 2017, Giada Arney, an astrobiologist at GSFC, modeled the behavior of hazes on early Earth—which she deems "the most alien planet we have geochemical data for."

At the time, billions of years ago, Earth's atmosphere was thought to be mostly nitrogen with some carbon dioxide, methane, and water vapor. That recipe would give rise to organic hazes similar to Titan's and water clouds like those on Earth today. Arney ran climate models to simulate the effects of these aerosols on Earth-like planets. She found that, in addition to hosting complex organic chemistry, some hazes reflect light and help keep a planet from overheating, whereas others reduce UV rays on the surface by up to 97%. Both effects could make an exoplanet more habitable.

She also found certain hazes only form when the atmosphere contains so much methane that living organisms must be making it.

Such a haze could itself be a biosignature, Arney says—and one that JWST might be able to detect. But not without "a good library of optical properties of hazes," she says.

AT LONG LAST, she's getting her wish. This week, Hörst and colleagues posted a study to arXiv that unveils optical properties across the entire JWST wavelength range for two of their exoplanet tholins—generated in the warm, water-rich atmospheres that produced the most haze.

The team plans to cook up several more haze analogs, coordinating its experimental conditions with incoming JWST observations and cataloging the most abundant tholins. Exoplanet astronomers are yearning to get their hands on the data, Gao says. "We've been waiting for this for decades, really," he says. "Sarah's work will be immediately used by groups around the world."

Still, Hörst's experiments will only explore a fraction of possible planetary conditions. Thankfully, she's not the only player in the tholin game. At NASA's Jet Propulsion Laboratory, Benjamin Fleury is exploring hazes that might form on much hotter exoplanets, the giant, close-in "hot Jupiters" that reach temperatures of more than 1200°C. At LATMOS, a research institute near Paris, scientists modified Titan haze experiments to approach conditions that might be found on an Earth-like exoplanet—by adding oxygen, for example.

Some researchers are focused instead on exoplanet clouds, including Alexandria Johnson, an atmospheric scientist at Purdue

University who grows and studies clouds in a chamber. She wonders how clouds and hazes might interact on an exoplanet—whether, for example, haze particles might promote cloud formation by providing "nucleation sites" for gases to condense. The experimental diversity is critical, says Thomas Gautier, a planetary scientist on the LATMOS team. "Nobody's trying to claim that we do it better than the other—we do it differently, and that's a good thing."

Partitioning the work only pays off if everyone's on the same page, though. Xinting Yu at UT San Antonio recently initiated the first cross-laboratory tholin comparison study—an effort that will standardize production and measurement techniques and boost confidence in the results. Meanwhile, Ella Sciamma-O'Brien at NASA's Ames Research Center is building a centralized database for the different teams to house their optical measurements.

The collaborations will come in handy as new JWST observations pour in—including ones of GJ1214b, the planet that started it all. In July 2022, Kempton, Kreidberg, and colleagues got about 40 hours of time on the telescope to look at it. They are still analyzing the observations, but—thanks to JWST's infrared vision and help from these experimental hazes—Kreidberg hopes to decode the atmosphere that has long evaded her.

"This planet is kind of like a white whale—we've been chasing after its secrets for over a decade now," Kreidberg says. "I think this time we finally caught it." ∎

INSIGHTS

SCIENCE AND THE HUMANITIES

"Storylistening" in the science policy ecosystem

Expert analysis of narrative can complement and strengthen scientific evidence

By **Claire Craig**[1] and **Sarah Dillon**[2]

From the climate crisis to the COVID-19 pandemic, many questions that practitioners and scientists are asking about how to improve the quality and usefulness of science advice require answers that exceed what many consider the definition of "science" (*1*). It has been argued that disaster follows from failing to learn from all possible areas of research and knowledge (*2*), yet many scientists see a systemic obstacle: the fear that by extending credibility to new forms of evidence, public reasoning enters a post-truth freefall. This fear must be balanced against the growing risk that science might actually become less influential: Because it is embedded in sys-

tems that are unable to accommodate other forms of rigorous knowledge, the focus of public debate may move on and away from academic rigor altogether, to everyone's loss. A "storylistening" framework shows how robust narrative evidence can complement and strengthen scientific evidence (*3*).

Stories, or narratives, when expertly incorporated, can help augment scientific knowledge. But the ubiquity of narratives, a general focus on the context of public reasoning on telling stories rather than listening to them, and the unruly power of a charismatic (persuasive or popular) narrative all mean that cognitive and collective functions of narratives are widely overlooked or dismissed as too difficult to include in the provision of expert evidence.

FOUR FUNCTIONS OF STORIES

In their investigation of how to put knowledge and reason at the heart of political de-

cision-making, the European Commission (EC) highlights the importance of framing, narrative, and metaphor (*1*). How an issue is framed determines from the very start what is taken to be the target system, the part of the world that matters most to the issue and determines what forms of evidence are deemed relevant and sought out.

New points of view

Storylistening provides new points of view to inform the framing of the target system and the policy debate. For example, in the science and policy of machine learning and artificial intelligence (AI), framings of human- or superhuman-level intelligence are charismatic, whether as motivations for research, such as developing systems to beat humans at chess or Go, or as popular stories from the *Terminator* films. But framing AI around humanoid intelligence potentially distracts from the issues of its

[1]The Queen's College, University of Oxford, Oxford, UK. [2]Faculty of English, University of Cambridge, Cambridge, UK. Email: claire.craig@queens.ox.ac.uk

use in the distributed systems through which, for the present, much bigger policy outcomes are at stake owing to concerns such as algorithmic bias. Stories about AI that have often been overlooked, but which could have helped or could still help with the reframing, include narrative models from science fiction, such as Asimov's "The Evitable Conflict" (1950), Heinlein's *The Moon is a Harsh Mistress* (1966), or the television series *Person of Interest* (2011–2016), narrative documentaries such as the film *Coded Bias* (2020), and testimonies of people's experiences of such systems.

Collective identities

Stories function to create and consolidate collective identities. As is well understood in the social sciences, the identification and understanding of collective identities matter to public reasoning. Storylistening offers new ways to explore what the collective identities relevant to a particular system are, and what they mean. The stories that AI researchers value and share illustrate some of their collective characteristics (*4*). Novels such as Kingsolver's *Flight Behaviour* (2012), or Eggers' *Zeitoun* (2010), model the differential impact of climate change and extreme weather events

on different collective identities and the interactions between them. Narrative evidence could be valuably included in evidence syntheses of multidisciplinary approaches to defining and exploring the collective identities that link to people's behaviors with respect to vaccination.

Models

Computational models are essential to major areas of public decision-making such as climate change and epidemiology, and such models serve multiple purposes that put them at the heart of science advice (*5*). Scientific models themselves are already "mixed instruments" in which stories play an integral role in model usage, both in prompting specific runs of the model and in relating the results to the target system (*6*).

Studies of narratives can extend the range of plausible causal accounts of the behaviors of the complex systems that matter most to policy, expanding the "ensembles" of models that are available with which to think and reason. For climate change, expertly considered stories could help link the global to the local, the physical to the social and biological, the probabilistic to the deterministic, and go much further than scientific models can alone in exploring the relationships between climate, weather, and the natural, physical, and human systems on which societies depend.

To take a controversial example, which also shows how narrative evidence should only be used as part of a pluralistic evidence base, consider Crichton's *State of Fear* (2004). Scientists exposed its misrepresentation of climate science and its data but, at the same time, experts from the social sciences and humanities have identified that the novel remains useful as a narrative model that enables surrogative reasoning about the politics of knowledge, facts, and truth—for example, by illustrating within the story how certain types of information presented as scientific evidence can be used to support directly opposing beliefs and political positions.

Anticipating

Anticipating the future, individually and collectively, is key to today's decisions. Narrative models and narrative futures methods, complementing computational ones, can create plausible futures about economics, about nonhumanoid forms of AI, about dealing with recurring extreme weather events, or about how a society might organize itself to achieve net zero greenhouse gas emissions.

One recent acknowledgment of the potential for narratives was the inclusion of novelist Kim Stanley Robinson at the United Nations Climate Change Conference

(COP26) in 2021. His novel *Aurora* (2015) anticipates in detail how a society might organize itself to live in a zero-waste economy, explored through the artificial constraint of deep space travel. Robinson's *The Ministry for the Future* (2020) was recently included in a list of seven books one should read to understand climate change (*7*). The novel encompasses all four functions of stories, reframing climate change as a challenge not just for the physical sciences but for global governance, economics, individual action, and the imagination; modeling the collective identities at play in addressing it, and the solutions needed (technological, diplomatic, economic, narrative); and anticipating a future in which through painstaking multilateral negotiation and a multipronged approach to solutions, successful abatement of climate change is achieved.

OPERATIONALIZING STORYLISTENING

In principle, narrative evidence, like scientific evidence, could usefully inform almost any policy question. But it would be reasonable to focus first where the outcomes at stake are high, where scientific or quantitative evidence matters, but where there are substantial gaps. The gaps might be so familiar that they are not "visible," and they are most likely to concern major uncertainties about social and political behaviors. These conditions are met in a number of different areas. One is climate change: for instance, arrangements for societies living with evolving and recurrent risks from extreme weather, or—as with Kim Stanley Robinson at COP26—the need for new forms of global governance. Another area is AI, such as developing new forms of distributed systems in city management, or arrangements for criminal justice. In space exploration, competition, ownership, aspiration, and technology rub up against very practical questions of current investment. And in economics, the notion that markets themselves use stories as data that inform behaviors is leading to important new insights (*8*): Studies of literature of the 2008 economic crunch show how "fictional works may tell truths about economic realities, while apparently factual works on economic realities may be infiltrated by fiction" (*9*).

In storylistening, the judgments about which stories to include and how are as expert-based as judgments about what observational data to include in a climate model. The experts might be scholars of literature, film, and cultural studies, as well as social scientists and anthropologists. But the very different intellectual and social structures of the humanities compared to the sciences pose an initial systemic ob-

stacle to the incorporation of different forms of knowledge into a pluralistic evidence base that goes much wider than storylistening. For comparison, discussion of the use of science in public reasoning is often implicitly underpinned by the commonly (mis)understood notion of a single scientific method, based on experimentation, observation, verification, and falsification. Scientists, then, do not have to be trustworthy as individuals, because the scientific system can be trusted (10).

There may be no such simply established thing as "the humanities method," but the guarantors of rigor in the humanities are perhaps not so different as might be imagined from those in the sciences. Both are based on the trustworthiness of systems rather than individuals: robust literature reviews; detailed close attention to the object of study using the tools and methods appropriate to that object; discovery of new objects of study; evidence-based conclusions; peer review; disciplinary interrogation; and cumulative knowledge.

For storylistening to work, scientists are asked to accept that, properly conducted, methodological diversity does not mean loss of rigor; in return, humanists and social scientists need to commit to better routine, effective communication of what guarantees rigor in their disciplines. Research across academic disciplines can then contribute together to informing better public policy.

Just as in the synthesis of scientific evidence, advisory systems can be relied on to make the necessary expert judgments about what research, and by whom, to include when synthesizing evidence within and across disciplines. Storylistening is then most effective if those experts survey a wide range of relevant stories, to identify convergence, oppositions, and gaps in the evidence. For example, in relation to climate change, stories might include accounts of floods and fires on the television news or social media, or narratives of people's memories of extreme weather events, as well as climate-change novels and films, reports from the Intergovernmental Panel on Climate Change (IPCC), and reports from the business and nongovernmental organization sectors.

A narrative synthesis, just as a scientific synthesis, needs to be as comprehensive as time and space allow, structuring its approach by looking for relevant narratives functioning in the four ways outlined above. In doing so, it might include obscure stories—for example, where there are few models of distributed AI systems in AI policy, or there are few positive anticipations in climate change. It might include popular stories in settings where there appeared to be a very dominant story, examining the evidential basis of that story—for example, why humanoid robot stories dominate mainstream fiction.

The synthesis of these findings follows established practical steps: oversight by relevant experts, peer review of the academic rigor, and quality assurance of the presentation and communication of findings intended for interdisciplinary debate and public reasoning (11). The narrative evidence produced through storylistening is set alongside scientific and other evidence as part of a pluralistic evidence base. Depending on the nature of the findings in each case, the narrative evidence can then contribute to final reports of evidence, and to public reasoning, in one or more of several ways. A nonexhaustive list includes prompting new questions for scientific modelers to consider; shifting the framing of debate, and inviting new areas of scientific inquiry or reformulating intractable policy problems so that established policy analysis approaches such as economics and law can more effectively act upon them (12); identifying or foregrounding different collective identities, again either to inform further research or to inform engagement with them; and, inviting public deliberation on potential new social, economic, or cultural arrangements where these are consistent with all forms of available evidence.

ADVISORY SYSTEM EVOLUTION

The many roles of storytelling in policy and science ecosystems are already acknowledged explicitly, such as through studies of policy narratives (13), narrative persuasion, and exploration of the tensions between scientists' intentions, and attempts to provide evidence that informs without persuasion. But storylistening needs to play a role, too.

To take the first steps toward incorporating narrative evidence in policy-relevant deliberations, a science-based advisory system such as the IPCC, the EC's Joint Research Centre, or the US President's Council of Advisors on Science and Technology, might start to operationalize storylistening within their existing programs. This experiment in reaching out to new forms of expertise would itself be in keeping with fundamental academic traditions of innovation, imagination, and rigor. As those considering the proposal for a new science-policy interface for sustainable food systems have argued, new advisory and engagement structures will do more harm than good if they do not embrace pluralism and ensure the rigorous inclusion of diverse forms of knowledge (14).

Increasing amounts of academic attention and innovative practice in advisory systems are also devoted to very different forms of public participation (15). The outputs of some of those forms could be included within the narrative evidence gathered by storylistening, such as when there is an eth-nographic study of stories circulating within a collective identity. Conversely, other forms of public participation might draw from evidence gathered by a storylistening exercise, using it as stimulus or framing material for public dialogue, or as evidence to be submitted alongside scientific evidence within a deliberative arrangement such as a citizens' jury or assembly. Storylistening is concerned with adding to the rigorous evidence available within or created by any given arrangement, rather than, of itself, attempting to change how policy-making power is distributed within the arrangement.

Embedding storylistening in advisory systems is not a threat to scientific evidence, but can strengthen it, offering a new opportunity to tackle long-standing gaps in evidence for policy. What is needed now is for innovative practitioners to start asking for the narrative evidence that might be relevant to their specific and pressing questions, and for researchers to take on the challenge of creating it. For scientists, the invitation is to welcome the inclusion of the humanities and work confidently together to enhance the overall evidence base, noting that, in addition, the inclusion of such fresh perspectives may stimulate new scientific questions and the search for new types of evidence. Done well, this inclusivity will complement and strengthen the use of science. ■

REFERENCES AND NOTES

1. D. Mair et al., Understanding Our Political Nature: How to Put Knowledge and Reason at the Heart of Political Decision-Making (Publications Office of the European Union, 2019).
2. N. Oreskes, E. M. Conway, The Collapse of Western Civilization: A View from the Future (Columbia Univ. Press, 2014).
3. S. Dillon, C. Craig, Storylistening: Narrative Evidence and Public Reasoning (Routledge, 2021).
4. S. Dillon, J. Schaffer-Goddard, Interdiscipl. Sci. Rev. 10.1080/03080188.2022.2079214 (2022).
5. M. Calder et al., R. Soc. Open Sci. 5, 172096 (2018).
6. M. S. Morgan, J. Econ. Methodol. 8, 361 (2001).
7. "What to read to understand climate change," The Economist (28 October 2022).
8. R. J. Shiller, Narrative Economics: How Stories Go Viral and Drive Major Economic Events (Princeton Univ. Press, 2019).
9. K. Shaw, Crunch Lit (Bloomsbury, 2015).
10. N. Oreskes, Why Trust Science? (Princeton Univ. Press, 2019).
11. The Royal Society and the Academy of Medical Sciences, Evidence synthesis for policy: A statement of principles (2018); https://royalsociety.org/-/media/policy/projects/evidence-synthesis/evidence-synthesis-statement-principles.pdf.
12. E. Roe, Narrative Policy Analysis (Duke Univ. Press, 1994).
13. M. Jones et al., Eds., The Science of Stories: Applications of the Narrative Policy Framework in Public Policy Analysis (Palgrave Macmillan, 2014).
14. E. Turnhout et al., Science 373, 1093 (2021).
15. OECD, Innovative Citizen Participation and New Democratic Institutions: Catching the Deliberative Wave (OECD Publishing, 2020).

NEUROSCIENCE

Mechanosensation and joint deformities

Dysfunction of a mechanosensor in sensory neurons causes joint contracture

By **Ulrich Müller**

Arthrogryposis is a condition that is characterized by limitation in the range of joint movement owing to shortening of connective tissue, tendon, and/or muscle. This genetic disorder affects 1 in 3000 live births globally (*1*). Distal arthrogryposis (DA) is a subtype of arthrogryposis that predominantly affects the joints of the distal limbs, including wrists, hands, ankles, and feet. Mutations in genes encoding proteins of the skeletal muscle contractile apparatus were initially linked to DA. However, mutations in genes with important functions outside of skeletal muscle have recently been shown to cause DA as well (*1, 2*) (see the figure). One such case is analyzed in the study by Ma *et al.* (*3*) on page 201 of this issue, which finds that excessive activity of piezo-type mechanosensitive ion-channel component 2 (PIEZO2) in sensory neurons can cause DA.

The perception of sensory stimuli such as touch and sound depends on ion channels that convert mechanical into electrochemical signals (*4*). These ion channels are expressed in the cell membrane of specialized sensory cells and neurons. Mechanical force affects the conformation of these ion channels and opens a pore that allows ions to cross the cell membrane. This ion flux initiates a cascade of electrochemical signals that propagate throughout the nervous system to elicit senses of touch and sound. Mechanically gated ion channels are also important for a myriad of other physiological processes such as the control of proper body posture, blood pressure, and bladder function (*4*). Several mechanically gated ion channels have been identified. Among these, PIEZO2 is the principal mechanosensor in somatosensory neurons for the perception of light touch and proprioception (the sense of the position of one's limbs in space). In addition, PIEZO2 enables mechanosensation in some internal organs (*5*). Notably, both dominant and recessive mutations in *PIEZO2* have been linked to DA, suggesting that too little and too much mechanical sensitivity can be pathogenic (*6, 7*). However, the mechanism by which *PIEZO2* mutations cause DA has remained elusive.

Based on the clinical manifestation, DA has been classified into 10 subcategories (*1, 2*). DA subtype 5 (DA5), which is caused by a dominant mutation in *PIEZO2* (*7–9*), is defined by contractures in distal joints, ophthalmoplegia (paralysis of the muscles that control eye movements), and restrictive lung disease (reduced lung elasticity leading to a decrease in the total volume of air that the lungs can hold). The mutations associated with the disease lead to a gain of function, enhancing the response of PIEZO2 to mechanical stimuli (*7*). Ma *et al.* generated a mouse model in which the normal *Piezo2* gene was replaced with a gain-of-function DA5-causing allele, in a spatially (cell type–specific) and temporally controlled manner. Using this strategy, the authors show that expression of the mutant *Piezo2* allele in proprioceptive neurons that innervate muscles and tendons is sufficient to cause joint contracture, shortened tendons, and poor performance on behavioral tests that depend on muscle strength and function. No such phenotypic changes were observed when the mutant *Piezo2* allele was expressed in skeletal muscles, cartilage, or tendons. Intramuscular injection of botulinum toxin (Botox), an inhibitor of neural transmission, substantially rescued joint and tendon defects in these genetically engineered mice. These data support the conclusion that overactive PIEZO2 in sensory neurons is sufficient to drive DA5-like pathology in mice.

Ma *et al.* went a step further and investigated the time window during which the overactive PIEZO2 protein acts to induce the pathological effects. Expression of the *Piezo2* gain-of-function allele in sensory neurons during embryonic and early postnatal stages, but not after early adulthood, led to DA5-like pathology in mice. These findings suggest that excessive mechanotransduction in somatosensory neurons during a critical developmental period causes limb malformation. Notably, DA symptoms manifest in humans at birth, suggesting that mutations in *PIEZO2* and perhaps in other genes that cause DA act during a critical developmental time window. This is consistent with the long-held view that a lack of fetal movement caused

Genes implicated in distal arthrogryposis

Distal arthrogryposis (DA) is characterized by contracture of the distal limbs. Mutations in genes linked to muscle function are associated with DA. Emerging evidence also links genes associated with neuronal function, such as *PIEZO2*, to DA. Thus, alterations in neurons that connect muscle and spinal cord can also cause DA.

Linked to muscle function

Gene	Protein
MYH3	Myosin heavy chain 3
MYH8	Myosin heavy chain 8
TPM2	Tropomyosin 2
MYL11	Myosin light chain 11
MYBPC1	Myosin binding protein C1
MYBPC2	Myosin binding protein C2

Linked to neuronal function

Gene	Protein
PIEZO2	Piezo-type mechanosensitive ion channel component 2
ECEL1	Endothelin-converting enzyme type 1

GRAPHIC: K. HOLOSKI/*SCIENCE*

Solomon H. Snyder Department of Neuroscience, Johns Hopkins University, Baltimore, MD, USA. Email: umuelle3@jhmi.edu

by contractures forming in joints contributes to the development of DA, likely because movement is required for normal joint development (*1*). In addition, mechanical forces regulate bone development, and the generation of tension by muscles is critical for normal tendon development.

Finding that expression of the gain-of-function allele of *Piezo2* in young adult mice does not cause DA symptoms is reassuring. It narrows down a time window for potential therapeutic intervention that could lead to lifelong improvement for the affected patients. One surprisingly simple treatment option is explored by Ma *et al.* The omega-3 polyunsaturated fatty acid eicosapentaenoic acid (EPA), a membrane lipid that is commonly found in fish and food supplements, affects PIEZO2 function and negates the gain-of-function effect of the DA5-causing *PIEZO2* mutation. Feeding the *Piezo2* mutant mice with a diet rich in EPA prevented joint malformations and the associated behavioral defects. Perhaps a similar treatment might help human patients, although this needs further clinical investigation.

The study by Ma *et al.* provides exciting new insights into the mechanisms that cause DA. Notably, both gain-of-function and loss-of function mutations in PIEZO2 have been linked to DA, but the different mutations lead to distinct pathologies. Moreover, there is patient-to-patient variability in the pathologies caused by the same mutation, with variability in the degree to which different joints, fine motor function, and touch sensation are affected; the manifestation of ophthalmoplegia and restrictive lung disease; or even the presence of cerebellar malformations (*1, 5, 6*). Further studies will be necessary to define the mechanisms by which dominant and recessive alleles of *PIEZO2* act in distinct cell types to cause various DA symptoms. The study of Ma *et al.* is an important step in this direction and sets the tone for further investigations into the clinical implications of PIEZO2-mediated pathogenesis. ∎

REFERENCES AND NOTES

1. J. Whittle, A. Johnson, M. B. Dobbs, C. A. Gurnett, *Genes* **12**, 943 (2021).
2. D. Desai, D. Stiene, T. Song, S. Sadayappan, *Front. Physiol.* **11**, 689 (2020).
3. S. Ma *et al.*, *Science* **379**, 201 (2023).
4. J. M. Kefauver, A. B. Ward, A. Patapoutian, *Nature* **587**, 567 (2020).
5. M. Szczot, A. R. Nickolls, R. M. Lam, A. T. Chesler, *Annu. Rev. Biochem.* **90**, 507 (2021).
6. S. L. Alper, *Curr. Top. Membr.* **79**, 97 (2017).
7. B. Coste *et al.*, *Proc. Natl. Acad. Sci. U.S.A.* **110**, 4667 (2013).
8. M. J. McMillin *et al.*, *Am. J. Hum. Genet.* **94**, 734 (2014).
9. M. Okubo *et al.*, *Am. J. Med. Genet. A.* **167**, 1100 (2015).

10.1126/science.adf6570

Insects as feed for livestock production

Insect farming for livestock feed has the potential to replace conventional feed

By **Arnold van Huis**[1] *and* **Laura Gasco**[2]

Livestock production makes up 70 to 80% of the world's agricultural land use and yet only produces ~18% of all calories and 25% of all proteins consumed by humans. To grow food for livestock uses 33% of the world's cropland. Although lifestyle changes, such as vegetarianism and veganism, may help to achieve sustainability in food production, the global demand for meat consumption is still increasing, so it is also crucial to consider more efficient ways to rear livestock. Insects as animal feed can supplement the current sources of livestock feed, which mostly comprise fishmeal and soybean meal. The use of insects as livestock feed can improve sustainability because insects can transform low-value organic wastes (e.g., fruits, vegetables, and even manure) into high-quality feed. Insect ingredients are also a valuable source of nutrition for animals with many possible health benefits.

Globally, domesticated animals receive more than 1.1 billion tons of feed every year, with 44% going to meat chickens and egg-laying hens, 28% to pigs, 4% to fishes and other seafood, and 3% to pets. The enormous demand for animal feed production creates sustainability concerns—for example, farming soy can involve deforestation, biodiversity loss, and the use of pesticides (*1*). Insect production emits few greenhouse gases and ammonia, and requirements for water and land are low. The largest environmental impact of their production is the feed when using mixed grain (*2*), but this could be overcome by using organic waste as feed instead. Insects have a high feed-conversion efficiency (animal weight gain divided by feed consumed), probably because insects are cold blooded (poikilotermic), which means that they do not expend energy maintaining a constant body temperature—it varies with that of the environment. The disadvantage of this dependence on ambient temperatures is that energy requirements for rearing insects are higher compared with growing crops for feed.

Insects are a valuable source of high-quality protein as well as other essential nutrients for animal feed. Beyond the nutrient supply, insects also provide active compounds that can exert a positive effect on animal health and act as potential antibiotic replacements (*3*). Chitin, a component of insects' exoskeletons, is a biopolymer that mammals lack and is therefore targeted by their immune system. In vivo trials performed on fish, poultry, and pigs showed that consumption of chitin boosted the immune system; halted pathogen proliferation; favorably modulated the host's intestinal bacterial communities; and had antioxidant, hypolipidemic, and hypocholesterolemic properties (*3*). Insects naturally produce a high diversity of antimicrobial peptides (*4*) to protect themselves from the microorganism-laden environment in which they live. Moreover, fatty acids, such as lauric acid (which is particularly abundant in black soldier fly larvae), also show strong antimicrobial properties when given as feed to animals (*3*).

Among the many insect species that can be reared as animal feed, those currently being used include flies—e.g., the black soldier fly (*Hermetia illucens*) and the common house fly (*Musca domestica*)—and mealworms, such as the yellow mealworm (*Tenebrio molitor*). Usually, the larval stages or prepupae of these species are used as feed. Black soldier flies are the preferred species because the larvae can be reared on a wide range of organic matter (including waste, such as agricultural and food waste) and can thrive in environments that are considered unhygienic (such as in manure) for other animals.

What is the effect of including insect products in the feed of fish, poultry, pigs, and pets? For aquaculture (fish) species, the inclusion of up to 30% full-fat or defatted insect meals had little observable difference compared with fishmeal, which remains the optimal protein source for aqua feeds (*5*). For marine species, attention should be paid to long-chain polyunsaturated fatty acids, which are absent in insect products unless added to the food source (the rearing substrate) for the insects. In poultry feeds, the

¹Laboratory of Entomology, Wageningen University & Research, Wageningen, Netherlands. ²Department of Agricultural, Forest and Food Sciences, University of Torino, Grugliasco, Italy. Email: arnold.vanhuis@wur.nl

Organic waste can be used to feed black soldier flies (*Hermetia illucens*), whose larvae are a rich source of animal protein.

PHOTO: BONIFACE MUTHONI/SOPA IMAGES/LIGHTROCKET/GETTY IMAGES

inclusion of insect feed up to ~30% has been reported to fully substitute soybean meal or other conventional plant protein sources. However, for black soldier fly meal, optimal inclusion seems to be ~10% because small histological issues in the intestines have been observed in poultry above this level (*6*). Live black soldier fly larvae also promote the natural foraging behavior of birds and decrease feather picking, which positively affects their welfare and health (*7*). Compared with aquaculture or poultry sectors, relatively little research has been performed on pigs where partial or full substitution of soybean meal or fishmeal was obtained using moderate (10 to 20%) amounts of yellow mealworm or black soldier fly (*8*). However, higher amounts of substitution of insect-based feed may lead to decreased digestibility for pigs (and possibly other animals). Although only 3% of all feed produced is for pets, currently ~50% of the insect industry is engaged in producing for this sector. During the past 2 years, large companies have advertised pet food containing insects, highlighting, among other things, the hypoallergenicity of insect-containing feed. Research on insect meal in pet food should focus on nutritional adequacy, food safety, and whether it is hypoallergenic (*9*).

The insect species, its development stage, rearing substrate, and processing method (such as whether it undergoes drying and defatting) all affect the overall nutritional value and therefore determine its inclusion level in feed formulation. There are large variations in nutrient composition within the same insect species because of different production methodologies (*10*). This makes it difficult to compare the results of trials using insects as livestock feed. Only when the nutrient composition and amino acid profile are properly balanced can total replacement of fishmeal

and soybean meal be possible without compromising animal performance, product quality, or animal health.

Currently, the quantities of insects produced are not enough to sustain the demand for agricultural feed, and the prices of insect feed are not competitive. Studies from a highly productive pilot plan demonstrated that feeding livestock with black soldier fly could become more beneficial (than soymeal or fishmeal) if insects are fed with unused organic matter (*11*). As has been done for other livestock species, the determination of the nutritional requirements of insects is a further fundamental step. This will allow maximum production by combining waste of different origins. Indeed, several waste types have been combined to match a feed formulation covering the nutritional needs of diverse insects (*12*, *13*). Because the farming of insects as "minilivestock" is very different from livestock farming, there are additional challenges and issues to overcome, including automation of production techniques, optimization of bioconversion by an efficient interaction between microbes in the insect gut and feed substrate, disease management, making use of the short life cycle of insects to select efficient strains of insects and microbes for certain diets, food safety issues, and processing. Standardization of research methodologies is desirable to allow the comparison of the efficiency of insects in bioconverting waste into high-quality nutrients (*14*).

Regulatory frameworks for insect-derived products are slowly being implemented. For example, in 2017, the European Union (EU) permitted the use of insects as aquafeed and authorized insect-derived processed animal proteins in poultry and pig feed in 2021. The use of live larvae is only permitted under national legislation in some countries.

Because pets (dogs and cats) do not enter the food chain, no restrictions apply to the use of insect-derived proteins in pet foods. Owing to safety concerns, in some countries (including EU countries), the use of catering waste, manure, slurry, or other products of animal origin as substrates to feed insects is forbidden. Insect producers' associations are working with legislators to change this restriction, but further research is required to assess the safety of using waste to avoid any pathogen transmission.

Functional benefits of insect protein in animals are promising but need further confirmation. A major challenge for the insect sector is to deliver reliable quantities of insect meal of high quality and consistency. The scaling up of production depends on whether cheap organic wastes can be safely used and easily biotransformed into high-quality insect products and whether legislative frameworks are conducive to this approach. ∎

REFERENCES AND NOTES

1. V. Voora, C. Larrea, S. Bermudez, "Global Market Report: Soybeans" (The International Institute for Sustainable Development, 2020).
2. D. G. A. B. Oonincx, I. J. M. de Boer, *PLOS ONE* **7**, e51145 (2012).
3. L. Gasco, A. Józefiak, M. Henry, *J. Insects Food Feed* **7**, 715 (2021).
4. A. Sahoo *et al.*, *Front. Microbiol.* **12**, 661195 (2021).
5. N. S. Liland *et al.*, *J. Insects Food Feed* **7**, 743 (2021).
6. S. Dabbou *et al.*, *J. Anim. Sci. Biotechnol.* **9**, 49 (2018).
7. A. F. Ipema, W. J. J. Gerrits, E. A. M. Bokkers, B. Kemp, J. E. Bolhuis, *Appl. Anim. Behav. Sci.* **230**, 105082 (2020).
8. S. Meyer *et al.*, *J. Anim. Sci. Biotechnol.* **11**, 20 (2020).
9. G. Bosch, K. S. Swanson, *J. Insects Food Feed* **7**, 795 (2021).
10. H. K. Ravi *et al.*, *Processes* **8**, 857 (2020).
11. S. Smetana, E. Schmitt, A. Mathys, *Resour. Conserv. Recycling* **144**, 285 (2019).
12. S. Bellezza Oddon, I. Biasato, L. Gasco, *J. Anim. Sci. Biotechnol.* **13**, 17 (2022).
13. S. Bellezza Oddon, I. Biasato, A. Resconi, L. Gasco, *Sci. Rep.* **12**, 10922 (2022).
14. G. Bosch *et al.*, *J. Insects Food Feed* **6**, 95 (2020).

Insects, such as grasshoppers (*Locusta migratoria* are shown), can be a nutritious addition to the human diet.

FOOD SECURITY

Human consumption of insects

Farming edible insects can help improve food security and boost developing economies

By **Arup Kumar Hazarika**[1] *and* **Unmilan Kalita**[2]

Food insecurity may emerge from climate change, extreme weather events such as prolonged droughts and floods, ongoing global supply chain problems, and unpredictable geopolitical conflicts. In particular, the growing populations of low- and middle-income countries (LMICs) will require more accessible, affordable, and sustainable nutrition. To this end, upscaling traditional agriculture and livestock production is not a sustainable solution because these industries are themselves a driver of the climate crisis. The growing popularity of vegetarianism and veganism and the shift to plant-based or lab-grown meat are commendable efforts to solve these problems, but they may not be applicable or practical for every country. Farming insects for food generally requires much less resources compared with meat production. Edible insects can also supplement other diets by providing a different roster of nutrients and present an opportunity to improve food security.

The increased demand for meat protein is unsustainable because large-scale animal farming requires large quantities of land, feed, and water. The meat industry is heavily resource-driven and characterized by market failures and policy misappropriations, and it represents a feedback loop wherein it is both the cause and victim of climate change (*1*). The carbon footprint of farming meat for human consumption is estimated to be higher than 7.1 billion tonnes CO_2 equivalent, which represents 14.5% of all anthropogenic greenhouse gas emissions (*2*). The Food and Agriculture Organization of the United Nations (FAO) projects a global population of 9.7 billion by 2050, and to feed them, the world will have to shift to low-cost and less resource-intensive nutrient sources (*3*).

In contrast to traditional livestock meat production, insect production requires much less feed and can enable a higher conversion of phytomass to zoomass. Given the efficient feed conversion ratio and that many edible insects can be eaten whole, they are much more economical than traditional livestock. The speed at which insects reach maturity is faster and the number of offspring produced by each individual insect is higher than for most farm animals. Insect farming also shares many of the same environmental benefits as plant-based or lab-grown meat. Operationally, lab-grown meat is lauded for its much lower carbon footprint compared with traditional livestock, but it incurs considerable start-up and operational costs and may not be practical for domestic producers in LMICs. Compared with plant-based alternative proteins, insects can be highly efficient in terms of water and space requirements (*4*). Although insects cannot replace vegetables in the human diet, they can be used to supplement human diets.

Rich in protein, fat, vitamins, minerals, and calories, edible insects can be a valuable alternative food source or dietary supplement for the human population (*5*). For example, house crickets (*Acheta domesticus*) have a very high iron and zinc content (*6*). Moreover, certain insect species have high bioavailability (the fraction of an ingested nutrient that becomes available for use and storage in the body) along with high nutrient compositions.

[1]Department of Zoology, Cotton University, Guwahati, India. [2]Department of Economics, Barnagar College, Barpeta, India. Email: arup.hazarika@cottonuniversity.ac.in; unmilankalita@barnagarcollege.ac.in

Insects also have higher amounts of certain nutrients than plant sources. For example, the larvae of palm weevil (*Rhynchophorus ferrugineus*) and house crickets contain larger quantities of essential amino acids such as lysine and tryptophan than most plants in the human diet. Insects also have high protein content (*7*). For example, dried house crickets comprise 65% protein, whereas the protein content of dried soybeans is 45%. The leucine content of house crickets is also higher than that of soybeans. Edible insects such as yellow mealworms (*Tenebrio molitor*), larvae of domestic silk moths (*Bombyx mori*), and certain species of emperor moths contain more protein by mass than does poultry or beef. House crickets also have high iron, calcium, and riboflavin content, and silk moth larvae have high vitamin C content. Edible insects are also a good source of polyunsaturated fatty acids (PUFAs) such as omega-3 (linolenic) and omega-6 (linoleic) fatty acids. However, commercially raised insects are often low in omega-3 PUFAs and have suboptimal omega-6/omega-3 ratios (*8*).

Insects have historically been part of the human diet in many cultures. More than 2000 insect species, including mealworms, house crickets, black soldier fly (*Hermetia illucens*) larvae, and grasshoppers, have been identified as edible insects worldwide (*9*). The eating of insects—which is mainly done in Asia, Africa, and Latin America—is often associated with a "yuck" factor in Western countries. Notably, the European Commission has recently identified edible insects as a "novel food" under Regulation (EU) 2015/2883. Novel food typically refers to any food or ingredient that has no history of substantial human consumption. In the EU, novel foods are regulated to ensure that they neither pose a danger to the consumer nor are nutritionally disadvantageous. The classification of insects as novel food therefore indicates the safety of insect-based products for human consumption and recognizes their acceptability as an alternative nutrient source. In the United States, the most recent cycle of Brood X cicadas in 2021 has also generated a considerable amount of interest in the consumption of insects. Other high-income countries such as Canada and Australia are also exploring the possibility of considering edible insects as food to sustain growing nutrition requirements.

Acceptability among consumers and concerns regarding food safety are important challenges to overcome. Previous studies suggest that key approaches for tackling these issues include providing widespread information about insects' nutritional value and food safety, giving people a taste experience through integration of insects in food preparation or association with attractive flavors, publishing insect cookbooks, emphasizing the similarity between crustaceans and insects, or serving them as expensive items in restaurants, akin to lobsters (*10*). However, changing a traditional eating habit such as enjoying the taste of meat and a lack of culinary knowledge in preparing insect-based meals are major impediments to the uptake of insects in food (*5*). Focus group studies in high-income countries have repeatedly revealed that consumer attitudes depend on lowering the feeling of disgust by making insect products delicious and providing positive gastronomic experiences (*11*). As such, when consumers are willing to try an insect-based product, such as a protein bar, tacos, or a burger, it should be palatable and appetizing; otherwise they might not be willing to eat one again.

Most safety risks of insects as food depend primarily on the insect species, the environment they are collected from or reared in, what they feed on, and the farm-processing methods. There have been reports of scombroid poisoning in Thailand and botulism in Africa from eating fried insects that were sourced from the wild rather than being reared. Insects reared under controlled conditions pose much lower allergen risks than those harvested from the wild or consumed raw. As such, FAO currently recommends the consumption of hygienically farmed insects, because allergens in insects can trigger harmful reactions in some individuals. But farmed insects can also be contaminated through feed materials, and decontaminating harvested insects can pose a practical challenge. For efficient production and commercialization of insects in food supply chains, there is still a need for insect-specific legislation, standards, and labeling regulations to ensure food safety in many countries.

Insect farming has potential in a circular economy that focuses on redirecting economic development toward a zero-waste model. Farming insects for food reduces consumption of natural resources, owing to a high feed conversion ratio (*12*). Additionally, using cheap organic waste material (such as pig slurry, compost, or food waste) as insect feed could reduce the environmental impact of insect farming while creating income from a circular waste-processing stream. However, it is unclear whether consumption of insects fed on organic waste poses any risk to human health.

The popularization of eating insects as food may also provide employment and income-earning opportunities, especially for people in LMICs (*13*). Currently, wild harvesting, semidomestication of insects in the wild, and farming are the three methods through which edible insects are obtained. With rapidly increasing semidomestication and farming of insects as food, the success of the edible insect market is expected to rely on its surprisingly small scale of farming, rapid breeding cycles, and limited barriers to entry (*14*). Farmed honey bees can be used as carriers of microbes that protect crops by thwarting harmful pests or pathogens, while the by-products of bee larvae and honey can be harvested as food. Moreover, insects such as silkworms possess this special quality of double production: They are not just used for food but also for producing premium fiber (silk). The production of every kilogram of raw silk is also estimated to generate 11 days of employment (*5*). Currently, the silkworm industry is a multimillion-dollar industry in India. In Thailand, new market opportunities in restaurants, street food, and gastronomy tourism have pushed this industry forward from rural to urban areas. In Mexico and Canada, insects, including canned ants, maguey caterpillars, and fried grasshoppers, are sold as exotic foods. It is estimated that of all edible insect products, the insect powder category will grow the fastest as the world sees a paradigm shift in the health and wellness market (*15*). In the next decade, the world edible insect market is expected to grow at an annual rate of 20 to 30%. Overall, there is relentless ongoing development of new insect-based products to accommodate the needs of various evolving markets globally. ∎

REFERENCES AND NOTES

1. B. Bajželj, K. S. Richards, *Land* **3**, 898 (2014).
2. P. J. Gerber *et al.*, *Tackling Climate Change Through Livestock – A Global Assessment of Emissions and Mitigation Opportunities* (FAO, 2013); http://www.fao.org/3/i3437e/i3437e.pdf.
3. G. Fischer, "World Food and Agriculture to 2030/50: How do climate change and bioenergy alter the long-term outlook for food, agriculture and resource availability?" Expert Meeting on How to Feed the World in 2050 (FAO, 2009); https://purochioe.rrojasdatabank.info/ak972e00.pdf.
4. P. Alexander *et al.*, *Glob. Food Secur.* **15**, 22 (2017).
5. A. van Huis *et al.*, "Edible insects: Future prospects for food and feed security," FAO Forestry Paper 171 (FAO, 2013); https://library.wur.nl/WebQuery/wurpubs/fulltext/258042.
6. A. K. Hazarika, U. Kalita, S. Khanna, *Curr. Nutr. Food Sci.* **17**, 699 (2021).
7. F. A. Madau, B. Arru, R. Furesi, P. Pulina, *Sustainability* **12**, 5418 (2020).
8. D. G. A. B. Oonincx, S. Laurent, M. E. Veenenbos, J. J. A. van Loon, *Insect Sci.* **27**, 500 (2020).
9. A. van Huis, in *Handbook of Eating and Drinking*, H. L. Meiselman, Ed. (Springer, 2020), pp. 965–980.
10. D. J. McClements, *Future Foods: How Modern Science Is Transforming the Way We Eat* (Springer, 2019), pp. 323–361.
11. M. A. Baker, T. S. Legendre, Y. W. Kim, in *The Routledge Handbook of Gastronomic Tourism*, S. K. Dixit, Ed. (Routledge, 2019), chap. 44.
12. A. C. Nowakowski, A. C. Miller, M. E. Miller, H. Xiao, X. Wu, *Crit. Rev. Food Sci. Nutr.* **62**, 3499 (2022).
13. A. K. Hazarika, U. Kalita, S. Khanna, T. Kalita, S. Choudhury, *PeerJ* **8**, e10248 (2020).
14. H. C. D. Tuhumury, *IOP Conf. Ser. Earth Environ. Sci.* **883**, 012029 (2021).
15. M. Skotnicka, K. Karwowska, F. Kłobukowski, A. Borkowska, M. Pieszko, *Foods* **10**, 766 (2021).

NEURODEGENERATION

Gut microbes modulate neurodegeneration

Microbiota mediate neuroinflammation in a genetic- and sex-specific manner in mice

By **Tanya Jain**[1,2] *and* **Yue-Ming Li**[1,2,3]

Amyloid-β (Ab), tau, and apolipoprotein E (APOE) are major players in the pathogenesis of Alzheimer's disease (AD), which involves neuroinflammation and neurodegeneration (1). Recently, gut microbes have emerged as an important factor implicated in neurodegeneration (2). However, how gut microbes interplay with APOE and tau remains elusive. On page 155 of this issue, Seo *et al.* (3) investigate tau-mediated neurodegeneration using mouse models in which animals were raised conventionally and in germ-free (GF, lacking all microbiota) conditions. They demonstrate that gut bacteria play a causative role in tau-mediated neurodegeneration through modulation of inflammation in the periphery and the central nervous system (CNS). This neuroinflammation arose in an APOE isoform–dependent and sex-specific manner.

Tau-mediated neurodegeneration and brain atrophy are strongly linked to cognitive decline in patients with AD. Although increased levels of phosphorylated-tau (p-tau) can directly contribute to neuronal cell death, reactive astrocytes and microglia are also required for disease progression. *APOE* encodes a regulator of Aβ clearance (4), tau pathology (5), and myelination (6). The *APOE4* variant of *APOE* is the strongest known genetic risk factor for AD (7), whereas the *APOE3* variant does not seem to influence AD risk. There is mounting evidence that the presence of different *APOE* alleles can lead to a differential configuration of the gut microbiota (8). It has been reported that treatment with antibiotics leads to a reduction in Aβ pathology in an amyloid mouse model of AD (9), and that this reduction depends on the function of microglia (10). However, the role of gut microbiota in tau-mediated neurodegeneration is currently unknown.

Seo *et al.* used mouse models in which animals carrying a mutant *MAPT* transgene (which encodes tau), with either *APOE3* or

¹Chemical Biology Program, Memorial Sloan Kettering Cancer Center, New York, NY, USA. ²Neuroscience Program, Weill Graduate School of Medical Sciences, Cornell University, New York, NY, USA. ³Pharmacology Program, Weill Graduate School of Medical Sciences, Cornell University, New York, NY, USA. Email: liy2@mskcc.org

APOE4 variants (5), were raised under GF or conventional conditions. Remarkably, GF conditions were strongly neuroprotective in male and female mice expressing *APOE3* and *APOE4*, with significant preservation of hippocampal volume and lateral ventricle size. This neuroprotection was reversed when GF mice underwent fecal microbiota transplant from sex-matched conventionally raised mice expressing *APOE4*.

Microbiota-mediated neuroinflammation

Mice expressing apolipoprotein E (*APOE*) variants and mutant tau exhibit neurodegeneration and gliosis. This is mediated by gut microbiota–produced short-chain fatty acids (SCFAs). These microbial metabolites activate peripheral immune cells which, in turn, produce cytokines that cross the blood-brain barrier (BBB) and elicit neuroinflammation and attendant neurodegeneration. When these mice are raised in germ-free conditions, gliosis and neurodegeneration do not arise.
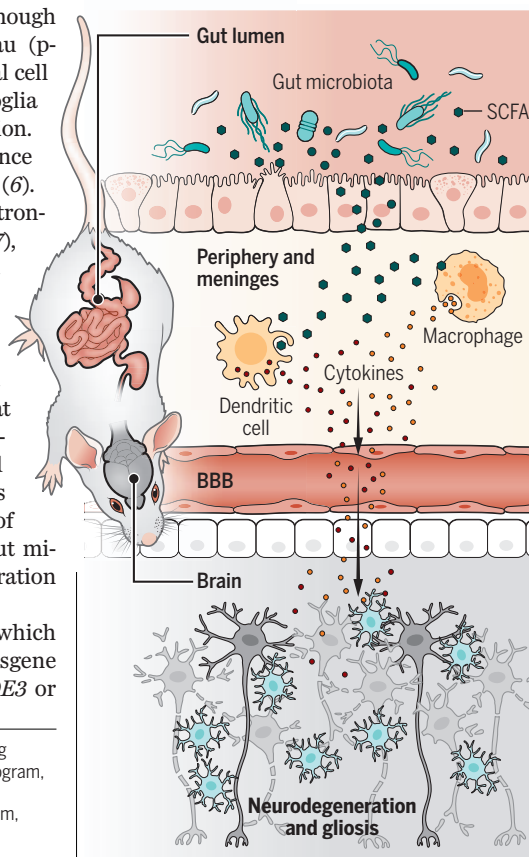
Can antibiotic treatment achieve similar neuroprotective effects? Seo *et al.* treated conventionally raised mice expressing mutant tau and APOE3, APOE4, or no APOE with an antibiotic cocktail for 6 days before weaning and observed striking APOE-isoform– and sex-dependent effects. An absence of APOE led to minimal neurodegeneration. Male mice treated with antibiotics and expressing APOE3, but not APOE4, had preserved hippocampal volume, reduced p-tau staining, and a more homeostatic astrocyte and microglial morphology. Males of all *APOE* genotypes that were treated with antibiotics had reduced p-tau levels, as well as significant attenuation of atrophy and significant improvement in nest-building behavior, albeit with a larger effect in mice expressing APOE3 than APOE4. Almost all these effects were seen only in males and not females. These results are reminiscent of previous findings that long-term antibiotic treatment leads to a reduction in Aβ pathology in male, but not female, mice of an amyloid model (9). Further studies are needed to understand why male mice benefit from antibiotic treatment whereas female mice do not, although it is possible that sex-specific hormones play a role in this discrepancy (11).

How do gut microbiota affect tau-mediated neurodegeneration? Seo *et al.* hypothesized that microbiota may be altering astrocytic and microglial responses and activation. Consistently, they found that GF male mice had reduced glial fibrillary acidic protein (GFAP), ionized calcium-binding adapter molecule 1 (IBA1), and CD68 expression, all of which are markers of glial activation (gliosis). Differential gene expression analysis from the hippocampi of male mice pointed to a down-regulation of innate immune response genes, as well as glial activation genes, in the absence of microbiota. Similarly, treatment with antibiotics led to changes in microglial and astrocytic gene expression, reinforcing that gut microbiota modulate glial responses. Seo *et al.* found that bacterial strains associated with the production of short-chain fatty acids (SCFAs), which are secreted microbial metabolites, may be involved in neuroinflammation in an APOE isoform– and sex-specific manner. Because glial cells do not seem to express SCFA receptors, gut bacteria–derived SCFAs likely interact with other

immune cells, such as natural killer cells, dendritic cells, and macrophages, which in turn release cytokines and chemokines, some of which can cross the blood-brain barrier and induce gliosis. Indeed, supplementing SCFAs in drinking water increased gliosis and p-tau pathology in GF APOE4-expressing mice (see the figure). Despite the potential role of peripheral cytokines in modulating neuroinflammation and tau-mediated neurodegeneration, it is important to note that the presence of APOE variants was essential to drive tau pathology.

A question that remains unanswered is why the benefits of antibiotic treatment seen in *APOE3*-carrying mice failed to apply to mice carrying *APOE4*, whereas a lifelong absence of gut microbiota in GF mice offers significant protection in both *APOE3*- and *APOE4*-carrying mice. The underlying mechanism could be unveiled if strains of bacteria and the SCFAs that are responsible for such a disparity can be identified. A defined microbiota composed of specific bacterial species has been developed for use in mouse studies (*12*). Using this defined gut microbial community may help identify strains, genes, and metabolites responsible for the observations reported by Seo *et al.*

A recent study reported that dietary sugar can induce changes in gut microbiota and drive metabolic disease (*13*). This is particularly interesting because there is evidence that intranasal administration of insulin, which reduces blood sugar levels, in AD patients seems to improve cognition in males carrying the *APOE2* or *APOE3* variants, but not in *APOE4* carriers or in females (*14*). It is possible that blood sugar levels may alter the composition of the gut microbiota, which may in turn lead to differential therapeutic effects in patients according to *APOE* variant and sex. Overall, these exciting results highlight the potential to harness the gut microbiota to prevent or slow the progression of AD and other tauopathies and raise awareness about the potential long-term effects of early-life diet. ∎

REFERENCES AND NOTES

1. D. S. Knopman *et al.*, *Nat. Rev. Dis. Primers* **7**, 33 (2021).
2. C. Willyard, *Nature* **590**, 22 (2021).
3. D. Seo *et al.*, *Science* **379**, eadd1236 (2023).
4. J. M. Castellano *et al.*, *Sci. Transl. Med.* **3**, 89ra57 (2011).
5. Y. Shi *et al.*, *Nature* **549**, 523 (2017).
6. J. W. Blanchard *et al.*, *Nature* **611**, 769 (2022).
7. Y. A. Martens *et al.*, *Neuron* **110**, 1304 (2022).
8. T. T. T. Tran *et al.*, *FASEB J.* **33**, 8221 (2019).
9. H. B. Dodiya *et al.*, *J. Exp. Med.* **216**, 1542 (2019).
10. H. B. Dodiya *et al.*, *J. Exp. Med.* **219**, e20200895 (2022).
11. R. Vemuri *et al.*, *Semin. Immunopathol.* **41**, 265 (2019).
12. A. G. Cheng *et al.*, *Cell* **185**, 3617 (2022).
13. Y. Kawano *et al.*, *Cell* **185**, 3501 (2022).
14. A. Claxton *et al.*, *J. Alzheimers Dis.* **35**, 789 (2013).

Nanofluidic computing makes a splash

Ionic computing raises the possibility of devices that operate similarly to the human brain

By **Aleksandr Noy**[1,2] and **Seth B. Darling**[3,4]

N euromorphic computing aims to mimic the energy-efficient information processing of the human brain. With its billions of neurons connected through trillions of synapses, the brain optimizes information flow and avoids the costly constant shuttling of data between the processor and memory, a hallmark of classic computer architecture (*1*). To enable brainlike processing, a new device architecture that forgoes the rigid computing language of zeros and ones is needed. What if devices used ions moving in fluids to carry and store information? Such nanofluidic computing promises lower energy consumption, hardware-level plasticity, and multiple information carriers (*2*). On pages 156 and 161 of this issue, Xiong *et al.* (*3*) and Robin *et al.* (*4*), respectively, describe nanofluidic synaptic devices that operate at voltage and power consumption close to those of biological systems, providing a glimpse into the possibilities of neuromorphic ionic computing.

Neurons communicate with electrical impulses, or "spikes," and use temporal sequence to encode analog input data (*5*). It is possible to implement this architecture in conventional solid-state device platforms (*5*), but it requires a large number of transistors, wiping out much of the potential energy savings. Instead of a transistor switch, neuromorphic computing will likely center on a memristor device that enables key synaptic functionality, such as connection switching and plasticity. Implementing such memristor-based neuromorphic architectures at scale and at low power and low cost would require the development of new materials and fabrication processes, as well as an en-

[1]Materials Science Division, Physical and Life Sciences Directorate, Lawrence Livermore National Laboratory, Livermore, CA 94550, USA. [2]School of Natural Sciences, University of California, Merced, CA 95343, USA. [3]Chemical Sciences and Engineering Division and Advanced Energy Technologies Directorate, Argonne National Laboratory, Lemont, IL 60439, USA. [4]Pritzker School of Molecular Engineering, University of Chicago, Chicago, IL 60637, USA. Email: noy1@llnl.gov; darling@anl.gov

hanced understanding of the physics that accompanies switching and learning in these devices.

Researchers have implemented memristor behavior in a variety of conventional platforms, including phase change, optical, magnetic, ferroelectric, and organic semiconductor materials (*6–9*). However, compared with the brain's nimble synapses, most of these devices are limited to a single information carrier, usually electrons, and cannot use chemical signals.

An early glimpse of the neuromorphic memristor concept posited how ionic transport in a nanometer-thick two-dimensional (2D) slit filled with a salt solution can produce neuron-like voltage spiking and mimic some memory functionality (*10*). Robin *et al.* created two versions of the proposed 2D slit device. One consists of two smooth molybdenum disulfide (MoS_2) flakes separated by graphene spacers to create a sub-1-nm–height slit. The other is a thicker (~10 nm) etched graphite slit-like channel with a highly charged surface. When either device is filled with electrolyte solution and subjected to time-variable voltages, it exhibits memristor-like current-voltage (*I-V*) behavior with an unusually long memory time scale ranging from seconds to hours. On an *I-V* relationship plot, the behavior appears as a nonlinear, "pinched" hysteretic loop (see the figure), where the *I-V* relationship depends on the history of the past voltage inputs into the device.

The physics enabling nanofluidic memristors is rooted in electrolyte behavior under nanoscale confinement. Switching between high- and low-conductance states comes from two distinct mechanisms that depend on the surface charge of the channel and electrolyte concentration. One involves formation of Bjerrum ion pairs under confinement, which suppresses ionic conductance under low applied voltage (*10*). Stronger applied voltage breaks these pairs and restores conductance, often triggering the formation of polyelectrolyte-like ion aggregates. Another mechanism stems from accumulation–depletion effects created by the asymmetry in channel entrances (*11*). A key discovery of Robin

et al. is the contribution of a third process rooted in the adsorption–desorption equilibrium at the channel surface. The small volume of the nanofluidic channel and strong adsorption of ions to the walls leads to the unusual situation in which ions spend most of their time bound to the walls. As a result, the ion equilibrium slows well beyond the diffusion time scale, enabling ion current response that is dependent on the frequency of applied voltage inputs and long-term memory effects.

Xiong *et al.* achieved similar results with a different device that confines anions in a nanopipette channel packed with polyelectrolyte imidazole brushes. The large surface charge density of the brushes slows down ionic equilibrium, leading to the hysteretic and frequency-dependent *I-V* characteristics that enable long-term memory effects. Richer chemistry of these charged polymer brushes allows more functionality than the simple charged surface used by Robin *et al.* As Xiong *et al.* observed, variations in the interaction strength of different anions with the imidazole units of the brush led to substantial changes in the *I-V* curve hysteresis and the corresponding memory time scales of the device. The authors also observed that polyelectrolyte nanofluidic memristors can mimic chemical signal transduction that occurs at neuronal synaptic junctions. Repeated delivery of an ion stimulus (perchlorate anion) into the device triggered a series of current spikes. These examples bring us closer to the realization of information processing with multiple carriers, a capability that would be nearly impossible in solid-state devices.

A notable feature of the systems of both Robin *et al.* and Xiong *et al.* is the reliable long- and short-term plasticity effects. The conductance of nanofluidic memristors increases after receiving multiple subsequent voltage spikes, mimicking short- and long-term potentiation in biological synapses. Robin *et al.* went a step further and implemented a form of Hebbian learning (spike time–dependent plasticity), a process in the brain that is fundamental to mastering new skills.

At the core of Hebbian learning is the strengthening of the synaptic connection between two neurons when they are activated simultaneously. Hebbian learning drives the establishment of muscle memory that is critical for abilities such as riding a bicycle or negotiating a difficult ski run. In the study of Robin *et al.*, the conductance of a nanofluidic memristor increased when the spikes from two neuron-mimicking inputs arrived close together and stayed unchanged when the spikes were separated by longer times, thus registering the time correlation between the two input signals. Xiong *et al.* observed that spike-timing coding could also be achieved by the (inverse) correlation of stimulation intensity and time lapse.

The road to nanofluidic computing is still riddled with formidable challenges. Xiong *et al.* estimated the power consumption of their somewhat large devices to be ~0.7 pJ per spike, which is higher than the 0.1 to 1 fJ per spike power consumption of a biological neuron (*12*). Improving energy efficiency of nanofluidic computers will require a better understanding of the physical mechanisms that govern ion diffusion, equilibria, and transport in these systems. True coupling between multiple ionic and chemical signals will depend on specific mechanisms for chemical recognition and careful mitigation of the cross-talk between them. A robust scale-up strategy is needed for building compact, interconnected nanofluidic circuits that can support the complexity required for meaningful computing capabilities. Other key elements of neuromorphic circuits must be developed, such as integrators and spiking devices that mimic neuronal soma bodies, long-distance information transmitters that mimic axons, and simple interconnects that mimic dendrites. A reliable nanofluidic computer will also require components that can endure billions of switching events. Nature gave each of us an amazingly powerful and compact computer that uses an amount of energy that would be insufficient to light a desk lamp. We are now bringing this level of efficiency to the computing devices that power civilization. ∎

Neuromorphic nanofluidic architectures

Two designs exploit the adsorption of ions to nanofluidic channel walls and spatial confinement to slow down ion equilibrium, which imparts the devices with hysteretic conductivity behavior and synapse-like functionality.
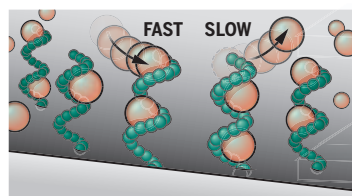
Polymer brushes
Ions adsorb to the charged polymer chains that line the wall of a nanopipette.
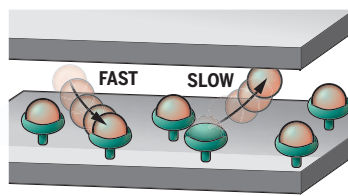
Two-dimensional slits
Ions adsorb to the charged wall of a nanochannel.

Memristor behavior
Ions enter the depleted channel and rapidly adsorb to charged walls (**1**). Ions accumulate in the channel (**2**). The channel starts to deplete, and ions slowly desorb from the walls (**3**). The channel is depleted, and the cycle starts again (**4**).
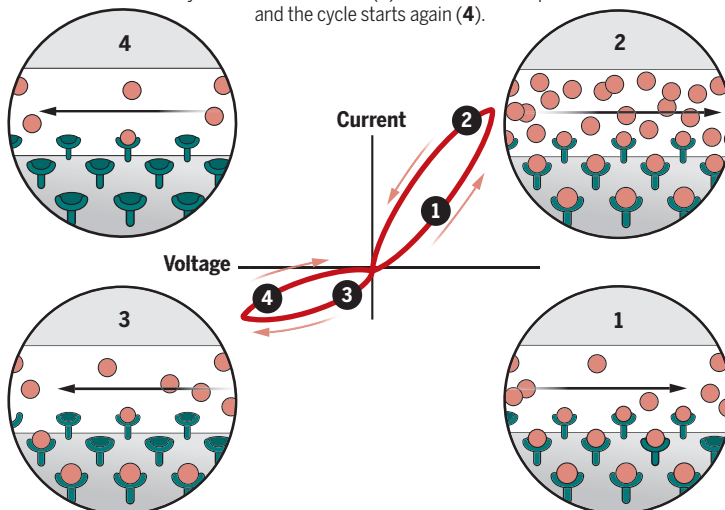
REFERENCES AND NOTES

1. I. K. Schuller, R. Stevens, R. Pino, M. Pechan, "Neuromorphic computing – From materials research to systems architecture" (US Department of Energy Office of Science, 2015).
2. D. W. M. Marr, T. Munakata, *Commun. ACM* **50**, 64 (2007).
3. T. Xiong *et al.*, *Science* **379**, 156 (2023).
4. P. Robin *et al.*, *Science* **379**, 161 (2023).
5. J. Misra, I. Saha, *Neurocomputing* **74**, 239 (2010).
6. D. B. Strukov, G. S. Snider, D. R. Stewart, R. S. Williams, *Nature* **453**, 80 (2008).
7. A. Chanthbouala *et al.*, *Nat. Mater.* **11**, 860 (2012).
8. Y. Li, Z. Wang, R. Midya, Q. Xia, J. J. Yang, *J. Phys. D Appl. Phys.* **51**, 503002 (2018).
9. Y. van de Burgt *et al.*, *Nat. Mater.* **16**, 414 (2017).
10. P. Robin, N. Kavokine, L. Bocquet, *Science* **373**, 687 (2021).
11. W.-J. Lan *et al.*, *Acc. Chem. Res.* **49**, 2605 (2016).
12. S. B. Laughlin, R. R. de Ruyter van Steveninck, J. C. Anderson, *Nat. Neurosci.* **1**, 36 (1998).

GRAPHIC: V. ALTOUNIAN/*SCIENCE*

BOOKS *et al.*

PUBLIC HEALTH

The unrecovered

A journalist's empathetic portrait of COVID-19 "long haulers" sheds light on the realities of postviral illness

By **Helen Ward**

The data aggregation website Worldometer reports that as of 5 January 2023, there have been more than 666 million cases of COVID-19 and over 6.7 million deaths worldwide (*1*). It also reports ~638 million cases as "recovered," a figure I am sure journalist Ryan Prior would dispute. In *The Long Haul*, Prior paints a compelling and moving picture of the lives of people devastated by persistent and often debilitating symptoms after acute infection with COVID-19. The individuals he profiles did not die, but they certainly did not recover. Drawing on his own experience with postviral illness and extensive interviews with those experiencing, researching, and caring for people with Long Covid, Prior provides an in-depth description of the lasting impact of COVID-19 infection.

Unlike infections and deaths, cases of Long Covid are not part of routine surveillance. Prior cites estimates that between 7 million and 14 million Americans (2.3 to 4.4% of the population) had experienced Long Covid—generally defined as ongoing health problems for 4 or more weeks after an initial infection with severe acute respiratory syndrome coronavirus 2, the virus that causes COVID-19—by early 2022, before the Omicron variants infected millions more. In the UK, an estimated 2.1 million people (3.3% of the population) were experiencing self-reported Long Covid in December 2022 (*2*).

Prior notes that the emergence of post-COVID syndromes was not a surprise to people with knowledge of chronic fatigue syndrome (CFS), nor to those who had seen long-term sequelae in people infected with the first severe acute respiratory syndrome virus in the early 2000s. However, it was not formal surveillance that revealed the extent of COVID's lasting effects, but rather individuals experiencing persistent symptoms. Prior describes in detail how some sufferers shared stories on social media, while others wrote articles about their experiences. Meanwhile, large online communities exchanging accounts of their experiences began to emerge in early 2020. These groups included physicians and researchers who—despite their often-debilitating symptoms—dedicated themselves to advocacy and conducting patient-led research. Prior situates this effort in the longer history of patient movements, particularly those advanced by "e-patient" communities, which interact in online spaces to provide peer support, share data, and facilitate novel patient and citizen research.

Throughout the book, Prior makes connections between Long Covid and other postviral illnesses, including CFS. There are clear parallels in terms of common symptoms such as postexertional fatigue, dysautonomia, brain fog, and pain. Another unfortunate similarity is a tendency for doctors to deny or minimize patients' lived experience, the impact of which can be profound. In addition to having damaging psychological effects, medical gaslighting can make it difficult for patients to access appropriate investigations, treatment, and clinical or welfare support.

Prior describes in detail many of the possible mechanisms that may underlie Long Covid symptoms, including disorders of inflammation, viral persistence, and autoimmune dysfunction. Understandably, he is impatient for treatments, hoping for a "theory of everything" that will explain common persistent symptoms and point to some generic treatment. While no such answer has yet emerged, the US National Institutes of Health (NIH) and other funding agencies have made substantial investments in Long Covid research.

Prior speaks to grant recipients who are optimistic that they may uncover key mechanisms underlying Long Covid and identify treatments. Here, he questions whether patients might have played a more central role in NIH-supported research decisions, many of which also fail to build on existing expertise in postviral sequelae. In the UK, by contrast, the National Institute for Health and Care Research has included a strong patient voice in decisions about Long Covid research, and patients have been involved in the design and conduct of research (*3*).

Prior's book is infused with empathy for those affected by chronic illness and stories of the hardships that many people with such illnesses experience. With the renewed investment in research and the strengths of the patient movement, he remains optimistic that Long Covid represents an opportunity for a real advance in how postviral illnesses are understood and managed. ∎

The Long Haul
Ryan Prior
Post Hill Press, 2022.
336 pp.

The reviewer is at the School of Public Health, Imperial College London, London SW7 2AZ, UK. Email: h.ward@imperial.ac.uk

REFERENCES AND NOTES

1. Worldometer, COVID-19 Coronavirus Pandemic; https://www.worldometers.info/coronavirus/.
2. UK Office for National Statistics, Prevalence of ongoing symptoms following coronavirus (COVID-19) infection in the UK: 5 January 2023; https://www.ons.gov.uk/peoplepopulationandcommunity/healthandsocialcare/conditionsanddiseases/bulletins/prevalenceofongoingsymptomsfollowingcoronaviruscovid19infectionintheuk/5january2023.
3. Imperial College London, Real-time Assessment of Community Transmission (REACT) Study, REACT Long COVID; https://www.imperial.ac.uk/medicine/research-and-impact/groups/react-study/studies/react-long-covid/.

10.1126/science.adf7568

GEOGRAPHY

In defense of public space

Parks, beaches, squares, and streets are vital sites for individuals, communities, and society to flourish

By **Helga Leitner**

In many cities across the globe, public spaces—including sidewalks, streets, squares, parks, beaches, museums, and libraries—have disappeared or been converted into privately owned and controlled spaces. Setha Low's book *Why Public Space Matters*, while acknowledging this reality, does not dwell on their disappearance, their growing surveillance, and the violence and fear often associated with public spaces. Rather, with conviction and great passion, she documents and analyzes how public space contributes to the flourishing of individuals, community, and society and to the building of an equitable and just city.

Low identifies six domains to which public space contributes: social justice and democratic practices; public health and well-being; play and recreation; the informal economy and social capital; environmental and ecological sustainability; and cultural identity and place attachment. These domains are featured in varying detail in the book's subsequent case study chapters, which disproportionately draw on research focused on public spaces—especially recreational spaces—in the New York metropolitan area. I was surprised, however, that the contribution of public space to the flourishing of democracy and citizenship rights received only marginal attention, given that public space has been a vital site for struggles for democracy and citizenship rights throughout history.

In chapters 3 to 5, readers learn about how public parks are used, inhabited, and remade by different social groups. Here, Low describes how, for example, Jones Beach was transformed from an exclusive middle-class space into a socially inclusive space that fosters respectful encounters across social differences. She also writes about the health benefits associated with green and open spaces, especially for individuals from low-income neighborhoods.

Later chapters venture beyond recreational public space and to some extent beyond New York, albeit more superficially. In chapter 6, Low discusses the informal economy on sidewalks, streets, and markets in New York City, Buenos Aires, and Baguio City. Public space, she notes, is vital for the thriving informal economy on which many depend in cities across the Global South. Meanwhile, in US cities, such spaces are crucial sites for new immigrants to secure employment and

Neighbors gather on a closed street during the COVID-19 pandemic.

income. Yet these types of spaces are under threat everywhere, as governments attempt to banish informal workers who are seen as inconsistent with modern cities.

Low highlights how green public space can advance environmental and ecological sustainability by mitigating risks posed by anthropocentric climate change. Her examples, again, come from New York, where community gardens and urban agriculture provide ecosystem services that mitigate the impact of global warming. As elsewhere, she insists that distributive and procedural social justice considerations should be central to environmental sustainability plans.

Next, Low discusses the role of public space in sustaining cultural identity, col-

lective memory, and the formation of place attachment, including struggles over whose cultural and sociopolitical identities, histories, and memories get represented in public space. Finally, she describes how COVID-19 transformed New Yorkers' relationship with public space as such spaces expanded and contracted, mediating public health and well-being. Here, Low acknowledges that public space need not be tangible, noting that virtual space burgeoned as access to physical public space became attenuated during the pandemic.

A notable feature of this book is the case it makes for the value of ethnographic methods for studying everyday life in public space, not only to better understand it but also to improve its accessibility, its ability to meet the needs of diverse populations, and its capacity to promote individual well-being and social justice. Low discusses numerous assessment tool kits and evaluation frameworks deploying these methods and their helpfulness for those studying and (re)designing public space. Although these tools are valuable, I would have liked to see her reflect also on their potential limitations. For example, we now know that some tools developed in the Global North are not applicable everywhere in the world. Further, some of these frameworks continue to perpetuate the problematic belief that planning and design can deliver adequate public space. Public space is not a commodity that can simply be delivered; space becomes public through people's involvement and actions. Finally, most tool kits focus on users—on their social relations and activity spaces. Human–environment relations and environmental processes require more attention.

Why Public Space Matters is a worthwhile and important read. Low brings decades of theoretical and practical engagement with public space to this project, allowing her to uncover the multiple ways public space enhances the quality of life for individuals, communities, and society, never leaving out of sight her ethico-political commitment to promoting social and environmental justice. This is a welcome contribution to the body of research on the threats facing public space. ∎

The reviewer is at the Department of Geography and the Institute of the Environment and Sustainability, University of California, Los Angeles, Los Angeles, CA 90095, USA. Email: hleitner@geog.ucla.edu

PHOTO: SETHA LOW

LETTERS

Community members at the foothills of Kilimanjaro in Tanzania collect seeds from the endangered *Prioria msoo* to be stored in a local restoration seed bank.

Seed banks needed to restore ecosystems

To address the global crises of climate change and biodiversity loss, the United Nations Decade on Ecosystem Restoration recognizes the urgent need to reverse ecosystem degradation (*1*). The current Global Biodiversity Framework, which also emphasizes these goals, was agreed upon in Montreal at the Conference of the Parties (COP15) in December 2022 (*2*). However, global restoration efforts are in danger of failing without adequate seed supply.

Biodiverse, properly sourced, native species are key to improving ecosystem integrity and human wellbeing (*1*, *3*), but wild seed sources are declining rapidly due to land degradation and climate change (*4*). Restoration projects also suffer from difficulty collecting genetically appropriate seeds and logistical challenges that lead to the waste of seeds, such as mismatch between wild seed availability and planting timelines and lack of adequate seed storage (*5*).

A wealth of scientific knowledge exists on seed banking to support species conservation, from Indigenous seed-saving groups [e.g., (*6*)] to technology-heavy seed banks at well-established research institutions [e.g., (*7*)]. Conservation seed banks, which focus on long-term storage, have made great progress on preserving threatened species in several regions (*8*). However, in most cases, they cannot provide enough seeds for ecosystem restoration.

To achieve the world's ambitious restoration goals (*1*, *9*), conservation seed bank knowledge should serve as the foundation for scaling up restoration seed banks, which focus on shorter-term storage and supplying planting projects with large quantities of appropriately sourced seeds. These seed banks can store common, abundant native species in quantities that are not generally found in conservation seed banks. Some can also hold threatened species, which are increasingly integrated into restoration to benefit biodiversity and conservation. Substantially increasing the number and capacity of seed banks for restoration would benefit planting projects by addressing challenges that lead to the waste of seeds (*10*, *11*). Reducing seed waste would, in turn, help prevent unsustainable harvests that can harm native ecosystems.

Creating a sufficient number of restoration seed banks will require joint efforts. Local restoration organizations should prioritize seed banking, which can provide economic opportunities to communities. Businesses should invest in restoration by sponsoring the establishment of seed banks. Governments and nongovernmental organizations can help connect new seed banks with local restoration efforts by facilitating the use of genetically appropriate, resilient seeds at finer geographic scales. All stakeholders should invest in decentralized restoration seed banks to support the immediate needs of restoration projects and fulfill the need for thousands of seed banks to address seed supply shortages in ecosystem restoration (*12*). Ensuring the availability of native seeds is a crucial step toward achieving global biodiversity targets for 2030 (*2*).

Uromi Manage Goodale[1,2], Alexandre Antonelli[3,4,5], Cara R. Nelson[6,7], Marian M. Chau[8,2]*

[1]Department of Health and Environmental Sciences, Xian Jiaotong Liverpool University, Suzhou, Jiangsu, China. [2]Seed Conservation Specialist Group, Species Survival Commission, International Union for Conservation of Nature, Gland, Switzerland. [3]Royal Botanic Gardens, Kew, Richmond, Surrey, UK. [4]Gothenburg Global Biodiversity Centre, Department of Biological and Environmental Sciences, University of Gothenburg, Gothenburg, Sweden. [5]Department of Biology, University of Oxford, Oxford, UK. [6]Department of Ecosystem and Conservation Sciences, University of Montana, Missoula, MT, USA. [7]Ecosystem Restoration Thematic Group, Commission on Ecosystem Management, International Union for Conservation of Nature, Gland, Switzerland. [8]Terraformation Inc., Kailua-Kona, HI, USA.
*Corresponding author.
Email: marian@terraformation.com

REFERENCES AND NOTES

1. United Nations Decade on Ecosystem Restoration, UNEP, FAO, International Union for Conservation of Nature's (IUCN's) Commission on Ecosystem Management, Society for Ecological Restoration, "Principles for ecosystem restoration to guide the United Nations Decade 2021–2030" (2021).
2. United Nations Biodiversity Conference COP15/ CP-MOP10/NP-MOP4 (2022); https://www.cbd.int/ article/cop15-cbd-press-release-final-19dec2022.
3. S. E. Andres *et al.*, *Plant. People Planet* **5**, 27 (2023).
4. B. R. Scheffers *et al.*, *Science* **354**, 6313 (2016).
5. R. Jalonen *et al.*, *Conserv. Lett.* **11**, 4 (2018).
6. R. A. Sanches, C. R. T. Futemma, *Desenvolv. Meio Ambiente.* **50**, 127 (2019).
7. E. Breman *et al.*, *Plants* **10**, 11 (2021).
8. S. Sharrock, "Plant Conservation Report 2020: A review of progress in implementation of the Global Strategy for Plant Conservation 2011–2020," Secretariat of the Convention on Biological Diversity, Botanic Gardens Conservation International (Technical Series No. 95, 2020).
9. J. F. Bastin *et al.*, *Science* **365**, 76 (2019).
10. D. J. Merritt, K. W. Dixon, *Science* **332**, 21 (2011).
11. P. León-Lobos *et al.*, *Restor. Ecol.* **28**, 2 (2020).
12. M. M. Chau *et al.*, "The global seed bank index" (Terraformation, 2022); https://www.terraformation. com/blog/seed-bank-index?.

10.1126/science.adg2171

Restore Iran's declining groundwater

Iran's climate varies from arid to semi-arid, but the country's use of groundwater is three times higher than the global average (*1*). In the past few decades, groundwater extraction through pumping has caused irreparable damage to Iran's plains (*2*). The groundwater supply, which is decreasing by 6 billion cubic meters annually, is the source of about 55% of Iran's water consumption (*3*). Iran must take steps to protect the quality and quantity of its groundwater.

Iran's groundwater quality is threatened by increasing contaminants, including runoff from septic wells, agriculture, landfills, and industrial waste (*4*). Although flooding can increase groundwater quantity, these contaminants, as well as saltwater, make their way more quickly to aquifers when flooding occurs (*5, 6*). Dams to control coastal flooding can prevent saltwater intrusion into coastal aquifers (*7, 8*), but the protection dams provide is insufficient.

Given that the effectiveness of natural environment filtration depends on groundwater levels and the soil media (*9*), improving the quantity of groundwater can also improve its quality. Therefore, to protect and restore Iran's groundwater, the country should take steps to control and monitor wells to prevent the illegal drilling that drains the aquifers. The government could improve monitoring by purchasing some of the wells used for agriculture and by installing smart water meters to track hourly and daily output (*1, 10*).

Once the capacity and water levels of each region have been determined, the amount of groundwater extraction permitted should be adjusted accordingly. Decisions about the extent and type of crops should also prioritize efficient water use. Preventing groundwater pollution is more affordable than water purification (*4*). By increasing its groundwater levels, Iran can ensure the availability of clean groundwater for consumption.

Babak Jaleh* and Mahtab Eslamipanah
Department of Physics, Faculty of Science, Bu-Ali Sina University, Hamedan, Iran.
*Corresponding author.
Email: jaleh@basu.ac.ir

REFERENCES AND NOTES
1. S. Samani, *Groundw. Sustain. Dev.* **12**, 100521 (2021).
2. H. Derakhshan, K. Davary, *Iran-Water Resour. Res.* **14**, 483 (2019).
3. S. J. Mirnezami, A. Bagheri, *Iran-Water Resour. Res.* **13**, 32 (2017).
4. H. Ghahremanzadeh, R. Noori, A. Baghvand, T. Nasrabadi, *Environ. Geochem. Health* **40**, 1317 (2018).
5. L. Karami, M. Alimohammadi, H. Soleimani, M. Askari, *Desalination Water Treat.* **148**, 119 (2019).
6. S. Boudaghpour, M. Bagheri, Z. Bagheri, *Arab. J. Sci. Eng.* **40**, 659 (2015).
7. R. Ghazavi, A. B. Vali, S. Eslamian, *Water Resour. Manag.* **26**, 1651 (2012).
8. A. Ranjbar, N. Mahjouri, *Environ. Earth Sci.* **77**, 1 (2018).
9. B. Oroji, *Geofis. Int.* **57**, 161 (2018).
10. A. Sarraf, A. Donyaii, M. Mardanifar, *J. Hydraul. Struct.* **6**, 21 (2020).

10.1126/science.adf9489

Clarify jurisdiction of US Clean Water Act

On 3 October 2022, the US Supreme Court heard arguments in *Sackett v. USEPA*, the latest in a series of cases seeking to clarify which waters are protected under the US Clean Water Act (*1*). Concurrently, the US Environmental Protection Agency (EPA) and the US Army Corps of Engineers are actively drafting rules for the third time in the past 10 years, after the Obama-era Clean Water Rule (*2*) was repealed (*3*) and the Trump-era Navigable Waters Protection Rule (*4*) was vacated and remanded (*5*). Consequently, enforcement of the Clean Water Act has reverted to 1986 agency guidance (*6*). Although scientific understanding of the physical, chemical, and biological connectivity of waters (*7*) and the ability to leverage geospatial data to guide jurisdictional determinations (*8, 9*) have grown substantially since 1986, the Clean Water Act enforcement and rulemaking have yet to catch up.

When the Clean Water Act was passed in 1972, it applied to "the Waters of the United States," an undefined term that remains ambiguous today (*10*). The precise definition was not critical when the nation's attention was focused on point-source pollution in large rivers, but Congress has never addressed how far Clean Water Act protections should extend into headwater streams, wetlands, and aquifers. Because of this uncertainty, the Supreme Court has adjudicated six cases disputing Clean Water Act jurisdictional scope (*8*), contributing to the Clean Water Act being their most-heard environmental issue (*11*). As the agencies embark on a third attempt at rulemaking this decade, Congress remains steadfastly silent, content to watch the courts mediate 50 years of sparring over implementation of the law.

Congress, the EPA, and the Army Corps of Engineers now have the opportunity—and responsibility—to clarify the scope of the Clean Water Act and implement evidence-based policy. We call on Congress to amend the Clean Water Act, clarifying their intent rather than leaving the agencies and courts to interpret vague language. Meanwhile, the agencies should engage and empower their own scientists to create transferable geospatial tools, embracing rather than eschewing mapping and predictive efforts (*12*). The EPA's Science Advisory Board can aid this effort by continuing to demand that the agency adhere to the best available science and take a proactive role in guiding transparent, effective, and science-informed rulemaking. Preserving and improving our nation's water quality future is at stake.

Adam S. Ward[1]*, Jeffrey Wade[2], Christa Kelleher[3], Rebecca L. Schewe[4]
[1]Department of Biological & Ecological Engineering, Oregon State University, Corvallis, OR, USA. [2]Department of Earth and Environmental Sciences, Syracuse University, Syracuse, NY, USA. [3]Department of Civil and Environmental Engineering, Lafayette College, Easton, PA, USA. [4]Department of Sociology, Syracuse University, Syracuse, NY, USA.
*Corresponding author.
Email: adam.ward@oregonstate.edu

REFERENCES AND NOTES
1. Federal Water Pollution Control Act Amendments of 1972 (33 U.S.C. §§ 1251–1387, 1972).
2. US Department of Defense, US Environmental Protection Agency, "Clean Water Rule: Definition of 'Waters of the United States,'" *Federal Register* **80**, 37054 (2015).
3. D. J. Trump, "Executive Order 13778: Restoring the rule of law, federalism, and economic growth by reviewing the 'Waters of the United States' rule," *Federal Register* **82**, 12497 (2017).
4. US Department of Defense, US Environmental Protection Agency, "The Navigable Waters Protection Rule: Definition of 'Waters of the United States,'" *Federal Register* **85**, 22250 (2020).
5. *Pascua Yaqui Tribe v. U.S. Environmental Protection Agency*, United States District Court, District of Arizona. CV-20-00266-TUC-RM (2021).
6. US Department of Defense, "Final Rule for Regulatory Programs of the Corps of Engineers," *Federal Register* **51**, 41217 (1986).
7. L. C. Alexander *et al.*, "Connectivity of streams and wetlands to downstream waters: A review and synthesis of the scientific evidence" (EPA/600/R-14/475F, 2013), p. 331.
8. R. Walsh, A. S. Ward, *WIREs Wat.* **9**, e1603 (2022).
9. J. Wade, C. Kelleher, A. S. Ward, R. L. Schewe, *Hydrol. Process.* **36**, e14747 (2022).
10. S. P. Mulligan, "Evolution of the meaning of 'Waters of the United States' in the Clean Water Act" (2019), pp. R44585–R44585.
11. S. Zellmer, "Treading water while Congress ignores the nation's environment" *Notre Dame L. Rev.* **88**, 2323 (2013).
12. US Department of Defense, US Environmental Protection Agency, "Navigable Waters Protection Rule fact sheet: Mapping and the Navigable Waters Protection Rule" (2020), p. 4.

10.1126/science.adf7391

RESEARCH

METABOLIC ADAPTATION
Loss leads to gain

Hummingbirds display true hovering flight, an incredibly energy-intensive activity. Although much is known about the physiology of this movement, little has been discovered about the genetics underlying its evolution. Osipova *et al*. screened newly generated and previously sequenced bird genomes to search for key changes facilitating this high-energy locomotion. They found that a gluconeogenic muscle enzyme, FBP2, was lost as hovering flight evolved. Knockouts of this gene in avian cell lines led to an increase in glycolysis, mitochondria production, and mitochondrial respiration, all leading to higher energy efficiency. These results also illustrate how the loss of a gene can be adaptive. —SNV
Science, abn7050, this issue p. 185

Loss of a gene in hummingbirds, such as the long-tailed hermit pictured here in flight, leads to increased muscle energy efficiency.

GENE EDITING
Editing away heart disease

Ischemia-reperfusion injury, tissue damage that occurs after oxygen deprivation, can be observed after a variety of insults, including common ones such as heart attack or stroke. A key protein that plays a role in this damage is calcium calmodulin-dependent protein kinase IIδ (CaMKIIδ). Lebek *et al*. found that targeting CaMKIIδ using CRISPR-Cas9 gene editing was a viable intervention to protect the heart tissue from ischemia-reperfusion damage in mouse models. Injecting gene-editing reagents soon after ischemia exposure was sufficient for the mice to recover from severe heart damage, suggesting that it may not be too late to intervene after a heart attack happens. —YN
Science, ade1105, this issue p. 179

CHEMICAL DYNAMICS
Steric effects in chemical reactions

Although steric (orientation-dependent) effects in reactive scattering are well known to exist in the theory of chemical dynamics, there is a need for combined experimental-theoretical studies that rigorously explore these effects at the most fundamental level. Using polarized stimulated Raman pumping to prepare the hydrogen-deuterium (HD) molecules with the HD bond axis aligned either parallel or perpendicular to the H atom velocity, Wang *et al*. obtained high-quality stereodynamical data for the H+HD→H_2+D reaction. These measurements demonstrate that the HD orientation has a substantial effect on this most fundamental chemical reaction, and is further supported by excellent agreement with quantum mechanical calculations. The present work is an important milestone in the field of reaction dynamics. —YS
Science, ade7471, this issue p. 191

ENZYME DESIGN
Fishing for the right puzzle piece

Recombination can be a good strategy to generate natural protein diversity while retaining function, but it also causes problems if the starting sequences are too dissimilar and cannot fit together properly to form a functional protein. Lipsh-Sokolik *et al*. developed a machine learning strategy to piece together fragments

PHOTO: WILDLIFE GMBH/ALAMY STOCK PHOTO

sourced from highly divergent natural enzymes to generate a million structurally diverse protein backbones. This step was then followed by mutagenesis and structural optimization to create stable, functional active sites. Isolation by high-throughput yeast display and activity-based profiling recovered thousands of functional enzyme variants. A second-generation model trained on preorganization of the active site was nearly 10-fold more efficient and provides valuable insights for enzyme design strategies across the board. —MAF

Science, ade9434, this issue p. 195

CYTOKINES
Germinal centers need some TSLP

Thymic stromal lymphopoietin (TSLP) promotes allergic responses within barrier tissues and is a target for therapeutic inhibition in severe asthma. The contributions of signaling through the TSLP receptor on B and T cells to germinal center (GC) antibody responses are poorly understood. Domeier *et al*. used mouse models lacking TSLP or its receptor to investigate how loss of TSLP signaling impairs antibody formation in GCs. Conditional deletion of the TSLP receptor in T cells impaired differentiation of T follicular helper cells that support GC B cells. However, conditional deletion of the TSLP receptor in B cells augmented antigen-specific GCs and memory B cells. TSLP is thus a key cytokine used by both B and T cells to achieve optimal GC function. —IRW

Sci. Immunol. **8**, eadd9413 (2023).

VOLCANOLOGY
Planetary impacts of volcanic eruptions

The undersea eruption of the Hunga Tonga-Hunga Ha'apai volcano in January 2022 was one of the largest events of its kind in recent history. Aside from lofting a volcanic plume into the mesosphere, with global climatic effects, this explosive eruption had other planetary-scale impacts. Garza-Girón *et al.* characterized these effects using the seismic record of the event, showing that force interactions between the solid Earth and its fluid envelope resulted in global-scale wave motions in Earth's lithosphere, hydrosphere, and atmosphere. —KVH

Sci. Adv. 10.1126/sciadv.add4931(2023).

METALLURGY
Putting steel through the process

High-strength steels with good ductility are attractive for a number of applications, but these alloys often require the use of expensive elements or complex processing methods. Li *et al*. found that a high-strength steel composed of iron, manganese, silicon, carbon, and vanadium can be made with a different processing strategy. A combination of forging, cryogenic treatment, and tempering creates an alloy with very high strength that also has good ductility and formability. The strategy should be an option for other compositions of steel. —BG

Science, add7857, this issue p. 168

SOLAR CELLS
Facet-stabilized films

The degradation of formamidinium−based lead iodide perovskite has been shown to depend on which crystal facets are exposed to the surface. Ma *et al*. found that water adhesion was stronger on the (100) facet than on the (111) facet and made these materials more prone to moisture-induced degradation. The authors show how ligand-assisted perovskite film growth could be used create (111)-dominated films with high stability against moisture (up to 85% relative humidity) and thermal stress (85ºC) without additional surface passivation. —PDS

Science, adf3349, this issue p. 173
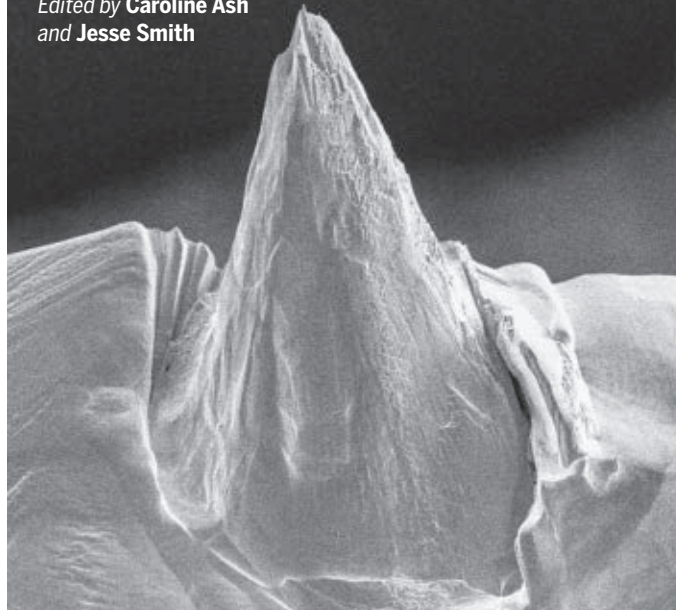
FIELD EMISSION
A tipping point for coherent electron emission

In electron microscopy, the better the quality of the electron beam, the better the imaging capability. The desired qualities for an electron source are narrow and tunable energy distribution, high brightness, small emission angle, and stability. Johnson *et al.* report on a fabrication and preparation process of an electron field emission source made from a superconducting niobium wire that meets these criteria. The key to the technique is the formation of a nanoprotrusion on the end of the tip created by a final annealing step. This protrusion results in a near-monochromatic electron source, narrow emission angle, high brightness, and stability over several hours while operating at cryogenic temperatures. Such tips should be useful for high-resolution electron spectroscopy. —ISO   *Phys. Rev. Lett.* **129**, 244802 (2022).

Scanning electron micrograph of a monocrystalline, superconducting niobium nanotip.

HUMAN EVOLUTION
Denisovan-endowed immunity

Unlike Neanderthals, we know little about the biology of Denisovans. Indeed, most of our knowledge of these archaic hominins is of their DNA, either from small fossil samples or the ancestry left in about 5% of the genomes of present-day indigenous Australasians. Vespasiani *et al.* examined the genomes of present-day Papua New Guineans to find out what Denisovans might have contributed to modern human physiology. Denisovan variants were not universally enriched in regions of active chromatin, but were enriched for gene expression in immune cells. This indicates that having Denisovan

PLANT SCIENCE
Drying to survive

The starchy endosperm in the seeds of flowering plants transitions from multinucleate to cellular tissue. By examining transcriptomes, Xu *et al.* found that a signal related to dehydration stress triggers formation of cells in the endosperm syncytium. Failure to cellularize often occurs when incompatible hybrid seeds are formed, leading to failure of embryonic development. The authors were able to override this hybridization block by increasing the concentration of a dehydration stress hormone, abscisic acid, which allowed incompatible hybrid seeds to germinate successfully. The work provides an alternative route for producing plant hybrids essential for agricultural research. —MRS

Plant Cell 10.1093/plcell/koac337 (2022).

Cell formation in developing *Arabidopsis* embryos is important for inducing dehydration tolerance and seed survival.

ancestry may be an advantage for protection against pathogens. —CNS

PLOS Genet. **18**, e1010470 (2022).

PALEONTOLOGY
Ichthyosaur aggregations

The bones of a giant Triassic ichthyosaur (*Shonisaurus popul10ris*) lie in a fossil bed in Nevada that was once covered by a large sea. This fossil site is unique in that there are multiple individuals preserved within a single time horizon. Kelley *et al.* investigated the geology, taphonomy, and fossil distribution across this site and others in the vicinity. The authors found that, aside from *Shonisaurus*, the site contains few other species. Moreover, the assemblage consists primarily of large adults, with a few neonates or embryos. This indicates that at the time of death, a large-scale aggregation of these animals was occurring, likely for breeding or feeding, as happens among many modern tetrapods such as whales. —SNV

Curr. Biol. **32**, 5398 (2022).

CONSERVATION
Protected areas protection

A concern in conservation is whether areas designated as protected really do protect species. Bird watching is a popular activity because species are relatively easy to observe and consistent, accurate data are straightforward to collect. The Breeding Bird Survey in the UK was started in 1994, and Sanderson *et al.* used these data to compare the effectiveness of protection to birds by two levels of designated conservation: the UK's Sites of Special Scientific Interest (SSSI) and the UK components of the European Natura 2000 network. In a related survey, Barnes *et al.* used data from large-scale citizen science projects to address the same question. Both studies showed that the larger Natura 2000 areas deliver the greatest positive benefits for rare and vulnerable species with specialized habitat needs. However, many of these areas have not been well managed, so they have the potential to offer even greater benefits to vulnerable species. —CA

Animal Conserv. 10.1111/acv.12832 (2022); *Nat. Ecol. Evol.* 10.1038/s41559-022-01927-4 (2022).

CLIMATE CHANGE
Patterns and persistence

How might anthropogenic climate warming affect atmospheric circulation over Europe? Dorrington *et al.* analyzed simulations from a collection of models run under the SSP5-8.5 climate change scenario. They found that although the spatial structure of wintertime anticyclonic circulation over Europe is expected to stay the same, the durations of these atmospheric blocking events are expected to decrease generally. In other words, although the persistence of these events will change, the emergence of new weather patterns is unlikely to occur. —HJS

Geophys. Res. Lett. **49**, e2022GL100811 (2022).

SPINTRONICS
Spinning a skyrmion lattice

Magnetic skyrmions, nanosized whirlpools of spin that can be generated in certain materials, are promising as information carriers in spin-based electronics. They remain tricky to control, however, especially on fast time scales. Tengdin *et al.* used femtosecond pulses of circularly polarized light to rapidly rotate a skyrmion lattice formed in the material Cu_2OSeO_3. The degree of rotation was dependent on the fluence of the laser light as well as on the time separation between the pulses. The nature of this dependence implied that a collective excitation of the skyrmion lattice and its interaction with disorder were responsible for the effect. —JS

Phys. Rev. X **12**, 041030 (2022).

ALSO IN *SCIENCE* JOURNALS

Edited by **Michael Funk**

VECTOR BIOLOGY
Ticks repurpose host IFN-γ to Dome-inate

Many arthropods use cytokine-like molecules such as Unpaired (UPD) to activate JAK–STAT signaling and drive robust anti-bacterial responses. Curiously, deer ticks (*Ixodes scapularis*), which serve as a vector for Lyme disease, lack identifiable UPD homologs. Rana *et al.* found instead in *I. scapularis* a receptor called Dome1 that binds to and is activated by mammalian interferon-γ ingested in the tick's blood meal. Dome1, which triggers the JAK–STAT pathway, not only enhances tick immunity but is also crucial for tick metamorphosis and organ development. Thus, deer ticks have successfully coopted mammalian host immune signaling for their own ends using pathways that could potentially be targeted in future ectoparasite control strategies. —STS

Science, abl3837, this issue p. 154

CLIMATE PROJECTION
Insider knowledge

For decades, some members of the fossil fuel industry tried to convince the public that a causative link between fossil fuel use and climate warming could not be made because the models used to project warming were too uncertain. Supran *et al.* show that one of those companies, ExxonMobil, had their own internal models that projected warming trajectories consistent with those forecast by the independent academic and government models. What they understood about climate models thus contradicted what they led the public to believe. —HJS

Science, abk0063, this issue p. 153

NEURODEGENERATION
Microbiota and tau-mediated disease

The accumulation of certain forms of the tau protein in the brain is linked to loss of nerve cells, inflammation, and cognitive decline in Alzheimer's disease and several other neurodegenerative diseases. Apolipoprotein-E (APOE), the strongest genetic risk factor for Alzheimer's disease, regulates brain inflammation and tau-mediated brain damage; however, the gut microbiota also regulates brain inflammation. In a mouse model of tau-mediated brain injury, Seo *et al.* found that manipulation of the gut microbiota resulted in a strong reduction of inflammation, tau pathology, and brain damage in a sex- and APOE-dependent manner (see the Perspective by Jain and Li). —SMH

Science, add1236, this issue p. 155; see also adf9548, p. 142

NANOFLUIDICS
Toward fluidic neuromorphic computing

There is considerable interest in strategies that mimic the structure of human brain and could lead to the development of next-generation neuromorphic devices. Many recent studies have focused on solid-state devices, although information in biological systems is conveyed by ions solvated in water, an approach now explored in two papers in this issue (see the Perspective by Noy and Darling). Robin *et al.* created nanofluidic devices consisting of nanometer-thick two-dimensional slits filled with a salt solution, whereas Xiong *et al.* present a nanofluidic ionic memristor based on confined polyelectrolyte-ion interactions. The two studies are focused on different aspects of neuromorphic engineering, but both show precise control of ion transport in water across nanoscale channels. These studies show promising directions for creating neuromorphic functions using energy-efficient fluidic memristors that could mimic biological systems down to their fundamental principles. —YS

Science, adc9931, adc9150, this issue p. 161, 156; see also adf6400, p. 143

NEURODEVELOPMENT
Mechanosensation guides joint development

Distal arthrogryposis is a rare disorder that affects peripheral joints, causing contractures. Some mutations that cause this condition are related to the joints and the muscles around them, but some instead lead to overactive PIEZO2, a somatosensory mechanosensory ion channel. S. Ma *et al.* used a mouse model to show that expression of overactive PIEZO2 during a developmentally sensitive period in proprioceptive neurons causes similar joint defects (see the Perspective by Müller). Treatment with a toxin that blocks neural transmission or a dietary fatty acid commonly found in fish lowered PIEZO2 activity and reduced joint defects. —PJH

Science, add3598, this issue p. 201; see also adf6570, p. 137

GUT PATHOGENS
Phosphate-stimulated virulence

To cause disease, enterohemorrhagic and enteropathogenic *Escherichia coli* must first adhere to intestinal cells. Adhesion requires the transcription factor Ler. Jia *et al.* identified a small RNA, EsrL, that promoted *E. coli* adhesion to cultured human cells and colonization of the rabbit colon. Under high-phosphate conditions similar to those in the gut, *esrL* expression was derepressed and EsrL stabilized the *ler* transcript. Stabilization of both transcripts likely contributes to *E. coli* virulence in the high-phosphate environment of the gut. —AMV

Sci. Signal. **16**, eabm0488 (2023).

LUNG CANCER
Autoantibodies help reveal cancer risk

Small-cell lung cancer (SCLC) is a major cause of cancer-related deaths, and effective early detection strategies for it are lacking. Lastwika *et al.* took advantage of a feature specific to SCLC to develop a candidate method for early detection. The authors developed a technique to identify targets of SCLC-associated autoantibodies, finding that many of the antibodies targeted disease-specific posttranslational modifications in extracellular proteins. The authors used these findings to generate a risk-prediction model using five autoantibody targets in combination with cigarette smoke consumption. This model was able to accurately predict disease in three independent cohorts, suggesting that circulating autoantibodies could provide an essential early detection method. —CSM

Sci. Transl. Med. **15**, eadd8469 (2023).
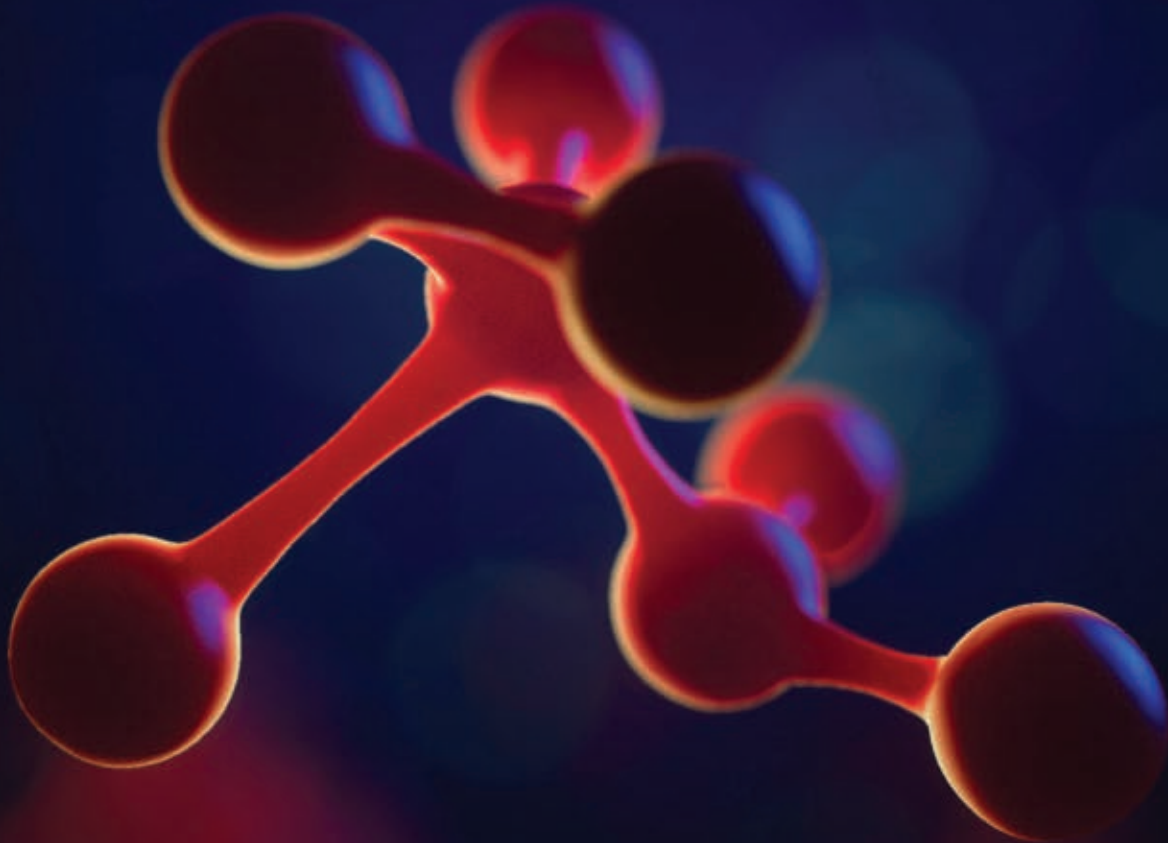
REVIEW SUMMARY

CLIMATE PROJECTION

Assessing ExxonMobil's global warming projections

G. Supran*, S. Rahmstorf, N. Oreskes

BACKGROUND: In 2015, investigative journalists discovered internal company memos indicating that Exxon oil company has known since the late 1970s that its fossil fuel products could lead to global warming with "dramatic environmental effects before the year 2050." Additional documents then emerged showing that the US oil and gas industry's largest trade association had likewise known since at least the 1950s, as had the coal industry since at least the 1960s, and electric utilities, Total oil company, and GM and Ford motor companies since at least the 1970s. Scholars and journalists have analyzed the texts contained in these documents, providing qualitative accounts of fossil fuel interests' knowledge of climate science and its implications. In 2017, for instance, we demonstrated that Exxon's internal documents, as well as peer-reviewed studies published by Exxon and ExxonMobil Corp scientists, overwhelmingly acknowledged that climate change is real and human-caused. By contrast, the majority of Mobil and ExxonMobil Corp's public communications promoted doubt on the matter.

ADVANCES: Many of the uncovered fossil fuel industry documents include explicit projections of the amount of warming expected to occur over time in response to rising atmospheric greenhouse gas concentrations. Yet, these numerical and graphical data have received little attention. Indeed, no one has systematically reviewed climate modeling projections by any fossil fuel interest. What exactly did oil and gas companies know, and how accurate did their knowledge prove to be? Here, we address these questions by reporting and analyzing all known global warming projections documented by—and in many cases modeled by—Exxon and ExxonMobil Corp scientists between 1977 and 2003.

Our results show that in private and academic circles since the late 1970s and early 1980s, ExxonMobil predicted global warming correctly and skillfully. Using established statistical techniques, we find that 63 to 83% of the climate projections reported by ExxonMobil scientists were accurate in predicting subsequent global warming. ExxonMobil's average projected warming was $0.20° \pm 0.04°C$ per decade, which is, within uncertainty, the same as that of independent academic and government projections published between 1970 and 2007. The average "skill score" and level of uncertainty of ExxonMobil's climate models (67 to 75% and ±21%, respectively) were also similar to those of the independent models.

Moreover, we show that ExxonMobil scientists correctly dismissed the possibility of a coming ice age in favor of a "carbon dioxide induced 'super-interglacial'"; accurately predicted that human-caused global warming would first be detectable in the year 2000 ± 5; and reasonably estimated how much CO_2 would lead to dangerous warming.

OUTLOOK: Today, dozens of cities, counties, and states are suing oil and gas companies for their "longstanding internal scientific knowledge of the causes and consequences of climate change and public deception campaigns." The European Parliament and the US Congress have held hearings, US President Joe Biden has committed to holding fossil fuel companies accountable, and a grassroots social movement has arisen under the moniker #ExxonKnew. Our findings demonstrate that ExxonMobil didn't just know "something" about global warming decades ago—they knew as much as academic and government scientists knew. But whereas those scientists worked to communicate what they knew, ExxonMobil worked to deny it—including overemphasizing uncertainties, denigrating climate models, mythologizing global cooling, feigning ignorance about the discernibility of human-caused warming, and staying silent about the possibility of stranded fossil fuel assets in a carbon-constrained world. ∎

S **READ THE FULL ARTICLE AT**
https://doi.org/10.1126/science.abk0063

Historically observed temperature change (red) and atmospheric carbon dioxide concentration (blue) over time, compared against global warming projections reported by ExxonMobil scientists.
(**A**) "Proprietary" 1982 Exxon-modeled projections. (**B**) Summary of projections in seven internal company memos and five peer-reviewed publications between 1977 and 2003 (gray lines). (**C**) A 1977 internally reported graph of the global warming "effect of CO_2 on an interglacial scale." (A) and (B) display averaged historical temperature observations, whereas the historical temperature record in (C) is a smoothed Earth system model simulation of the last 150,000 years.
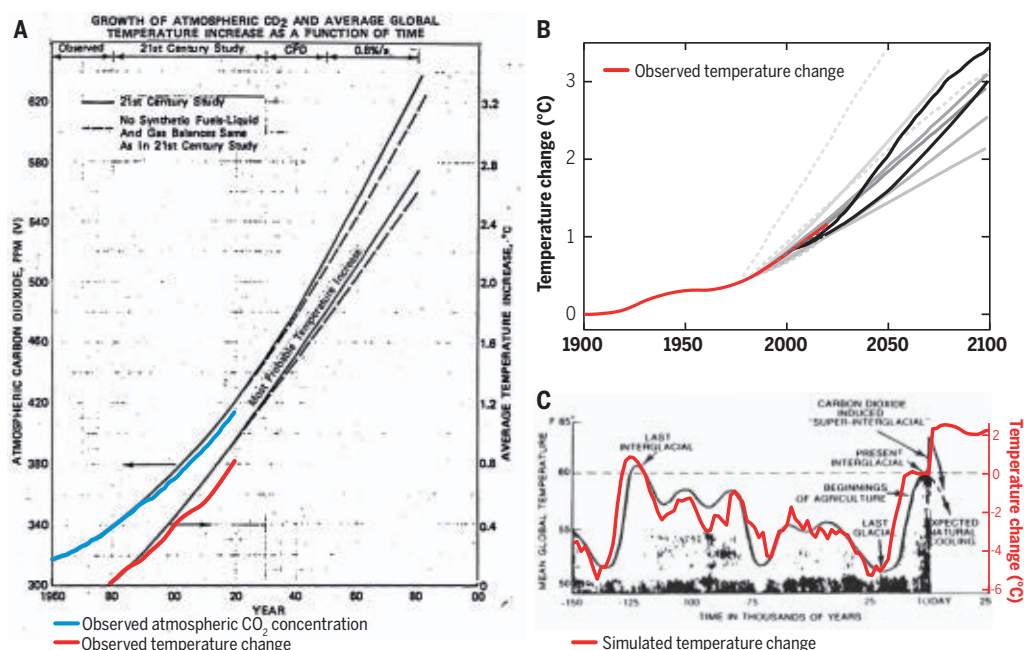
CLIMATE PROJECTION

Assessing ExxonMobil's global warming projections

G. Supran[1]*†, S. Rahmstorf[2,3], N. Oreskes[1,4]

Climate projections by the fossil fuel industry have never been assessed. On the basis of company records, we quantitatively evaluated all available global warming projections documented by—and in many cases modeled by—Exxon and ExxonMobil Corp scientists between 1977 and 2003. We find that most of their projections accurately forecast warming that is consistent with subsequent observations. Their projections were also consistent with, and at least as skillful as, those of independent academic and government models. Exxon and ExxonMobil Corp also correctly rejected the prospect of a coming ice age, accurately predicted when human-caused global warming would first be detected, and reasonably estimated the "carbon budget" for holding warming below 2°C. On each of these points, however, the company's public statements about climate science contradicted its own scientific data.

I n 2015, investigative journalists uncovered internal company documents showing that Exxon scientists have been warning their executives about "potentially catastrophic" anthropogenic (human-caused) global warming since at least 1977 (1, 2). Researchers and journalists have subsequently unearthed additional documents showing that the US oil and gas industry writ large—by way of its trade association, the American Petroleum Institute—has been aware of potential human-caused global warming since at least the 1950s (3); the coal industry since at least the 1960s (4); electric utilities, Total oil company, and General Motors and Ford motor companies since at least the 1970s (5–8); and Shell oil company since at least the 1980s (9).

This corpus of fossil fuel documents has attracted widespread scholarly, journalistic, political, and legal attention, leading to the conclusion that the fossil fuel industry has known for decades that their products could cause dangerous global warming. In 2017, we used content analysis to demonstrate that Exxon's internal documents, as well as peer-reviewed studies authored or coauthored by Exxon and ExxonMobil Corp scientists, over-whelmingly acknowledged that global warming is real and human-caused (10). By contrast, we found that the majority of Mobil and ExxonMobil Corp's public communications promoted doubt on the matter. Cities, counties, and states have accordingly filed dozens of lawsuits variously accusing ExxonMobil Corp and other companies of deceit and responsi-

bility for climate damages (11). The attorney general of Massachusetts, for instance, alleges that ExxonMobil has had a "long-standing internal scientific knowledge of the causes and consequences of climate change" and waged "public deception campaigns" that misrepresented that knowledge (12). Civil society campaigns seeking to hold fossil fuel interests accountable for allegedly misleading shareholders, customers, and the public about climate science have emerged under monikers such as #ExxonKnew, #ShellKnew, and #TotalKnew (13–15) (see Box 1 for more examples).

But what exactly did the fossil fuel industry understand about the role of fossil fuels in causing global warming, and how accurate did their understanding prove to be? Several of the documents in question include explicit projections of the amount of warming that could be expected to occur over time in response to rising atmospheric greenhouse gas concentrations. Yet, whereas the text of these documents has been interrogated in detail, the numerical and graphical data in them have not. Indeed, no one has systematically reported climate modeling projections by any fossil fuel interest, let alone assessed their accuracy and skill. This contrasts with academic climate models, whose performance has been extensively scrutinized (16–24).

In this Review, we report and analyze all known projections of global mean surface temperature (hereafter "temperature") change reported by company scientists working for Exxon and/or for ExxonMobil Corp after Exxon's merger with Mobil Oil Corp in 1999. (Hereafter, we collectively refer to Exxon and ExxonMobil Corp as "ExxonMobil" or the "company.") Some projections resulted from models built or run in-house by ExxonMobil scientists, sometimes in collaboration with independent researchers. Others were produced by third parties and then discussed by

ExxonMobil scientists in internal reports. Where relevant, we distinguish these provenances, but otherwise we collectively refer to these projections as "reported" by ExxonMobil scientists.

We test the accuracy and modeling skill of ExxonMobil's global warming projections by retrospectively comparing them against subsequent observed temperature changes. We also compare their performance against assessments of models published in independent scientific literature. [Here and throughout, we use the term "climate models" to generically refer to computer simulations of Earth's climate system. All of the models investigated here—both from ExxonMobil and from independent academic and government scientists—are variants of Energy Balance Models, rather than the higher-resolution, more comprehensive General Circulation Models that succeeded them in the late 1980s (25–27).] Having quantified ExxonMobil's early understanding of climate science, we contrast it with public claims made by the company and its allies. We then offer three illustrations of how quantitative historical analysis of the fossil fuel industry's documents can yield further historical insights into the disconnect between its private understanding of climate science and its public climate denial.

We focus on global mean surface temperature changes because they are a primary driver of climate impacts, are central to climate policy-making, are the most common output of early climate models, and are accurately captured by observational records. We limit our analysis to global warming projections reported by scientists at ExxonMobil, as compared to other companies, for several reasons. First, ExxonMobil's extensive climate research program is well documented. Second, ExxonMobil documents contain the largest public collection of global warming projections recorded by a single company, allowing us to develop a coherent picture of the early understanding of climate science by a specific industry actor. Third, the company has been active in challenging climate science in general and climate models specifically, such that its work on the matter may be of particular interest to researchers, reporters, advocates, shareholders, fund managers, politicians, and legal investigators examining corporate responsibility for climate change (Box 1).

Materials and methods

We analyzed 32 internal documents produced in-house by ExxonMobil scientists and managers between 1977 and 2002, and 72 peer-reviewed scientific publications authored or coauthored by ExxonMobil scientists between 1982 and 2014. The internal documents were collated from public archives provided by ExxonMobil Corp (28), *InsideClimate News* (29), and Climate Investigations Center (30).

[1]Department of the History of Science, Harvard University, Cambridge, MA, USA. [2]Potsdam Institute for Climate Impact Research, Potsdam, Germany. [3]Institute of Physics and Astronomy, University of Potsdam, Potsdam, Germany. [4]Department of Earth and Planetary Sciences, Harvard University, Cambridge MA, USA.
*Corresponding author. Email: gjsupran@fas.harvard.edu
†Present address: Department of Environmental Science and Policy, Rosenstiel School of Marine, Atmospheric, and Earth Science, University of Miami, Miami, FL, USA.

There are an increasing number of lawsuits, political investigations, and civil society campaigns seeking to hold ExxonMobil Corp and other companies accountable for allegedly misleading shareholders, customers, and the public about climate science.

Lawsuits

Cities, counties, and states have filed dozens of lawsuits accusing ExxonMobil Corp and others of deceptive marketing, misleading shareholders, and culpability for climate damages (two of the authors, G.S. and N.O., have provided expert input to some of these cases) (11).

Political mobilizations

• In 2019, the European Parliament held a first-of-its-kind hearing on climate change denial by ExxonMobil Corp and other actors (to which one author, G.S., testified) (64).
• In 2019, hearings were held in the House and Senate of the United States (US) Congress regarding "oil industry efforts to suppress the truth about climate change" and "dark money and barriers to climate change," respectively (one author, N.O., testified to both) (65, 66).
• In 2021, the US House Committee on Oversight and Reform requested documents and testimony from ExxonMobil Corp and other oil and gas companies and trade associations as part of an ongoing investigation into the fossil fuel industry's "coordinated effort to spread disinformation" about climate change (67).
• US President Joe Biden has issued repeated commitments to hold fossil fuel companies accountable, including a 2020 environmental justice plan to "strategically support ongoing plaintiff-driven climate litigation against polluters" (68); a 2020 statement that "We should go after" the fossil fuel industry "just like we did the drug companies, just like we did with the tobacco companies" (69); and a 2021 Executive Order "to hold polluters accountable" (70).
• In 2022, the Commission on Human Rights of the Philippines (to which one author, G.S., testified) ruled that the "Carbon Majors," including ExxonMobil Corp, "engaged in willful obfuscation [of climate science] and obstruction to prevent meaningful climate action" and that all such acts "may be bases for liability" (71).

Civil society campaigns

• International fossil fuel divestment movement, including specific calls for—and institutional commitments to—divestment from climate denying fossil fuel companies (two of the authors, G.S. and N.O., have supported these campaigns) (72–74).
• "Pay Up Climate Polluters" campaign (75).
• Array of distributed activism under the moniker #ExxonKnew (13).

The peer-reviewed publications were obtained by identifying all peer-reviewed documents among ExxonMobil Corp's lists of "Contributed Publications," except for three articles discovered independently during our research (31) [see supplementary materials (SM) section S2 for details on the assembly of the corpus]. These constitute all publicly available internal ExxonMobil documents concerning anthropogenic global warming of which we are aware, and all ExxonMobil peer-reviewed publications concerning global warming disclosed by the company.

Using manual content analysis, we identify all documents that reported climate model outputs of (i) a time series of projected future temperature, and (ii) future external radiative forcings [including at least atmospheric carbon dioxide (CO_2) concentration] (see SM section S1.1 for coding details). For models driven by more than one forcing time series (i.e., for high- and low-CO_2 scenarios as well as a central, "nominal" one), each resulting temperature time series is treated as a separate and individual projection. Our figures and tables therefore distinguish between "nominal," "high," and "low" model projections. By contrast, for a given CO_2 scenario, temperature time series accompanied by uncertainty bars (corresponding, for example, to different model climate sensitivities) are treated as single projections with uncertainty bounds given by those uncertainty bars. This yields 12 documents published between 1977 and 2003, which contain 16 distinct temperature projections presented in the form of 12 unique graphs and one table (summarized in SM section S2.2). The 12 documents comprise seven internal memos (1977 to 1985) and five peer-reviewed papers (1985 to 2003). Twelve of the 16 temperature projections came from models built or run in-house by ExxonMobil scientists, typically in collaboration with independent researchers. Once identified, all original temperature and forcing projections are converted for analysis by digitizing graphs and extracting tables.

We assess each model projection over the period from the publication year of its contain-ing document through 2019 (or through the final projected year, if earlier). First, we overlay all original temperature time series with observed temperature changes. Observations are aligned with respect to the earliest reference year(s) for which model projection data are available and, unless noted otherwise, reflect the smoothed annual average of five historical time series. Following Hausfather et al. (2020) and the Intergovernmental Panel on Climate Change (IPCC), we compare observations to model projections in two quantitative ways: (i) change in temperature versus time; and (ii) change in temperature versus change in radiative forcing (the "implied transient climate response," or iTCR) (16, 24). The iTCR metric enables us to assess model performance while accounting for any differences in the assumptions about future radiative forcings driving the models. For each projected and observed temperature time series, per-decade temperature changes are calculated by fitting an ordinary least squares model over the projection period and multiplying the resulting gradient coefficient by 10. Analogously, iTCR is calculated by regressing temperature against anthropogenic radiative forcing over the projection period and multiplying the result by the forcing associated with doubled atmospheric CO_2 concentrations, $F_{2x} = 3.7 \text{W/m}^2$ (16):

$$iTCR = F_{2x}\Delta T / \Delta F_{\text{anthro}}$$

For model projections, ΔF_{anthro} was based on explicit external forcing values when provided and was otherwise estimated from model CO_2 concentration scenarios as

$$\Delta F_{\text{anthro}} = 5.35 \cdot \ln\left(\frac{p'_{CO_2}}{p_{CO_2}}\right)$$

where p_{CO_2} is the initial CO_2 concentration (in parts per million) at the start of the projection period and p'_{CO_2} is the CO_2 concentration during each subsequent year through 2019 (16). In the real world, of course, global temperature changes are driven by multiple natural and anthropogenic factors, including but not limited to CO_2. Nevertheless, even when model projections are driven by CO_2-only anthropogenic forcing scenarios, retrospectively comparing projections to observations offers a robust, independent, and established test of model skill. This is because (i) global warming has been almost entirely human-caused since the late 19th century (32, 33) and (ii) total anthropogenic forcing over the past 150 years has been, to first order, similar to the forcing of CO_2 alone, because the warming effects of other greenhouse gases and the cooling effects of other sources cancel one another out (34). For further discussion of the implications and limitations of model-versus-observation comparisons, see SM section S1.2.7. Observed

ΔF_{anthro} values, meanwhile, were based on a 1000-member ensemble of observationally informed forcing estimates reported by Dessler and Forster (2018) (*35*).

Evaluated in terms of each of the above metrics, we deem model projections and historical observations to be consistent if and only if the 95% confidence intervals of the differences between the two include zero. As detailed in SM sections S1.2.2 and S1.2.3, these confidence intervals were calculated to reflect two sources of uncertainty: (i) statistical uncertainty in regression coefficients and (ii) structural uncertainty due to different model climate sensitivities, as and when indicated by error bars in projections reported by ExxonMobil scientists.

As an additional measure of performance, we calculate the "skill score" of each model by comparing the root-mean-squared errors of a model projection with those of a zero temperature change null hypothesis (*20*). For each projection, we calculate skill scores with respect to (i) each of the five observational temperature records for the temperature-versus-time metric and (ii) the 5000 estimates of $\Delta T / \Delta F_{anthro}$ for the iTCR metric. (See SM section 1.2 for details on graphical overlays and on calculation of consistency and skill scores and their accompanying uncertainties.)

Accurate and skillful climate modeling

Overall, ExxonMobil's global warming projections closely track subsequent observed temperature increases.

Figure 1 reproduces all 12 identified unique graphs, which contain 15 of the 16 identified temperature projections (the 16th was reported as a table). For example, panel 3 of Fig. 1 is a graph showing "an estimate of the average global temperature increase" under the "Exxon 21st Century Study–High Growth scenario" for CO_2. It was included in a 1982 internal briefing on the "CO_2 'Greenhouse' Effect" prepared by Exxon Research and Engineering Company and circulated widely to Exxon management

- ■ Observed temperature change
- ■ Observed atmospheric CO_2 concentration
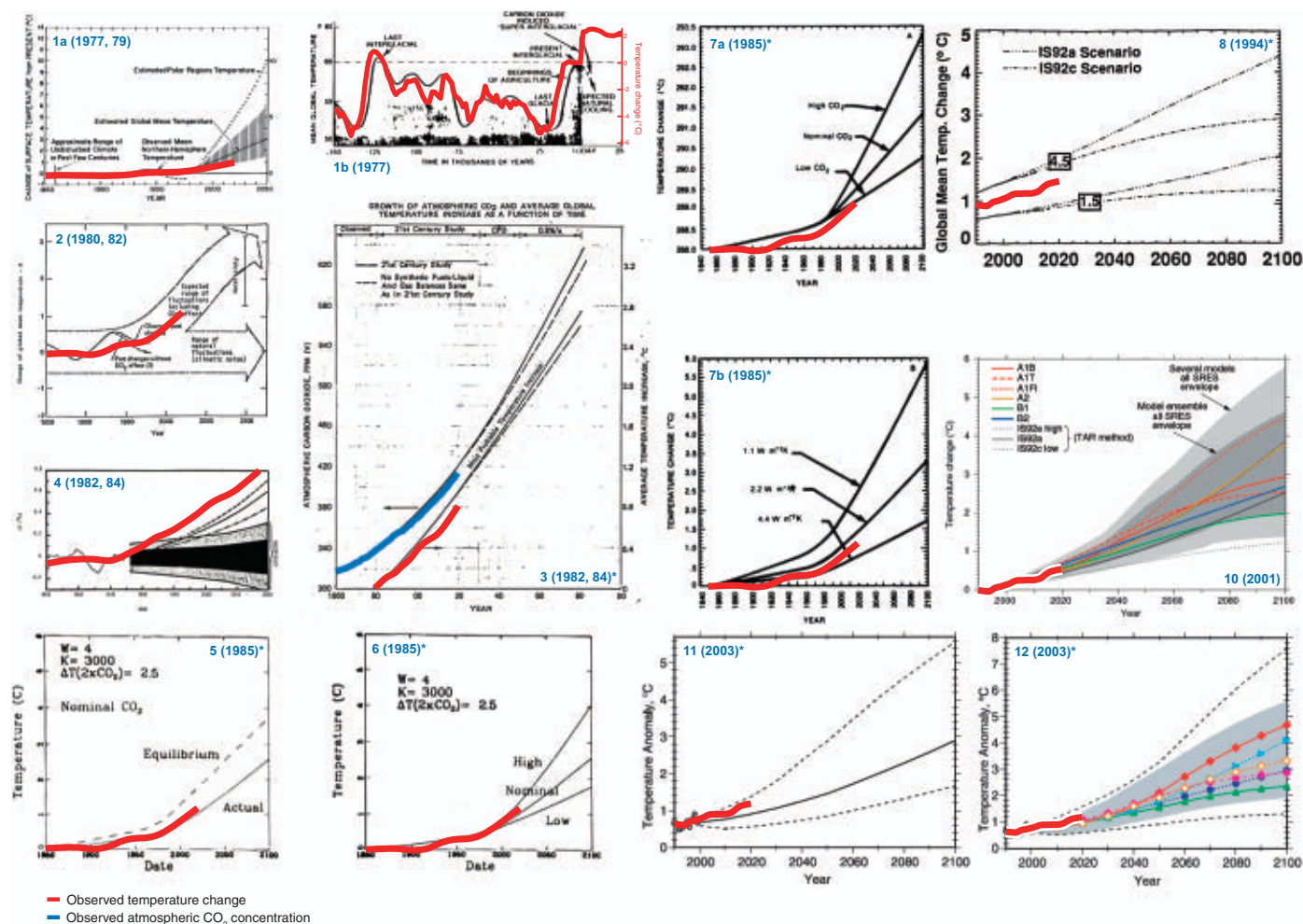
Fig. 1. Historically observed temperature change versus time (red) compared against global warming projections reported by ExxonMobil scientists in internal documents and peer-reviewed publications. Panel numbers indicate projections reported in internal documents: (1a, b) Black (1977, vugraphs 10 and 11, respectively) (*54*) and Mastracchio (1979) (*88*), (2) Shaw (1980) (*89*) and Glaser (1982, fig. 9) (*36*), (3) Glaser (1982, fig. 3) (*36*) and Shaw (1984) (*37*), (4) Weinberg *et al.* (1982) (*42*) and Callegari (1984) (*41*), (5, 6) Flannery (1985, pages 23 and 24, respectively) (*39*); and in peer-reviewed publications: (7a, b) Hoffert and Flannery (1985, figs. 5.16A and B, respectively) (*38*), (8) Jain *et al.* (1994) (*40*), (10) Albritton *et al.* (2001) (*90*), (11, 12) Kheshgi and Jain (2003, figs. 7c and 8c, respectively) (*91*). Asterisks indicate global

warming projections modeled by ExxonMobil scientists themselves. Panels have been numbered to match the labels in Fig. 2; this means that (9) Kheshgi *et al.* (1997) (*92*), which reports projections in tabulated rather than graphical form, is represented in Fig. 2 but is not included here. Temperature observations reflect the smoothed annual average of five historical time series. The only exception to this is the historical temperature record in (1b), which reflects a smoothed Earth system model simulation of the last 150,000 years driven by orbital forcing only, with an appended moderate anthropogenic emissions scenario. Panel 3 additionally compares projected atmospheric carbon dioxide concentrations against annual mean observations (blue). For data sources and plotting details, see SM sections S1 and S2.

Fig. 2. Summary of all global warming projections (nominal scenarios) reported by ExxonMobil scientists in internal documents and peer-reviewed publications (gray lines), superimposed on historically observed temperature change (red). Solid gray lines (and asterisked numerical labels) indicate global warming projections modeled by ExxonMobil scientists themselves; dashed gray lines indicate projections internally reproduced by ExxonMobil scientists from third-party sources. Shades of gray and numerical labels scale with model start dates, from earliest (1977: lightest, "1") to latest (2003: darkest, "12"). Numerical labels correspond to panels in Fig. 1, which displays all original graphical projections reported by ExxonMobil scientists. Observations reflect the smoothed annual average of five historical time series. For data sources and plotting details, see SM sections S1 and S2.
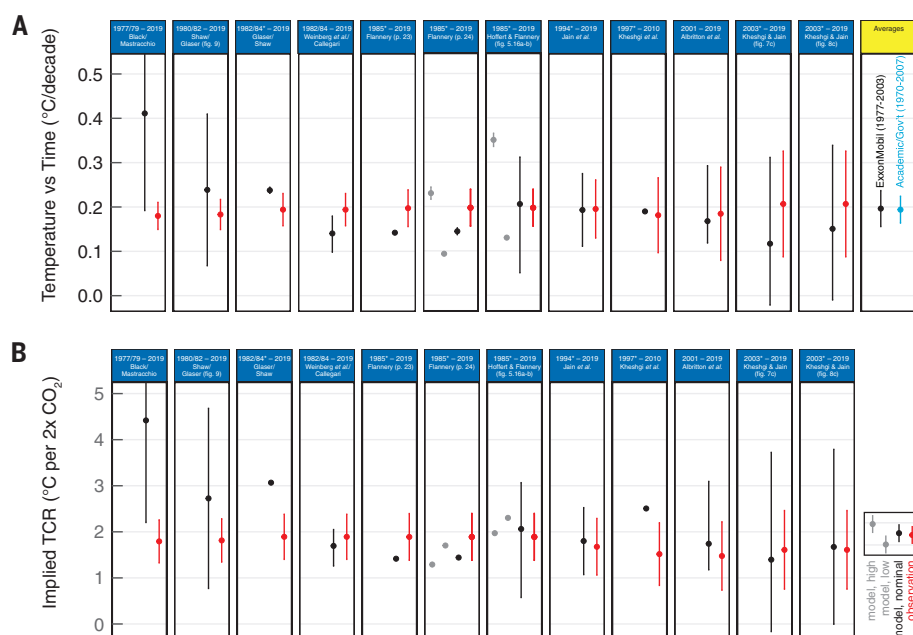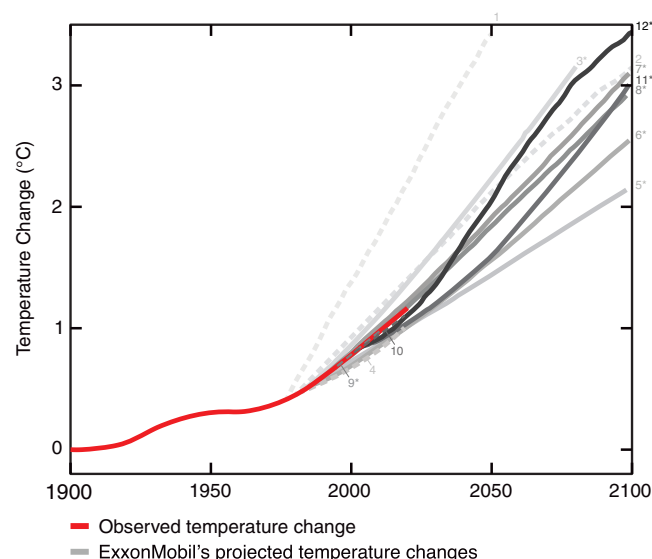
Fig. 3. Comparison of (red) historical temperature observations and (gray or black) global warming projections reported by ExxonMobil scientists in internal documents and peer-reviewed publications, as illustrated in Figs. 1 and 2. Observed and projected trends are compared in terms of (**A**) temperature change versus time and (**B**) temperature change versus change in radiative forcing ("implied TCR"). iTCR is defined as the change in temperature versus change in radiative forcing (see materials and methods and SM section S1.2.3 for details). The left-to-right order of panels corresponds to the numbering of projections ("1" to "12") in Figs. 1 and 2. Trends are computed over model projection periods indicated in the blue boxes above each panel. Asterisks indicate global warming projections modeled by ExxonMobil scientists themselves. The yellow-labeled box in (A) displays averages and bootstrapped standard errors of (black) the 16 projections reported by ExxonMobil scientists spanning 1977 to 2003 and (cyan) 18 academic and government climate model projections spanning 1970 to 2007 reported by Hausfather et al. (2020) (16).

(36). The briefing was labeled as "proprietary information for authorized company use only." The graph appeared a second time in an Exxon manager's presentation on "CO$_2$ greenhouse and climate issues" at an internal company environmental conference in 1984 (37).

Panel 3 of Fig. 1 displays one of 12 unique temperature projections (out of a total of 16 projections) that were output by models built or run in-house by ExxonMobil scientists (the 12 projections are indicated by asterisks in Figs. 1 to 3 and Table 1). To our knowledge,

the temperature projection in panel 3 was independently produced by Exxon scientists as part of "technology forecasting activities in 1981" operated by the company's Corporate Planning Department (37). The temperature projection was based on "calculations" of future atmospheric CO$_2$ concentrations "recently completed at Exxon Research and Engineering Company" (36). The remaining 11 temperature projections were produced by models developed by ExxonMobil scientists in collaboration with academic coauthors. Specifically, the seven unique temperature projections shown in panels 5 to 7b in Fig. 1 derived from a one-dimensional upwelling-diffusion Energy Balance Model to study how the "climatic transient response from fossil fuel burning is damped...by heat storage in the world's oceans..." (38). The Exxon scientist leading the collaboration internally described their climate modeling as "sophisticated" and "state of the art" (39). The remaining four unique temperature projections (three in panels 8, 11, and 12 in Fig. 1 and the fourth designated by "9" in Fig. 2) were generated by an "Integrated Science Model which consists of coupled modules for carbon cycle, atmospheric chemistry of other trace gases, radiative forcing by greenhouse gases, energy balance model for global temperature, and a model for sea level response" (40).

In Fig. 1, we overlay the original graphs with observed atmospheric CO$_2$ concentrations and temperature changes, shown in blue and red, respectively. In general, observations closely track projections.

In Fig. 2, we digitize all of ExxonMobil scientists' temperature projections corresponding to "nominal" (i.e., central) CO$_2$ scenarios in all 12 graphs (and one table). These projections, shown in gray, are plotted from the observed temperature change, shown in red,

Table 1. Skill scores of global warming projections reported by ExxonMobil scientists in internal documents and peer-reviewed publications. Scores are shown for ($\Delta T/\Delta t$) temperature change versus time; and ($\Delta T/\Delta F$) temperature change versus change in radiative forcing ("implied TCR"). Average skill scores are summarized for (i) all projections and (ii) projections modeled by ExxonMobil scientists themselves (indicated by asterisks). A skill score of 100% indicates perfect agreement with observations; a score less than zero indicates worse performance than a zero temperature change null hypothesis. For each projection, median scores and 5th and 95th percentile confidence intervals are shown, all as percentages. For each average skill score, the mean and the 1σ standard error of the mean are shown. Confidence intervals for projections over short periods—such as Kheshgi et al. (1997), Albritton et al. (2001), and Kheshgi and Jain (2003)—are large, primarily owing to the substantial impact of interannual and subdecadal variability on short-term temperature trends.

Projection	Reference	Time frame	Skill $\Delta T/\Delta t$ (%)	Skill $\Delta T/\Delta F$ (%)
1977 Black (vugraph 10); 1979 Mastracchio | nominal	(54, 88)	1977–2019	22 (−55 to −4)	−49 (−102 to 0)
1980 Shaw; 1982 Glaser (fig. 9) | nominal	(36, 89)	1980–2019	73 (53 to 84)	49 (16 to 78)
1982* Glaser (fig. 3/table 4); 1984 Shaw | nominal	(36, 37)	1982–2019	82 (61 to 92)	37 (1 to 68)
1982 Weinberg et al.; 1984 Callegari | nominal	(41, 42)	1982–2019	70 (64 to 82)	90 (73 to 99)
1985* Flannery (page 23) | nominal	(39)	1985–2019	70 (63 to 83)	76 (61 to 92)
1985* Flannery (page 24) | high	(39)	1985–2019	87 (66 to 97)	69 (55 to 84)
1985* Flannery (page 24) | low	(39)	1985–2019	46 (42 to 55)	90 (73 to 99)
1985* Flannery (page 24) | nominal	(39)	1985–2019	71 (64 to 84)	77 (62 to 94)
1985* Hoffert and Flannery (fig. 5.16) | high	(38)	1985–2019	28 (−5 to 44)	92 (71 to 99)
1985* Hoffert and Flannery (fig. 5.16) | low	(38)	1985–2019	64 (58 to 76)	77 (49 to 97)
1985* Hoffert and Flannery (fig. 5.16) | nominal	(38)	1985–2019	99 (80 to 99)	89 (65 to 99)
1994* Jain et al. | nominal	(40)	1994–2019	97 (71 to 99)	89 (54 to 99)
1997* Kheshgi et al. | nominal	(92)	1997–2010	93 (49 to 98)	34 (−43 to 80)
2001 Albritton et al. | nominal	(90)	2001–2019	84 (60 to 98)	81 (18 to 98)
2003* Kheshgi and Jain (fig. 7c) | nominal	(91)	2003–2019	56 (41 to 85)	85 (55 to 98)
2003* Kheshgi and Jain (fig. 8c) | nominal	(91)	2003–2019	72 (51 to 95)	88 (37 to 99)
Average of all projections			67 (60 to 74)	67 (58 to 76)
Average of ExxonMobil models			72 (66 to 78)	75 (70 to 81)

Box 2. How ExxonMobil Corp exaggerated the uncertainties of climate science and modeling

• In 2000, ExxonMobil Corp CEO Lee Raymond wrote that "[W]e do not now have a sufficient scientific understanding of climate change to make reasonable predictions and/or justify drastic measures...the science of climate change is uncertain...." (76). The report speculated about a "natural period of warming," "solar activity," and "[v]olcanic eruptions, El Nino." "With all this natural climate 'noise' and the complexities of measurement," it said, "science is not now able to confirm that fossil fuel use has led to any significant global warming."
• In 2001, an ExxonMobil Corp press release said of the "Hockey Stick" graph showing anthropogenic global warming: "The error bars are huge, yet some prefer to ignore them" (77).
• In 2005, Lee Raymond said in a television interview: "There is a natural variability that has nothing to do with man...It has to do with sun spots...with the wobble of the Earth...[T]he science is not there to make that determination [as to whether global warming is human-caused]...[T]here are a lot of other scientists that do not agree with [the National Academy and IPCC]...[T]he data is [sic] not compelling" (78).
• In 2007, ExxonMobil Corp's website stated that "[G]aps in the scientific basis for theoretical climate models and the interplay of significant natural variability make it very difficult to determine objectively the extent to which recent climate changes might be the result of human actions" (79).
• In 2013, ExxonMobil Corp CEO Rex Tillerson said: "[T]he facts remain there are uncertainties around the climate...what the principal drivers of climate change are...[T]here are other elements of the climate system that may obviate this one single variable [of burning fossil fuels]...And so that's that uncertainty issue..." (80).

at the start of each projection period. The darkness of the projection lines scales with their start years, from 1977 (lightest gray) to 2003 (darkest gray). Solid gray lines indicate projections modeled by ExxonMobil scientists themselves, whereas dashed gray lines indicate projections reproduced from third-party peer-reviewed papers. With the exception of the earliest projection (designated by "1"), which overestimated future warming, projections lie close to and evenly distributed around observations.

In Fig. 3A, we compare trends in temperature change versus time for historical ob-servations (in red) and for all 16 projections reported by ExxonMobil scientists (in gray or black). Over the course of their respective projection periods (indicated in blue boxes at the top of each panel in Fig. 3), the average predicted warming was 0.20° ± 0.04°C per decade. Ten of the 16 projections are consistent with historical observations (differences between models and projections are shown in fig. S1A). Of the remaining six projections, two forecast more warming than observed and four forecast less. Treating each unique graph and table—rather than each forcing scenario—as independent, 10 out of the 12 unique projection datasets are consistent with observations. Of the remainder, one forecasts more warming than observed and one forecasts less. Notably, these two projections are among the only three (out of 12) that were reported without uncertainty bars. They therefore have less "room for uncertainty" in our consistency tests. Overall, the models perform very well.

When we account for mismatches between forecast and observed forcings by using the iTCR metric, 12 of the 16 projections reported by ExxonMobil scientists are consistent with observations. Figure 3B uses the iTCR metric to compare trends in observed and projected iTCRs, and fig. S1B shows their differences. Treating each unique graph and table as independent, 9 out of 12 datasets are consistent.

> **Box 3. How Mobil and ExxonMobil Corp cultivated the myth of a 1970s global cooling scientific consensus**
>
> • In 1997, Mobil CEO Lee Raymond questioned whether "the Earth [is] really warming" by claiming that "In the 1970s, some of today's prophets of doom from global warming were predicting the coming of a new ice age" (*81*).
> • In 2001, an ExxonMobil Corp press release said: "[T]here is no consensus about long-term climate trends and what causes them...during the 1970's [sic], people were concerned about global cooling" (*82*).
> • In 2003, US Senator James Inhofe, who has to date received $2.3 million in campaign contributions from oil and gas companies, including ExxonMobil, argued that the issue of human-caused global warming "is far from settled" by pointing to "those who warned us in the 1970s that the planet was headed for a catastrophic global cooling" (*56*, *83–85*).
> • In 2004, a report published by the ExxonMobil Corp-funded Cato Institute stated that "Thirty years ago there was much scientific discussion among those who believed that humans influenced the...reflectivity [which would] cool the earth, more than...increasing carbon dioxide, causing warming. Back then, the 'coolers' had the upper hand...But nature quickly shifted gears...Needless to say, the abrupt shift in the climate caused almost as abrupt a shift in the balance of scientists who predictably followed the temperature" (*56*, *86*).

The three outliers forecast more warming than observed; two of them do not have uncertainty bars.

We also calculate skill scores for the temperature-versus-time and iTCR metrics (Table 1). A skill score of 100% indicates perfect agreement between projections and observations; a score between zero and 100% indicates some degree of skill; and a score less than zero indicates a performance worse than a zero-change null hypothesis (*16*, *20*).

With respect to temperature change versus time, we find the average of the median skill scores of all 16 reported projections to be 67 ± 7%. Across projections modeled by ExxonMobil scientists themselves, it is 72 ± 6%. These scores indicate highly skillful predictions. The highest-scoring projection was a 1985 peer-reviewed publication [Hoffert and Flannery (1985, nominal CO_2 scenario)], with a skill score of 99% (*38*). The 1982/1984 projection discussed earlier (Fig. 1, panel 3) has a skill score of 82% [although it marginally failed the consistency test (Fig. 3 and fig. S1)]. Only three of the 16 projections have skill scores below 50%. For comparison, NASA scientist James Hansen's global warming predictions presented to the US Congress in 1988 have been found to have skill scores ranging from 38 to 66% across the three different forcing scenarios that he reported (*16*, *20*).

Using the iTCR metric, the average skill of the 16 projections is 67 ± 9%. Among projections modeled by ExxonMobil scientists themselves, it is 75 ± 5%. Seven projections score 85% or above. Hoffert and Flannery (1985, high CO_2 scenario) is again the highest scorer (92%), closely followed by two projections scoring 90%, which are featured in three internal reports in 1982/1984 and 1985, respectively (*38*, *39*, *41*, *42*). Only four projections have skill scores below 50% for the iTCR

metric. Again, for comparison, Hansen's 1988 projections had skill scores in terms of the iTCR metric ranging from 28 to 81% (*16*).

We can compare these metrics with Hausfather *et al.* (2020), who calculated the average skill scores of 18 academic and government climate model projections published between 1970 and 2007. They obtained a value of 69% for both temperature-versus-time and iTCR metrics (*16*). On average, therefore, global warming projections reported by ExxonMobil scientists were as skillful as those of independent scientists of their day, and their own models were especially skillful. (As described earlier, ExxonMobil scientists did not simply rerun existing models; they developed their own models, typically in collaboration with academic coauthors, which independently corroborated the findings of other climate scientists.) To the extent that these projections represented contemporary knowledge of the likely effects of fossil fuel burning on global temperature, we can conclude that Exxon knew as much in the 1970–1990s as academic and government scientists knew. The average warming projected by the 18 academic and government models was 0.19° ± 0.03°C per decade, which is, within uncertainty, the same as ExxonMobil's average of 0.20° ± 0.04°C per decade.

We note that 2 of the 18 projections analyzed by Hausfather *et al.* (2020) are among those reported by ExxonMobil scientists. However, excluding these two projections has negligible effect on the average warming predicted by ExxonMobil or on the average skill scores of all ExxonMobil projections with respect to both temperature change versus time and iTCR (see sensitivity analyses, SM section S1.2.5 and table S1). Our conclusions also hold true when considering only the 12 (of 16) temperature projections from models built or run in-house

by ExxonMobil scientists, indicated by asterisks in Figs. 1 to 3 and Table 1 (see SM section S1.2.5 and table S1).

In summary, climate projections reported by ExxonMobil scientists between 1977 and 2003 were accurate and skillful in predicting subsequent global warming. Some projections suggested slightly too much warming and others not quite enough, but most (63 to 83%, depending on the metric used) were statistically consistent with subsequently observed temperatures, particularly after accounting for discrepancies between projected and observed changes in atmospheric CO_2 concentrations. ExxonMobil's projections were also consistent with, and as skillful as, those of academic and government scientists. All told, ExxonMobil was aware of contemporary climate science, contributed to that science, and predicted future global warming correctly. These findings corroborate and add quantitative precision to assertions by scholars, journalists, lawyers, politicians, and others that ExxonMobil accurately foresaw the threat of human-caused global warming, both prior and parallel to orchestrating lobbying and propaganda campaigns to delay climate action (*1*, *2*, *10*, *11*, *13*, *43–48*), and refute claims by ExxonMobil Corp and its defenders that these assertions are incorrect (*49*).

What ExxonMobil knew versus what they said

Our findings about the company's early understanding of climate science contradict many of the claims that the company and its allies have made in public.

Emphasizing uncertainties

It has been established that, for many years, Exxon's public affairs strategy was—as a 1988 internal memo put it—to "emphasize the uncertainty in scientific conclusions regarding the potential enhanced greenhouse effect" (*10*, *44*, *50*). However, our analysis shows that in their reports and briefings to management, ExxonMobil's own scientists did not particularly emphasize uncertainty; on the contrary, the level of uncertainty indicated by their global warming projections (bootstrapped 2σ standard error of the mean = ±21%) was commensurate with that reported by independent academics (±16%). Crucially, it excluded the possibility of no anthropogenic global warming; at no point did company scientists suggest that human-caused global warming would not occur. Nor did they conclude that the uncertainties were too great to permit differentiation of human and natural drivers. Yet publicly, ExxonMobil Corp made these claims until at least the early 2010s (see Box 2).

Denigrating climate models

ExxonMobil has often specifically claimed or suggested in public that climate models are

"unreliable" (51). In 1999, for example, ExxonMobil Corp's chief executive officer (CEO) Lee Raymond said future climate "projections are based on completely unproven climate models, or, more often, sheer speculation." (2) In 2013, his successor, Rex Tillerson, called climate models "not competent" (52). In 2015, he stated: "We do not really know what the climate effects of 600 ppm versus 450 ppm will be because the models simply are not that good" (53). The company's own modeling contradicts such statements. Exxon's 1982 projection shown in Fig. 1 (panel 3), for example, suggests that 600 ppm of atmospheric CO_2 would lead to 1.3°C more global warming than 450 ppm.

Quantifying ExxonMobil's broader climate knowledge

We gain additional insights into how Exxon-Mobil misled the public and other stakeholders by further evaluating the company's climate projections and comparing them to its public communications.

Mythologizing global cooling

Panel 1b of Fig. 1 is a graph of the global warming "effect of CO_2 on an interglacial scale" originally published by climate scientist J. Murray Mitchell Jr. in March 1977 and reproduced by Exxon scientist James Black in a private briefing to the Exxon Corporation Management Committee 4 months later (54, 55). This dataset was not included in our preceding analysis because its long time scale does not permit accurate digitization of its projected post-industrial anthropogenic global warming. Nonetheless, overlaying the original graph with the temperatures simulated by a modern Earth system model (in red) shows that Exxon scientists were accurate in warning their superiors of the prospect of a "carbon dioxide induced 'super-interglacial,'" as Mitchell Jr. termed it, that would render Earth hotter than at any time in at least 150,000 years (56). This shows that Exxon scientists correctly sided with the majority of the peer-reviewed literature in the 1970s that foresaw human-caused global warming overwhelming any possibility of global cooling and a (natural) ice age. [According to Peterson et al. (2008), only ~14% of the peer-reviewed literature between 1965 and 1977 anticipated global cooling (56).] It also shows that "the myth of the 1970s global cooling scientific consensus" cultivated in public by Mobil in the 1990s and ExxonMobil Corp in the 2000s (see Box 3) was false and contradicted the conclusion of their own scientists that global cooling was unlikely (56).

Claiming ignorance about discernibility

A second insight involves ExxonMobil's predictions as to when anthropogenic global warming would be discernible against the backdrop of natural climate fluctuations. Ten internal reports and one peer-reviewed publication spanning 1979–1985 offered quantitative estimates, with a median year of 2000 ± 5. (For each document, we infer the predicted year from its corresponding supporting quotations, summarized in table S4; see SM section S1.2.6 for method details.) This is consistent with what in fact occurred. In 1995, the IPCC declared that a human effect on global temperatures had been detected, a conclusion they reiterated with higher confidence in 2000 and in all subsequent IPCC assessment reports (57, 58). In other words, ExxonMobil's understanding of climate science was sufficient not only to project long-term warming accurately but also to predict when it would be discernible. Yet, ExxonMobil publicly asserted that the science was too uncertain to know when—or if—human-caused global warming might be measurable. In 2004, for example, they stated that "scientific uncertainties continue to limit our ability to make objective, quantitative determinations regarding the human role in recent climate change," a claim that was contrary to the analysis of their own scientists (59).

Staying silent on stranded assets

A third insight concerns the "carbon budget"—the amount of CO_2 that can be added to the atmosphere—while holding anthropogenic global warming below 2°C. Five ExxonMobil studies published between 1982 and 2005 address the question. They conclude that to stabilize CO_2 concentrations below 550 ppm and/or limit warming to 2°C would impose a carbon budget of 251 to 716 gigatonnes of carbon (GtC) between 2015 and 2100 (10). For comparison, recent calculations have narrowed the uncertainty and place the figure at 442 to 651 GtC (60). Thus, ExxonMobil's calculations of the carbon budget were consistent with today's best estimates. Yet, to our knowledge, ExxonMobil did not alert investors, consumers, or the general public to this constraint.

Quantifying climate knowledge

The substantial body of literature documenting the history of climate lobbying and propaganda by fossil fuel interests has been described as a "vast blind spot" of major climate assessments—ignored, in particular, in all but the most recent IPCC assessment report (61–63). Yet bringing quantitative techniques from the physical sciences to bear on a discipline traditionally dominated by qualitative journalistic and historical approaches offers one path to remedying this blind spot. Here, it has enabled us to conclude with precision that, decades ago, ExxonMobil understood as much about climate change as did academic and government scientists. Our analysis shows that, in private and academic circles since the late 1970s and early 1980s, ExxonMobil scientists (i) accurately projected and skillfully modeled global warming due to fossil fuel burning; (ii) correctly dismissed the possibility of a coming ice age; (iii) accurately predicted when human-caused global warming would first be detected; and (iv) reasonably estimated how much CO_2 would lead to dangerous warming. Yet, whereas academic and government scientists worked to communicate what they knew to the public, ExxonMobil worked to deny it.

REFERENCES AND NOTES

1. N. Banerjee, L. Song, D. Hasemyer, J. H. Cushman Jr., Exxon: The road not taken. *InsideClimate News* (2015). https://perma.cc/99YY-2MWV.
2. S. Jerving, K. Jennings, M. M. Hirsh, S. Rust, "What Exxon knew about the Earth's melting Arctic," *Los Angeles Times*, 9 October 2015; https://perma.cc/NA86-5PWH.
3. B. Franta, Early oil industry knowledge of CO_2 and global warming. *Nat. Clim. Chang.* 8, 1024–1025 (2018). doi: 10.1038/s41558-018-0349-9
4. É. Young, Coal Knew, Too. *HuffPost* 22 November 2019; https://perma.cc/5E52-F3JX.
5. M. Joselow, GM, Ford knew about climate change 50 years ago. *E&E News* 26 October 2020; https://perma.cc/KT5C-VHDT.
6. D. Anderson, M. Kasper, D. Pomerantz, "Utilities Knew: Documenting Electric Utilities' Early Knowledge and Ongoing Deception on Climate Change From 1968-2017 (Energy and Policy Institute)" (2017); https://perma.cc/KX2Y-E8QY.
7. C. Bonneuil, P.-L. Choquet, B. Franta, Early warnings and emerging accountability: Total's responses to global warming, 1971–2021. *Glob. Environ. Change* 71, 102386 (2021). doi: 10.1016/j.gloenvcha.2021.102386
8. D. Anderson, M. Kasper, D. Tait, "Southern Company Knew (Energy and Policy Institute)" (2022); https://perma.cc/2BFN-W8AJ.
9. B. Franta, "Shell and Exxon's secret 1980s climate change warnings," *The Guardian*, 19 September 2018; https://perma.cc/4RYL-S5ZC.
10. G. Supran, N. Oreskes, Assessing ExxonMobil's climate change communications (1977–2014). *Environ. Res. Lett.* 12, 084019 (2017). doi: 10.1088/1748-9326/aa815f
11. Sabin Center for Climate Change Law at Columbia Law School, Arnold & Porter, U.S. Climate Change Litigation (climatecasechart.com) (2021); https://perma.cc/ZHZ3-5HTX) [accessed 30 March 2021].
12. "Commonwealth of Massachusetts v. Exxon Mobil Corporation (1984-CV-03333-BLS1, Amended Complaint)" (2020); https://perma.cc/3XZM-F536.
13. #ExxonKnew, https://exxonknew.org.
14. Fossil Free Europe, #ShellKnew, "After decades of deception, it's time to divest" (2017); https://perma.cc/BW3X-PA6V.
15. #TotalKnew, https://totalknew.com.
16. Z. Hausfather, H. F. Drake, T. Abbott, G. A. Schmidt, Evaluating the Performance of Past Climate Model Projections. *Geophys. Res. Lett.* 47, 1–10 (2020). doi: 10.1029/2019GL085378
17. V. Eyring et al., Taking climate model evaluation to the next level. *Nat. Clim. Chang.* 9, 102–110 (2019). doi: 10.1038/s41558-018-0355-y
18. S. Rahmstorf et al., Recent climate observations compared to projections. *Science* 316, 709 (2007). doi: 10.1126/science.1136843; pmid: 17272686
19. S. Rahmstorf, G. Foster, A. Cazenave, Comparing climate projections to observations up to 2011. *Environ. Res. Lett.* 7, 044035 (2012). doi: 10.1088/1748-9326/7/4/044035
20. J. C. Hargreaves, Skill and uncertainty in climate models. *WIREs Clim. Change.* 1, 556–564 (2010). doi: 10.1002/wcc.58
21. R. J. Stouffer, S. Manabe, Assessing temperature pattern projections made in 1989. *Nat. Clim. Chang.* 7, 163–165 (2017). doi: 10.1038/nclimate3224
22. D. J. Frame, D. A. Stone, Assessment of the first consensus prediction on climate change. *Nat. Clim. Chang.* 3, 357–359 (2013). doi: 10.1038/nclimate1763
23. J. Hansen et al., Global temperature change. *Proc. Natl. Acad. Sci. U.S.A.* 103, 14288–14293 (2006). doi: 10.1073/pnas.0606291103; pmid: 17001018
24. A. M. T. Chen, D., M. Rojas, B. H. Samset, K. Cobb, A. Diongue Niang, P. Edwards, S. Emori, S. H. Faria, E. Hawkins, P. Hope, P. Huybrechts, M. Meinshausen, S. K. Mustafa,

G. K. Plattner, in *Climate Change 2021: The Physical Science Basis. Contribution of Working Group I to the Sixth Assessment Report of the Intergovernmental Panel on Climate Change*, V. Masson-Delmotte, P. Zhai, A. Pirani, S. L. Connors, C. Péan, S. Berger, N. Caud, Y. Chen, L. Goldfarb, M. I. Gomis, M. Huang, K. Leitzell, E. Lonnoy, J. B. R. Matthews, T. K. Maycock, T. Waterfield, O. Yelekçi. R. Yu, B. Zhou, Eds. (Cambridge Univ. Press, 2021), pp. 147–286; https://perma.cc/5KMV-NNDN.

25. P. N. Edwards, *A Vast Machine—Computer Models, Climate Data, and the Politics of Global Warming* (MIT Press, 2013).

26. Carbon Brief, Q&A: How do climate models work? *carbonbrief. org* (2018). https://perma.cc/7WYN-4NMF.

27. S. Easterbrook, "Nobel Prize for Climate Modeling," Serendipity, 5 October 2021; https://perma.cc/SY7K-F2LP.

28. ExxonMobil Corp, Supporting Materials; https://perma.cc/D862-KB2N.

29. ICN, Documents (Exxon: The road not taken). *InsideClimate News*. https://perma.cc/KCG8-M9ZM.

30. Climate Files, *Climate Investigations Center*; https://www.climatefiles.com.

31. ExxonMobil Corp, "ExxonMobil Contributed Publications "(2021); https://perma.cc/4SFW-Y3PD [accessed 1 June 2021].

32. Core Writing Team, *Climate Change 2014: Synthesis Report. Contribution of Working Groups I, II and III to the Fifth Assessment Report of the Intergovernmental Panel on Climate Change* (IPCC, 2014).

33. V. Eyring, N. P. Gillett, K. M. Achuta Rao, R. Barimalala, M. Barreiro Parrillo, N. Bellouin, C. Cassou, P. J. Durack, Y. Kosaka, S. McGregor, S. Min, O. Morgenstern, Y. Sun, Human Influence on the Climate System, in *Climate Change 2021: The Physical Science Basis. Contribution of Working Group I to the Sixth Assessment Report of the Intergovernmental Panel on Climate Change*, V. Masson-Delmotte, P. Zhai, A. Pirani, S. L. Connors, C. Péan, S. Berger, N. Caud, Y. Chen, L. Goldfarb, M. I. Gomis, M. Huang, K. Leitzell, E. Lonnoy, J. B. R. Matthews, T. K. Maycock, T. Waterfield, O. Yelekçi. R. Yu, B. Zhou, Eds. (Cambridge Univ. Press, 2021).

34. T. F. Stocker, D. Qin, G.-K. Plattner, M. Tignor, S. K. Allen, J. Boschung, A. Nauels, Y. Xia, V. Bex, P. M. Midgley, Eds., *Climate Change 2013: The Physical Science Basis. Contribution of Working Group I to the Fifth Assessment Report of the Intergovernmental Panel on Climate Change* (Cambridge Univ. Press, 2013).

35. A. E. Dessler, P. M. Forster, An Estimate of Equilibrium Climate Sensitivity From Interannual Variability. *J. Geophys. Res. Atmos.* **123**, 8634–8645 (2018). doi: 10.1029/2018JD028481

36. M. B. Glaser, "CO_2 'Greenhouse' Effect" (Internal Document, 1982). Accessible via one or more of the following public archives: ExxonMobil Corp (https://perma.cc/D862-KB2N); *InsideClimate News* (https://perma.cc/KCG8-M9ZM); and Climate Investigations Center (https://www.climatefiles.com). Additional citation information is included in the SM section S2.

37. H. Shaw, in *EUSA/ER&E Environmental Conference, Florham Park* (New Jersey, 28 March 1984, Internal Document, 1984). Accessible via one or more of the following public archives: ExxonMobil Corp (https://perma.cc/D862-KB2N); *InsideClimate News* (https://perma.cc/KCG8-M9ZM); and Climate Investigations Center (https://www.climatefiles.com/). Additional citation information is included in SM section S2.

38. M. I. Hoffert, B. P. Flannery, in *Projecting the Climatic Effects of Increasing Carbon Dioxide*, M. C. MacCracken, F. M. Luther, Eds. (US Department of Energy, Washington, DC, 1985), pp. 149–190.

39. B. P. Flannery, "CO_2 greenhouse update 1985" (Internal Document, 1985). Accessible via one or more of the following public archives: ExxonMobil Corp (https://perma.cc/D862-KB2N); *InsideClimate News* (https://perma.cc/KCG8-M9ZM); and Climate Investigations Center (https://www.climatefiles.com/). Additional citation information is included in SM section S2.

40. A. K. Jain, H. S. Kheshgi, D. J. Wuebbles, in *87th Annual Meeting and Exhibition of the Air and Waste Management Association* (94-TP59.08), Cincinnati, OH, 19 to 24 June 1994.

41. A. J. Callegari, "Corporate Research Program in Climate/CO2-Greenhouse" (Internal Document, 1984). Accessible via one or more of the following public archives: ExxonMobil Corp (https://perma.cc/D862-KB2N); *InsideClimate News* (https://perma.cc/KCG8-M9ZM); and Climate Investigations Center (https://www.climatefiles.com/). Additional citation information is included in SM section S2.

42. R. W. Cohen, "Untitled ('meeting with Exxon Corp. re CO2' between Weinberg H N, Cohen R, Callegari A, Flannery B P, 'Sci &

Tech', 'Exxon Public Affairs', et al., 24 August 1982)" (Internal Document, 1982). Accessible via one or more of the following public archives: ExxonMobil Corp (https://perma.cc/D862-KB2N); *InsideClimate News* (https://perma.cc/KCG8-M9ZM); and Climate Investigations Center (https://www.climatefiles.com/). Additional citation information is included in SM section S2.

43. B. McKibben, Exxon Knew Everything There Was to Know About Climate Change by the Mid-1980s—and Denied It, *The Nation*, 20 October 2015. https://perma.cc/78HE-JWF9.

44. R. Brulle, Center for Climate Integrity, The Chesapeake Climate Action Network, J. Farrell, B. Franta, S. Lewandowsky, N. Oreskes, G. Supran, Union of Concerned Scientists, "Amicus Brief to the United States Fourth Circuit Court of Appeals (Case No. 1:18-cv-02357-ELH, 23 September 2019)" (2019); https://perma.cc/43PK-B978.

45. J. Cook, G. Supran, S. Lewandowsky, N. Oreskes, E. Maibach, "America misled: How the fossil fuel industry deliberately misled Americans about climate change" (2019); https://perma.cc/K465-XJ6C.

46. A. Dessler, "Prediction of the future from 1982 by @exxonmobil," Tweet by @AndrewDessler, 14 May 2019; https://perma.cc/S55Q-CNP2.

47. S. Rahmstorf, Nir Shaviv erklärt den Klimawandel für die AfD im Bundestag. *Spektrum.de (SciLogs)* (2018). https://perma.cc/F5BN-AGU3.

48. "So they knew": Ocasio-Cortez questions Exxon scientist on climate crisis denial, *The Guardian*, 23 October 2019; https://perma.cc/F5Q2-HBSY.

49. G. Supran, N. Oreskes, Reply to Comment on 'Assessing ExxonMobil's climate change communications (1977-2014).' *Environ. Res. Lett.* **15**, 118002 (2020). doi: 10.1088/1748-9326/abbe82

50. J. M. Carlson, "The Greenhouse Effect" (Internal Document, 1988). Accessible via one or more of the following public archives: ExxonMobil Corp (https://perma.cc/D862-KB2N); *InsideClimate News* (https://perma.cc/KCG8-M9ZM); and Climate Investigations Center (https://www.climatefiles.com/). Additional citation information is included in SM section S2.

51. ExxonMobil, "Political cart before a scientific horse" (Advertorial), *The New York Times* (2000).

52. ExxonMobil Corporation CEO Hosts Annual Shareholder Meeting (Transcript, 29 May 2013). *Seek. Alpha* (2013). https://perma.cc/262V-87MY.

53. C. Mooney, Rex Tillerson's view of climate change: It's just an "engineering problem," *The Washington Post*, 13 December 2016; https://perma.cc/TXT9-29GX.

54. J. Black, "The Greenhouse Effect" (Internal Document, 1978). Accessible via one or more of the following public archives: ExxonMobil Corp (https://perma.cc/D862-KB2N); *InsideClimate News* (https://perma.cc/KCG8-M9ZM); and Climate Investigations Center (https://www.climatefiles.com/). Additional citation information is included in SM section S2.

55. J. J. M. Mitchell, Carbon dioxide and future climate. *Environmental Data Service* (March): 3–9 (1977); https://perma.cc/AU3M-3K4S.

56. T. C. Peterson, W. M. Connolley, J. Fleck, The myth of the 1970s global cooling scientific consensus. *Bull. Am. Meteorol. Soc.* **89**, 1325–1338 (2008). doi: 10.1175/2008BAMS2370.1

57. R. T. Watson, H. Rodhe, H. Oeschger, U. Siegenthaler, M. Andreae, R. Charlson, R. Ciceerone, J. Coakley, R. G. Derwent, J. Elkins, F. Fehsenfeld, *Climate change - the IPCC scientific assessment. Contribution of Working Group I to the First Assessment Report of the Intergovernmental Panel on Climate Change* (Cambridge Univ. Press, 1990).

58. D. Albritton, B. Bolin, B. Callander, K. Denman, R. Dickinson, L. Gates, H. Grassi, M. Grubb, N. Harris, J. Houghton, P. Jonas, A. Kattenberg, K. Maskell, G. McBean, M. McFarland, G. Meira, J. Melillo, N. Nicholls, *Climate Change 1995: The Science of Climate Change, Summary for Policymakers. Contribution of Working Group I to the Second Assessment Report of the Intergovernmental Panel on Climate Change* (Cambridge Univ. Press, 1996).

59. ExxonMobil, Weather and climate (Advertorial), *The New York Times* (2004).

60. J. Rogelj *et al*., Differences between carbon budget estimates unravelled. *Nat. Clim. Chang.* **6**, 245–252 (2016). doi: 10.1038/nclimate2868

61. G. Readfearn, "Vast Blind Spot": IPCC Accused of Ignoring "Decades Long" Fossil Fuel Misinformation Campaign on Climate, *DeSmog*, 12 October 2021; https://perma.cc/6FVK-VERK.

62. Z. Colman, K. Mathiesen, Climate scientists take swipe at Exxon Mobil, industry in leaked report, *Politico*, 2 July 2021; https://perma.cc/5HAU-XAJD.

63. K. M. Hicke, J.A., S. Lucatello, L.D., Mortsch, J. Dawson, M. Domínguez Aguilar, C.A.F. Enquist, E.A. Gilmore, D.S. Gutzler, S. Harper, K. Holsman, E.B. Jewett, T.A. Kohler, in *Climate Change 2022: Impacts, Adaptation and Vulnerability. Contribution of Working Group II to the Sixth Assessment Report of the Intergovernmental Panel on Climate Change*, B. R. H.-O. Pörtner, D. C. Roberts, M. Tignor, E. S. Poloczanska, K. Mintenbeck, A. Alegría, M. Craig, S. Langsdorf, S. Löschke, V. Möller, A. Okem, Eds. (Cambridge Univ. Press, 2022).

64. A. Neslen, ExxonMobil faces EU parliament ban after no show at climate hearing, *The Guardian*, 22 March 2019; https://perma.cc/6QUS-RNXG.

65. Examining the Oil Industry's Efforts to Suppress the Truth about Climate Change (U.S. House Committee on Oversight and Reform, 23 October 2019) (2019); https://perma.cc/48VP-PE6C.

66. Dark Money and Barriers to Climate Action (US Senate Democrats' Special Committee on the Climate Crisis, 29 October 2019) (2019); https://perma.cc/3T4F-EMER.

67. U.S. House Committee on Oversight and Reform, Oversight Committee Launches Investigation of Fossil Fuel Industry Disinformation on Climate Crisis (press release, 16 September 2021) (2021); https://perma.cc/V42G-Z3FN.

68. Biden for President (joebiden.com), "The Biden plan to secure environmental justice and equitable economic opportunity" (2020); https://perma.cc/9WTD-KVU5 [accessed 11 June 2021].

69. "Cooper presses Biden on 2020 fundraiser" (CNN) (2020); https://perma.cc/26LJ-UFRP.

70. The White House, Executive Order on Protecting Public Health and the Environment and Restoring Science to Tackle the Climate Crisis (2021); https://perma.cc/22M4-6D9S.

71. Commission on Human Rights of the Philippines, "National inquiry on climate change report" (2022); https://perma.cc/577C-FSDR.

72. P. Achakulwisut, B. Scandella, G. Supran, B. Voss, "Ending ExxonMobil sponsorship of the American Geophysical Union - How ExxonMobil's past and present climate misinformation violates the AGU's Organizational Support Policy and scientific integrity" (2016); https://perma.cc/PBN7-V59J.

73. G. Supran, "Until universities divest from fossil fuels they will undermine all they stand for," *The Guardian*, 8 April 2015; https://perma.cc/QS9R-NYPU.

74. Barnard University, "Divesting from Deniers" (2017); https://perma.cc/W8BJ-YKH6.

75. Center for Climate Integrity, "Pay Up Climate Polluters," payupclimatepolluters.org; https://perma.cc/K4JK-XPB6.

76. ExxonMobil, "Global Climate Change—A Better Path Forward" (2000); https://perma.cc/PJ4Q-WG32.

77. ExxonMobil, "Global Climate Change (press release 'climate talking points')" (2001); https://perma.cc/VS2Y-CDXT.

78. Lee Raymond on "Charlie Rose" (8 November 2005), *Charlie Rose PBS* (2005); https://perma.cc/MS36-9WAD.

79. ExxonMobil, "Climate science." ExxonMobil web version of 2005 Corporate Citizenship Report (20f07); https://perma.cc/AF2B-7YT6 [archived 16 February 2007, accessed 12 June 2019].

80. R. Tillerson on "Charlie Rose" (7 March 2013). *Charlie Rose PBS* (2013). https://perma.cc/ERS4-RCEY.

81. L. R. Raymond in Speech at World Petroleum Congress (13 October 1997); https://perma.cc/N28G-LBJ4.

82. ExxonMobil, Media Statement—Global Climate Change. *ExxonMobil Newsroom* (2001); https://perma.cc/72EW-2GC9 [archived 5 December 2004, accessed 12 June 2019].

83. Sen. Inhofe Delivers Major Speech on the Science of Climate Change (29 July 2003) (2003); https://perma.cc/JLT4-R4AX [accessed 4 June 2021].

84. OpenSecrets.org, Sen. James M. Inhofe - Campaign Finance Summary. *OpenSecrets.org* (2021); https://perma.cc/LYG2-R9CW [accessed 13 October 2021].

85. E. Negin, ExxonMobil's Climate Disinformation Campaign is Still Alive and Well. *The Equation* (Union of Concerned Scientists) (2018). https://perma.cc/FQ6W-BEGV.

86. ExxonSecrets Factsheet, Cato Institute. *ExxonSecrets.org* (2021); https://perma.cc/SA7S-AZTE [accessed 30 March 2021].

87. G. Supran, S. Rahmstorf, N. Oreskes, Supran, Rahmstorf, and Oreskes (2022) Data and code repository, Harvard Dataverse (2022); https://doi.org/10.7910/DVN/R4MOAE.doi: 10.7910/DVN/R4MOAE

88. R. L. Mastracchio, "Controlling Atmospheric CO_2" (Internal Document, 1979). Accessible via one or more of the following public archives: ExxonMobil Corp (https://perma.cc/D862-KB2N); *InsideClimate News* (https://perma.cc/KCG8-M9ZM); and Climate Investigations Center (https://www.climatefiles.com/). Additional citation information is included in SM section S2.

89. H. Shaw, P. P. McCall, "Exxon Research and Engineering Company's Technological Forecast CO2 Greenhouse Effect" (Internal Document, 1980). Accessible via one or more of the following public archives: ExxonMobil Corp (https://perma.cc/D862-KB2N); *InsideClimate News* (https://perma.cc/KCG8-M9ZM); and Climate Investigations Center (https://www.climatefiles.com/). Additional citation information is included in SM section S2.

90. D. L. Albritton, M. R. Allen, P. M. Alfons, J. A. Baede, U. C. Church, D. Xiaosu, D. Yihui, D. H. Ehhalt, C. K. Folland, F. Giorgi, J. M. Gregory, D. J. Griggs, *Climate Change 2001: The Scientific Basis, Summary for Policymakers. Contribution of Working Group I to the Third Assessment Report of the Intergovernmental Panel on Climate Change* (Cambridge Univ. Press, 2001).

91. H. S. Kheshgi, A. K. Jain, Projecting future climate change: Implications of carbon cycle model intercomparisons. *Global Biogeochem. Cycles* **17**, 16 (2003). doi: 10.1029/2001GB001842

92. H. S. Kheshgi, A. K. Jain, D. J. Wuebbles, in *Proceedings of the Air and Waste Management Association's 90th Annual Meeting and Exhibition*, 8 to 13 June 1997, Toronto, Ontario, Canada.

SUPPLEMENTARY MATERIALS

science.org/doi/10.1126/science.abk0063
Materials and Methods
Fig. S1
Tables S1 to S4
References (*93–120*)

Where Science Gets Social.

AAAS.ORG/COMMUNITY

AAAS' Member Community is a one-stop destination for scientists
and STEM enthusiasts alike. It's "Where Science Gets Social":
a community where facts matter, ideas are big and there's
always a reason to come hang out, share, discuss and explore.

Member COMMUNITY
AAAS

AMERICAN ASSOCIATION FOR THE ADVANCEMENT OF SCIENCE

VECTOR BIOLOGY

Dome1–JAK–STAT Signaling Between Parasite and Host Integrates Vector Immunity and Development

Vipin S. Rana, Chrysoula Kitsou, Shraboni Dutta, Michael H. Ronzetti, Min Zhang, Quentin Bernard, Alexis A. Smith, Julen Tomás-Cortázar, Xiuli Yang, Ming-Jie Wu, Oleksandra Kepple, Weizhong Li, Jennifer E. Dwyer, Jaqueline Matias, Bolormaa Baljinnyam, Jonathan D. Oliver, Nallakkandi Rajeevan, Joao H F Pedra, Sukanya Narasimhan, Yan Wang, Ulrike Munderloh, Erol Fikrig, Anton Simeonov, Juan Anguita, Utpal Pal*

INTRODUCTION: Ticks have evolved into a monophyletic group of highly adapted blood-feeding ectoparasites that originated from a clade of free-living scavenger mites nearly 225 million years ago. Unlike most geographically confined tick species that prefer a single vertebrate host, *Ixodes* spp. can parasitize many vertebrates and transmit diverse pathogens. Ixodid ticks undergo only three feeding events during their multiyear lifespan, ingesting blood meals that are nearly 100 times their weight. Their characteristic physiological adaptations were likely shaped by their sophisticated hematophagy and associations with coevolving vertebrate hosts. The molecular basis of how ticks maintain their complex postembryonic developmental program as well as their vectorial competence remains unclear. Ticks contain a functional JAK–STAT signaling cascade that induces robust antibacterial responses capable of limiting the proliferation of tick-borne pathogens. The pathway is activated in many arthropods by cytokine-like molecules such as Unpaired (UPD). However, the *Ixodes scapularis* genome is unusually devoid of recognizable UPD orthologs.

RATIONALE: We recently discovered a cross-species cell signaling pathway in which a mammalian interferon (IFN-γ) ingested with the tick blood meal activates the *Ixodes* JAK–STAT pathway, generating potent microbicidal activities within the vector. To further elucidate a parallel interferon-like defense system in ticks, we have explored the identity and characteristics of the tick receptor for IFN-γ to uncover the mechanisms and biological significance of a cross-species cell signaling cascade that extends from mammals to their ectoparasites.

RESULTS: We identified an *I. scapularis* receptor, Dome1, which binds with high selectivity and affinity to vertebrate (mouse, human, and avian) IFN-γ. Unlike Dome orthologs in other arthropods, including non-*Ixodes* ticks, Dome1 features unique extracellular regions found in vertebrate cytokine receptors. Dome1 colocalizes with IFN-γ on the luminal surface of the tick gut epithelium. The receptor is induced by ingested IFN-γ and regulates microbicidal responses orchestrated by the JAK–STAT pathway. Unexpectedly, Dome1 not only augmented tick immune responses, but was also required for *I. scapularis* development. Systemic *Dome1* knockdown persisted from subadult to female *I. scapularis* and their offspring, and severely impaired tick fecundity and postembryonic development, reflected by failure to molt, loss of bilateral symmetry, and malformed internal organs and appendages, including missing legs, mouthparts, and anal pore structures. The Dome1–JAK–STAT pathway, present in most Ixodid tick genomes, directed the maintenance of the gut proteome and microbiome, in addition to supporting the regeneration and proliferation of gut cells, including stem cells. Dome1–JAK–STAT signaling dictated tick metamorphosis and organ development through the Hedgehog and Notch–Delta biochemical networks, ultimately impacting the ability of *Ixodes* to transmit *Borrelia burgdorferi*, the Lyme disease pathogen, to naïve murine hosts.

CONCLUSION: We identify how certain conserved metazoan cell signaling pathways flexibly adapt vertebrate IFN-γ for use in arthropod immunity and development through the Dome1 receptor. Our studies highlight the evolutionary dependence of the major blood-feeding arthropod *I. scapularis* on mammalian hosts through cross-species signaling mechanisms that extend from mammals to their ectoparasites and influence arthropod immunity, vectorial competence, and development.∎
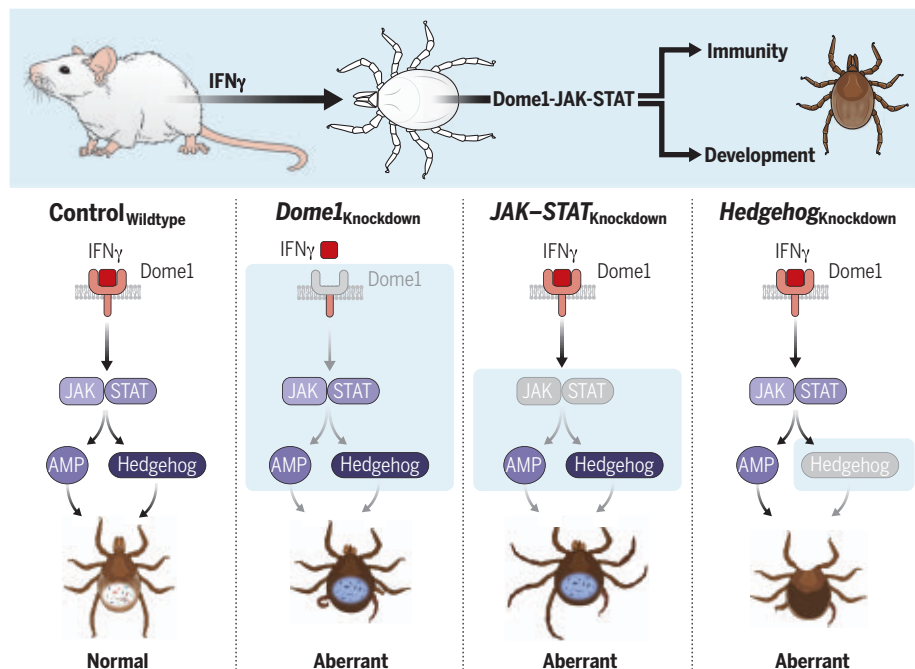
Mammalian-arthropodal crosstalk integrates vector immunity and development. The *Ixodes scapularis* protein Dome1 recruits mammalian IFN-γ from the tick's blood meal. The interaction activates the tick JAK–STAT pathway, triggering signaling intermediaries, including an antimicrobial protein and Hedgehog protein, which affects tick metamorphosis, gut homeostasis, and pathogen transmission. Knockdowns of pathway components highlight the biological significance of cross-species signaling between mammals and their ectoparasites, which converge to regulate both arthropod immunity and development.

S **READ THE FULL ARTICLE AT**
https://doi.org/10.1126/science.abl3837

VECTOR BIOLOGY

Dome1–JAK–STAT signaling between parasite and host integrates vector immunity and development

Vipin S. Rana[1], Chrysoula Kitsou[1], Shraboni Dutta[1], Michael H. Ronzetti[2], Min Zhang[1], Quentin Bernard[1], Alexis A. Smith[1], Julen Tomás-Cortázar[3]†, Xiuli Yang[1], Ming-Jie Wu[4], Oleksandra Kepple[1], Weizhong Li[1], Jennifer E. Dwyer[5], Jaqueline Matias[4], Bolormaa Baljinnyam[2], Jonathan D. Oliver[6], Nallakkandi Rajeevan[7], Joao H F Pedra[8], Sukanya Narasimhan[4], Yan Wang[9], Ulrike Munderloh[6], Erol Fikrig[4,10], Anton Simeonov[2], Juan Anguita[3,11], Utpal Pal[1,12]*

Ancestral signaling pathways serve critical roles in metazoan development, physiology, and immunity. We report an evolutionary interspecies communication pathway involving a central *Ixodes scapularis* tick receptor termed Dome1, which acquired a mammalian cytokine receptor motif exhibiting high affinity for interferon-gamma (IFN-γ). Host-derived IFN-γ facilitates Dome1-mediated activation of the *Ixodes* JAK–STAT pathway. This accelerates tick blood meal acquisition and development while upregulating antimicrobial components. The Dome1–JAK–STAT pathway, which exists in most Ixodid tick genomes, regulates the regeneration and proliferation of gut cells—including stem cells—and dictates metamorphosis through the Hedgehog and Notch–Delta networks, ultimately affecting *Ixodes* vectorial competence. We highlight the evolutionary dependence of *I. scapularis* on mammalian hosts through cross-species signaling mechanisms that dually influence arthropod immunity and development.

Ticks thrive in nature through prolonged periods of environmental extremes and metabolic quiescence (*1*). During their multiyear lifespan, *Ixodes* ticks undergo three feeding cycles, marked by a nearly 100-fold increase in body volume (*2*). Blood meal ingestion is aided by bursts of cellular proliferation, differentiation, and hypertrophy, which are central to organ development. Host specialization in ticks (*3*), including highly evolved hematophagy, supports the tick's unique physiological adaptations, particularly blood meal ingestion and storage, survivability through extended intermolt periods, and the maintenance of complex reproductive and developmental programs (*4*), the molecular aspects of which remain unknown.

Arthropod vectors transmit diverse human pathogens, accounting for 17% of all infectious diseases around the globe (*5*). Among all arthropods, ticks constitute the most ancient and predominant group of vectors as they can parasitize almost any vertebrate class, including primeval reptiles (*1*). Although most tick species are confined within a given geographical region and prefer a single host, *Ixodes* spp. parasitize various hosts across multiple continents (*6*). In the US, ~95% of vector-borne diseases, including common infections similar to Lyme disease, are associated with ticks—particularly *Ixodes scapularis* (*7*). Despite their importance, the molecular aspects of *Ixodes* postembryonic development and biology remain enigmatic, partly because of their long life cycle, genetic intractability, and phylogenetic distance from model arthropods. Comparative genomics studies have also suggested unique molecular properties within ticks (*8*). The *Ixodes* genome encodes known components of eukaryotic cell signaling pathways, but with puzzling omissions (*9–11*). For instance, the immunodeficiency (IMD) signaling pathway is operative in *I. scapularis*, but its central molecule, IMD, and a few other components do not appear to be present (*10*). Ticks also have a functional JAK–STAT pathway, which evolved in the earliest branching events of metazoan animals (*12*), comprising a few principal components (*13*). However, the biological effects of its activation are complicated by the use of several ligands, including cytokines (*14*), and its interaction with other pathways (*15*). Most arthropods produce their own cytokine-like

molecules. Unpaired (UPD), for example, can bind a transmembrane receptor called Dome, which activates the JAK–STAT pathway that can support arthropod immunity (*16*) and development (*17*). Dome proteins, despite showing high sequence diversification, feature an extracellular region with a cytokine-binding homology module and multiple fibronectin type-III domains (*18*). Although flies encode multiple UPD ligands for Dome (*17*), there is a surprising absence of UPD orthologs in the *I. scapularis* genome (*9, 19*). Here we report that an *I. scapularis* Dome ortholog, which binds mammalian interferon-gamma (IFN-γ) acquired from the blood meal, triggers downstream tick JAK–STAT signaling cascades that integrate critical episodes of vector immunity and development. This study therefore highlights the adaptive flexibility of ancestral signal transduction pathways (*12, 20*) through the co-option of cross-species signaling between mammals and their ectoparasites.

Results

Identification of a mammalian IFN-γ-binding tick receptor

We previously found that mammalian IFN-γ acquired during a tick's blood meal can trigger a potent antimicrobial response within the vector (*21*). As hematophagy in ticks originated with primeval vertebrates and evolved to include modern mammals (*4*), we explored whether the *I. scapularis* genome acquired a cytokine receptor that binds IFN-γ, such as through lateral gene transfer (*22*), with the ability to trigger immune signaling in ticks. We adopted an unbiased approach using co-immunoprecipitation (Co-IP) assay with whole tick lysates and mammalian IFN-γ as bait, coupled with mass spectrometry. We found that mouse IFN-γ bound a tick protein, annotated as B7P6I6 and termed hereafter as Dome1 (ISCW001458), which has similarity to *Drosophila* Dome (fig. S1). Basic Local Alignment Search Tool analysis revealed that the *Ixodes* genome encodes four additional Dome orthologs (*23*) bearing 23 to 67% identity to Dome1, termed hereafter as Dome2 (ISCW013495), Dome3 (ISCW013496), Dome4 (ISCW008121), and Dome5 (ISCW016699) (fig. S2) (*9*), although these were not identified in our assay. In addition to transmembrane and cytoplasmic regions, Dome1 features a large extracellular amino-terminal region containing a signal peptide, immunoglobulin (IG) domain, and three putative fibronectin type-III domains (Fig. 1A). The extracellular region also contains a mammalian cytokine-binding motif, the interfer-bind PF09294 (*24, 25*), present in rodents (natural hosts of *I. scapularis*) and humans (incidental hosts) but absent in non-*Ixodes* arthropods, including flies, mites, spiders, and other ticks (Fig. 1B). A ClustalW2 sequence alignment revealed homology between

[1]Department of Veterinary Medicine, University of Maryland, College Park, MD, USA. [2]National Center for Advancing Translational Sciences, National Institutes of Health, Rockville, MD, USA. [3]CIC bioGUNE-BRTA (Basque Research & Technology Alliance), 48160 Derio, Bizkaia, Spain. [4]Section of Infectious Diseases, Department of Internal Medicine, Yale University School of Medicine, New Haven, CT, USA. [5]Laboratory of Cancer Biology and Genetics, National Cancer Institute, National Institutes of Health, Bethesda, MD, USA. [6]Department of Entomology, University of Minnesota, Minneapolis, MN, USA. [7]Yale Center for Medical Informatics, Yale University School of Medicine, New Haven, CT, USA. [8]Department of Microbiology and Immunology, University of Maryland School of Medicine, Baltimore, MD, USA. [9]Mass Spectrometry Facility, National Institute of Dental and Craniofacial Research, National Institutes of Health, Bethesda, MD, USA. [10]Howard Hughes Medical Institute, Chevy Chase, MD, USA. [11]Ikerbasque, Basque Foundation for Science, 48011 Bilbao, Bizkaia, Spain. [12]Virginia-Maryland College of Veterinary Medicine, College Park, MD, USA.
*Corresponding author. Email: upal@umd.edu
†Present address: School of Biomolecular and Biomedical Science, University College Dublin, Dublin, Ireland.
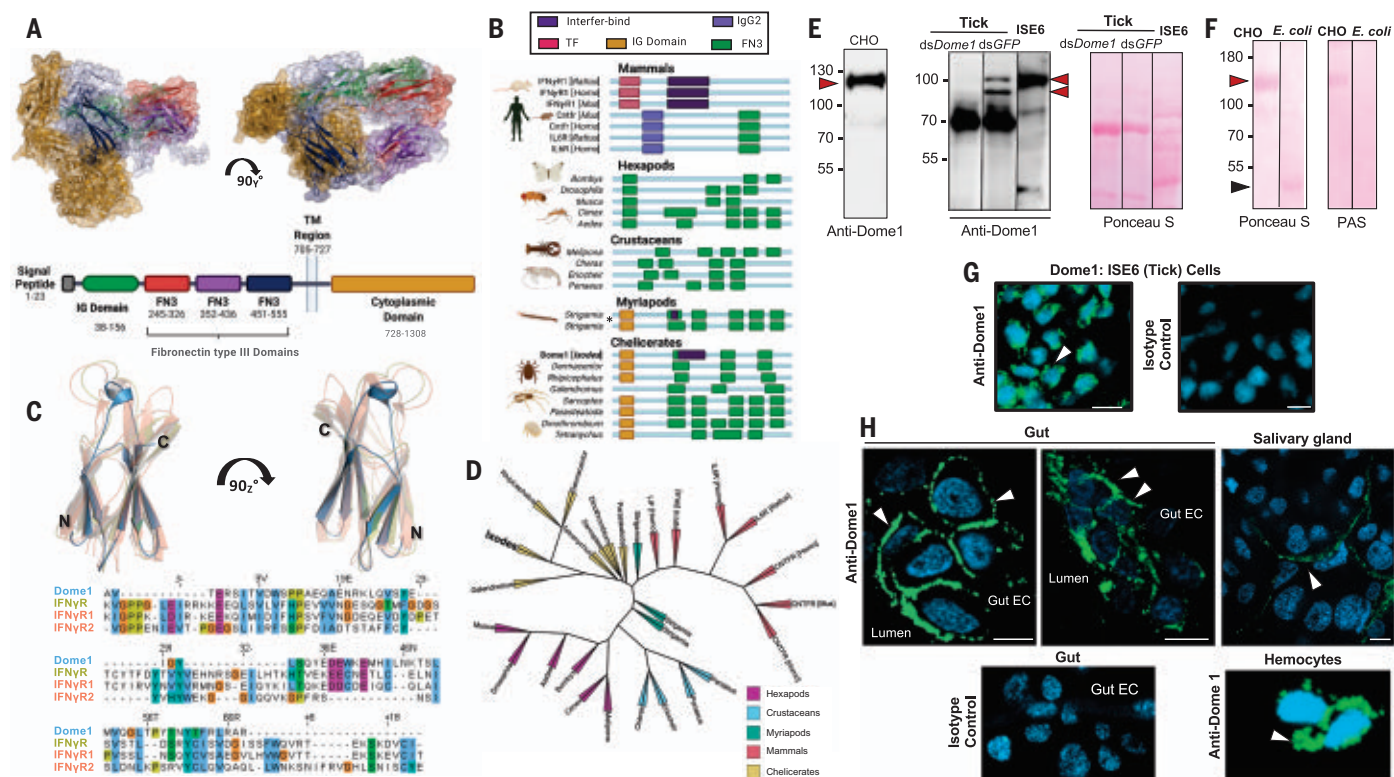
Fig. 1. Identification and characterization of *Ixodes scapularis* Dome1. (**A**) A homology-guided model of Dome1 and a diagram showing its features and domains. The domains [IG, three fibronectin type-III (FN3), transmembrane (TM), and cytoplasmic] are color-coded in the 3D structure (top) and schematic diagram (bottom). (**B**) Acquisition of mammalian interfer-bind motif in Dome1. Sequence comparison of identifiable domains in mammalian cytokine receptors and Dome proteins from selected species of arthropod subphyla are shown (asterisk: two orthologs in the same species). (**C**) Predicted structure and sequence alignment of the cytokine (interfer-bind)–binding motifs from Dome1 (dark-colored helices) and IFN-γ receptors (IFNGR) from mice and humans (light-colored helices). IFNGR (*Mus musculus*) and IFNGR1 and IFNGR2 (*Homo sapiens*) are superimposed to show alignment. (**D**) Phylogenetic tree of basal eukaryotic lineage highlighting conservation of Dome1 through arthropod subphyla and selected mammals. (**E**) Dome1 in a mammalian cell line (CHO), *I. scapularis* cell line (ISE6), and nymphal tick lysates

from partially (24 hour) fed ticks. Lysates from control (ds*GFP*-injected) and *Dome1*-knockdown (ds*Dome1*-injected) ticks were used. Unlike Dome1 in CHO or ISE6 cells, native Dome1 in whole tick lysates appeared as multiple proteins (arrowheads). Protein loading is shown by Ponceau S staining. (**F**) Dome1 is a glycoprotein. Electrophoresed full or truncated ectodomains (red and black arrowheads, respectively) were visualized by periodic acid–Schiff (PAS) staining. Protein loading is indicated by Ponceau S. (**G**) Dome1 localization (arrowhead) in tick cells. Nuclei were labeled with DAPI. (**H**) Detection of Dome1 in nymphal guts, salivary glands, and hemocytes by confocal immunofluorescence microscopy. More Dome1 immunoreactivity (arrowheads) was detectable on the surface of gut epithelial cells facing the lumen (upper left and middle panels) and the surface of hemocytes (lower right panel). Results are representative of three independent biological replicates. For [(G) and (H)], IgG from normal mouse sera served as isotype controls; Dome1: green; DAPI: blue; scale bar: 10 μm.

the Dome1 interfer-bind motif and bona fide IFN-γ receptors in mice and humans (Fig. 1C), as further supported by a phylogenetic tree analysis of basal eukaryotic lineages (Fig. 1D). The Dome1 interfer-bind motif was widespread across phyla, including a limited selection of bacterial species (fig. S3).

As Dome1 was predicted to be a glycoprotein of 1308 amino acids with a large extracellular domain (~704 residues), we generated recombinant versions of the entire ectodomain and additional truncations, using mammalian and bacterial expression systems, respectively, and generated antibodies in mice (fig. S4, A to C). The recombinant Dome1 ectodomain produced in transfected mammalian cells migrated as a single 125-kDa protein. By contrast, native Dome1 in the ISE6 tick cell line or in fed nymphal tick guts was detected as multiple

proteins of 70 to 100 kDa, suggesting additional post translational processing (Fig. 1E). The Dome1 ectodomain housed several N- and O-linked glycosylation sites (fig. S4A) and was glycosylated only when produced in mammalian cells, but not in *Escherichia coli* (Fig. 1F). Confocal immunofluorescence analysis indicated that native Dome1 was localized on the surfaces of ISE6 cells (Fig. 1G) and tick gut epithelial cells facing the lumen (Fig. 1H). The protein did not appear to be exclusive to the gut, as immunoreactivity was detected in other tick samples, including hemocytes and the salivary gland (Fig. 1H).

We next confirmed the interaction of recombinant Dome1 with mammalian IFN-γ. A yeast two-hybrid assay showed a selective interaction between mouse IFN-γ and Dome1 (Fig. 2A). In a pull-down assay, Dome1 interacted with

IFN-γ (Fig. 2B). A microtiter well-based assay indicated that immobilized Dome1 bound IFN-γ, but not tumor necrosis factor (TNF) (Fig. 2C), reaching saturation with the addition of IFN-γ (Fig. 2D). The binding kinetics assessed by bio-layer interferometry (BLI) showed that Dome1 bound IFN-γ with high affinity (K_D of ~40 nM) (Fig. 2E). Notably, Dome1 also bound chicken and human IFN-γ with high affinities (Fig. 2, F to H). IFN-γ and Dome1 were found to colocalize on the surface of ISE6 cells as well as on the tick gut surface in vivo (Fig. 2I). Thus, Dome1 specifically binds mammalian IFN-γ on the luminal surface of the tick gut epithelium.

IFN-γ induces the microbicidal JAK–STAT signaling pathway in ticks through Dome1

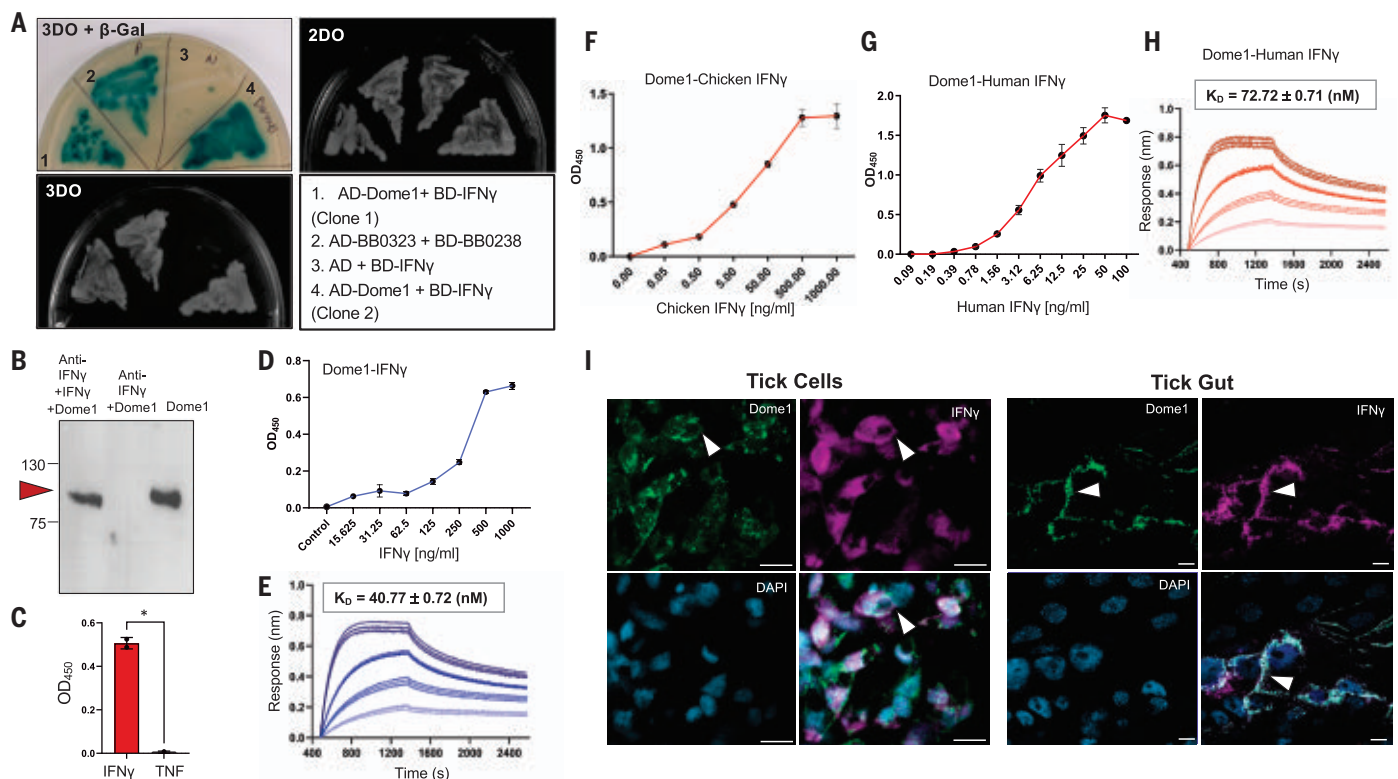The transmembrane Dome receptor activates the JAK–STAT signaling pathway (*17*).

Fig. 2. Dome1 specifically interacts with IFN-γ. (**A**) Yeast two-hybrid assay demonstrates specific interaction between Dome1 and IFN-γ. Although all yeast cells grew on the double-dropout (2DO) media, only those with reporter gene activation grew on triple-dropout (3DO) media and expressed γ-Gal (blue color), confirming interactions between Dome1-IFN-γ or positive controls. (**B**) Anti-IFN-γ antibody pulls down soluble flag-tagged Dome1 in the presence of IFN-γ (left lane), but not in its absence (middle lane), confirming a Dome1–IFN-γ interaction. The pulled-down Dome1 was detected by immunoblot using anti-flag antibodies (right lane). (**C**) A microtiter well-based assay demonstrates a specific Dome1–mouse IFN-γ interaction. By contrast, no interaction was observed between mouse TNF and Dome1. Each data point shows the average of duplicate wells from one of three independent biological replicates, with similar results. (**D**) Dose-dependent binding of mouse IFN-γ to recombinant Dome1. The assay was performed as in (C), suggesting a dose-dependent increase in Dome1–IFN-γ interaction. (**E**) Bio-layer interferometry (BLI) sensorgrams of Dome1–IFN-γ interaction. The affinity constant of this interaction is presented above the sensorgram. (**F** and **G**) Dose-dependent binding of recombinant chicken IFN-γ (F) or human IFN-γ (G) to recombinant Dome1. These assays were performed as detailed in (C). (**H**) BLI sensorgrams of Dome1–human IFN-γ interaction, confirming a high-affinity interaction with human IFN-γ, analogous to those highlighted in the mouse BLI data. (**I**) Dome1 and IFN-γ colocalization on the surface of tick cells (left panel) and in tick gut cells (right panel). Recombinant mouse IFN-γ was incubated with ISE6 cells or dissected tick guts and probed with specific antibodies against Dome1 and IFN-γ, followed by FITC- or Alexa Fluor 568-labeled secondary antibodies. In both tick cells and gut tissues, IFN-γ colocalized with endogenous Dome1 protein (arrows). Error bars denote mean ± standard deviation (SD). Results are representative of 2 to 4 independent experiments. White bar: 10 μm. *$P < 0.05$, Student's t test.

We therefore explored whether Dome1 induces the *Ixodes* JAK–STAT pathway, which can trigger microbicidal responses. *Dome1* mRNA (Fig. 3A) and protein (fig. S4D) were both induced in feeding nymphs. Expression was enhanced during nymphal infestation on *Borrelia burgdorferi*-infected hosts (*B. burgdorferi* is a common Lyme disease agent) (fig. S4E), which produce systemic IFN-γ (Fig. 3A, rightmost panel and fig. S6A) acquired in the tick's blood meal. The induction of *Dome1* (Fig. 3A) and other known immune components (*21*) appeared specific to spirochetal infection as their expression remained unaltered in ticks exposed to another pathogen, *Anaplasma phagocytophilum* (fig. S5). Although *Dome1* mRNA was detectable in multiple tick organs (Fig. 3B), protein expression was most obvious in the gut (fig. S6B). Using mutant mice that either could produce IFN-γ (*Ifngr1*-knockout) or were deficient in IFN-γ (*Ifng*-knockout), we found that *Dome1* was induced by interferon in the tick gut but not in other organs (Fig. 3, C and D). Host IFN-γ influenced blood meal engorgement in ticks, as most nymphs that parasitized animals lacking the cytokine fed to repletion at least 24 hours later than those that engorged on IFN-γ–producing mice (Fig. 3E).

To further understand the biological significance of interferon signaling in ticks—particularly the roles of its arthropod receptor, Dome1—we generated *Dome1*-knockdown ticks through RNA interference (RNAi) (fig. S6B). The microinjection of double-stranded RNA (dsRNA) targeting *Dome1* in the tick gut substantially reduced its expression 48 hours after feeding in comparison to control (ds*GFP*) nymphs (Fig. 3F). *Dome1* knockdown, which was concurrently observed in the salivary glands and hemolymph (fig. S6B), did not affect the expression of other *Dome* homologs, except for a small but detectable decrease in *Dome5* transcripts (fig. S7). The impact on Dome5 protein levels was minimal, however (fig. S7). To assess whether Dome1 deficiency impaired the activation of the JAK–STAT pathway, we allowed nymphal ticks to parasitize *B. burgdorferi*-infected mice. The knockdown of *Dome1* resulted in lower levels of *JAK* mRNA (Fig. 3G), STAT phosphorylation (Fig. 3H), and transcripts of antimicrobial gene *Dae2* (Fig. 3I). In addition, Dome1 deficiency reduced *B. burgdorferi* levels in the guts of knockdown ticks (Fig. 3,
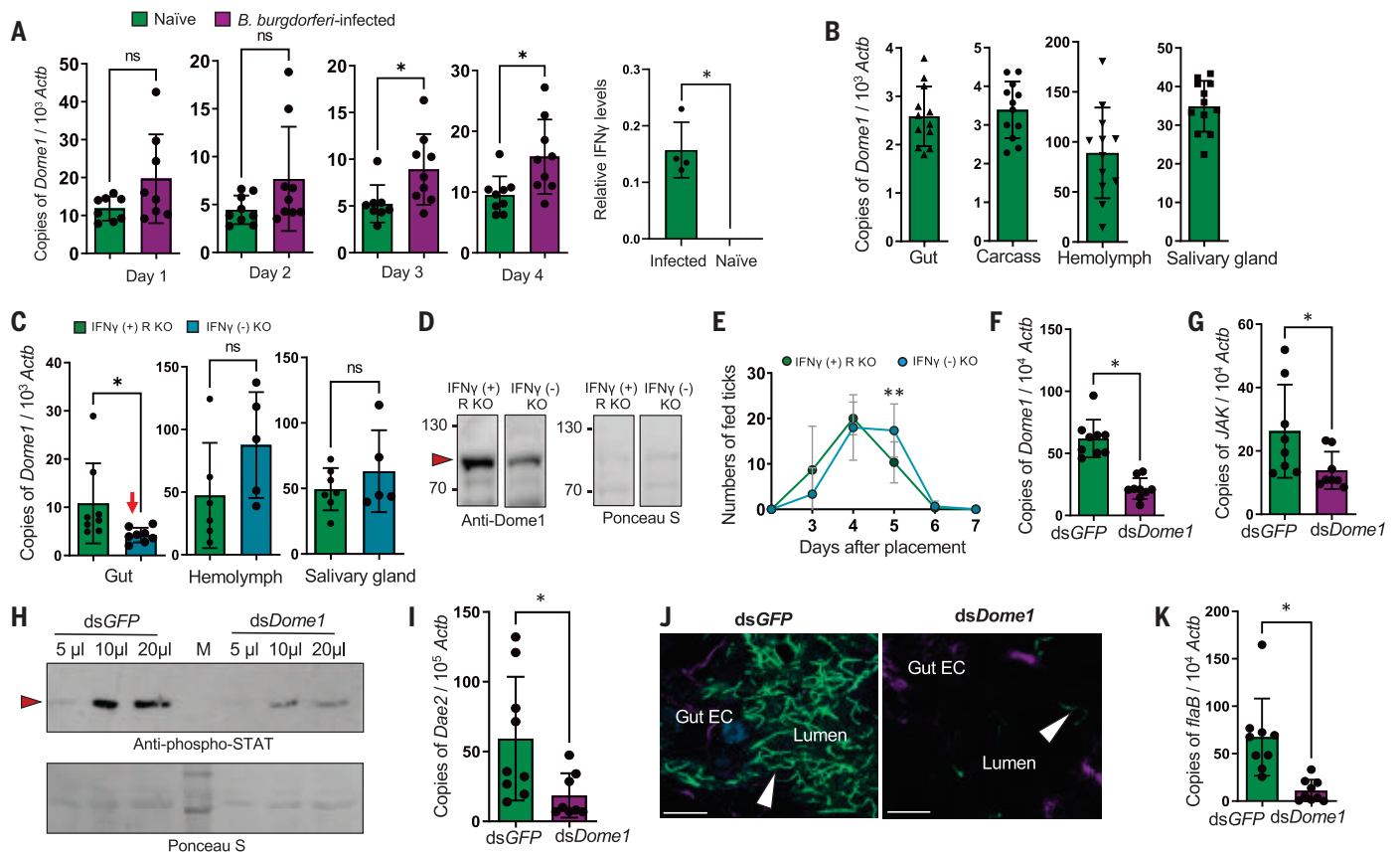
Fig. 3. Dome1, induced by host-derived IFN-γ, regulates tick borreliacidal responses through the JAK–STAT pathway. (**A**) *Dome1* is induced during tick engorgement and *B. burgdorferi* infection. The reverse transcription-quantitative polymerase chain reaction (RT-qPCR) analysis of *Dome1* transcripts in nymphs fed on naïve or infected mice (left panel). The right panel shows IFN-γ levels in murine blood. (**B**) Expression of *Dome1* in various tick tissues. Nymphs parasitized mice for 48 hours, and tissues were processed for *Dome1* transcripts and normalized against tick *Actb* levels. (**C**) *Ifng* deficiency down-regulates *Dome1* in tick guts (arrow). Groups of three *Ifngr1*-knockout mice, which produce the cytokine (IFN-γ + R KO) or *Ifng*-knockout mice (IFN-γ −KO) were parasitized by nymphs (30 ticks per group) for 48 hours. *Dome1* transcripts were analyzed in tick tissues. (**D**) IFN-γ deficiency downregulates Dome1 in fed tick gut. Protein loading is indicated by Ponceau S staining. (**E**) Influence of host IFN-γ on blood meal acquisition by ticks. In the absence of IFN-γ, engorgement time is delayed at day 5, when nymphs ingest the major portion of the

blood meal. **P < 0.05, determined using two-tailed Student's t test. (**F**) RNAi-mediated *Dome1* knockdown by microinjection of unfed nymphs (20 ticks per group), which then fed on *Borrelia*-infected mice for 48 hours. *Dome1* mRNA levels were measured by RT-qPCR. (**G** to **I**) *Dome1* knockdown reduces levels of *JAK* transcripts (G); STAT phosphorylation ("M" and arrowhead denote molecular weight markers and phosphorylated STAT protein, respectively) (H); and *Dae2* transcripts (I) in 48-hour-fed ticks. (**J**) *Dome1* knockdown affects colonization of *B. burgdorferi* (green, arrowhead) in the tick gut; nuclei and actin are labeled with DAPI (blue) and rhodamine phalloidin (violet). The image represents one of three biological replicates with similar results. (**K**) RT-qPCR analysis of *B. burgdorferi*, assessed by measuring *flaB* transcripts normalized to *Actb* levels. Results represent two to five independent experiments, where quantitative data are shown as individual data points; error bars show the means ± SDs (n = 9 to 30). White bar: 10 μm. *P < 0.05, determined using two-tailed Mann-Whitney U test; n.s., not significant.

J and K). Higher reactive oxygen species (ROS) activity was detected in *Dome1*-knockdown guts, as well as the altered expression of representative enzymes associated with oxidative stress, which may have contributed to the decreased spirochete levels (fig. S8). The regulation of tick microbicidal immune responses was specifically triggered by *Dome1* and did not involve other homologs, such as *Dome5*. Indeed, a separate knockdown of *Dome5* had no effect on tick immune responses, biology, or vectorial competence (fig. S9). Thus, Dome1 can recognize mammalian IFN-γ and trigger a cross-species immune signaling cascade through the JAK–STAT pathway, ultimately influencing *B. burgdorferi* levels.

Dome1 contributes to tick intermolt development through the JAK–STAT pathway

Dome1-knockdown ticks, despite complete blood meal acquisition (Fig. 4A), began to display reduced body weights and discolored cuticles 10 to 20 days after feeding (Fig. 4B). *Dome1* mRNA and protein deficiency was maintained throughout the intermolt stage and in newly molted adults (fig. S6C). Most of the *Dome1*-knockdown nymphs were unable to molt after feeding, in contrast to control ticks (Fig. 4C). This suggested that Dome1—in addition to orchestrating mammalian interferon–induced microbicidal immune responses within the vector—also plays a critical role in tick inter-

molt development. To better understand the role of Dome1 in subadult ticks, we performed systemic RNAi in newly engorged larvae. *Dome1*-knockdown intermolt larvae showed severe growth defects 20 days after dsRNA treatment and blood meal engorgement, with most ticks unable to molt (Fig. 4D). By contrast, nearly all control larvae molted to nymphs. The few *Dome1*-knockdown ticks that were able to molt displayed a loss of bilateral symmetry and morphological defects, ranging from malformed mouthparts (palps and/or hypostome) to leg abnormalities, including unequal numbers of limbs on either side of the body (three versus four limbs) and rudimentary or underdeveloped legs without a base (coxa), in addition to
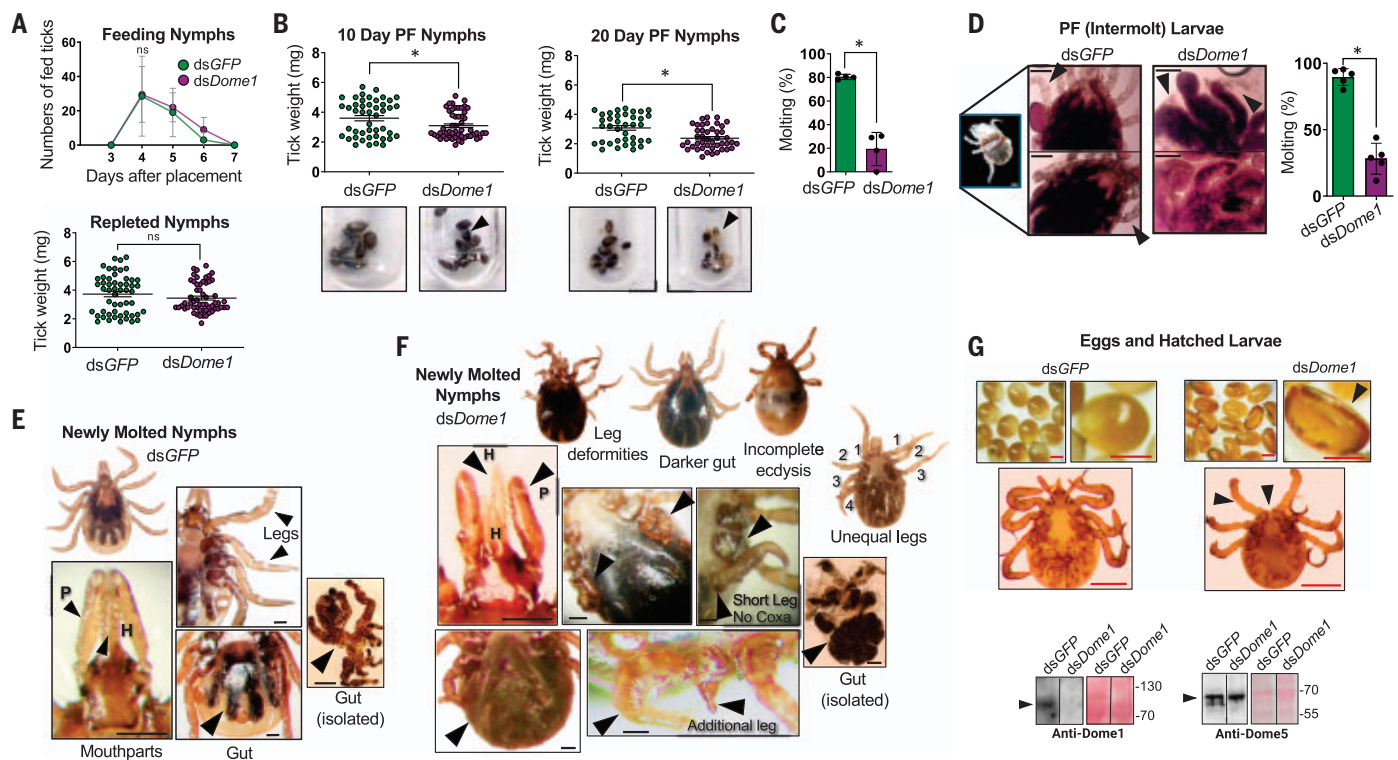
Fig. 4. Dome1 is essential for optimal tick metamorphosis. (**A**) Host blood meal acquisition in *Dome1*-knockdown ticks. Number of fed ticks (left panel) and tick engorgement weights (right panel) are shown. (**B**) Intermolt ticks. Compared with controls, *Dome1*-knockdown post-fed (PF) ticks displayed lower weights (upper panels) and different body colors with exposed exuviae or even death (lower panels, arrowheads). (**C**) Impairment of molting success in *Dome1*-knockdown nymphal ticks, as assessed by the percentage of molted ticks. (**D**) *Dome1* silencing in fed larvae impairs development and molting. The control intermolt ticks (left panels) at 20 days post-fed (PF) reveal newly formed legs (arrowheads) which were absent or malformed in *Dome1*-knockdown groups (right panels, arrows). The percentage of molted ticks is shown in the rightmost panel. (**E** and **F**) Compared with controls (E), transstadial *Dome1*-knockdown ticks (F) showed deformities (arrows), including in hypostome (H) and palps (P),

uneven legs with unequal lengths, stunted legs without coxa, and darker abdomens with incomprehensible gut diverticula. (**G**) Dome1 is essential for fecundity and larval development. The data represent an experiment where 80 adult ticks were microinjected with ds*Dome1* or ds*GFP* (control) RNA and allowed to engorge on groups of rabbits. Dome1 deficiency resulted in abnormal egg and larval development (top right panels), compared with the controls (top left panels). *Dome1* knockdown was sustained in the mature eggs, which were analyzed for Dome1 (bottom left panels) or Dome5 (bottom right panels) protein levels by immunoblot. See additional results for hatched larvae in fig. S11. Results are representative of two to five independent experiments where quantitative data are shown as individual data points; error bars show the means ± SDs (*n* = 6 to 50). Black or white bar: 100 μm; red bar: 50 μm. *P < 0.05, determined using two-tailed Mann-Whitney U test; n.s., not significant.

darker abdomens and incomplete ecdysis (Fig. 4, E and F, and fig. S10).

To evaluate whether Dome1 was critical for fecundity and early larval development, *Dome1*-deficient adult females were allowed to parasitize rabbits and subsequently lay eggs. Similar to nymphs (Fig. 4A), a knockdown in *Dome1* did not influence the repletion time or engorgement weight of fed adults, but did affect the quality, number, and size of the egg masses as well as the emergence of larvae, many of which were born with growth defects (Fig. 4G and fig. S11), similar to those previously observed in nymphs.

Dome1, but not Dome5, was the main driver of these phenotypic defects because eggs and emerged larvae from *Dome1*-knockdown females produced Dome5 protein at levels comparable to control ticks, whereas Dome1 protein remained largely undetectable (Fig. 4G and fig. S11). These Dome1-regulated developmen-

tal abnormalities were likely driven by the *Ixodes* JAK–STAT pathway, as the separate and systemic RNAi silencing of *JAK* or *STAT* transcripts yielded comparable effects on tick development (Fig. 5 and fig. S12, A to D). Although *Dome1*-knockdown ticks exhibited the most prominent body deformities (Fig. 4, E and F), some similarities were observed in the overall appearances of *JAK*- or *STAT*-knockdown ticks, including the presence of darkened abdomens (fig. S12B). Moreover, newly molted nymphs in which the expression of *Dome1*, *JAK*, or *STAT* was separately knocked down also displayed comparable developmental defects, including shorter hypostomes and palps, as well as deformities in the palp bases, legs, and anal pores (Fig. 5 and fig. S12, B to D). Cross-sections of whole nymphal ticks revealed a completely digested blood meal with normal development in control ticks, whereas *Dome1*-,

JAK-, or *STAT*-knockdown ticks presented enlarged and abnormally developed bodies surrounding a large bolus of blood meal, suggesting impaired digestive activities in the gut (Fig. 5H). Thus, Dome1 contributes to tick intermolt development through the JAK–STAT pathway.

Gut biology and microbial homeostasis are maintained by Dome1

As Dome1 deficiency affected multiple aspects of tick immunity and development, we assessed possible alterations in the gut proteome and microbial homeostasis, in addition to the influence of *B. burgdorferi* on Dome1 signaling. Both *Dome1* knockdown and *B. burgdorferi* infection affected the tick gut proteome (Fig. 6A and tables S1 to S4). Compared with naïve hosts, the impact of *Dome1* knockdown in ticks feeding on *B. burgdorferi*-infected hosts was reflected by the more robust down-regulation
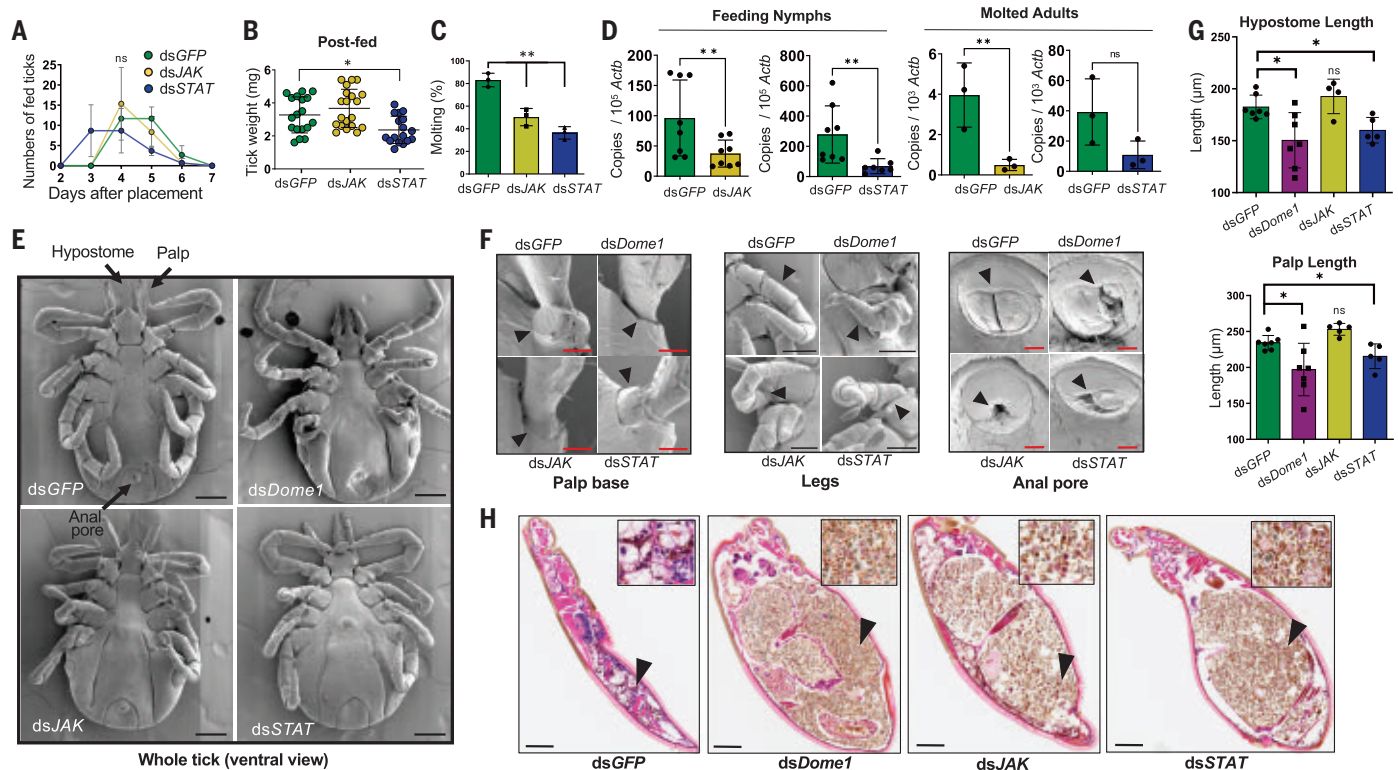
Fig. 5. The *Ixodes* JAK–STAT pathway contributes to Dome1-mediated tick metamorphosis. (**A**) Knockdown of *STAT*, but not *JAK*, impairs tick attachment. Ticks (25 nymphs per group) were microinjected with target dsRNA and placed on naïve mice. Detached fed ticks were enumerated. (**B**) *STAT* knockdown impairs tick weight. Ticks were weighed after feeding to repletion. (**C**) Molting success of knockdown ticks. Compared with controls, a reduction in molting was evident in *JAK*- and *STAT*-knockdown ticks. **$P < 0.05$, determined using two-tailed Student's *t* test. (**D**) RNAi-mediated *JAK* and *STAT* knockdown effects are maintained transstadially. The ticks were analyzed as 48-hour-fed nymphs and as molted adults. **$P < 0.05$, determined using two-tailed Student's *t* test. (**E**) Scanning electron micrographs of knockdown ticks. Unlike normal structures in control nymphs (arrows), *Dome1*-, *JAK*-, and *STAT*-knockdown ticks presented abnormal appearances, most noticeably in their malformed mouthparts, legs, and anal pores. (**F**) Close-up view of the morphological defects highlighted in (E), indicating defective palp bases, legs, and anal pores. (**G**) Quantitative assessment of morphological defects highlighted in (E), denoting shorter hypostome and palps in *Dome1*- and *STAT*-knockdown ticks. Additional results are presented in figs. S10 and S12. (**H**) Histological analysis of ticks. Engorged larvae were subjected to standard H&E staining. Enlarged and abnormally developed bodies surrounding a large bolus of improperly digested blood meal were seen in *Dome1*-, *JAK*-, or *STAT*-deficient ticks. The inset shows a magnified view of the gut contents (arrow), revealing the presence of the remnants of blood cells and microbes, which are predominant in all groups except for the control (ds*GFP*) ticks. Results are representative of two to three independent experiments where quantitative data are shown as individual data points; error bars show the means ± SDs ($n = 3$ to 30). Black bar: 100 μm; red bar: 20 μm. *$P < 0.05$, determined using two-tailed Mann-Whitney U test; n.s., not significant.

of several proteins known to support organ development, homeostasis, replication, and immune responses (table S4). Thus, Dome1 signaling is more critical for the correct functioning of the gut when *B. burgdorferi* is present. Dome1 regulated pathogen levels and influenced the STAT protein (Fig. 3), which is known to affect the acellular gut barrier known as the peritrophic matrix (PM), important for gut homeostasis (*26*). Therefore, we examined the influence of Dome1 deficiency on PM function and the gut microbiome. The expression of gut peritrophin gene *PM5* was reduced in *Dome1*-knockdown ticks (Fig. 6B). The PM barrier was also compromised, as indicated by the altered permeability of the fluorescein-conjugated high molecular weight dextran (Fig. 6C). Furthermore, *Dome1* knockdown affected the diversity of the gut microbiome, including predominant bacterial genera such as

Rickettsia, irrespective of *B. burgdorferi* infection (Fig. 6D). JAK–STAT-suppressed ticks showed similar effects on tick biology and gut microbial homeostasis (fig. S13), indicating that they constitute key drivers of Dome1-induced responses. Thus, Dome1 regulates gut homeostasis and microbial diversity.

Dome1 supports gut regeneration and stem cell proliferation through the Notch–Delta and Hedgehog signaling pathways

We next investigated the cellular and molecular mechanisms by which the silencing of *Dome1* affects gut homeostasis. During feeding, the tick gut undergoes bursts of developmental and remodeling events to acquire, ingest, and store a large volume of blood. To perturb this process, we induced experimental colitis in ticks by microinjection of 2% dextran sodium sulfate (DSS). DSS–treated ticks showed im-

paired feeding, as indicated by the reduced number of engorged ticks (Fig. 7A) and overall lower body weights (Fig. 7B). There were no differences in engorgement weights of ticks treated with only DSS and those coinjected with DSS and *GFP* dsRNA, but reduced weights were observed in ticks coinjected with DSS and *Dome1* dsRNA (Fig. 7B), suggesting that Dome1 is required for the regeneration or remodeling of gut tissues.

Dome1 contributed to the optimal maintenance of gut cell populations (Fig. 7C), likely by supporting their proliferation (Fig. 7D). Experimental tissue injury with DSS triggered extensive cell proliferation in nymphal guts, evidenced by a significant increase in 5-ethynyl-2′-deoxyuridine (EdU)-positive cells (Fig. 7E). The proliferative population, which highly expressed *Dome1* (Fig. 7F), was decreased in DSS-treated *Dome1*-knockdown ticks (Fig. 7E, right
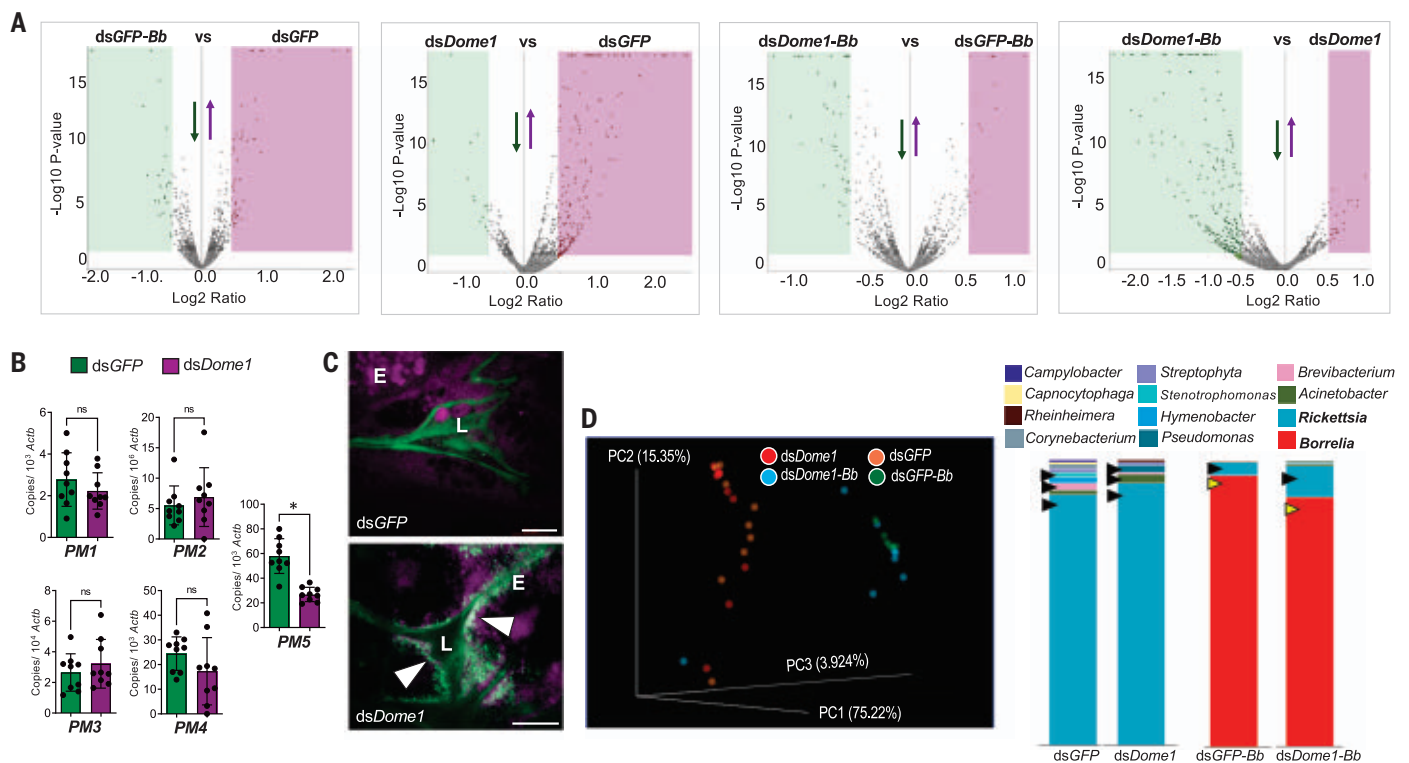
Fig. 6. Dome1 supports gut homeostasis in feeding ticks. (**A**) Differential production of gut proteins in *Dome1*-knockdown ticks, in the presence or absence of *B. burgdorferi*, analyzed as follows: (i) *B. burgdorferi*-infected versus naïve control (ds*GFP-Bb* versus ds*GFP*), (ii) naïve *Dome1*-knockdown versus naïve control (ds*Dome1* versus ds*GFP*), (iii) *B. burgdorferi*-infected *Dome1*-knockdown versus *B. burgdorferi*-infected naïve control (ds*Dome1-Bb* versus ds*GFP-Bb*), and (iv) *B. burgdorferi*-infected *Dome1*-knockdown versus naïve *Dome1*-knockdown (ds*Dome1-Bb* versus ds*Dome1*). The down- and up-regulated proteins are indicated by green or purple areas, respectively (see tables S1 to S4). (**B**) RT-qPCR assays show the down-regulation of a peritrophin gene, *PM5*, in *Dome1*-knockdown ticks. (**C**) Alteration of PM permeability in *Dome1*-knockdown ticks. Confocal microscopy showed the guts of 48-hour-fed nymphs, which had been microinjected with either ds*Dome1* or ds*GFP* RNA and were then capillary fed with fluorescein-conjugated 500,000 (green) or rhodamine red-conjugated 10,000 (violet) MW dextran molecules. The fluorescent beads are marked by arrowheads. L, lumen; E, epithelial cells. (**D**) 16S rRNA amplicon analysis of gut microbiota in *Dome1*-knockdown (ds*Dome1*) and control (ds*GFP*) ticks, in the presence or absence of *B. burgdorferi* (32 nymphs per group), indicates alterations in microbial composition. The left panel denotes the principal coordinate analysis of weighted UniFrac distances of microbial communities; the right panel shows the genus-specific total bacterial abundance of *Dome1*-knockdown and control ticks in naïve (ds*GFP* versus ds*Dome1*) or infected (ds*GFP-Bb* versus ds*Dome1-Bb*) conditions. In naïve ticks, *Dome1* deficiency altered the abundance of selected microbes (black arrowheads). In infected ticks, *Dome1* knockdown decreased the abundance of *Borrelia* and enhanced the level of *Rickettsia* (yellow and black arrowheads, respectively). Results are representative of two to three independent experiments where quantitative data are shown as individual data points; error bars show the means ± SDs (*n* = 9 to 20). White bar: 20 μm. *P < 0.05, determined using two-tailed Mann-Whitney U test; n.s., not significant.

panels), suggesting that Dome1 plays an essential role in cell proliferation after tissue injury. *I. scapularis* also displayed heightened gut cell proliferation when parasitizing IFN-γ–sufficient mice compared with IFN-γ–deficient mice (fig. S14), underscoring the influential roles of host IFN-γ in the up-regulation of *Dome1* and the acceleration of blood meal engorgement in ticks (Fig. 3E). Dome1-mediated regulation of proliferative cells also involves gut stem cells, as their numbers were reduced in knockdown ticks (Fig. 7G).

The function of Dome1 likely involves developmental transcription factors, such as components of the Notch–Delta, epidermal growth factor receptor (EGFR), and Hedgehog signaling pathways. Enhanced expression of *Dome1* was observed during early molting from larva to nymph (fig. S15A), whereas the

knockdown of *Dome1* impaired the expression of representative transcription factors from the Notch–Delta, EGFR, and Hedgehog pathways in nymphs (fig. S15B). *Hox* genes, a group of downstream transcription factors, were also induced after larval molting (fig. S15C). Notably, these genes were down-regulated in *Dome1*-knockdown ticks, compared with control ticks, whereas other transcription factors, such as *SET* and *POU*, remained unaffected (fig. S15D). Because *Hox* genes are regulated by the Hedgehog pathway (*27*), we created *Hedgehog*-knockdown ticks using RNAi. Similar to *Dome1*-, *JAK*-, or *STAT*-knockdown larvae, *Hedgehog*-silenced ticks were also unable to complete molting, displayed defects in multiple organs including the anal pore and legs, presented darkened abdomens, and often exhibited a complete loss of mouthparts (fig. S16). Furthermore, *Hedgehog* knockdown affected the expression of *Notch*, suggesting that their expression is connected during tick intermolt development. Thus, Dome1 regulates cellular proliferation and the homeostasis of gut tissues through JAK–STAT signaling through the Hedgehog and Notch–Delta pathways.

Ixodes Dome1–JAK–STAT pathway is required for optimal feeding of *B. burgdorferi*-infected ticks and pathogen transmission

We next assessed whether *Dome1* or the JAK–STAT pathway affects pathogen survival throughout the tick intermolt stages as well as pathogen transmission to naïve hosts. In *B. burgdorferi*-infected larvae, the suppression of *Dome1* mRNA and protein, along with *JAK* and *STAT* mRNA, was maintained in molted nymphs (Fig. 8A and fig. S12E). Notably, despite the substantial
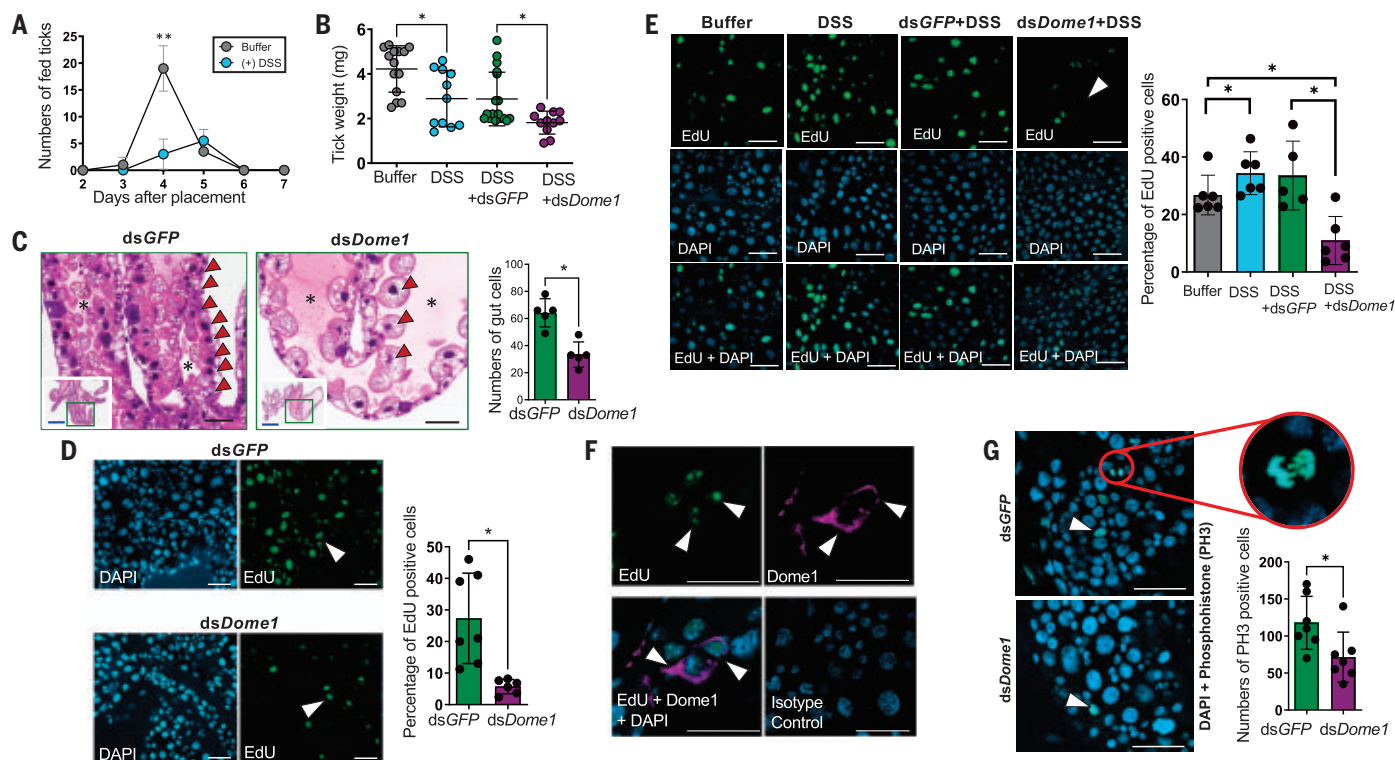
Fig. 7. Dome1 maintains gut homeostasis through tissue regeneration and stem cell proliferation. (**A**) Incomplete blood meal engorgement after induction of experimental colitis in DSS-treated ticks. **$P < 0.05$, determined using two-tailed Student's t test. (**B**) Dome1 assists in tissue regeneration after injury. Ticks injected with DSS and coinoculated with ds*Dome1* RNA showed reductions in weight compared with the DSS-injected controls (ds*GFP*). (**C**) Dome1 maintains optimal gut cell population, as assessed by histology. The middle panel denotes the altered distribution of gut cells in *Dome1*-knockdown nymphs, showing cellular reduction (arrowheads) and an enlarged lumen (asterisk), compared with controls (left panel). The insets show the whole gut diverticula, with green boxes denoting the areas of magnified images. The right panel shows the microscopic enumeration of gut cells. (**D**) Cell proliferation in nymphal guts. *Dome1*-knockdown and control (ds*GFP*) nymphs fed on naïve mice for 72 hours to initiate gut cell proliferation. Proliferative EdU⁺ cells are marked by arrows (middle panels). The right panel shows the quantification of EdU⁺ cells. (**E**) Dome1 is essential for cell proliferation after gut injury. Nymphs were microinjected with buffer or DSS, in the presence or absence of dsRNA (ds*Dome1* or ds*GFP*). DSS-triggered gut cell proliferation activity was impaired by *Dome1* deficiency (left panel, arrow), also shown by a reduction in cell counts (right panel). (**F**) Dome1 is expressed in proliferative cells. EdU⁺ cells were positive for Dome1 expression (violet). (**G**) Dome1 regulation of proliferative cells includes gut stem cells. *Dome1*-knockdown or control ticks fed on mice for 48 hours and were stained with anti-phospho-histone H3 (PH3) antibody (left panels, arrow), and enumerated (right panel). The circle represents a dividing stem cell nucleus in the control tick. Results are representative of two to three independent experiments where quantitative data are shown as individual data points; error bars show the means ± SDs ($n = 6$ to 25). For [(D) to (G)], nuclei are labeled with DAPI (blue) or EdU (green); white or black bars: 50 μm; blue bar: 300 μm. *$P < 0.05$, determined using two-tailed Mann-Whitney U test.

impact of Dome1–JAK–STAT on gut homeostasis and *B. burgdorferi* acquisition in ticks from infected hosts (Fig. 3 and Fig. 6), lower levels of spirochetes were detected throughout the intermolt period and in newly molted nymphs (Fig. 8B). When *Dome1*, *JAK*, or *STAT* were silenced in *B. burgdorferi*-infected ticks, only control (ds*GFP*) or *JAK*-knockdown ticks completed feeding on naïve C3H mice, whereas only a minority of the *Dome1*- or *STAT*-knockdown ticks (0 to 6%) were able to attach or engorge (fig. S12F). Control or *JAK*-knockdown ticks displayed regular hypostomes and normal engorgement, but some of the *Dome1*- or *STAT*-knockdown ticks that attempted host attachment exhibited malformed mouthparts, such as broken or distorted palps or hypostomes (Fig. 8C). Impaired feeding in *Dome1*- or *STAT*-knockdown ticks was further demonstrated

by the reduced average time of tick attachment (Fig. 8D), numbers of fed ticks (Fig. 8E), and engorgement weights (Fig. 8F). After tick infestation, *B. burgdorferi* was undetectable in mice parasitized by *Dome1*-knockdown ticks, whereas low levels were recorded in *STAT*- and *JAK*-knockdown groups (Fig. 8, G and H, and fig. S12G). Despite the detection of spirochete-specific signals in the *JAK*-knockdown group (Fig. 8H), culture analysis further confirmed that most animals remained uninfected (table S5).

Given the critical role of the *I. scapularis* Dome1–JAK–STAT pathway in the utilization of cross-species IFN-γ signaling mechanisms, we searched for these signaling components in the major tick genomes. Representative components of the Dome1–JAK–STAT pathway were present in all examined major tick vectors (fig. S17), providing support for their

more widespread and evolutionary roles across diverse tick species. Despite the conservation of Dome1 orthologs, there was a high degree of diversification across major tick groups (fig. S18). However, the core Dome1 functions were likely maintained in ticks. For example, the interfer-bind motif was absent in Dome1 orthologs from most non-*Ixodes* tick genera (fig. S17) whereas the transcripts for *Dome1* orthologs were detectable in the American dog tick (*Dermacentor variabilis*) and lone star tick (*Amblyomma americanum*), which were expressed during tick engorgement on mammalian hosts (fig. S19). Silencing of the *Dome1* ortholog in *D. variabilis* showed that it supported cellular proliferation and microbial homeostasis in the gut (fig. S20), similar to its *I. scapularis* counterpart. Thus, the role of Dome1 is conserved across diverse tick genera.
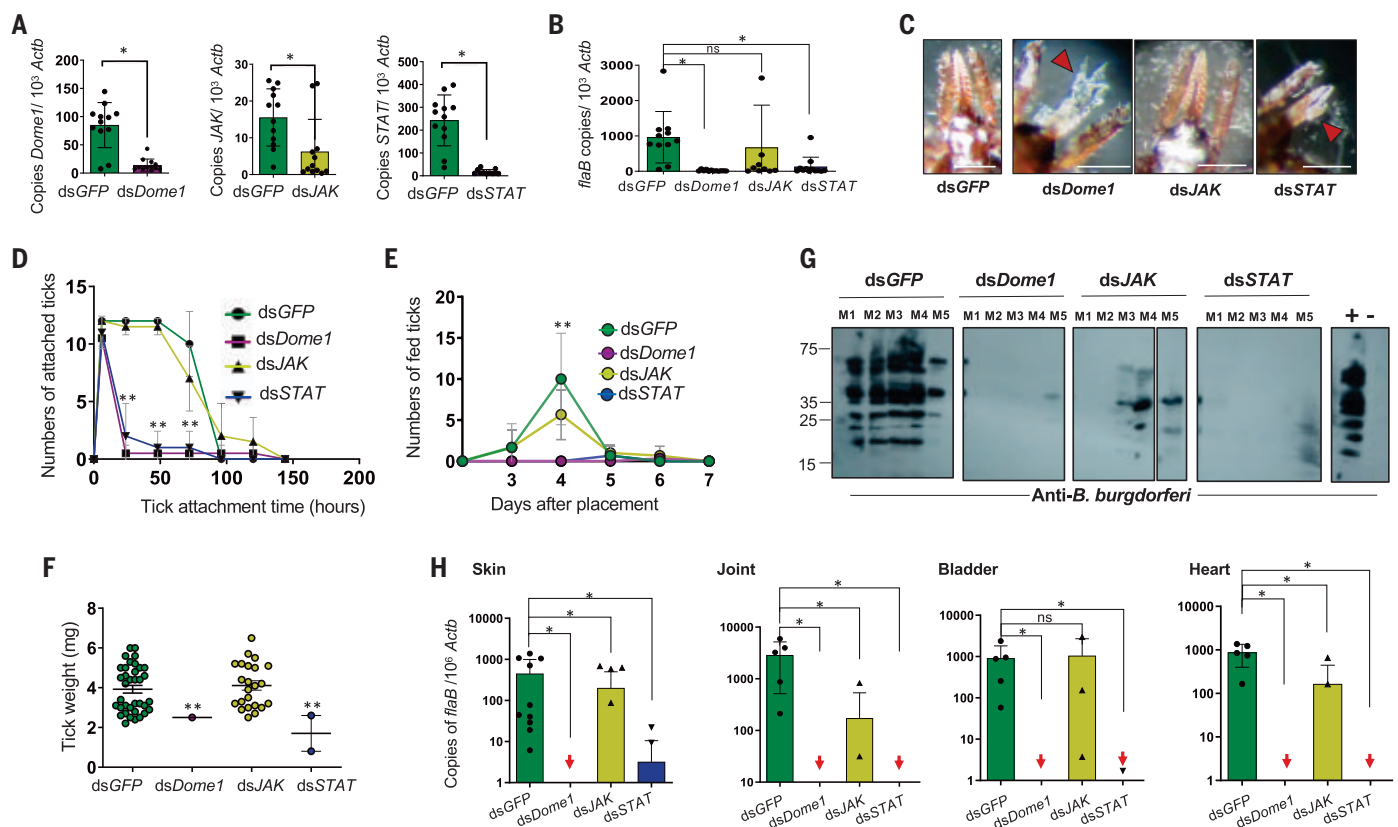
Fig. 8. *Ixodes* Dome1 and JAK–STAT signaling pathway is required for optimal blood meal engorgement of *B. burgdorferi*-infected ticks and spirochete transmission to mice. (A) Transstadial knockdown of *Dome1*, *JAK*, and *STAT* in infected nymphs. Larvae that had engorged on *B. burgdorferi*-infected mice were microinjected with target dsRNA and allowed to molt. Transcripts in the infected nymphs were analyzed by RT-qPCR. (B) *B. burgdorferi* levels in unfed nymphs, as measured by the RT-qPCR assessment of *flaB* transcripts normalized against tick *Actb* levels. (C) Damaged tick mouthparts. Unlike the control or *JAK*-knockdown ticks, the detached *Dome1*- or *STAT*-knockdown ticks displayed distorted mouthparts (arrowheads). (D to F) The feeding parameters for the various groups are presented as the tick attachment time (D), number of fed ticks (E), and engorgement weight (F). Asterisks denote significant differences between ds*Dome1* or ds*STAT* to other groups. **$P < 0.05$, determined using two-tailed Student's *t* test. (G and H) Assessment of pathogen transmission to mice. 12 days after tick feeding, infection in individual animals was assessed by sera immunoblotting (G), or RT-qPCR assays (H) using one tissue sample per organ, except for proximal and distant skin samples relative to tick bite sites, by measuring copies of *B. burgdorferi flaB* transcripts normalized against mouse *Actb* levels. Arrows indicate murine tissue samples in ds*Dome1* or ds*STAT* groups where *flaB* transcripts remain undetectable. For immunoblotting, sera from naïve mice and mice that were previously infected with *B. burgdorferi* were used as negative (−) and positive (+) controls, respectively. Loading controls are presented in fig. S12. Results are representative of three independent experiments where quantitative data are shown as individual data points; error bars show the means ± SDs ($n = 9$ to 36). White bar: 100 μm. *$P < 0.05$, determined using two-tailed Mann-Whitney U test; n.s., not significant.

Discussion

This study highlights the complex roles of Dome1 as a central receptor for a mammal–arthropod signaling cascade with converging effects on vector immunity and development. The protein is essential for the interspecies regulation of gut homeostasis, immunity, and blood meal digestion through the tick JAK–STAT pathway. These events, triggered by the incoming blood meal and expedited by the interaction between host-acquired IFN-γ and Dome1, are crucial for the tick's postembryonic development and organogenesis, and are further supported by the Hedgehog and Notch–Delta biochemical networks. The integration of immunity and developmental functions in a single gut receptor enables ticks to sense danger signals emanating from infected hosts, thereby accelerating blood meal acquisition, which is essential for tick metamorphosis. Overall, this study underscores the notable flexibility of conserved cell signaling pathways, in addition to the commandeering of elements that can drive the complex cross-species regulation of immune responses, gut homeostasis, and organ development. It also emphasizes the intimate evolutionary relationship between ticks and their hosts at paramount points in the arthropod life cycle, marked by critical episodes of blood meal acquisition.

Mammalian cytokines affect the immunity and physiology of blood-feeding vectors (*21, 28, 29*), although the origin of cytokine receptors in arthropods remains unknown. Ticks, such as *I. scapularis*, are cosmopolitan in their selection of hosts, including lizards. As ancient ticks fed on primeval reptiles, it is possible that Dome1 originated early in the evolution of tick hematophagy. Indeed, Dome1 orthologs are present in representative reptilian, avian, and mammalian species (fig. S3), in addition to all examined tick groups (fig. S18). The occurrence of an IFN-γ–binding motif in Dome1 highlights how the evolution of vector parasitism offers opportunities for the acquisition of novel gene traits. The integration of Dome1's interfer-bind motif in multiple tick species (figs. S17 and S18), together with its high-affinity interactions with mammalian or avian interferons, likely provides ticks with an ability to intercept immunity signals from a variety of infected mammals. Notably, although it remains unknown how *I. scapularis* evolved the ability to bind IFN-γ, the interfer-bind motif is detectable in several bacterial species, including *Roseburia* spp., which exist in the guts of both mammals and *I. scapularis*

(30, 31), pointing to lateral gene transfer events as a possibility (22, 32). Regardless, IFN-γ-induced Dome1 controls the proliferation of *I. scapularis* gut cells, which would favor the intake of a large blood meal, augmenting tick survivability. Moreover, microbicidal responses triggered by Dome1–JAK–STAT signaling may support tick development by preserving essential nutrients, such as N-acetylglucosamine, the building block of tick chitin and bacterial peptidoglycan (33, 34). The silencing of the JAK–STAT pathway or the knockdown of *Dome1* with multiple RNAi strategies (fig. S21) impairs organ development and tick metamorphosis, which suggests that these vectors reset their postembryonic development with each feeding cycle, revealing a critical role for a limited ancestral cell signaling pathway in the subadult development of ticks.

Because the role of the Dome1–JAK–STAT pathway on tick development is evident in the absence of IFN-γ or *B. burgdorferi* infection, it is likely that Dome1 binds endogenous tick ligands or other blood meal–derived factors. However, we were unable to identify additional Dome1 ligands in ticks, including UPD orthologs. Some other arthropods also lack genes encoding UPD, including non-*Ixodes* ticks (35), although some can alternatively produce endogenous ligands, such as Vago in *Aedes* mosquitoes (16) and novel C-type lectins in shrimp (14), that bind transmembrane Dome receptors and activate the JAK–STAT pathway, triggering antimicrobial immune responses. The biological significance of the expression of five Dome homologs in a single species such as *I. scapularis* remains puzzling, although the functions associated with Dome1 seem to be nonredundant to that of its homologs. The interference with tick development and metamorphosis through the knockdown of *Dome1*, *JAK*, or *STAT* impedes pathogen transmission from infected ticks to mammalian hosts, suggesting that these proteins may represent potential targets of anti-tick measures.

These data enhance our understanding of how eumetazoan cell signaling pathways (20, 36) have evolved. They highlight the flexibility and capacity of these pathways to adapt by integrating new components into existing networks that are likely important for the emergence of distinct immunological and physiological functions, which are in turn essential for animal survival in nature, particularly for ticks and other ectoparasites whose intimate host associations and complex hematophagy influence their persistence.

Materials and Methods
Bacteria, mice, and ticks

A clonal low-passage *B. burgdorferi* B31 isolate A3, grown in Barbour-Stoenner-Kelly H (BSK-H) media, was used throughout (21). *A. phagocytophilum* strain HZ was also used,

as detailed (10). Four-to-six-week-old female C3H/HeN mice, *Ifng*-knockout (B6.129S7-*Ifng*^tm1Ts^/J) mice, and *Ifngr1*-knockout (B6.129S7-*Ifngr1*^tm1Agt^/J) mice, as well as 6-to-9-week-old female Dunkin Hartley guinea pigs and 6-week-old inbred female New Zealand white rabbits, were purchased from Charles River Laboratories or Jackson Laboratories. *Ixodes scapularis*, *Dermacentor variabilis*, and *Amblyomma americanum* ticks originating from the tick rearing facility at Oklahoma State University were maintained in the laboratory (21, 37, 38). All experiments were performed in accordance with the guidelines approved by the Institutional Animal Care and Use Committee and the Institutional Biosafety Committee.

Nucleic acid isolation and PCR

Total RNA isolation was performed as previously detailed (39, 40). Assessment of spirochete acquisition or transmission between ticks and C3H mice were performed as described (40, 41). The relative number of targeted gene transcripts in cDNA was measured using reverse transcription quantitative PCR (RT-qPCR) following published methods (42). The oligonucleotide primers used for the RT-qPCR analysis are indicated in table S6. Primers for the detection of various microbial species in the tick gut (43) and expression analyses of various peritrophin genes have been previously described (26). Primers for amplifying tick *Actb* from *D. variabilis* and *A. americanum* were designed as reported earlier (44, 45). The RNAi studies on *D. variabilis* were conducted on the Dome ortholog after cloning and sequencing the gene, which is submitted in GenBank with the nucleotide accession number OP503541.

Recombinant protein expression, purification, and antibody production

Protein induction and purification, as well as the production of polyclonal antibodies, were carried out using previously described methods (46, 47), with the following modifications. Secretory signal peptides and a Flag tag were added to the N-terminal, whereas a polyhistidine tag was linked to the C-terminal. The Dome1 gene was ligated to the pcDNA 3.0 vector using the Gibson Assembly Master Mix (New England Biolabs) following the manufacturer's instructions and transfected into CHO cells using PEI reagent (Polysciences, Inc). G418-resistant clones were selected and analyzed for the secretion of the recombinant Dome1 protein.

Immunoprecipitation and pull-down assays

Recombinant mouse IFN-γ (BioLegend) was immobilized to anti-mouse IFN-γ monoclonal antibody (mAb) (clone R4-6A2, BioLegend) that was conjugated with Protein G-Sepharose 4B resin (Thermo Fisher Scientific). Precleaned whole tick lysates were incubated with the immobilized IFN-γ for 2 hours and bound pro-

teins were then analyzed by mass spectrometry. The anti-mouse IFN-γ mAb conjugated with Protein G-Sepharose 4B resin binding proteins was used as a negative control. For the pulldown assay, purified Dome1-extracellular domain protein was incubated with immobilized mouse IFN-γ, followed by immunoblot analysis (48).

Protein–protein interaction assays

Analysis of IFN-γ interaction with Dome1 and other proteins was performed using a microtiter assay as reported (49). The ability of Dome1 to bind IFN-γ was measured by bio-layer interferometry (BLI) using the Octet Red384 system (ForteBio, Pall Corp.). Data were acquired in kinetics mode with standard settings and analyzed using the Data Analysis software v9.0 (ForteBio, Pall Corp.). Briefly, anti-Penta-HIS (HIS1K) biosensors (ForteBio, Pall Corp.) were prehydrated for 30 min in 200 µl of Kinetics Buffer (KB) (PBS+ 0.02% Tween 20, 0.1% BSA, and 0.05% NaN₃). Dome1 was then loaded onto sensors at a final concentration of 25 nM. IFN-γ was diluted in KB to a final concentration of 5.5 nM to 0.7 µM and a kinetics assay was performed at 30°C. The results were analyzed with a global fit and 2:1 heterogeneous ligand-binding model using reference subtracted sensors with ligand or analyte-only controls, according to the manufacturer's software platform. For protein–protein interactions in vivo, a yeast two-hybrid assay was used as detailed previously (50). AD-Dome1 and BD-IFN-γ constructs were cotransformed into yeast gold strains (Takara Bio Inc.) as per the manufacturer's instructions and were plated on selective double dropout (2DO) media lacking leucine and trypsin and then incubated at 30°C for 3 to 4 days. The colonies were further restreaked on high stringency synthetic 3DO medium missing leucine, trypsin, and histidine. Colony growth was observed for 7 to 14 days.

Quantitative proteomics analysis

Samples for proteomics analysis were prepared as described with minor modifications (51). Processed tick proteins were labeled with the TMTPro 16-plex set (Thermo Fisher Scientific), fractionated with offline high pH, and analyzed using nanoscale liquid chromatography–tandem mass spectrometry (nano LC–MS/MS) with an orbitrap Fusion Lumos mass spectrometer interfaced to an Ultimate3000 nano HPLC system.

Measurement of reactive oxygen species

ROS levels in the tick gut tissues were measured as described (52). Dissected tick samples were incubated with 60 µM dihydroethidium (DHE, Sigma-Aldrich), washed with PBS, and analyzed by confocal immunofluorescence microscopy (ZEISS LSM 800) for red fluorescence, using 10X lens and Zen imaging software (version 2.6), as previously reported (21).

Tick manipulation and infection studies

Gene silencing in ticks was performed according to previously published methods (21, 26) using primers detailed in table S6. For murine infection studies, wild-type C3H, *Ifng*-knockout, or *Ifngr1*-knockout mice were injected with 10^5 *B. burgdorferi* and maintained for 14 days. Microinjected, control, or naïve ticks were allowed to feed on infected mice (25 ticks per mouse). For tick engorgement and transmission studies, each experimental group included two to five animals. The ticks were collected at various time points (24, 48, or 72 hours) or when fully fed, and were then analyzed using RT-qPCR (21). Similarly, groups of 25 adult *I. scapularis* were microinjected using microcapillaries carrying 5 to 10 μl of various dsRNA preparations (4 mg/ml), and infested on rabbit ears. For studies using *D. variabilis* or *A. americanum*, separate groups of nymphs (up to 50 per group) were placed on each individual guinea pig as detailed (53), and allowed to feed to repletion for 7 to 8 days. Parallel groups of ticks were also microinjected using microcapillaries carrying 5 μl of various dsRNA preparations (3 to 5 mg/ml). Some of the partially fed ticks were collected at various time points (24, 48, 72, and 96 hours) and were stored at −80°C before processing for cell proliferation assays, immunoblotting, or RT-qPCR assays. For cell proliferation experiments, partially fed (48 or 72 hours) nymphal ticks were microinjected using microcapillaries carrying 5 μl of 10 mM 5-ethynyl-2′-deoxyuridine (EdU) solution (Thermo Fisher Scientific), incubated for 4 to 5 hours and dissected to isolate gut samples, and fixed overnight with 4% paraformaldehyde in PBS. Following three washes with PBS, samples were permeabilized with acetone for 10 min at room temperature. The samples were subsequently blocked with 5% normal goat serum in PBS for two hours and incubated with Click-iT reaction cocktails (Thermo Fisher Scientific) for 45 min, and subsequently stained with DAPI and processed for confocal immunofluorescence microscopy. Artificial feeding of nymphs was performed as described in previously published methods (54). To induce colitis, groups of 25 nymphs, 2 to 4 weeks after molting, were microinjected using microcapillaries carrying 5 μl of 2% DSS (MP Biomedicals), then allowed to engorge on mice the following day, and processed accordingly.

Microscopy and histological analysis

To localize *B. burgdorferi*, Dome1, phosphohistone H3 (PH3), or other structures including nuclei, within tick organs or cells, the samples were processed for confocal microscopy using published procedures (39). To avoid red—green juxtapositions in immunofluorescence images, the red Alexa Fluor 568 or rhodamine phalloidin signals in some of the samples were converted to an alternate pseudocolor (violet spectrum) in the ZEISS LSM 800 confocal microscope according to the manufacturer's instructions. Dome1 or other primary antibodies were visualized using Alexa 488-labeled anti-rabbit IgG or Alexa 568-labeled anti-mouse or secondary antibodies. The specificity of these secondary antibodies was tested in samples without primary antibodies or in the presence of normal mouse IgG (isotype controls), which did not generate non-specific immunofluorescence signals, as shown in Fig. 1H (see table S7 for a list of all antibodies used in the study). Briefly, tick organs were fixed in 4% paraformaldehyde at 4°C overnight, and permeabilized with acetone for 10 min following three washes with PBS. Samples were blocked with 5% normal goat serum in PBS-T (PBS with 0.05% Tween 20) for 2 hours at room temperature and then incubated with primary antibodies at 4°C overnight. Following three washes with PBS-T, the tissues were incubated overnight with Alexa Fluor secondary antibodies. The cell nuclei or F-actin were stained with DAPI or rhodamine phalloidin, respectively (Thermo Fisher Scientific) and mounted with antifade mounting medium (Thermo Fisher Scientific). Confocal images were acquired using either a 10X dry, 40X water, or 63X oil objective lens and ZEN imaging software (version 2.6, ZEISS). Electron microscopic analyses were performed as detailed earlier (55). The images of whole ticks were captured using a Canon SX720HS digital camera under the Olympus SZ61 microscope. For histology, tick samples were cross-sectioned and subjected to standard hematoxylin and eosin (H&E) staining as reported (40). The stained slides were processed using a Leica Biosystems anatomic pathology scanner and captured using ImageScope software. For quantitative analysis, at least 10 random microscopic areas from three sections were enumerated for cell nuclei. All microscopic analyses were performed in a double-blinded manner.

Microbiome analysis

DNA from ds*GFP*- or ds*Dome1*-microinjected nymphal ticks, either naïve or infected with *B. burgdorferi* (32 ticks per group), was prepared as described (56). Bacterial 16S rDNA amplicons were then generated using barcoded 16S universal primers (515F/806R), sequenced, and analyzed using the QIIME2, version 2020.11 (57). Operational Taxonomic Units were generated using Deblur (58) and assigned to taxonomic units using a pretrained Naïve Bayes classifier on the V3-V4 region of the 16S rRNA sequences from the Greengenes database, release 13.8 (59) at 99% similarity.

Bioinformatics and statistical analysis

Multiple sequence alignments were performed in Jalview 2.11.1.4 and aligned using TCoffee (60) with default running conditions. Homologs to the Dome1 protein were detected using HHPred (MPI Bioinformatics Toolkit) with three iterations of MSA sequence generation with at least 40% minimum coverage (61). UniProt accession IDs were obtained using R (4.0.1) and the packages MAPDB (v0.1) and UniProt.ws (v.2.30.0). Phylogenetic analysis (also see table S8) was performed using either the neighbor-joining method or the maximum likelihood method with 1000 replicate bootstrapping (62, 63) and Interactive Tree of Life (64). The I-TASSER automated modeling suite (65) was used on NIH HPC resources to construct all models. Structures were annotated and visualized using PyMol (Schrödinger, Inc.) and figures were created using BioRender (66). Dome orthologs were predicted by flyBase (67) and the domains and motifs were identified using SMART (68) as well as Pfam and Motif Search (24, 25) databases.

Quantitative results are expressed as means ± standard deviation (SD). The statistical significance of the difference between the mean values of groups was analyzed using the two-tailed Mann–Whitney U or Student's t test and one-way ANOVA methods. Results were analyzed using GraphPad Prism v9 (GraphPad Software Inc.); $P < 0.05$ was considered significant.

REFERENCES AND NOTES

1. P. Parola, D. Raoult, Ticks and tickborne bacterial diseases in humans: An emerging infectious threat. *Clin. Infect. Dis.* **32**, 897–928 (2001). doi: 10.1086/319347; pmid: 11247714

2. J. Perner *et al.*, RNA-seq analyses of the midgut from blood- and serum-fed Ixodes ricinus ticks. *Sci. Rep.* **6**, 36695 (2016). doi: 10.1038/srep36695; pmid: 27824139

3. K. D. McCoy, E. Léger, M. Dietrich, Host specialization in ticks and transmission of tick-borne diseases: A review. *Front. Cell. Infect. Microbiol.* **3**, 57 (2013). doi: 10.3389/fcimb.2013.00057; pmid: 24109592

4. C. Kitsou, E. Fikrig, U. Pal, Tick host immunity: Vector immunomodulation and acquired tick resistance. *Trends Immunol.* **42**, 554–574 (2021). doi: 10.1016/j.it.2021.05.005; pmid: 34074602

5. WHO, Vector-borne diseases. https://www.who.int/mediacentre/factsheets/fs387/en/, (WHO, 2016).

6. D. E. Sonenshine, Range Expansion of Tick Disease Vectors in North America: Implications for Spread of Tick-Borne Disease. *Int. J. Environ. Res. Public Health* **15**, 478 (2018). doi: 10.3390/ijerph15030478; pmid: 29522469

7. C. D. Paddock, R. S. Lane, J. E. Staples, M. B. Labruna, "Changing paradigms for tick-borne diseases in the Americas" in *Global Health Impacts of Vector-Borne Diseases: Workshop Summary* (National Academies Press, 2016), pp. 221–258

8. W. J. Palmer, F. M. Jiggins, Comparative Genomics Reveals the Origins and Diversity of Arthropod Immune Systems. *Mol. Biol. Evol.* **32**, 2111–2129 (2015). doi: 10.1093/molbev/msv093; pmid: 25908671

9. M. Gulia-Nuss *et al.*, Genomic insights into the Ixodes scapularis tick vector of Lyme disease. *Nat. Commun.* **7**, 10507 (2016). doi: 10.1038/ncomms10507; pmid: 26856261

10. D. K. Shaw *et al.*, Infection-derived lipids elicit an immune deficiency circuit in arthropods. *Nat. Commun.* **8**, 14401 (2017). doi: 10.1038/ncomms14401; pmid: 28195158

11. A. A. Smith, U. Pal, Immunity-related genes in Ixodes scapularis—Perspectives from genome information. *Front. Cell. Infect. Microbiol.* **4**, 116 (2014). doi: 10.3389/fcimb.2014.00116; pmid: 25202684

12. S. A. Nichols, W. Dirks, J. S. Pearse, N. King, Early evolution of animal cell signaling and adhesion genes. *Proc. Natl. Acad. Sci. U.S.A.* **103**, 12451–12456 (2006). doi: 10.1073/pnas.0604051103; pmid: 16891419

13. D. A. Harrison, The Jak/STAT pathway. *Cold Spring Harb. Perspect. Biol.* **4**, a011205 (2012). doi: 10.1101/cshperspect.a011205; pmid: 22383755

14. J. J. Sun, J. F. Lan, X. F. Zhao, G. R. Vasta, J. X. Wang, Binding of a C-type lectin's coiled-coil domain to the Domeless receptor directly activates the JAK/STAT pathway in the shrimp immune response to bacterial infection. *PLOS Pathog.* **13**, e1006626 (2017). doi: 10.1371/journal.ppat.1006626; pmid: 28931061

15. D. S. Aaronson, C. M. Horvath, A road map for those who don't know JAK-STAT. *Science* **296**, 1653–1655 (2002). doi: 10.1126/science.1071545; pmid: 12040185

16. P. N. Paradkar, L. Trinidad, R. Voysey, J. B. Duchemin, P. J. Walker, Secreted Vago restricts West Nile virus infection in Culex mosquito cells by activating the Jak-Stat pathway. *Proc. Natl. Acad. Sci. U.S.A.* **109**, 18915–18920 (2012). doi: 10.1073/pnas.1205231109; pmid: 23027947

17. S. C. Herrera, E. A. Bach, JAK/STAT signaling in stem cells and regeneration: From *Drosophila* to vertebrates. *Development* **146**, dev167643 (2019). doi: 10.1242/dev.167643; pmid: 30696713

18. S. Brown, N. Hu, J. C. Hombría, Identification of the first invertebrate interleukin JAK/STAT receptor, the Drosophila gene domeless. *Curr. Biol.* **11**, 1700–1705 (2001). doi: 10.1016/S0960-9822(01)00524-3; pmid: 11696329

19. J. R. Miller et al., A draft genome sequence for the *Ixodes scapularis* cell line, ISE6. *F1000 Res.* **7**, 297 (2018). doi: 10.12688/f1000research.13635.1; pmid: 29707202

20. A. Pires-daSilva, R. J. Sommer, The evolution of signalling pathways in animal development. *Nat. Rev. Genet.* **4**, 39–49 (2003). doi: 10.1038/nrg977; pmid: 12509752

21. A. A. Smith et al., Cross-Species Interferon Signaling Boosts Microbicidal Activity within the Tick Vector. *Cell Host Microbe* **20**, 91–98 (2016). doi: 10.1016/j.chom.2016.06.001; pmid: 27374407

22. L. Boto, Horizontal gene transfer in the acquisition of novel traits by metazoans. *Proc. Biol. Sci.* **281**, 20132450 (2014). doi: 10.1098/rspb.2013.2450; pmid: 24403327

23. Flybase Consortium, Flybase: Gene: Dmel\dome (2022). http://flybase.org/reports/FBgn0043903.

24. T. Paysan-Lafosse et al., InterPro in 2022. *Nucleic Acids Research*, gkac993 (2022). doi: 10.1098/rspb.2013.2450; pmid: 24403327

25. GenomeNet, MOTIF Search (2022); https://www.genome.jp/tools/motif/.

26. S. Narasimhan et al., Gut microbiota of the tick vector *Ixodes scapularis* modulate colonization of the Lyme disease spirochete. *Cell Host Microbe* **15**, 58–71 (2014). doi: 10.1016/j.chom.2013.12.001; pmid: 24439898

27. A. R. Rodrigues et al., Integration of Shh and Fgf signaling in controlling *Hox* gene expression in cultured limb cells. *Proc. Natl. Acad. Sci. U.S.A.* **114**, 3139–3144 (2017). doi: 10.1073/pnas.1620767114; pmid: 28270602

28. N. Pakpour, L. Akman-Anderson, Y. Vodovotz, S. Luckhart, The effects of ingested mammalian blood factors on vector arthropod immunity and physiology. *Microbes Infect.* **15**, 243–254 (2013). doi: 10.1016/j.micinf.2013.01.003; pmid: 23370408

29. S. Luckhart et al., Mammalian transforming growth factor beta1 activated after ingestion by Anopheles stephensi modulates mosquito immunity. *Infect. Immun.* **71**, 3000–3009 (2003). doi: 10.1128/IAI.71.6.3000-3009.2003; pmid: 12761076

30. K. Kasahara et al., Interactions between *Roseburia intestinalis* and diet modulate atherogenesis in a murine model. *Nat. Microbiol.* **3**, 1461–1471 (2018). doi: 10.1038/s41564-018-0272-x; pmid: 30397344

31. D. T. Yuan, A Metagenomic study of the tick midgut. The University of Texas MD Anderson Cancer Center UTHealth Graduate School of Biomedical Sciences Dissertations and Theses, (2010).

32. S. Chou et al., Transferred interbacterial antagonism genes augment eukaryotic innate immune function. *Nature* **518**, 98–101 (2015). doi: 10.1038/nature13965; pmid: 25470067

33. W. Vollmer, D. Blanot, M. A. de Pedro, Peptidoglycan structure and architecture. *FEMS Microbiol. Rev.* **32**, 149–167 (2008). doi: 10.1111/j.1574-6976.2007.00094.x; pmid: 18194336

34. C. W. Sze et al., Study of the response regulator Rrp1 reveals its regulatory role in chitobiose utilization and virulence of *Borrelia burgdorferi*. *Infect. Immun.* **81**, 1775–1787 (2013). doi: 10.1128/IAI.00050-13; pmid: 23478317

35. N. Jia et al., Large-Scale Comparative Analyses of Tick Genomes Elucidate Their Genetic Diversity and Vector Capacities. *Cell* **182**, 1328–1340.e13 (2020). doi: 10.1016/j.cell.2020.07.023; pmid: 32814014

36. S. Barolo, J. W. Posakony, Three habits of highly effective signaling pathways: Principles of transcriptional control by

developmental cell signaling. *Genes Dev.* **16**, 1167–1181 (2002). doi: 10.1101/gad.976502; pmid: 12023297

37. T. J. Schuijt et al., Identification and characterization of Ixodes scapularis antigens that elicit tick immunity using yeast surface display. *PLOS ONE* **6**, e15926 (2011). doi: 10.1371/journal.pone.0015926; pmid: 21246036

38. A. Sajid et al., mRNA vaccination induces tick resistance and prevents transmission of the Lyme disease agent. *Sci. Transl. Med.* **13**, eabj9827 (2021). doi: 10.1126/scitranslmed.abj9827; pmid: 34788080

39. X. Yang, A. A. Smith, M. S. Williams, U. Pal, A dityrosine network mediated by dual oxidase and peroxidase influences the persistence of Lyme disease pathogens within the vector. *J. Biol. Chem.* **289**, 12813–12822 (2014). doi: 10.1074/jbc.M113.538272; pmid: 24662290

40. Q. Bernard et al., Plasticity in early immune evasion strategies of a bacterial pathogen. *Proc. Natl. Acad. Sci. U.S.A.* **115**, E3788–E3797 (2018). doi: 10.1073/pnas.1718595115; pmid: 29610317

41. M. Ye et al., HtrA, a Temperature- and Stationary Phase-Activated Protease Involved in Maturation of a Key Microbial Virulence Determinant, Facilitates Borrelia burgdorferi Infection in Mammalian Hosts. *Infect. Immun.* **84**, 2372–2381 (2016). doi: 10.1128/IAI.00360-16; pmid: 27271745

42. K. Promnares et al., Borrelia burgdorferi small lipoprotein Lp6.6 is a member of multiple protein complexes in the outer membrane and facilitates pathogen transmission from ticks to mice. *Mol. Microbiol.* **74**, 112–125 (2009). doi: 10.1111/j.1365-2958.2009.06853.x; pmid: 19703109

43. S. Narasimhan et al., Modulation of the tick gut milieu by a secreted tick protein favors Borrelia burgdorferi colonization. *Nat. Commun.* **8**, 184 (2017). doi: 10.1038/s41467-017-00208-0; pmid: 28775250

44. P. Sunyakumthorn, N. Petchampai, M. T. Kearney, D. E. Sonenshine, K. R. Macaluso, Molecular characterization and tissue-specific gene expression of Dermacentor variabilis α-catenin in response to rickettsial infection. *Insect Mol. Biol.* **21**, 197–204 (2012). doi: 10.1111/j.1365-2583.2011.01126.x; pmid: 22221256

45. R. L. Bullard, Characterization of Glycine Rich Proteins From the Salivary Glands of the Lone Star Tick Amblyomma americanum. (The University of Southern Mississippi Dissertations 339, 2016); https://aquila.usm.edu/dissertations/339

46. T. Kariu et al., BB0323 and novel virulence determinant BB0238: Borrelia burgdorferi proteins that interact with and stabilize each other and are critical for infectivity. *J. Infect. Dis.* **211**, 462–471 (2015). doi: 10.1093/infdis/jiu460; pmid: 25139020

47. T. Kariu, A. Smith, X. Yang, U. Pal, A chitin deacetylase-like protein is a predominant constituent of tick peritrophic membrane that influences the persistence of Lyme disease pathogens within the vector. *PLOS ONE* **8**, e78376 (2013). doi: 10.1371/journal.pone.0078376; pmid: 24147133

48. X. Yang et al., Characterization of multiprotein complexes of the *Borrelia burgdorferi* outer membrane vesicles. *J. Proteome Res.* **10**, 4556–4566 (2011). doi: 10.1021/pr200395b; pmid: 21875077

49. U. Pal et al., Attachment of Borrelia burgdorferi within *Ixodes scapularis* mediated by outer surface protein A. *J. Clin. Invest.* **106**, 561–569 (2000). doi: 10.1172/JCI9427; pmid: 10953031

50. U. Pal et al., TROSPA, an Ixodes scapularis receptor for Borrelia burgdorferi. *Cell* **119**, 457–468 (2004). doi: 10.1016/j.cell.2004.10.027; pmid: 15537536

51. X. Yang et al., Analysis of Borrelia burgdorferi Proteome and Protein-Protein Interactions. *Methods Mol. Biol.* **1690**, 259–277 (2018). doi: 10.1007/978-1-4939-7383-5_19; pmid: 29032550

52. A. Vaccaro et al., Sleep Loss Can Cause Death through Accumulation of Reactive Oxygen Species in the Gut. *Cell* **181**, 1307–1328.e15 (2020). doi: 10.1016/j.cell.2020.04.049; pmid: 32502393

53. M. L. Levin, G. E. Zemtsova, L. F. Killmaster, A. Snellgrove, L. B. M. Schumacher, Vector competence of *Amblyomma americanum* (Acari: Ixodidae) for *Rickettsia rickettsii*. *Ticks Tick Borne Dis.* **8**, 615–622 (2017). doi: 10.1016/j.ttbdis.2017.04.006; pmid: 28433728

54. X. Yang et al., A novel tick protein supports integrity of gut peritrophic matrix impacting existence of gut microbiome and Lyme disease pathogens. *Cell. Microbiol.* **23**, e13275 (2021). doi: 10.1111/cmi.13275; pmid: 33006213

55. E. R. Fischer, B. T. Hansen, V. Nair, F. H. Hoyt, D. W. Dorward, Scanning electron microscopy. *Curr Protoc Microbiol* mc02b02s25 (2012) .doi: 10.1002/9780471729259.mc02b02s25

56. S. T. Singh et al., Diversity and phylogenetic analysis of endosymbiotic bacteria from field caught Bemisia tabaci from different locations of North India based on 16S rDNA library screening. *Infect. Genet. Evol.* **12**, 411–419 (2012). doi: 10.1016/j.meegid.2012.01.015; pmid: 22293464

57. E. Bolyen et al., Reproducible, interactive, scalable and extensible microbiome data science using QIIME 2. *Nat. Biotechnol.* **37**, 852–857 (2019). doi: 10.1038/s41587-019-0209-9; pmid: 31341288

58. A. Amir et al., Deblur Rapidly Resolves Single-Nucleotide Community Sequence Patterns. *mSystems* **2**, e00191–e16 (2017). doi: 10.1128/mSystems.00191-16; pmid: 28289731

59. T. Z. DeSantis et al., Greengenes, a chimera-checked 16S rRNA gene database and workbench compatible with ARB. *Appl. Environ. Microbiol.* **72**, 5069–5072 (2006). doi: 10.1128/AEM.03006-05; pmid: 16820507

60. C. Notredame, D. G. Higgins, J. Heringa, T-Coffee: A novel method for fast and accurate multiple sequence alignment. *J. Mol. Biol.* **302**, 205–217 (2000). doi: 10.1006/jmbi.2000.4042; pmid: 10964570

61. F. Gabler et al., Protein Sequence Analysis Using the MPI Bioinformatics Toolkit. *Curr. Protoc. Bioinformatics* **72**, e108 (2020). doi: 10.1002/cpbi.108; pmid: 33315308

62. S. Kumar, G. Stecher, M. Li, C. Knyaz, K. Tamura, MEGA X: Molecular Evolutionary Genetics Analysis across Computing Platforms. *Mol. Biol. Evol.* **35**, 1547–1549 (2018). doi: 10.1093/molbev/msy096; pmid: 29722887

63. G. Stecher, K. Tamura, S. Kumar, Molecular Evolutionary Genetics Analysis (MEGA) for macOS. *Mol. Biol. Evol.* **37**, 1237–1239 (2020). doi: 10.1093/molbev/msz312; pmid: 31904846

64. I. Letunic, P. Bork, Interactive Tree Of Life (iTOL) v4: Recent updates and new developments. *Nucleic Acids Res.* **47**, W256–W259 (2019). doi: 10.1093/nar/gkz239; pmid: 30931475

65. Zhang Lab, Univ. of Michigan, I-TASSER: Protein Structure and Function Predictions (2022); https://zhanglab.ccmb.med.umich.edu/I-TASSER.

66. Biorender (2022); www.biorender.com.

67. Flybase Consortium, Flybase: A Database of *Drosophila* Genes & Genomes (2022); http://flybase.org.

68. J. Schultz, F. Milpetz, P. Bork, C. P. Ponting, SMART, a simple modular architecture research tool: Identification of signaling domains. *Proc. Natl. Acad. Sci. U.S.A.* **95**, 5857–5864 (1998). doi: 10.1073/pnas.95.11.5857; pmid: 9600884

SUPPLEMENTARY MATERIALS

science.org/doi/10.1126/science.abl3837
Figs. S1 to S21
Tables S1 to S8
MDAR Reproducibility Checklist

RESEARCH ARTICLE SUMMARY

NEURODEGENERATION

ApoE isoform– and microbiota-dependent progression of neurodegeneration in a mouse model of tauopathy

Dong-oh Seo, David O'Donnell, Nimansha Jain, Jason D. Ulrich, Jasmin Herz, Yuhao Li, Mackenzie Lemieux, Jiye Cheng, Hao Hu, Javier R. Serrano, Xin Bao, Emily Franke, Maria Karlsson, Martin Meier, Su Deng, Chandani Desai, Hemraj Dodiya, Janaki Lelwala-Guruge, Scott A. Handley, Jonathan Kipnis, Sangram S. Sisodia, Jeffrey I. Gordon, David M. Holtzman*

INTRODUCTION: Alzheimer's disease (AD) is characterized by early deposition of amyloid-β (Aβ) plaques followed by pathological tau accumulation. Although Aβ is a necessary factor in AD pathogenesis, its accumulation in and of itself is insufficient for neurodegeneration and cognitive decline. By contrast, pathological tau accumulation is closely linked with neurodegeneration and cognitive decline in AD and primary tauopathies. Alterations of the gut microbiota have been reported in AD, which suggests that the microbiota may contribute to AD progression. Animal studies to date have focused mainly on how gut microbiota alterations affect Aβ pathology and not tauopathy and neurodegeneration. Additionally, recent studies have suggested that apolipoprotein E (ApoE) isoforms, which strongly influence AD risk and regulate tau-mediated neurodegeneration, differentially affect the gut microbiota. Therefore, further investigations to characterize the contribution of the gut microbiota to tauopathy and neurodegeneration are important.

RATIONALE: We assess the hypothesis that the gut microbiota regulates tau pathology and tau-mediated neurodegeneration in an ApoE isoform–dependent manner. A mouse model of tauopathy (*P301S* tau transgenic mice) expressing human ApoE isoforms (ApoE3 and ApoE4), referred to as TE3 and TE4, was subjected to the manipulation of the gut microbiota using two approaches: (i) being raised in germ-free (GF) conditions and (ii) short-term antibiotic (ABX) treatment early in life. Animals were fed a standard mouse chow diet ad libitum until euthanasia at 40 weeks of age, when this mouse model typically has severe brain atrophy.

RESULTS: The gut microbiota manipulations resulted in a notable reduction of tau pathology and neurodegeneration in an ApoE isoform–dependent manner. Both male and female GF TE4 mice showed a marked decrease in brain atrophy compared with conventionally raised (Conv-R) mice. Conv-R ABX-treated TE3 mice had significantly milder hippocampal atrophy compared with controls. ABX-treated TE4 animals showed trends of milder hippocampal atrophy, but the effect did not achieve statistical significance. These phenotypic effects of ABX treatment were not observed in females.

Male GF TE4 mice and male ABX-treated TE3 mice showed significantly lower phosphorylated tau (p-tau) in the hippocampus compared with their controls. Astrocyte and microglial morphology and transcriptomic analysis revealed that the manipulation of the gut microbiota drives glial cells to a more homeostatic-like state, which indicates that gut microbiota strongly influence neuroinflammation and tau-mediated neurodegeneration. Microbiome and metabolite analysis suggests that microbially produced short-chain fatty acids (SCFAs) are mediators of the neuroinflammation-neurodegeneration axis. Supplementation of SCFAs to GF TE4 mice resulted in more reactive glial morphologies and gene expression as well as increased p-tau pathology.

CONCLUSION: The findings reveal mechanistic and translationally relevant interrelationships between the microbiota, the immune response, and tau-mediated neurodegeneration. ApoE-associated gut microbiota targeting may provide an avenue to further explore the prevention or treatment of AD and primary tauopathies. ∎

P301S tau transgenic mice expressing human APOE (TE mice). The dysregulated gut-brain axis and its effect on tauopathy and tau-mediated neurodegeneration. Dysbiosis, unbalanced gut microbiota composition (bottom center), contributes to tau-mediated neurodegeneration by generating bacterial metabolites (e.g., SCFAs) that influence peripheral immune cells. These cells promote central nervous system (CNS) inflammation and contribute to tau aggregation and neurodegeneration. Short-term antibiotics (bottom right) or germ-free conditions (bottom left) reshape or eliminate gut microbiota and reduce their metabolites. These microbiota manipulations influence effects of peripheral immune cells on CNS inflammation and tau-mediated neurodegeneration. ApoE4 in the CNS exacerbates local toxicity and blood-brain barrier dysfunction.

S **READ THE FULL ARTICLE AT**
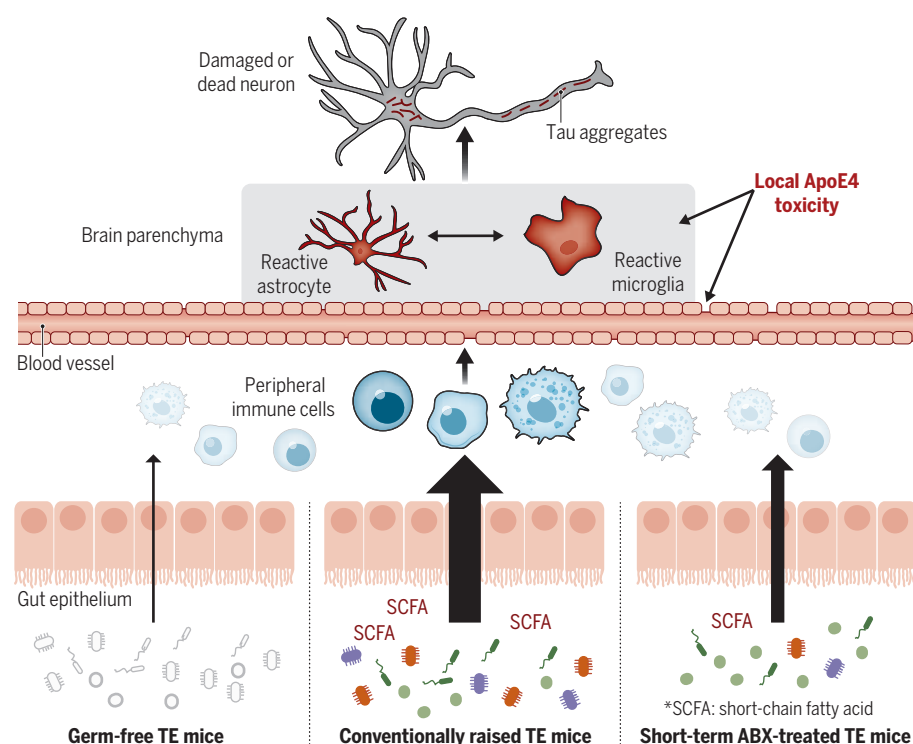https://doi.org/10.1126/science.add1236

NEURODEGENERATION

ApoE isoform– and microbiota-dependent progression of neurodegeneration in a mouse model of tauopathy

Dong-oh Seo[1], David O'Donnell[2], Nimansha Jain[1], Jason D. Ulrich[1], Jasmin Herz[3,4], Yuhao Li[5], Mackenzie Lemieux[3,4], Jiye Cheng[2], Hao Hu[1], Javier R. Serrano[1], Xin Bao[1], Emily Franke[1], Maria Karlsson[2], Martin Meier[2], Su Deng[2], Chandani Desai[2], Hemraj Dodiya[6], Janaki Lelwala-Guruge[2], Scott A. Handley[4], Jonathan Kipnis[3,4], Sangram S. Sisodia[6], Jeffrey I. Gordon[2,4], David M. Holtzman[1,7]*

Tau-mediated neurodegeneration is a hallmark of Alzheimer's disease. Primary tauopathies are characterized by pathological tau accumulation and neuronal and synaptic loss. Apolipoprotein E (ApoE)–mediated neuroinflammation is involved in the progression of tau-mediated neurodegeneration, and emerging evidence suggests that the gut microbiota regulates neuroinflammation in an APOE genotype–dependent manner. However, evidence of a causal link between the microbiota and tau-mediated neurodegeneration is lacking. In this study, we characterized a genetically engineered mouse model of tauopathy expressing human ApoE isoforms reared under germ-free conditions or after perturbation of their gut microbiota with antibiotics. Both of these manipulations reduced gliosis, tau pathology, and neurodegeneration in a sex- and ApoE isoform–dependent manner. The findings reveal mechanistic and translationally relevant interrelationships between the microbiota, neuroinflammation, and tau-mediated neurodegeneration.

Alzheimer's disease (AD) is a fatal, progressive neurodegenerative disease, characterized by early deposition of amyloid-β (Aβ) plaques followed by pathological tau accumulation in the limbic system and neocortex, the latter of which is strongly linked to neuronal loss and brain atrophy (*1*). Evidence is mounting that there is a link between gut microbiota perturbations and Aβ deposition, potentially through effects on neuroinflammation and metabolic homeostasis (*2–4*). However, the contribution of the gut microbiota to tau-mediated neurodegeneration, which is strongly correlated with cognitive decline in AD and other tauopathies, has not been characterized. Furthermore, recent studies have reported that the configuration of the gut microbiota is differentially affected by apolipoprotein E (APOE), the strongest genetic risk factor for AD and a known regulator of tau-mediated neurodegeneration (*5*, *6*). We used a mouse model of tauopathy with animals ex-pressing different human ApoE isoforms to explore the hypothesis that the gut microbiota regulates tau-mediated neurodegeneration in an ApoE isoform–dependent manner.

TE4 germ-free mice are protected against tau-mediated neurodegeneration

We began by rearing genetically engineered C57BL6J mice containing a *P301S* human tau-expressing transgene and a knocked-in human *APOE4* gene (*Tau/APOE4*, abbreviated TE4) (*7*) under germ-free (GF) conditions. A second group of TE4 mice was exposed to microbes originating from their TE4 dams beginning at birth; these conventionally raised (Conv-R) mice were subsequently maintained under specified pathogen-free conditions in a mouse barrier facility. A third group of mice was reared under GF conditions until 12 weeks of age, when they received an oral gavage of fecal microbiota sampled from 40-week-old Conv-R TE4 (Ex-GF) mice (Fig. 1A). All mice were given a standard rodent chow rich in plant polysaccharides. We euthanized animals from all groups at 40 weeks of age—a time point when Conv-R TE4 mice display substantially greater tau-mediated neurodegeneration compared with (i) Conv-R P301S mice harboring other human APOE isoforms in their genomes or (ii) Conv-R animals lacking both mouse and human APOE (*7*, *8*). Unless otherwise indicated, all analyses were performed using biospecimens obtained from 40-week-old mice.

Conv-R male and female TE4 mice displayed severe regional brain atrophy, manifested by hippocampal volume loss and lateral ventricle (LV) enlargement relative to E4 mice lacking the tau transgene (Fig. 1, B and D). However, GF male and female TE4 mice had significant preservation of brain tissue compared with their Conv-R TE4 counterparts, as judged by hippocampal and LV sizes as well as by measurements of hippocampal neuronal layer thickness—a direct estimate of neuronal loss (fig. S1, C and D). Comparison of these areas of the brain in 12- and 40-week-old TE4 mice provided evidence that the protective effect produced by the GF state reflected a blockade of progression of neurodegeneration (fig. S1, E and F). We did not detect rescue from neurodegeneration in the entorhinal-piriform cortex of GF TE4 animals (fig. S1G).

The GF rescue from neurodegeneration was reversed when animals were colonized with fecal microbial communities harvested from sex-matched Conv-R TE4 animals (fig. S1, H to J); 28 weeks after colonization, 40-week-old Ex-GF mice exhibited hippocampal and LV volumes and hippocampal neuronal layer thicknesses comparable to those documented in Conv-R mice (Fig. 1, B and D, and fig. S1D). Staining brain sections with a phospho-tau antibody (AT8) revealed a marked decrease in tau phosphorylation in 40-week-old GF compared with 40-week-old Conv-R mice (Fig. 1, C and E). By contrast, we did not observe any differences in hippocampal AT8 staining between 12-week-old GF and 12-week-old Conv-R mice (fig. S1, K and L). Thus, the microbiota greatly affects the later appearance of tau-mediated neurodegeneration.

TE4 GF mice exhibit reduced reactive gliosis

Although elevated levels of pathological phosphorylated tau (p-tau) may directly contribute to neuronal degeneration and death, there is strong evidence that reactive microglia and astrocytes are required for tau-mediated neurodegeneration (*7*, *9–11*). Recent studies have indicated that the gut microbiota contribute to glial functions (*12–14*), leading us to hypothesize that the microbiota may modulate tau-mediated neurodegeneration in our model by altering glial reactivity. Therefore, we first stained brain sections with markers for astrocytes and microglia [glial fibrillary acidic protein (GFAP), Iba1, and CD68]. Consistent with the amount of degeneration, expression of all these glial markers in the hippocampus was strongly reduced in GF compared with Conv-R male mice (Fig. 2, A and B). Furthermore, analysis of glial morphology in the hippocampus (fig. S2, A to D) revealed that astrocytes in GF mice were larger with more branched processes compared with those in Conv-R mice. These morphological alterations of glial cells in GF mice were also observed at 12 weeks of age, when there is mild p-tau

[1]Department of Neurology, Hope Center for Neurological Disorders, Washington University School of Medicine, St. Louis, MO, USA. [2]The Edison Family Center for Genome Sciences and Systems Biology and the Center for Gut Microbiome and Nutrition Research, Washington University School of Medicine, St. Louis, MO, USA. [3]Center for Brain Immunology and Glia (BIG), Washington University School of Medicine, St. Louis, MO, USA. [4]Department of Pathology and Immunology, Washington University School of Medicine, St. Louis, MO, USA. [5]Division of Infectious Diseases, Department of Medicine, Washington University School of Medicine, St. Louis, MO, USA. [6]Department of Neurobiology, The University of Chicago, Chicago, IL, USA. [7]Knight Alzheimer Disease Research Center, Washington University School of Medicine, St. Louis, MO, USA.
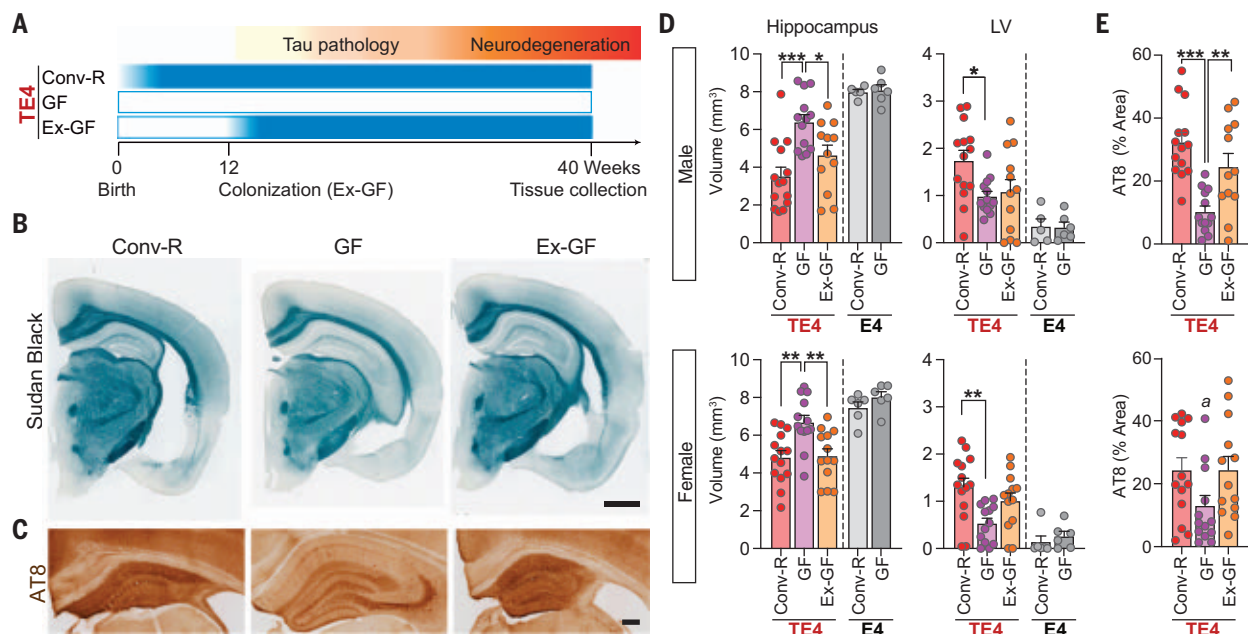*Corresponding author. Email: holtzman@wustl.edu

Fig. 1. TE4 GF mice are protected against tau-mediated neurodegeneration.
(**A**) Experimental design. TE4 mice were reared in a vivarium in a specified pathogen-free state (Conv-R; $n = 14$ per sex) or under GF conditions in gnotobiotic isolators (GF; $n = 13$ to 14 per sex) until they were euthanized at 40 weeks of age. A separate group of 12-week-old GF mice were colonized with fecal microbiota harvested from sex-matched 40-week-old Ex-GF mice ($n = 12$ per sex). (**B**) Representative images of 40-week-old male Conv-R, GF, and Ex-GF mouse brain sections stained with Sudan black. Scale bar, 1 mm. (**C**) Representative images of p-tau staining (AT8) in the hippocampus of male mice. Scale bar, 250 μm.

(**D**) Volumes of the hippocampus (left) and LVs (right) in male (top) and female (bottom) mice. E4 represents APOE4 knock-in mice that lack a P301S tau transgene. (**E**) Percentage area covered by AT8 staining in sections prepared from the hippocampus of 40-week-old male (top) and female (bottom) TE4 mice. Data are presented as mean values ± SEMs. Statistical significance was defined using a one-way ANOVA with Tukey's post hoc test. *$P < 0.05$; **$P < 0.01$; ***$P < 0.001$. The letter "*a*" in (E) indicates that, in the post hoc analysis, Tukey did not reveal significant differences, but least significant difference (LSD) showed $P < 0.05$ (GF versus Conv-R and Ex-GF). See table S1 for full statistical results.

pathology but no evidence for neurodegeneration (fig. S3).

Analysis of differential gene expression using nCounter (NanoString Technologies) showed that at 40 weeks of age, the GF state was associated with down-regulation of genes related to innate immune responses (including *sox9* and *cx3cr1*), apoptosis, and autophagy and up-regulation of genes related to neuronal activity and epigenetics (fig. S4A and data S2). No significant differences in gene expression were detected when comparing Conv-R with Ex-GF mice (data S3). Weighted gene coexpression network analysis using the Nanostring data identified five coexpression modules, two of which (modules Grey and Turquoise) exhibited significant correlation with either microbial colonization status or hippocampal size (fig. S4, B to D). Gene ontology (GO) analysis demonstrated that module Grey was enriched for genes related to epigenetics, T cell–mediated immunity (e.g., *Foxp3*, which is associated with regulatory T cells), and gliogenesis (e.g., *Tmem119*, which is typically up-regulated in homeostatic microglia). Module Turquoise was enriched for genes related to cytokine production, cell death, and defense response, including *APOE* (fig. S4, E and F, and data S4). Analysis of eigengene (the first principal component of the

expression matrix of the corresponding module) expression in modules Grey and Turquoise by individual animal verified that increased and decreased expression, respectively, in these modules were tightly linked to the protective effect of the GF condition (fig. S4, G to J). Thus, GF conditions affect microglia and astrocyte reactivity or activation associated with tau-mediated neurodegeneration.

Antibiotic-induced gut microbiota perturbation protects against tau-mediated neurodegeneration

To test whether the gut microbiota regulates tau-mediated neurodegeneration in an ApoE isoform–dependent manner, we treated groups of Conv-R TE4 mice, *P301S* tau transgenic mice expressing human APOE3 (TE3), and P301S tau animals without APOE (TEKO) with an antibiotic cocktail (ABX) composed of kanamycin, gentamicin, colistin, metronidazole, and vancomycin (*4*). Gavage with the antibiotic cocktail (or water in the case of controls) occurred daily from postnatal days 16 to 22. The fecal microbiota was serially sampled, and animals were euthanized at 40 weeks of age (Fig. 3A). The short-term ABX treatment produced a marked, immediate decrease in the total number of viable bacteria; although this

decrease in viability was transient, culture-independent methods disclosed that the proportional representation of various bacterial taxa in the microbiota of ABX-treated groups remained different from controls throughout life (see fig. S5, A to E, and below).

Volumetric analysis revealed that 40-week-old male mice in the H_2O-treated control groups (TE3-H_2O and TE4-H_2O animals) had statistically significant hippocampal atrophy compared with mice lacking the APOE gene (TEKO) (Fig. 3, B and C) (*8*). However, TE3-ABX but not TE4-ABX mice showed significant hippocampal preservation relative to controls. Enlargement of the LV and entorhinal-piriform cortical atrophy were also significantly attenuated by ABX treatment independent of APOE genotype, but the degree of ABX effect was higher in TE3 compared with TE4 mice in general (i.e., the $\log_2$ fold changes by ABX in the LV size were −0.86 in TE3 and −0.34 in TE4 mice; the $\log_2$ fold changes by ABX in the entorhinal-piriform cortex size were 0.57 in TE3 and 0.36 in TE4 mice; Fig. 3C and fig. S5F). ABX treatment also prevented thinning of hippocampal neuronal cell layers independent of APOE genotype (fig. S5G). These phenotypic effects of ABX treatment were seen in TE3 and TE4 males but not in females,

Fig. 2. TE4 GF mice exhibit reduced reactive gliosis.
(**A**) Representative immunofluorescence images of hippocampal sections from 40-week-old male Conv-R, GF, and Ex-GF mice stained with antibodies to GFAP (red), Iba-1 (green), and CD68 (cyan) as well as DAPI (blue). Scale bar, 25 μm. GCL, granule cell layer. (**B**) Percent of the area of sections taken from the hippocampus covered by GFAP (left), Iba-1 (middle), and CD68 (right) staining. Mean values ± SEMs are shown (n = 12 to 14 per group). Statistical significance was defined by one-way ANOVA with Tukey's post hoc test. *P < 0.05; ***P < 0.001. See table S1 for full statistical results.
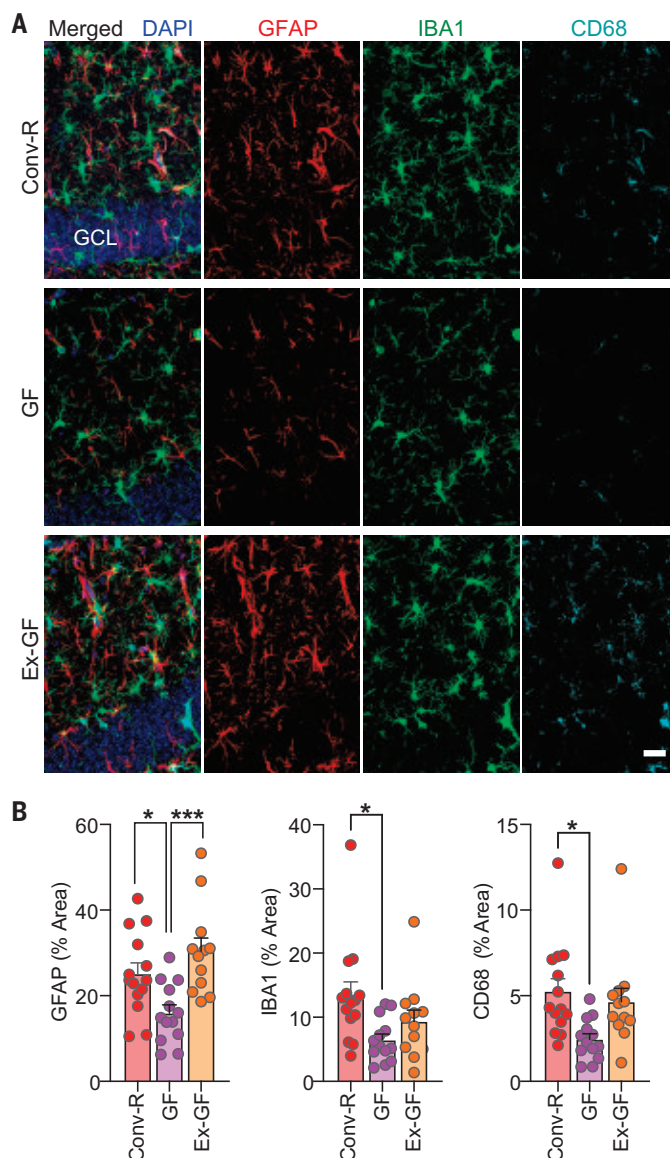
except in the case of the CA1 pyramidal layer, which was slightly, albeit significantly, thicker in ABX-treated males and females (fig. S5G). In concert with hippocampal brain atrophy, male TE3-ABX mice showed significantly lower AT8 staining relative to male TE3-H$_2$O mice (Fig. 3, D and E).

ABX treatment did not influence brain volume or early tau pathology in 12-week-old male TE3 mice (fig. S5, H to K). At 40 weeks of age, analysis of male cortical tissue also revealed that ABX treatment reduced p-tau levels in the detergent-soluble fraction (RIPA) and both p-tau and human tau levels in the insoluble fraction (FA) across the three APOE genotype groups (fig. S6). Furthermore, nest-building behaviors, known to be sensitive to hippocampus damage and neurodegenerative disease (15), showed significant improvement in male TE3 and TE4 mice treated with ABX,

which correlated with hippocampal volumes (fig. S7).

Antibiotic treatment alters astrocyte and microglial gene expression and morphological responses

Single-nucleus RNA sequencing (snRNA-seq) of hippocampal tissue collected from Conv-R 40-week-old males that belonged to all three APOE genotype groups and were not exposed to antibiotics identified 20 distinct clusters, which were categorized into excitatory and inhibitory neurons, astrocytes, microglia, oligodendrocytes, and oligodendrocyte progenitor cells (fig. S8, A and B). Cell proportion analysis showed that certain neuronal populations (e.g., exc1, exc2, and exc5) were reduced in the presence of tau pathology and expanded again with ABX treatment, in agreement with the hippocampal volumetric data. The astrocyte population was reduced twofold with ABX in the

presence of tau pathology. The microglial population, which expanded approximately sevenfold (by proportion) with tau pathology, was reduced two- to threefold with ABX treatment.

The astrocyte cluster was rescaled and reclustered, revealing four subclusters (astro0 to astro3; Fig. 4A and fig. S8C). Reclustering of the microglia cluster identified three subclusters (micro0 to micro2; Fig. 4H and fig. S8D). Tau pathology resulted in a strong shift from astro0 to astro1 and micro0 to micro1. ABX treatment reversed these shifts in TE3 but not TE4 male mice, consistent with a stronger protective effect with ABX treatment in TE3 compared with TE4 male mice. Further differentially expressed gene (DEG) analysis between two clusters associated with pathological shifts revealed that the top up-regulated pathways in astrocyte subcluster DEG (astro1 versus astro0; data S5) were associated with GO terms related to gliogenesis and cellular chemical homeostasis (Fig. 4B), whereas the top up-regulated pathways in the microglial subcluster DEG (micro1 versus micro0; data S6) were associated with GO terms related to cell activation and small guanosine triphosphatase (GTPase)–mediated signal transduction (Fig. 4I). We used quantitative polymerase chain reaction (qPCR) to verify up-regulation of a subset of astro1 genes (e.g., *Gfap* and *Vim*) and micro1 genes (e.g., *Arhgap25* and *Itgax*) (fig. S9, A and B). An alteration of glial gene expression was also observed in ABX-treated TE3 mice at 12 weeks of age, well before neurodegeneration (fig. S9C). Thus, the gut microbiota regulates expression of genes that are involved in reactive gliosis.

Reactive gliosis is a complex process that involves changes in gene expression and morphological remodeling. In general, homeostatic glial cells display highly branched thin processes in the homeostatic state, but in activated cells, processes become shorter as they retract and become hypertrophic (16). To further assess reactive gliosis, we performed GFAP, Iba1, and CD68 immunostaining. Although the coverage area of the immunostaining did not reveal significant ABX effects (fig. S10A), morphometric analysis revealed that ABX drove astrocytes and microglia to a more homeostatic-like morphological state (e.g., increased length of processes and size of cells) in male TE3 mice but not in male TE4 and TEKO, female TE3, or male 12-week-old TE3 mice (Fig. 4, C to G and J to L, and fig. S10, B to K). Thus, ABX-induced perturbation of the microbiota protects against tau-mediated neurodegeneration most strongly in male TE3 mice, and this effect is manifested by changes in multiple cell types, including astrocytes and microglia.

Antibiotic treatment reshapes the bacterial communities and reduces short-chain fatty acids

The microbiota perturbation induced by ABX was evidenced by (i) measurements of cecal
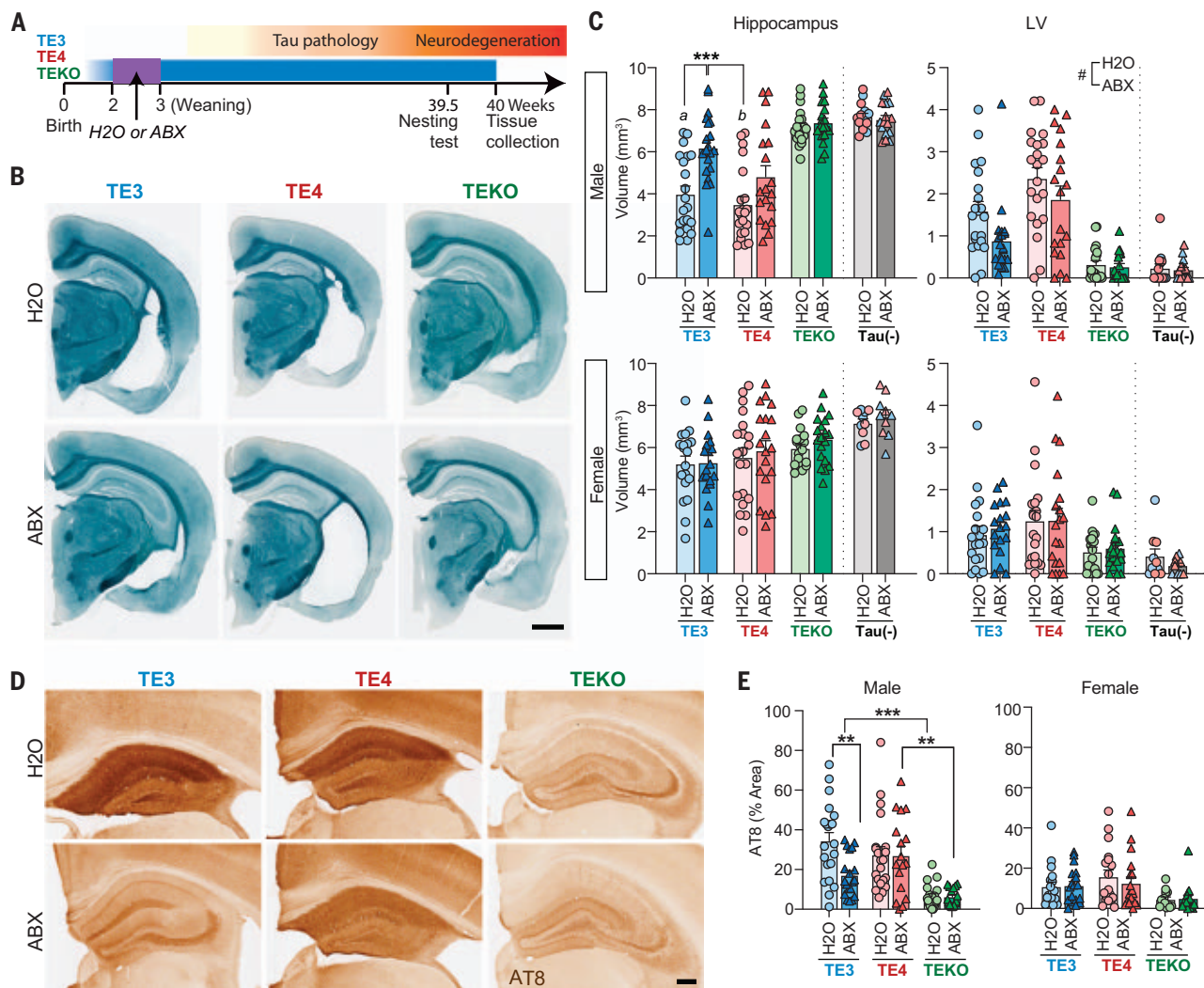
Fig. 3. Antibiotic treatment and perturbation of the gut microbiota markedly protects against tau-mediated neurodegeneration in a sex- and ApoE isoform–dependent manner. (**A**) Male and female TE3, TE4, and TEKO transgenic mice (*n* = 18 to 21 per group) received a gastric gavage of a combination of antibiotics (ABX) from postnatal days 16 to 22. Controls were gavaged with water (H₂O). Mice were euthanized at 40 weeks of age. (**B**) Representative images of male TE3, TE4, and TEKO mouse brain sections stained with Sudan black. Scale bar, 1 mm. (**C**) Volumes of the hippocampus (left) and LVs (right) in male (top) and female (bottom) animals. Tau(-) represents APOE3 (blue) or APOE4 (red) knock-in mice that lack a P301S tau transgene. (**D**) Representative images of p-tau staining (AT8) of hippocampal sections prepared from male mice. Scale bar, 250 μm. (**E**) Percentage of the area covered by AT8 staining of hippocampal sections prepared from male (left) and female (right) mice. Mean values ± SEMs are shown. Statistical significance defined by two-way ANOVA with Tukey's post hoc test. *P < 0.05; **P < 0.01; ***P < 0.001. Statistical significance of the main effects of treatments (H₂O versus ABX) were indicated as #P < 0.05. In (C) (male hippocampus), *a* indicates statistical significance compared with TEKO-H₂O and TEKO-ABX groups (P < 0.001), and *b* indicates statistical significance compared with TE3-ABX, TEKO-H₂O, and TEKO-ABX (P < 0.001). See table S1 for full statistical results.

weight compared with body weight (known to be markedly increased in GF compared with Conv-R animals and rapidly reduced in Ex-GF mice; fig. S1, A and B, and fig. S5, D and E) and (ii) culture-independent analysis of the relative abundances of bacterial taxa in feces. The latter approach was based on sequencing PCR amplicons generated from variable region 4 of bacterial 16S ribosomal RNA (rRNA) genes [amplicon sequence variants (ASVs)] and grouping these ASVs into taxonomic bins. Alterations in alpha and beta diversity as well

as the representation of phylum- and genus-level groups are summarized in figs. S11 to S13. Phylum- and genus-level changes in ABX-treated groups remained different from H₂O-treated controls up to the time of euthanasia (fig. S11, D and E).

Linear discriminant analysis revealed that the members of the genera *Helicobacter*, *Ruminococcus*, and *Butyricicoccus* had lower relative abundance in the fecal microbiota of ABX-treated groups across male APOE isoform groups (Fig. 5A and fig. S12, A to C) but not in female TE3

mice (Fig. 5B and fig. S13D). Recent studies have suggested that the microbiota modulates glial activation through the production of microbial metabolites, such as short-chain fatty acids (SCFAs) (*12*, *13*). *Ruminococcus* and *Butyricicoccus* are associated with SCFA production. Also, the relative abundance of several bacterial family-level taxa known to produce SCFAs, such as *Ruminococcaceae* and *Lachnospiraceae*, were reduced with ABX across APOE genotypes (fig. S12D). The representation of these taxa was greater in male compared with

Fig. 4. Glial transcriptional and morphological responses to tau pathology are regulated by ABX treatment. (**A**) (Left) UMAP plot of a reclustered astrocyte population that identifies four distinguishable clusters (astrocyte cluster 0 to 3). (Right) Relative frequency of all astrocyte clusters per genotype and treatment. (**B**) GO biological process terms significantly enriched among DEGs (astrocyte cluster 1 versus 0). (**C**) (Left) Representative images of male TE3 mouse brain sections stained with GFAP and DAPI. (Right) Traces of GFAP expression generated using Simple Neurite Tracer, corresponding to the images on the left. Scale bar, 10 μm. (**D** to **G**) Morphometric analysis of astrocyte process lengths (D), size of GFAP+ astrocytes (from Convex Hull analysis) (E), total number of process intersections (F), and the end radius (from Sholl analysis) (G). (**H**) (Left) UMAP plot of the reclustered microglial population showing three distinguishable clusters (microglia clusters 0, 1, and 2). (Right) Relative frequency (proportion of nuclei) of all microglia clusters per genotype and treatment group. (**I**) GO terms enriched in up-regulated and down-regulated DEGs (microglia cluster 1 versus 0). (**J**) Imaris-based automatic reconstruction image of Iba1+ microglia. Scale bar, 10 μm. (**K** and **L**) Morphometric analysis of process lengths (K) and the number of branches (L) of Iba1+ microglial cells in male TE3, TE4, and TEKO mice. Tau(-) represents APOE3 (blue) or APOE4 (red) knock-in mice that lack a P301S transgene. Mean values ± SEMs are presented with statistical significance defined by two-way ANOVA with Tukey's post hoc test. *$P < 0.05$; **$P < 0.01$; ***$P < 0.001$. *a* and *b* indicate statistical significance compared with TEKO-H$_2$O (*a*) and TEKO-ABX (*b*) ($P < 0.05$). See table S1 for full statistical results.
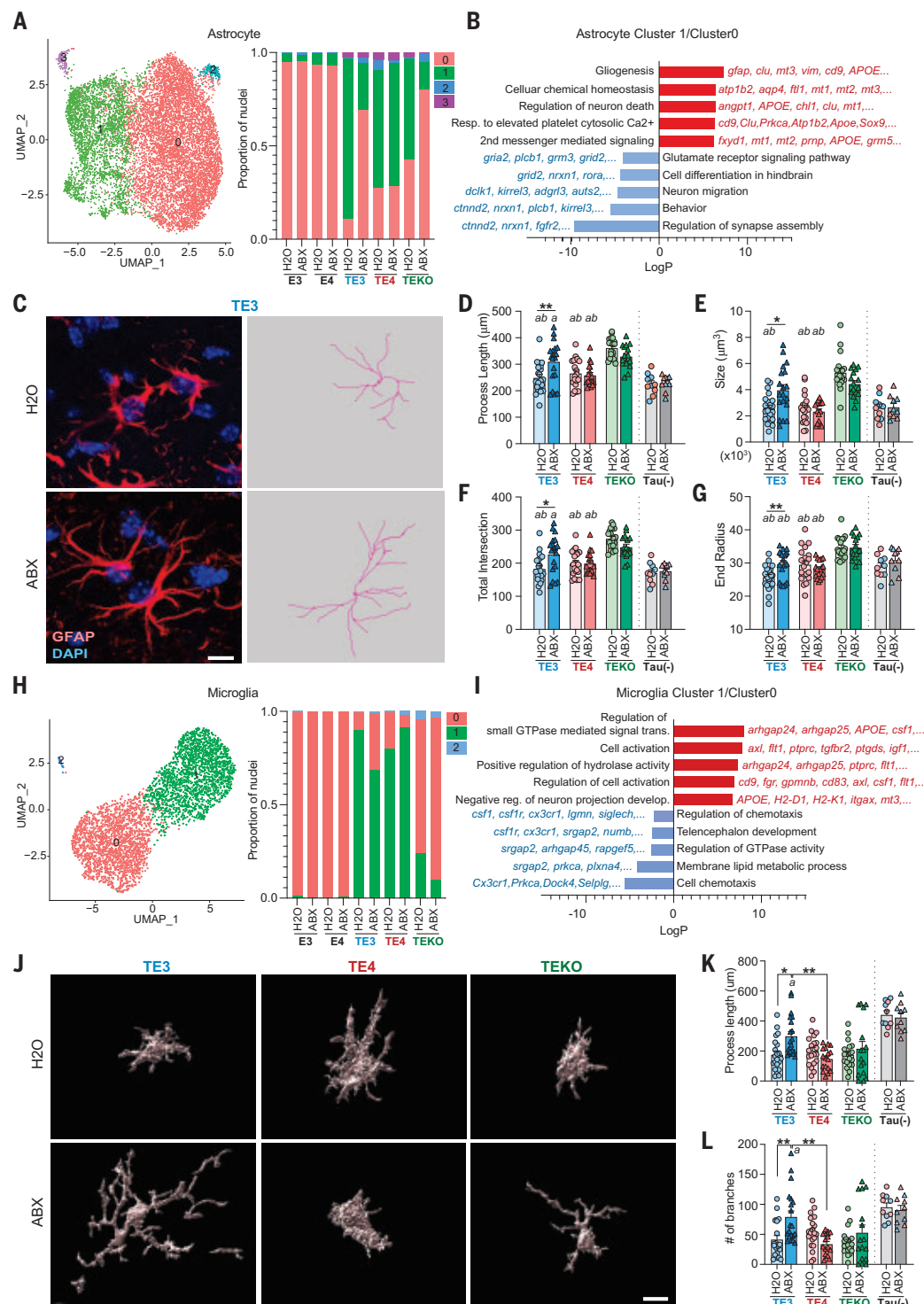
female members of the TE3-H$_2$O treatment group (Fig. 5C) and lower in TE3 compared with TE4 mice (fig. S13, B and C). Gas chromatography–mass spectrometry (GC-MS) of cecal samples disclosed that, consistent with our observation that SCFA-producing bacteria were reduced with ABX treatment in males, acetate, propionate, and butyrate were significantly reduced across APOE genotypes in males, cor-

relating with biomarkers of tau pathology (Fig. 5, D and E, and fig. S13A), but not in females (fig. S13E).

ABX-induced gut microbiota perturbation alters the peripheral immune system and the effects of SCFA on TE4 GF mice

It is unclear whether SCFAs act directly on glial cells because SCFA receptor–encoding

genes (e.g., Ffar2) are not expressed in glial cells (*12*). However, we postulated that SCFAs could affect other inflammatory mediators or immune cells that directly access the brain or the immune milieu around the brain (i.e., the meninges). We found reductions in meningeal natural killer (NK) and plasmacytoid dendritic cells (pDC) cells in ABX-treated TE3 mice. Furthermore, γδ T and pDC cells were reduced
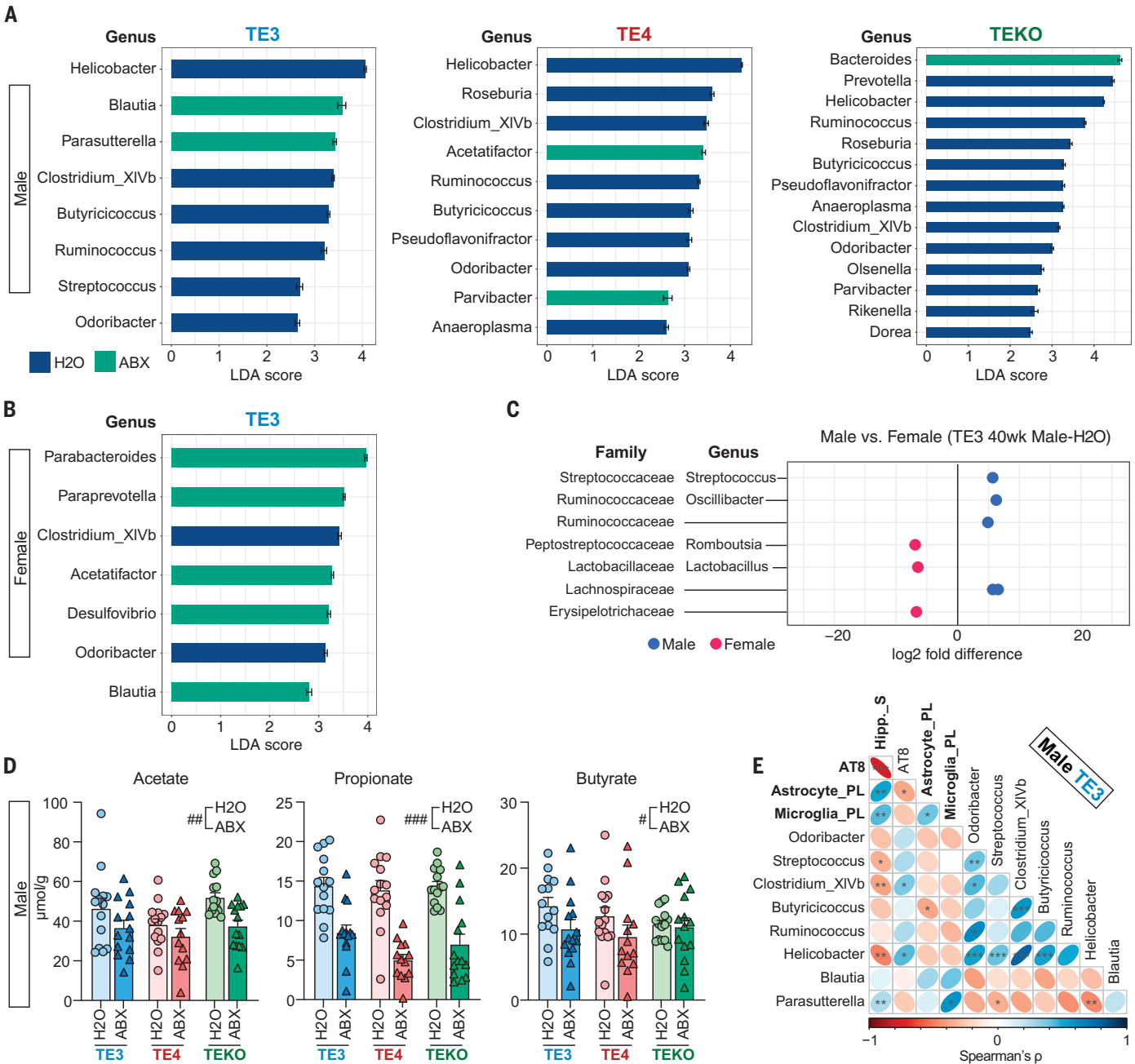
Fig. 5. Effects of ABX treatment on fecal microbiota composition and cecal levels of SCFAs. (**A** and **B**) Linear discriminant analysis (LDA) scores. Horizontal bars represent the LDA scores for each genus-level taxon in male TE3, TE4, and TEKO mice (A) and in female TE3 mice (B). Indigo and green bars represent taxon features with significantly higher representation in mice belonging to the control H2O and versus ABX treatment groups, respectively (LDA scores > 2). (**C**) Comparison of relative abundance of genera between 40-week-old male and female TE3-H2O mice. Family and genus assignments are shown. (**D**) Targeted GC-MS analysis of cecal SCFAs in male 40-week-old TE3, TE4, and TEKO mice treated with ABX or H2O (n = 14 per group), tested by two-way ANOVA. Statistical significance of the main effects of treatments (H2O versus ABX) were indicated as #P < 0.05, ##P < 0.01, and ###P < 0.001. (**E**) Correlogram showing the relationship between (i) eight genera identified as having differences in their relative abundance in male 40-week-old TE3 H2O- versus ABX-treated mice and (ii) biomarkers of tauopathy. These biomarkers (bold) include hippocampus size (Hipp._S; smaller value reflecting greater neurodegeneration), coverage of AT8 staining, process length of astrocytes (astrocyte_PL), and process length of microglial cells (microglia_PL). *P < 0.05; **P < 0.01; ***P < 0.001. See table S1 for full statistical results.

in GF mice (fig. S14, A to C). These latter cells are known to release cytokines, such as interleukin-17 (IL-17), interferon (IFN) type-I, and others, which may affect neuroinflammation in the brain (*17–19*).

Multiplex cytokine profiling revealed that plasma levels of MCP-3, IL-2R, BAFF, and Eotaxin were significantly reduced by ABX in mice (fig. S15). The degree of reduction of Eotaxin, which can cross the blood-brain bar-

rier and activate glial cells, was greater in TE3 mice compared with those belonging to the other genotype groups. Gut microbiota can modulate systemic immunity, including peripheral macrophages (*20*). ABX treatment of

male TE3 mice significantly altered lung alveolar macrophage gene expression (fig. S16). In turn, their cytokine release or interaction with adaptive immune cells could potentially affect brain pathology. The cytokine profiling data showed that some cytokines released by macrophages, such as IP-10 and BAFF, or those that can stimulate macrophages, such as MIP-1a, were affected by ABX treatment. Brain border innate and infiltration of peripheral immune cells also may act on the tau pathology and neurodegeneration. Additional snRNA-seq analysis using hippocampal tissue revealed that the populations of brain border and peripheral immune cells were increased in the tau mice at 40 weeks of age and were decreased by ABX treatment (fig. S14D). Although changes in peripheral cytokines may be important to activate glial cells to drive tau-mediated neurodegeneration, the presence of ApoE in the brain is still necessary to drive tau-mediated neurodegeneration because these cytokines in the plasma display high levels in TEKO mice that only display mild brain atrophy (Fig. 3C and fig. S15B). Finally, to begin to test whether SCFAs may be mediating the effects of GF conditions or ABX, we administered SCFAs or control in drinking water to 10-week-old or 31-week-old TE4 GF mice for 5 or 4 weeks, respectively. SCFA treatment altered alveolar macrophage gene expression in both the younger and older mice (fig. S17). SCFA supplementation increased gliosis and p-tau pathology in the hippocampus of the older TE4 GF mice (fig. S18), supporting the possibility that SCFA may be a key modulator of the microbiota effect on tau-mediated neurodegeneration.

Conclusion

Taken together, we have found that GF conditions are strongly neuroprotective against tau-mediated neurodegeneration in male and female TE4 mice. ABX treatment is also neuroprotective, but its effect was limited to males and was greater in the presence of APOE3 compared with APOE4. Our results also suggest that APOE isoforms and sex differentially modulate the microbial response to ABX, resulting in significantly lower levels of SCFAs. The microbiota-associated metabolic changes are associated with altered peripheral cytokine responses and strong changes in the innate immune response in the brain.

We hypothesize that the gut microbiota regulates the brain's innate immune response to influence tau-mediated neurodegeneration in the brain. We speculate that in TE3 mice, the ABX-induced microbiota perturbation that reduces peripheral immune activation may moderate the brain's innate immune response and eventually attenuate tau-mediated neurodegeneration. By contrast, in TE4 mice, the microbiota-associated peripheral immune changes were not altered as much by ABX treat-

ment. It is possible that the gain of function of APOE4 toxicity and the effects on the local innate immune response in the brain were stronger than that of APOE3, and ABX treatment ultimately failed to protect against tau-mediated neurodegeneration to the same degree. On the other hand, with the complete absence of the microbiota, even in TE4 mice, the depletion of microbially produced metabolic and immune signals results in a strong reduction of the disease-associated astrocyte and microglial phenotypes, leading to a decrease in tau-mediated neurodegeneration (consistently, SCFA supplementation reversed the reduced gliosis and tau pathology in TE4 GF mice).

Further studies are needed to test these hypotheses and to gain greater understanding of how sex, microbiota manipulation, microbiota-linked metabolites, central or peripheral immune response, and the pathogenesis of neurodegeneration are related. A starting point for these follow-up analyses could involve gnotobiotic mice colonized with gut microbiota harvested from Conv-R mice with different sex, age, and ApoE isoforms and from human donors (with or without tau-mediated neurodegeneration). It is possible that the TE4 GF mice colonized with different types of microbiota (e.g., harvested from wild-type mice, not necessarily from TE4–Conv-R mice) would reverse the GF rescue from neurodegeneration. It may be that the host genetic makeup in TE4 mice could reshape the effects of the transferred microbiota composition derived from a more general bacterial community and be sufficient to activate the metabolic-neuroinflammation axis. Alternatively, the sex, age, ApoE isoform status, and state of neurodegeneration may be critical in regard to the source from which the transferred microbiota are derived. Future studies are needed to sort out these possibilities. Nonetheless, these results raise the possibility that gut microbiota targeting may provide ways to prevent or treat progression of AD and primary tauopathies (21, 22).

Materials and methods
Animals

All animal experiments were performed using protocols approved by the Institutional Animal Care and Use Committee (IACUC) at Washington University School of Medicine. All phenotyping and data analyses were performed by researchers who were completely blind to the experimental hypothesis and the treatments of mice.

P301S tau transgenic mice (PS19tg; Stock No. 008169, Jackson Laboratories) contain a transgene, where expression of the human P301S tau mutant is driven by a mouse prion protein (Prnp) promoter. These animals had been backcrossed to C57BL/6 mice (Stock No.

027, Charles River) for more than 10 generations. P301S mice were crossed with human APOE knock-in mice, where the endogenous mouse ApoE gene was replaced by a human APOE gene flanked by LoxP sites (23) (APOE3$^{flox/flox}$ or APOE4$^{flox/flox}$ or ApoE knockout mice) to generate P301S::APOE3/wt, APOE4/wt, or EKO/wt animals [wild-type (wt)]. These mice were then crossed to homozygous APOE3, APOE4, or EKO mice to generate P301S::ApoE3/ApoE3, ApoE4/ApoE4, or EKO/EKO mice (abbreviated as TE3, TE4, and TEKO, respectively). Sires and dams were randomly assigned from different litters to produce experimental animals. Dams that had received an antibiotic cocktail (see below) were euthanized after weaning their pups on postnatal day 23 and were not used for further breeding or any other experiments. At weaning (postnatal day 23), pups were housed in same-sex, -genotype, and -treatment groups (2 to 5 animals per cage). Conv-R mice were housed in a mouse barrier facility under specified pathogen-free conditions until they were euthanized at 40 weeks of age. All Conv-R mice in the antibiotic experiment were given the same type of food (no. 53WU, LabDiet, St. Louis, MO) ad libitum. All groups of animals were housed under the same conditions: same type of cage, bedding materials (no. Bed-o'Cobs 1/8 BB40; the Andersons, Quakertown, PA), and nestlets (no. NES7200; Ancare, Bellmore, NY) in the same room in the vivarium. A complete mouse cage consisted of a polycarbonate shoebox bottom equipped with a wire bar lid and a polycarbonate filter top containing a filter insert.

Conv-R TE4 mice were rederived as GF by embryo transfer. Embryos were harvested 1 day after mating and transferred under sterile conditions to a pseudopregnant GF mother generated by mating to a vasectomized GF male. The transgenic GF descendants were intercrossed to produce TE4 GF mice. GF animals were reared in plastic flexible film gnotobiotic isolators (Class Biologically Clean Ltd., Madison, WI). GF status was verified by PCR of feces using universal bacterial 16S rRNA gene primers and by culturing fecal and skin swabs. The equivalent generation of Conv-R mice were used as controls.

GF mice were colonized with fecal microbiota samples collected from 40-week-old Conv-R TE4 mice to create Ex-GF animals. To do so, fecal samples from 4 to 5 mice per sex were pooled, homogenized in sterile reduced phosphate-buffered saline (PBS) containing 0.05% cysteine-HCL and 20% glycerol (5 pellets/10 mL) and stored in −80°C until the time of the fecal microbiota transplantation. A 200-μL aliquot of the resulting suspension was thawed and administered to sex-matched 12-week-old GF mice by oral gavage on two occasions, separated by a 4-day interval. The Ex-GF mice were maintained in plastic flexible

film gnotobiotic isolators (Class Biologically Clean Ltd., Madison, WI) (2 to 5 mice of the same sex per cage).

All Conv-R, GF, and Ex-GF mice (2 to 5 mice of the same sex per cage) were given the same type of autoclaved food (Teklab certified global 18% protein rodent diet; catalog no. T2018SC.15) ad libitum. All animals were maintained under a strict light cycle (lights on at 0600 hours and off at 1800 hours). Fresh fecal pellets from each animal were collected directly in sterile 2-mL centrifuge tubes (Axygen; SCT-200-SS-R-S) and immediately stored in −80°C until the time of DNA extraction. All fecal pellet samples were collected at between 1500 hours and 1700 hours to minimize circadian rhythm effects.

Antibiotic treatment

Pups assigned to the ABX treatment group were gavaged with 100 μL of an antibiotic cocktail that contained 4 mg/mL kanamycin (Sigma-Aldrich K4000), 0.35 mg/mL gentamicin (Sigma-Aldrich G1914); 8500 U/mL colistin (Sigma-Aldrich C4461), 2.15 mg/mL metronidazole (Sigma-Aldrich M1547), and 0.45 mg/mL vancomycin (Sigma-Aldrich V2002) (prepared using autoclaved water). Gavage occurred daily from postnatal day 16 to 22 using animal feeding needles (Cadence; catalog no. 7901). Control mice were gavaged with 100 μL of water (4, 24). After each gavage, mice were transferred to a new sterile cage to avoid contamination from accumulated feces in the old cages.

Nest-building behavior

A few days before euthanasia, group-housed mice were switched to individual housing (7, 25). Preweighed nestlets (2.5 g; no. NES7200, Ancare, Bellmore, NY) were introduced into each cage at ~1600 hours. The next morning at 1000 hours, the remaining nestlet was weighed. A 5-point scale was used to score the results; the scoring system is based on the percentage of nesting material remaining plus the shredding conditions: score = 1, nest shredding <25%; 2, nest shredding 25 to 50%; 3, nest shredding 50 to 90%; 4, nest shredding >90%, but nest was not compacted yet; 5, complete nest built (fig. S7A).

Tissue collection

Mice received a lethal intraperitoneal injection of pentobarbital (200 mg/kg). After perfusion with a solution of cold Dulbecco's PBS containing 3 U/ml heparin, the brains were removed. The left hemisphere was fixed in 4% paraformaldehyde for 24 hours before being transferred to 30% sucrose and stored at 4°C until sectioning. Brains were cut coronally into 50-μm-thick sections on a freezing sliding microtome (Leica SM1020R) and stored in cryoprotectant solution (0.2 M PBS, 15%

sucrose, 33% ethylene glycol) at −20°C until use. Right hemispheres were dissected, flash-frozen on dry ice, and stored at −80°C for biochemical analyses.

Volumetric analysis

Volumetric analysis of the hippocampus, LV, and entorhinal-piriform (Ent-Piri) cortex was performed using a stereological method that involved assessing every sixth coronal brain section (300 μm between sections), starting rostrally from bregma −1.4 mm to bregma −3.1 mm. All sections from each mouse were mounted on a glass slide. All mounted sections were completely dried, rinsed in water for 1 min, and stained with 0.1% Sudan black in 70% ethanol at room temperature for 20 min, then washed in 70% ethanol for 1 min (three times). Sections were then washed in Milli-Q water three times and cover-slipped with Fluoromount. The stained sections were imaged with a NanoZoomer microscope (Hamamatsu); areas of interest were traced and measured in each section using the NDP viewer (Hamamatsu). Volume was calculated by the sum of area × 0.3 mm (7, 8). All staining and analysis of data obtained were performed by someone who was blind to the experimental hypothesis and the treatments of the animals being assessed.

Neuronal layer thickness measurement

Left hemi-brain sections from each mouse, corresponding approximately to bregma coordinates −1.7 and −2.7 mm, were mounted and stained in cresyl violet for 5 min at room temperature (7). Slices were sequentially dehydrated in 50%, 70%, 95% (three times), and 100% ethanol (twice) (1 min per treatment) then cleared in xylene for 4 min (twice), and cover-slipped in cytoseal60 (Thermo Fisher Scientific, catalog no. 8310-16). Images were taken using Cytation 5 (Biotek) and analyzed with Gen5 Software (Biotek). Quantification of the thickness of the dentate granular cell layer and the CA1 pyramidal layer were measured by drawing a scale line that crossed the cell layers at two areas each section and obtaining the average value. All staining and analysis of data obtained were performed by individuals blind to the experimental hypothesis and the treatments of the animals being assessed.

Immunohistochemistry

Left hemi-brain sections, corresponding approximately to bregma coordinates −1.5 and −1.8 mm, were used for immunohistochemistry. For AT8 staining, brain sections were washed in Tris-buffered saline (TBS) buffer three times followed by incubation in 0.3% hydrogen peroxide in TBS for 10 min at room temperature. After three washes in TBS, sections were blocked with 3% milk in 0.25%

TBS-X (Triton X-100) for 30 min followed by incubation at 4°C overnight with biotinylated AT8 antibody (Thermo Scientific, catalog no. 1020B, 1:500 solution). The next day, after washing three times with TBS, all sections were treated at room temperature for 60 min with reagents included in the VECTASTAIN Elite ABC-HRP Kit, followed by three washes in TBS. Finally, sections were developed and stained using ImmPACT DAB EqV Peroxidase Substrate. Slides were cover-slipped with cytoseal60 and scanned using a Nanozoomer microscope at 20X magnification. Images were extracted by using the NDP viewer and analyzed with ImageJ software (National Institutes of Health, Bethesda, Maryland, USA, https://imagej.nih.gov/ij/).

For immunofluorescence, sections were washed in TBS three times (5 min/cycle). After washing, sections were blocked with a solution containing 3% BSA and 3% normal donkey serum in 0.25% TBS-X for 1 hour at room temperature, followed by an overnight incubation at 4°C with primary antibodies [mouse GFAP (EMD Millipore, MAB3402, 1:1000), rabbit Iba1: Wako, (1:2000); rat CD68 (SeroTec, 1:500)]. The next day, after three washes in TBS, slides were incubated with fluorescent-labeled secondary antibodies (Molecular Probes, 1:500) for one hour at room temperature. Sections were washed and incubated with 0.1% Sudan black solution in 70% ethanol for 10 min, washed once more, and mounted in ProLong Gold Antifade mounting medium (Molecular Probes, P36931). Images were obtained by using a Leica Stellaris 5 confocal microscope and analyzed with ImageJ software.

Brain tissue sample processing for enzyme-linked immunosorbent assay (ELISA)

Mouse posterior cortex was sequentially processed in (i) RAB buffer (100 mM MES, 1 mM EGTA, 0.5 mM $MgSO_4$, 750 mM NaCl, 20 mM NaF, 1 mM Na_3VO_4, pH 7.0) supplemented with protease inhibitors (Complete, Roche) and phosphatase inhibitors (PhosSTOP, Roche); (ii) RIPA buffer (150 mM NaCl, 50 mM Tris, 0.5% deoxycholic acid, 1% Triton X-100, 0.1% SDS, 5 mM EDTA, 20 mM NaF, 1 mM Na_3VO_4, pH 8.0) supplemented by Complete and PhosSTOP; and (iii) 70% formic acid buffer as previously described (8). The tissue was then weighed and homogenized using a pestle (10 μL RAB buffer/1 mg tissue). After centrifugation at 50,000 ×g for 20 min, the supernatant was taken as the RAB-soluble fraction, and the pellet was dissolved in RIPA buffer (10 μL buffer/1 mg tissue) by sonication (1 min at 20% pulse, 1 s interval; Fisher scientific FB120, Pittsburgh, PA). After centrifugation at 50,000 ×g for 20 min, the supernatant was taken as the RIPA-soluble fraction. The pellet was sonicated (1 min at 20% pulse, 1 s interval) in 70% formic acid (10 μL/1 mg tissue) and

centrifuged at 50,000 ×*g* for 20 min. The supernatant was taken as the formic acid–soluble fraction. All fractions were stored in –80 °C until they were analyzed.

Sandwich ELISA

The levels of human total tau, p-tau, and human ApoE were measured by sandwich ELISA and normalized to tissue weight. TAU-5 (mouse monoclonal, 20 μL/mL) was used as the coating antibody for the human tau ELISA, HJ14.5 (mouse monoclonal, 20 μL/mL) for the p-tau ELISA, and HJ15.3 (mouse monoclonal, 5 μL/mL) for the human ApoE ELISA. Biotinylated HT7 (mouse monoclonal, 200 ng/mL; Thermo Fisher) was used to detect antibodies for the human tau ELISA, biotinylated AT8 (mouse monoclonal, 300 ng/mL) for the p-tau ELISA, and biotinylated HJ15.7 (mouse monoclonal, 150 ng/mL) for the human ApoE ELISA.

Astrocyte morphology analysis

Z-stacks (20 μm) of 4′,6-diamidino-2-phenylindole (DAPI)– and GFAP-labeled immunofluorescence images were acquired on a Leica Stellaris 5 confocal microscope with a 40X objective and 1024-pixel by 1024-pixel resolution. Simple Neurite Trace (SNT; ImageJ plug-in open-source tool) was used to reconstruct tridimensional arbors of GFAP-positive astrocytic main processes by semiautomatic tracing (*26*). For each mouse, three astrocytes were randomly selected in each section from two separate brain sections on the basis of GFAP-stained structures enclosing a single DAPI-stained nucleus. The six astrocytes chosen from each mouse did not have processes that touched the edges of the field or were truncated. Fully traced astrocytes in SNT were used to obtain morphometric data; i.e., process length, end radius, the number of process branches, the total number of interactions between process branches and radius from Sholl analysis (*27*), and the volume occupied by the astrocytic process from Convex Hull analysis (*28*).

Microglia morphology analysis

Z-stacks (20 μm) of Iba1-labeled immunofluorescence images were acquired on an LSM 880 II Airyscan FAST confocal microscope (Zeiss) with a 60X objective, 1.8X zoom, and 1024-pixel by 1024-pixel resolution, For each mouse, a total of four z-stacks of the dentate gyrus region were taken from two separate brain sections. Microglia morphology analysis was performed on three-dimensional (3D) images using Imaris 9.5 software (Bitplane). Morphology was analyzed using the Filament Tracer, with no loops allowed and spot detection mode to determine process start and end points per cell. Process reconstruction was made using the following custom settings: detect new starting points; largest diameter 9.00 μm, seed points 2.00 μm; remove seed points around

starting points; and diameter of sphere regions: 15 μm. All filament parameters were exported into separate Excel files and used for analyzing the number of process branches, process length, and process volume per cell. Image processing, 3D reconstruction, and data analysis were performed in a blinded manner with regards to the experimental conditions.

Nanostring gene expression assay

RNA was isolated from mouse hippocampus using the RNeasy Mini Kit (QIAGEN, catalog no. 74104). Quality control checks were performed on all samples to determine RNA concentration and integrity (RIN scores > 9.3). For the Nanostring gene expression assay, isolated RNA samples were processed by the Genome Technology Access Core at Washington University, using NanoString's nCounter Neuroinflammation panel (735 genes were detected out of 770 targeted genes). Background noise in the data was corrected to a thresholding count value of 20. Lane-by-lane technical variation was corrected by using the geometric median value of the positive-control set. Gene expression normalization was performed subsequently using the geNorm algorithm to select the optimal housekeeping genes (*Mto1*, *Csnk2a2*, *Aars*, *Supt7l*, *Fam104a*, *Tbp*, *Ccdc127*, *Tada2b*, *Lars*, and *Cnot10*)

Differential gene expression was performed using nSolver 4.0 and the Advanced Analysis 2.0 plugin (NanoString). Fold-change expression and *P* values were calculated by linear regression analysis using negative binomial or log-linear models. *P* values were corrected for multiple comparisons using the Benjamini-Hochberg method. Coexpression analysis was performed using the Weighted Gene Correlation Network Analysis (WGCNA) package in R (*29*). A soft thresholding power of 8 was selected to calculate the unsigned adjacency for normalized gene counts. Hierarchical clustering of the topological overlap matrix dissimilarity was used to produce a gene dendrogram. Gene modules were identified using a dynamic tree cut with a minimum module size of 20 genes. Eigengenes for each module were calculated, and correlations with dummy-coded APOE genotype or the size of the hippocampus as an index of neurodegeneration level were calculated. GO enrichment analysis was performed using Metascape (*30*).

snRNA-seq of frozen hippocampal tissue

Frozen hippocampus from *n* = 5 mice of the same genotype and treatment were pooled as a single sample. Samples were selected based on those being closest to the mean values of hippocampal volumes. Tissue was homogenized using a Dounce homogenizer in 1 mL of lysis buffer [10 mM Tris-HCl (pH 7.4), 10 mM NaCl, 3 mM MgCl$_2$; 0.005% NP40; and 0.2 U/mL RNase Inhibitor (prepared using nuclease-free

water and chilled to 4°C)] and incubated on ice for 15 min. A 30-mm MACS SmartStrainer was used to remove cell debris and large clumps, followed by centrifugation at 500 ×*g* for 5 min at 4°C. After carefully removing the supernatant, the pellet containing nuclei was resuspended with 5 mL of nuclei wash and resuspension buffer (1% BSA plus 0.2 U/mL RNase Inhibitor in 1 X PBS). The cell debris removal step, centrifugation, and resuspension steps were repeated twice. Only 500 μL of nuclei wash and resuspension buffer was added in the last resuspension step. The resulting solution was mixed with 900 μL of Sucrose Cushion Buffer I [prepared by mixing 2.7 mL of Nuclei Pure 2M Sucrose Cushion Solution (MilliporeSigma, St. Louis) with 300 mL Nuclei Pure Sucrose Cushion Solution (MilliporeSigma, St. Louis) and then carefully layered to the top of 500 μl Sucrose Cushion Buffer I in a 2-mL eppendorf tube]. After centrifugation at 13,000 ×*g* for 45 min at 4°C, the nuclear pellet was resuspended in 500 μL nuclei wash and resuspension buffer. The concentration of nuclei was determined using a Countess instrument (Invitrogen) and DAPI staining. The concentration was adjusted to 1200 nuclei/mL using nuclei wash and resuspension buffer before snRNA-seq.

Isolated nuclei were used for droplet-based snRNA-seq using the Chromium Single Cell 3′ Reagent Kit (10x Genomics). Libraries were sequenced using a NovaSeq 6000 instrument (Illumina). Sample demultiplexing, barcode processing, and single-nuclei 3′ counting was performed using the Cell Ranger Single-Cell Software Suite (10x Genomics). Cell Ranger count was used to (i) align samples to a custom pre-mRNA reference package (mm10) containing the human *APOE* gene, (ii) quantify reads, and (iii) filter those reads with a quality score below 30.

The Seurat v3 and SoupX R packages were used for subsequent analysis of the datasets (*31–33*). Contaminating cell-free RNA from each sample group was removed using SoupX. Nuclei with mitochondrial content >5% or total gene counts <200 or >5000 were removed (Seurat). For each group, the percent of mitochondria was regressed out as a nuisance variable, gene counts were normalized, and variable features identified using the SCTransform function in Seurat. The top 3000 variable genes were used to integrate experimental groups using the PrepSCTIntegration, FindIntegrationAnchors, and IntegrateData commands in Seurat. Principal components analysis (PCA) was performed on the integrated dataset and the first 30 principal components were selected for downstream analysis using FindNeighbors. Clusters were identified using the FindClusters function with a granularity ranging from 0.1 to 1.2. Final clustering was performed using a resolution of 0.3. The

first 30 principal components were passed into UMAP using the RunUMAP command with default parameters. Differential gene expression between each cell cluster and all other clusters was performed on SCT data to identify marker genes for each individual cell cluster. Clusters containing high mitochondrial genome content, or marker genes for more than one broad cell type (i.e., microglia and excitatory neurons) were removed and data were reclustered using the first 30 principal components and a resolution of 0.3. In total, 143,835 nuclei with a median UMI of 2735 and median gene number of 1664 across all 10 experimental groups were used in the final analysis.

Differential gene expression to identify marker genes was again performed using MAST (*34*), and broad cell types were identified on the basis of known cell type–specific markers. For subclustering analysis, nuclei from astrocyte or microglia clusters were extracted from the dataset, RNA counts were renormalized, and the percentage of mitochondrial genes regressed out using the SCTransform command. PCA analysis was performed and the nuclei reclustered. For astrocytes, in addition to regressing the percentage of mitochondrial genes, the percentage of Gh (growth hormone) and Prl (Prolactin) transcripts were also regressed out due to detection in the TEKO-H_2O treatment group. The first 20 principal components were used, and clustering performed at a resolution of 0.15 (data S5). For microglia, the first 10 PCs were used, and clustering performed at a resolution of 0.1 (data S6). Marker genes for subclusters were identified using MAST (data S5 and S6). The SCTransform function from the Seurat package was used to generate graphs from the data containing log-normalized values (*35*). Expression level represents the log-normalized values of gene counts. Gene counts for each cell were divided by the total counts for that cell and scaled before natural log transformation. GO enrichment analysis was performed using Metascape (*30*).

Fluidigm Biomark HD real-time PCR

Hippocampus tissues were used for the gene expression analysis. Samples were selected on the basis of the mean values of hippocampal volumes. RNA was exacted from frozen tissues using RNeasy Mini Kit (Qiagen) and converted to cDNA using the high-capacity RNA-to-cDNA kit from Thermo Fisher and the manufacturer's instructions. Gene expression was carried out using Fluidigm Biomark HD real-time PCR system. Using Taqman primers, gene expression was quantitatively measured after normalization the housekeeping gene, *Gapdh*.

16S rRNA amplicon sequencing and analysis

For bacterial V4-16S rDNA amplicon sequencing, each frozen fecal sample was resuspended in 500 μl of a phenol:chloroform:isoamyl alcohol mixture (25:24:1), followed by addition of 710 μL of 2X Buffer A (200 mM NaCl, 200 mM Trizma base, 20 mM EDTA) and 20% SDS (500:210). The solution was shaken in a Mini-Beadbeater-96 (BioSpec Products) for 4 min with ~250 μl of 0.1 mm zirconia/silica beads and one 3.97-mm steel ball. After centrifugation at 3220 ×*g* for 4 min, 420 μL of the resulting aqueous phase was transferred to a well of a 96-well plate. A 100 μL aliquot of the crude extract was mixed with 400 μL of a mixture of Qiagen buffer PM and 3M NaOAc, pH5.5 (675:45), and the mixture was passed through a Qiagen QiaQuick 96 plate by centrifugation at 3220 ×*g* for 10 min, washed twice with 900 μL of Buffer PE by centrifugation, and finally eluted with 130 μL Buffer EB. Purified DNA was quantified using Invitrogen Quant-iT dsDNA BR kit and normalized to 2 ng/μL. Variable region 4 of the bacterial 16S rRNA gene was amplified by PCR using the following conditions: denaturation (94°C for 2 min) followed by 26 cycles of 94°C for 15 s, 50°C for 30 s, and 68°C for 30 s, followed by incubation at 68°C for 2 min.

Sample-associated 16S rDNA amplicons were quantified, pooled, and subjected to sequencing (Illumina MiSeq instrument, paired-end 250 nt reads). Reads were demultiplexed, trimmed to 200 nucleotides, and merged, followed by removal of chimeric sequences (DADA2 v. 1.13.0). ASVs were generated from demultiplexed paired-end reads with DADA2 and taxonomy was assigned on the basis of the DADA2-formatted training dataset (*36*). Read quality control and the resolution of ASVs were performed with the dada2 R package (*37*, *38*). ASVs that were not assigned to the kingdom Bacteria were filtered out. The remaining reads were assigned taxonomy using the Ribosomal Database Project (RDP trainset 16/release 11.5) 16S rRNA gene sequence database (*38*).

Analyses of alpha-diversity (richness, Faith's phylogenetic diversity) and beta-diversity (weighted UniFrac distances) were performed using PhyloSeq and additional R packages (*39*). Taxa (ASVs) whose relative abundances differed significantly between sample groups were identified by performing pairwise comparisons using DESeq2 and MicrobiotaProcess packages (*40*). A correlation matrix was generated and plotted as ellipses using the corrplot package (*41*). R codes to generate 16S rRNA-related results and figures in this manuscript are available at GitHub: https://github.com/shandley/neurodegeneration_16S.

GC-MS of SCFAs

SCFAs were quantified by GC-MS using a previously described protocol (*42*). Cecal contents were weighed and placed in 2 mL glass screw cap vials. Ten microliters of a mixture of internal standards (20 mM of acetic acid-$^{13}C_2$, D_4, propionic acid-D_6, butyric acid-$^{13}C_4$, lactic acid-3,3,3-D_3, and succinic acid-$^{13}C_4$) was added to each vial, followed by 20 μL of 33% HCl and 1 mL diethyl ether. The solution was vortexed vigorously for 10 min. The two phases were separated by centrifugation (4000 ×*g* for 5 min). The upper organic layer was transferred into another vial and a second 1 ml diethyl ether extraction was performed. After combining the two ether extracts, a 60 μL aliquot was mixed with 20 μL N-tert-butyldimethylsilyl-N-methyltrifluoroacetamide (MTBSTFA) in a GC auto-sampler vial with a 200 μL glass insert, and the mixture was incubated for 2 hours at room temperature. Samples were analyzed in a randomized order. Derivatized samples (1 μL) were injected with 15:1 split into an Agilent 7890A GC system coupled with 5975C MS detector (Agilent). Analyses were carried on a HP-5MS capillary column (30 m × 0.25 mm, 0.25 μm film thickness, Agilent J & W Scientific) using electronic impact (70 eV) as ionization mode. Helium was used as a carrier gas at a constant flow rate of 1.26 mL/min, and the solvent delay time was set to 3.5 min. The column head pressure was 10 psi. The temperatures of injector, transfer line, and quadrupole were 270°, 280°, and 150°C, respectively. The GC oven was programmed as follows; 45°C held for 2.25 min, increased to 200°C at a rate of 20°C/min, increased to 300°C at a rate of 100°C/min, and finally held for 3 min. Quantification of SCFA was performed by isotope dilution GC-MS using selected ion monitoring (SIM). For SIM analysis, the m/z for native and labeled molecular peaks for SCFA quantified were 117 and 122 (acetate), 131 and 136 (propionate), 145 and 149 (butyrate), 261 and 264 (lactate), and 289 and 293 (succinate), respectively. Various concentrations of standards were spiked into control samples to prepare the calibration curves for quantification.

Flow cytometry

Mice were given a lethal dose of pentobarbital sodium (Fatal-Plus, Vortech) intraperitoneally and perfused through the heart with ice-cold PBS supplemented with 5 U/mL heparin. The dural meninges and spleen were dissected and digested with 1.4 U/mL of Collagenase VIII (Sigma Aldrich, catalog no. C2139) and 35 U/mL of DNAse I (Sigma Aldrich, catalog no. DN25) for 20 to 30 min at 37°C. After the digestion step, the tissue was passed through 70-μm nylon mesh cell strainers (Fisher Scientific). Cells were then centrifuged at 340 ×*g* for 5 min or 450 ×*g* for 4 min at 4°C, and then stained in PBS with Zombie NIR Fixable Viability Kit (1:500, BioLegend, catalog no. 423105) for 15 min on ice. After one wash with fluorescence-activated cell sorting (FACS) buffer (PBS with 2% fetal bovine serum or PBS with 1% bovine serum albumin, 2 mM EDTA, 25 mM HEPES)

Fc-receptors were blocked with anti-CD16/32 (1:100, BioLegend, clone 93, catalog no. 101302) for 15 min on ice. An equal volume of primary antibody mix was added, and cells were stained for 20 min on ice at 1:300 final dilution. Samples were then washed twice with FACS buffer and acquired on a spectral flow cytometer (Aurora, Cytek Biosciences). Data were unmixed using Spectral flow software (Cytek) and then gated and quantified using FlowJo v10.8.2 (Treestar).

The following antibodies were used for flow cytometry; anti-CD4 BUV395 (BD, GK1.5, catalog no. 563790), anti-CD5 BUV496 (BD, 53-7.3, catalog no. 741048), anti-CD27 BUV563 (BD, LG.3A10, catalog no. 741275), anti-CD44 BUV615 (BD, IM7, catalog no. 751414), anti-CD11c BUV737 (BioLegend, N418, catalog no. 749039), anti-TCRb BUV805 (BD, H57-597, catalog no. 748405), Ly6G BV421 (BioLegend, 1A8, catalog no. 127628), anti-CD25 Pacific Blue (BioLegend, PC61, catalog no. 102022), anti-CD19 BV480 (BD, 1D3, catalog no. 566107), anti-I-A/I-E BV510 (BioLegend, M5/114.15.2, catalog no. 107641), anti-CXCR3 (eBioscience, CXCR3-173, catalog no. 63-1831), B220 BV650 (BD, RA3-6B2, catalog no. 563893), anti-CD49a BV711 (BD, Ha31/8, catalog no. 564863), anti-CD45 BV750 (BD, 30-F11, catalog no. 746947), anti-Ly-6C AlexaFluor488 (BioLegend, HK1.4, catalog no. 128022), anti-CD8a AlexaFluor532 (eBioscience, 53-6.7m catalog no. 58-0081), anti-CD122 BrilliantBlue700 (BD, TM-b1, catalog no. 742112), CD69 PE (BioLegend, H1.2F3, catalog no. 104508), anti-CD186 (CXCR6) PE-Dazzle 594 (BioLegend, SA051D1, catalog no. 151117), anti-CD127 PE-Cy5 (BioLegend, A7R34, catalog no. 135016), anti-NK1.1 PE-Cy7 (eBioscience, PK136, catalog no. 108714), anti-TCRg/d AlexaFluor647 (BioLegend,GL3, catalog no. 118134), and anti-F4/80 AlexaFluor700 (BioLegend, BM8, catalog no. 123130).

FACS for lung macrophage isolation

Lung samples were harvested from the mice and chopped up with scissors into 1- to 2-mm sizes. The sliced lung samples were digested in digestion buffer containing 50 U/mL DNase (Sigma), 100 U/mL Hyaluronidase (Sigma), and 0.28 U/mL Liberase (Roche) at 37°C for 45 min. The mixtures were gently inverted a few times every 5 to 10 min. A final concentration of 10% FBS was used to stop the reaction and the samples were smashed through a 70-μm-diameter cell strainer. The cell suspensions were pelleted down by centrifugation at 456 ×g for 5 min. Red blood cells were removed with 5 mL ACK buffer (150 mM ammonium chloride, 10 mM potassium bicarbonate, and 0.1 mM EDTA) at room temperature for 2 min. The reaction was stopped by adding 1 mL of FBS, and cells were passed through a 70-μm strainer one more time. Cells were pelleted and ~5 × 10^6 cells were used for staining.

Cell sorting was completed on a FACS AriaII. Staining was performed at 4°C in the presence of Fc block (2.4G2; Leinco) in magnetic-activated cell-sorting (MACS) buffer (PBS + 0.5% BSA + 2 mM EDTA). The following antibodies were used from Biolegend: BV510 anti-CD45 (30-F11), APC-Cy7 anti-CD11b (M1/70), Pacific-Blue anti-MHC-II (I-A/I-E) (M5/114.15.2), PercP-Cy5.5 anti-Ly6C/Ly6G (Gr-1) (RB6-8C5), and APC anti-CD64 (X54-5/7.1). Antibodies obtained from Invitrogen included: PE-Cy7 anti-CD11c (N418) and PE anti-SiglecF (1RNM44N). The alveolar macrophages were sorted as CD45+ SiglecF+ CD11c+ CD64+ CD11b^{lo} cells.

RNA-seq and analysis

RNA was extracted from FACS-sorted lung macrophages (described above) using the RNeasy Plus Micro Kit (QIAGEN, catalog no. 74034). RNA samples were prepared according to library kit manufacturer's protocol, indexed, pooled, and sequenced on an Illumina Nova-Seq 6000. Basecalls and demultiplexing were performed with Illumina's bcl2fastq2 software. RNA-seq reads were then aligned and quantitated to the Ensemble release 101 primary assembly with an Illumina DRAGEN Bio-IT on-premise server running version 3.9.3-8 software.

All gene counts were then imported into the R/Bioconductor package EdgeR and TMM normalization size factors were calculated to adjust for samples for differences in library size (43). Ribosomal genes and genes not expressed in the smallest group size minus one sample greater than one count-per-million were excluded from further analysis. The TMM size factors and the matrix of counts were then imported into the R/Bioconductor package Limma (44). Weighted likelihoods based on the observed mean-variance relationship of every gene and sample were then calculated for all samples and the count matrix was transformed to moderated $\log_2$ counts-per-million with Limma's voomWithQuality-Weights (45). The performance of all genes was assessed with plots of the residual standard deviation of every gene to their average log-count with a robustly fitted trend line of the residuals. Differential expression analysis was then performed to analyze for differences between conditions; the results were filtered for only those genes with Benjamini-Hochberg false-discovery rate adjusted P values ≤0.05. GO enrichment analysis was performed using Metascape (30).

Quantification and statistical analysis

All data were expressed as mean values ± SEMs. Statistical analysis was performed with JMP15 Pro (SAS Institute, Cary, NC, RRID: SCR_014242) and GraphPad Prism 9. Means between two groups were compared with a two-tailed, unpaired Student's t test. Comparisons of means from three groups with each other were analyzed with one-way analysis of variance (ANOVA). Two-way ANOVAs were used to analyze between-subjects designs with two variable factors. Repeated-measures designs were analyzed using mixed-effects restricted maximum likelihood (REML) model. Tukey was used for post hoc pairwise comparisons. Fisher's exact test was used to analyze probability distributions. The strength of the linear relationship between two different variables was analyzed using Pearson's or Spearman's correlation. The null hypothesis was rejected at the $P < 0.05$ level. Statistical significance was taken as *$P < 0.05$, **$P < 0.01$, and ***$P < 0.001$. Statistical significance of the main effects without the interactions of two variables was indicated as #$P < 0.05$, ##$P < 0.01$, and ###$P < 0.001$. All statistical information is listed in table S1.

REFERENCES AND NOTES

1. J. M. Long, D. M. Holtzman, Alzheimer Disease: An Update on Pathobiology and Treatment Strategies. *Cell* **179**, 312–339 (2019). doi: 10.1016/j.cell.2019.09.001; pmid: 31564456

2. D. O. Seo, D. M. Holtzman, Gut Microbiota: From the Forgotten Organ to a Potential Key Player in the Pathology of Alzheimer's Disease. *J. Gerontol. A Biol. Sci. Med. Sci.* **75**, 1232–1241 (2020). doi: 10.1093/gerona/glz262; pmid: 31738402

3. T. Harach *et al.*, Reduction of Abeta amyloid pathology in APPPS1 transgenic mice in the absence of gut microbiota. *Sci. Rep.* **7**, 41802 (2017). doi: 10.1038/srep41802; pmid: 28176819

4. H. B. Dodiya *et al.*, Sex-specific effects of microbiome perturbations on cerebral Aβ amyloidosis and microglia phenotypes. *J. Exp. Med.* **216**, 1542–1560 (2019). doi: 10.1084/jem.20182386; pmid: 31097468

5. I. J. Parikh *et al.*, Murine Gut Microbiome Association With APOE Alleles. *Front. Immunol.* **11**, 200 (2020). doi: 10.3389/fimmu.2020.00200; pmid: 32117315

6. T. T. T. Tran *et al.*, APOE genotype influences the gut microbiome structure and function in humans and mice: Relevance for Alzheimer's disease pathophysiology. *FASEB J.* **33**, 8221–8231 (2019). doi: 10.1096/fj.201900071R; pmid: 30958695

7. C. Wang *et al.*, Selective removal of astrocytic APOE4 strongly protects against tau-mediated neurodegeneration and decreases synaptic phagocytosis by microglia. *Neuron* **109**, 1657–1674.e7 (2021). doi: 10.1016/j.neuron.2021.03.024; pmid: 33831349

8. Y. Shi *et al.*, ApoE4 markedly exacerbates tau-mediated neurodegeneration in a mouse model of tauopathy. *Nature* **549**, 523–527 (2017). doi: 10.1038/nature24016; pmid: 28959956

9. Y. Shi *et al.*, Microglia drive APOE-dependent neurodegeneration in a tauopathy mouse model. *J. Exp. Med.* **216**, 2546–2561 (2019). doi: 10.1084/jem.20190980; pmid: 31601677

10. R. Mancuso *et al.*, CSF1R inhibitor JNJ-40346527 attenuates microglial proliferation and neurodegeneration in P301S mice. *Brain* **142**, 3243–3264 (2019). doi: 10.1093/brain/awz241; pmid: 31504240

11. C. N. Mann *et al.*, Astrocytic α2-Na$^+$/K$^+$ ATPase inhibition suppresses astrocyte reactivity and reduces neurodegeneration in a tauopathy mouse model. *Sci. Transl. Med.* **14**, eabm4107 (2022). doi: 10.1126/scitranslmed.abm4107; pmid: 35171651

12. D. Erny *et al.*, Host microbiota constantly control maturation and function of microglia in the CNS. *Nat. Neurosci.* **18**, 965–977 (2015). doi: 10.1038/nn.4030; pmid: 26030851

13. S. Spichak *et al.*, Microbially-derived short-chain fatty acids impact astrocyte gene expression in a sex-specific manner.

Brain Behav. Immun. Health **16**, 100318 (2021). doi: 10.1016/j.bbih.2021.100318; pmid: 34589808

14. T. R. Sampson *et al.*, Gut Microbiota Regulate Motor Deficits and Neuroinflammation in a Model of Parkinson's Disease. *Cell* **167**, 1469–1480.e12 (2016). doi: 10.1016/j.cell.2016.11.018; pmid: 27912057

15. P. Jirkof, Burrowing and nest building behavior as indicators of well-being in mice. *J. Neurosci. Methods* **234**, 139–146 (2014). doi: 10.1016/j.jneumeth.2014.02.001; pmid: 24525328

16. I. D. Vainchtein, A. V. Molofsky, Astrocytes and Microglia: In Sickness and in Health. *Trends Neurosci.* **43**, 144–154 (2020). doi: 10.1016/j.tins.2020.01.003; pmid: 32044129

17. R. Di Marco Barros, Z. Fitzpatrick, M. R. Clatworthy, The gut-meningeal immune axis: Priming brain defense against the most likely invaders. *J. Exp. Med.* **219**, e20211520 (2022). doi: 10.1084/jem.20211520; pmid: 35195681

18. K. Alves de Lima *et al.*, Meningeal γδ T cells regulate anxiety-like behavior via IL-17a signaling in neurons. *Nat. Immunol.* **21**, 1421–1429 (2020). doi: 10.1038/s41590-020-0776-4; pmid: 32929273

19. M. Colonna, G. Trinchieri, Y. J. Liu, Plasmacytoid dendritic cells in immunity. *Nat. Immunol.* **5**, 1219–1226 (2004). doi: 10.1038/ni1141; pmid: 15549123

20. T. J. Schuijt *et al.*, The gut microbiota plays a protective role in the host defense against pneumococcal pneumonia. *Gut* **65**, 575–583 (2016). doi: 10.1136/gutjnl-2015-309728; pmid: 26511795

21. Y. Sun *et al.*, The Gut Microbiome as a Therapeutic Target for Cognitive Impairment. *J. Gerontol. A Biol. Sci. Med. Sci.* **75**, 1242–1250 (2020). doi: 10.1093/gerona/glz281; pmid: 31811292

22. D. O. Seo, B. D. Boros, D. M. Holtzman, The microbiome: A target for Alzheimer disease? *Cell Res.* **29**, 779–780 (2019). doi: 10.1038/s41422-019-0227-7; pmid: 31488883

23. T. V. Huynh *et al.*, Lack of hepatic apoE does not influence early Aβ deposition: Observations from a new *APOE* knock-in model. *Mol. Neurodegener.* **14**, 37 (2019). doi: 10.1186/s13024-019-0337-1; pmid: 31623648

24. A. T. Stefka *et al.*, Commensal bacteria protect against food allergen sensitization. *Proc. Natl. Acad. Sci. U.S.A.* **111**, 13145–13150 (2014). doi: 10.1073/pnas.1412008111; pmid: 25157167

25. R. M. Deacon, Assessing nest building in mice. *Nat. Protoc.* **1**, 1117–1119 (2006). doi: 10.1038/nprot.2006.170; pmid: 17406392

26. G. Tavares *et al.*, Employing an open-source tool to assess astrocyte tridimensional structure. *Brain Struct. Funct.* **222**, 1989–1999 (2017). doi: 10.1007/s00429-016-1316-8; pmid: 27696155

27. D. A. Sholl, Dendritic organization in the neurons of the visual and motor cortices of the cat. *J. Anat.* **87**, 387–406 (1953). pmid: 13117757

28. M. Augusto-Oliveira *et al.*, Plasticity of microglia. *Biol. Rev.* **97**, 217–250 (2022). doi: 10.1111/brv.12797; pmid: 34549510

29. P. Langfelder, S. Horvath, WGCNA: An R package for weighted correlation network analysis. *BMC Bioinformatics* **9**, 559 (2008). doi: 10.1186/1471-2105-9-559; pmid: 19114008

30. Y. Zhou *et al.*, Metascape provides a biologist-oriented resource for the analysis of systems-level datasets. *Nat. Commun.* **10**, 1523 (2019). doi: 10.1038/s41467-019-09234-6; pmid: 30944313

31. A. Butler, P. Hoffman, P. Smibert, E. Papalexi, R. Satija, Integrating single-cell transcriptomic data across different conditions, technologies, and species. *Nat. Biotechnol.* **36**, 411–420 (2018). doi: 10.1038/nbt.4096; pmid: 29608179

32. T. Stuart *et al.*, Comprehensive Integration of Single-Cell Data. *Cell* **177**, 1888–1902.e21 (2019). doi: 10.1016/j.cell.2019.05.031; pmid: 31178118

33. M. D. Young, S. Behjati, SoupX removes ambient RNA contamination from droplet-based single-cell RNA sequencing data. *Gigascience* **9**, giaa151 (2020). doi: 10.1093/gigascience/giaa151; pmid: 33367645

34. G. Finak *et al.*, MAST: A flexible statistical framework for assessing transcriptional changes and characterizing heterogeneity in single-cell RNA sequencing data. *Genome Biol.* **16**, 278 (2015). doi: 10.1186/s13059-015-0844-5; pmid: 26653891

35. C. Hafemeister, R. Satija, Normalization and variance stabilization of single-cell RNA-seq data using regularized negative binomial regression. *Genome Biol.* **20**, 296 (2019). doi: 10.1186/s13059-019-1874-1; pmid: 31870423

36. B. J. Callahan *et al.*, DADA2: High-resolution sample inference from Illumina amplicon data. *Nat. Methods* **13**, 581–583 (2016). doi: 10.1038/nmeth.3869; pmid: 27214047

37. J. R. Cole *et al.*, Ribosomal Database Project: Data and tools for high throughput rRNA analysis. *Nucleic Acids Res.* **42**, D633–D642 (2014). doi: 10.1093/nar/gkt1244; pmid: 24288368

38. P. J. McMurdie, S. Holmes, phyloseq: An R package for reproducible interactive analysis and graphics of microbiome census data. *PLOS ONE* **8**, e61217 (2013). doi: 10.1371/journal.pone.0061217; pmid: 23630581

39. M. I. Love, W. Huber, S. Anders, Moderated estimation of fold change and dispersion for RNA-seq data with DESeq2. *Genome Biol.* **15**, 550 (2014). doi: 10.1186/s13059-014-0550-8; pmid: 25516281

40. S. Xu, G. Yu, MicrobiotaProcess: An R Package for Analysis, Visualization and Biomarker Discovery of Microbiome, version 0.84 (2021).

41. T. Wei, V. R. Simko, R package "corrplot": Visualization of a Correlation Matrix (2021).

42. F. E. Rey *et al.*, Metabolic niche of a prominent sulfate-reducing human gut bacterium. *Proc. Natl. Acad. Sci. U.S.A.* **110**, 13582–13587 (2013). doi: 10.1073/pnas.1312524110; pmid: 23898195

43. M. D. Robinson, D. J. McCarthy, G. K. Smyth, edgeR: A Bioconductor package for differential expression analysis of digital gene expression data. *Bioinformatics* **26**, 139–140 (2010). doi: 10.1093/bioinformatics/btp616; pmid: 19910308

44. M. E. Ritchie *et al.*, limma powers differential expression analyses for RNA-sequencing and microarray studies. *Nucleic Acids Res.* **43**, e47 (2015). doi: 10.1093/nar/gkv007; pmid: 25605792

45. R. Liu *et al.*, Why weight? Modelling sample and observational level variability improves power in RNA-seq analyses. *Nucleic Acids Res.* **43**, e97 (2015). doi: 10.1093/nar/gkv412; pmid: 25925576

SUPPLEMENTARY MATERIALS

science.org/doi/10.1126/science.add1236
Figs. S1 to S18
Table S1
MDAR Reproducibility Checklist
Data S1 to S8

NANOFLUIDICS

Neuromorphic functions with a polyelectrolyte-confined fluidic memristor

Tianyi Xiong[1,2], Changwei Li[1,3], Xiulan He[1], Boyang Xie[1,2], Jianwei Zong[1,2], Yanan Jiang[4], Wenjie Ma[1], Fei Wu[1], Junjie Fei[3], Ping Yu[1,2]*, Lanqun Mao[1,4]*

Reproducing ion channel–based neural functions with artificial fluidic systems has long been an aspirational goal for both neuromorphic computing and biomedical applications. In this study, neuromorphic functions were successfully accomplished with a polyelectrolyte-confined fluidic memristor (PFM), in which confined polyelectrolyte–ion interactions contributed to hysteretic ion transport, resulting in ion memory effects. Various electric pulse patterns were emulated by PFM with ultralow energy consumption. The fluidic property of PFM enabled the mimicking of chemical-regulated electric pulses. More importantly, chemical-electric signal transduction was implemented with a single PFM. With its structural similarity to ion channels, PFM is versatile and easily interfaces with biological systems, paving a way to building neuromorphic devices with advanced functions by introducing rich chemical designs.

The development of artificial systems with brainlike functions (i.e., neuromorphic devices) is rapidly expanding because of their promising applications in neuromorphic computing (1, 2), bioinspired sensorimotor implementation (3, 4), brain–machine interfaces (5, 6), and neuroprosthetics (7, 8). So far, neuromorphic functions with diverse patterns have been achieved and incorporated into applications in various ways, mainly with history-dependent solid-state resistance-switchable devices, including two-terminal memristors (9–11) and three-terminal transistors (12, 13). However, most of the neuromorphic functions achieved thus far are based on the emulation of the electric pulse pattern using solid-state devices. An analog to the biological synapse—especially the emulation of a chemical synapse in a solution-based context—remains very challenging with these solid-state devices. In this regard, a fluidic-based memristor is highly desirable to achieve neuromorphic functions in an aqueous environment, because of its superior compatibility with biological systems and the larger number of functions endowed to the neuromorphic devices by introducing diverse chemistries (14).

Previous attempts have revealed that ion-based micro- or nanofluidic devices with advanced functionalities [e.g., the ion diode (15), ion transistor (16), or ion switch (17)] are achievable by confining an electrolyte into micro- or nanochannels. Several studies reported that these confined systems feature memresistance and memcapacitance (18–20). Moreover, long-term plasticity was obtained with nanochannels by introducing an ionic liquid–electrolyte interface (21). Despite these efforts, realizing neuromorphic functions in aqueous media is still a long-standing challenge, mainly because the strong shielding effect in an aqueous environment greatly hinders interionic interactions, thereby limiting the formation of memory in fluidic-based systems. In 2021, a milestone theoretical model predicted that ion memory functions could be accomplished with two-dimensional extremely confined channels (22), which has been experimentally realized by the same group (23).

Here, we report a polyelectrolyte-confined fluidic memristor (PFM) that can successfully accomplish various neuromorphic functions for mimicking not only electric pulse patterns but also chemical-electric signal transduction. Inspired by biological ion channels that function as natural memristors by controlling ion flux with spatial confinement and molecular recognition (24) (Fig. 1A), we designed and fabricated a polyimidazolium brush (PimB)–confined fluidic channel (Fig. 1B). We selected polyimidazolium because of its high charge density, rich chemistry, and versatile ability to recognize different anions (25). Typically, PimBs were grown onto the inner wall of the glass micro- or nanopipette by surface-initiated atomic transfer radical polymerization (26) (fig. S1, A and B). In this way, the fluid was confined by PimBs, in which the establishment of anion concentration equilibrium and charge balance between the inside and outside of PimBs under the stimulation of electric fields or chemicals would be hysteretic, resulting in history-dependent ion memory.

Polyelectrolyte-confined fluidic memristor

The device was constructed by a PimB-confined conically fluidic channel, an electrolyte, and, to complete the electric connection, two Ag/AgCl electrodes (fig. S1C). A triangle wave voltage was applied to the device to investigate the current-voltage (I-V) relationship. The rectified I-V curve was recorded with a modified micropipette (Fig. 1C, red) because of the geometric asymmetry of the conical channel and the anion selectivity of the positively charged PimB (26). Meanwhile, the pinched I-V curve collected under this periodic voltage with a nonzero cross-point voltage (V_{cp}) satisfied the history-dependent memristor nature according to Chua's theory (27). This offset (V_{cp}) originates from the influence of surface charge in this asymmetric channel (28), which is usually observed for biological memristors, such as the K^+ ion channel (29). In contrast, the bare micropipette only yields the linear ohmic I-V curve (Fig. 1C, blue), demonstrating the essential role of PimB in this pinched hysteretic loop.

We further investigated the dependence of current on voltage scanning frequency (i.e., scan rates, ν). The I-V curve experiences a transition from the hysteretic and rectified form at lower scan rates to the linear-like form at higher scan rates (Fig. 1D and fig. S2). The area (S) inside the hysteresis loop shrinks as the scan rate increases and degenerates to zero at infinite scan rate, as suggested by the fitting of the S-ν relationship (Fig. 1E and supplementary text). The pinched hysteresis loop, reduced loop area with increasing frequency, and the linear I-V relationship under infinite frequency satisfy three fingerprints of a memristor (29).

To explore the origin of memristive behavior of the PFM, we conducted dynamic monitoring of ion conductivity under different constant bias voltages (Fig. 1F). At a voltage equal to V_{cp} (53 mV), PFM maintains a static ion conductivity over time (Fig. 1F, yellow). At a voltage higher than V_{cp} (200 mV), the conductivity gradually increases to reach a plateau in ~2 s (Fig. 1F, red), whereas it decreases to leveling in 1 s at a voltage lower than V_{cp} (−200 mV) (Fig. 1F, blue). These results confirm that the ion conductivity change of PFM is a time-dependent process.

The conductivity change is closely associated with ion dynamic distribution inside the channel. We carried out finite element modeling (FEM) to describe the changes of ion distribution over time under different bias voltages (supplementary text and fig. S3A).

[1]Beijing National Laboratory for Molecular Sciences, Key Laboratory of Analytical Chemistry for Living Biosystems, Institute of Chemistry, Chinese Academy of Sciences (CAS), Beijing 100190, China. [2]School of Chemical Sciences, University of Chinese Academy of Sciences, Beijing 100049, China. [3]Key Laboratory of Environmentally Friendly Chemistry and Applications of Ministry of Education, College of Chemistry, Xiangtan University, Xiangtan 411105, China. [4]College of Chemistry, Beijing Normal University, Beijing 100875, China.
*Corresponding author. Email: yuping@iccas.ac.cn (P.Y.); lqmao@bnu.edu.cn (L.M.)

Fig. 1. Conductivity changes of PFM. (**A** and **B**) Schematic illustration of the neural functions realized by interaction-gated ion current in biological neurons (A) and a PimB-confined fluidic system (B). (**C**) *I-V* curves of PFM (red) and a bare micropipette (blue) in 10 mM KCl aqueous solution under a triangle wave with a scan rate of 50 mV/s. The hysteresis loop area is shaded in purple. The arrows show the scan direction. (**D**) *I-V* curves of PFM in 10 mM KCl under triangle waves with a fast (10 V/s, red) and a slow (10 mV/s, blue) scan rate. (**E**) Plot of the hysteresis loop area (*S*) with scan rate (ν). (Inset) Zoom-in of the plot at low-scan rate. (**F**) Time-dependent conductivity changes of PFM in 10 mM KCl under a constant bias voltage equal to V_{cp} (53 mV, yellow), higher than V_{cp} (+200 mV, red), and lower than V_{cp} (−200 mV, blue). (**G**) Simulated *I-t* curves of PFM in 10 mM KCl under +1 V (top) and −1 V (bottom) bias voltages. (**H**) Schematic illustration of time-dependent ion redistribution processes in PFM at potentials higher than V_{cp} (from I to III) and lower than V_{cp} (from I to V).
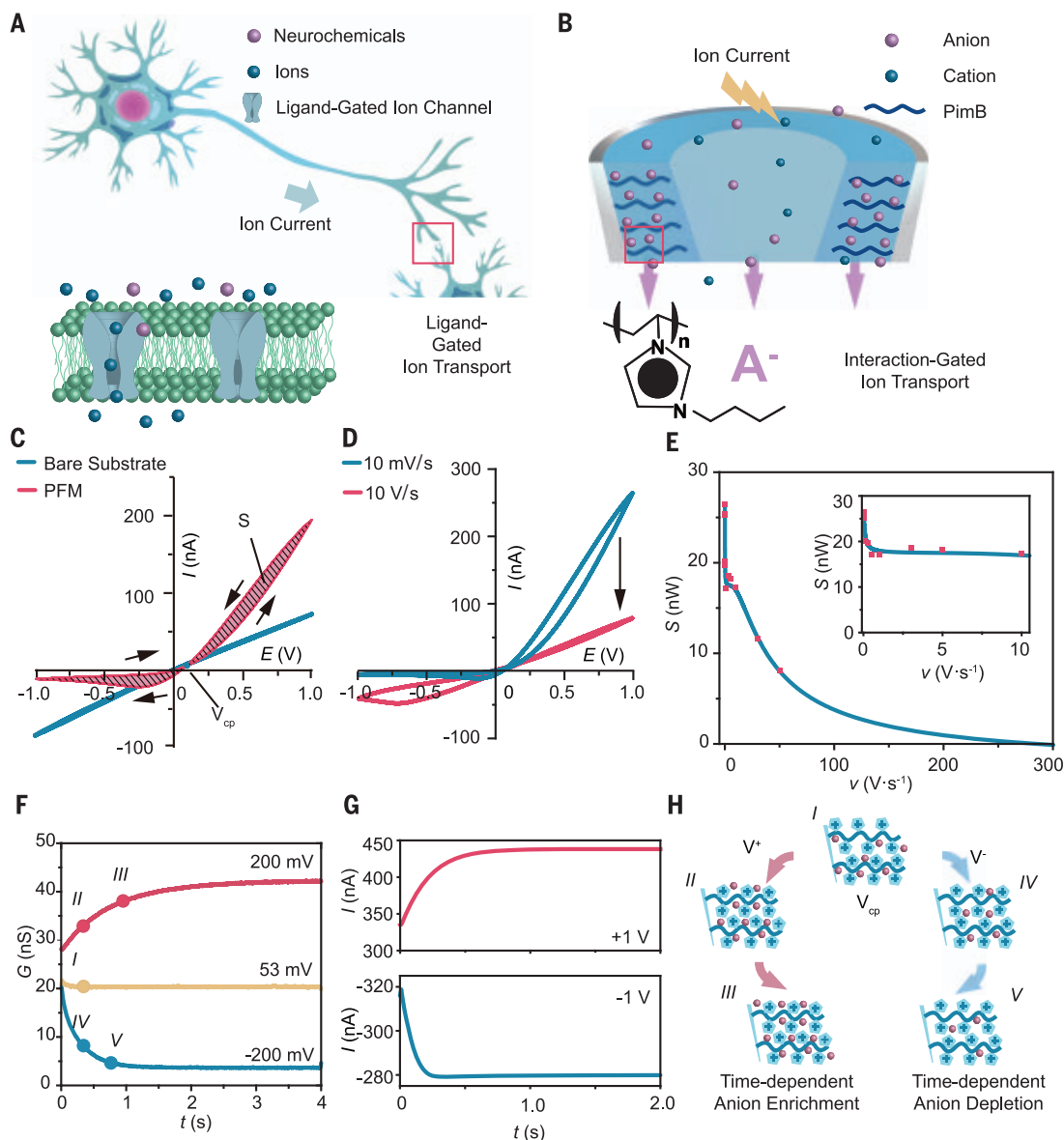
Without a bias voltage, cation (K^+) and anion (Cl^-) concentrations in the bulk layer are balanced to maintain charge neutrality, which are equal to the bulk electrolyte concentration (fig. S3B). While in the positively charged PimB layer, Cl^- ions overwhelm K^+ ions with a high concentration (~104.5 mM) owing to the strong electrostatic attraction between anions and the imidazolium moieties (fig. S3B). This high surface charge density of the PimB confers large anion storage, and the anions in PimB have relatively slow diffusion dynamics, necessitating prolonged enrichment of Cl^- in the PimB layer from the rest state to reach steady ion distribution at +1 V (Fig. 1H and fig. S3C). Therefore, the ion current undergoes a gradual increase to its steady state (Fig. 1G, red). Similarly, the slowed depletion of Cl^- in the PimB layer at −1 V (Fig. 1H and fig. S3D)

results in the gradual decrease of ion current (Fig. 1G, blue). These simulated consequences match well the temporal profiles of ion conductivity at constant bias potentials (Fig. 1F), suggesting that the relatively slow diffusion dynamics of anions into and out of the PimBs leads to time-dependent ion memory and, consequently, the memristive behavior of the device.

Mimicking short-term plasticity patterns with PFM

To mimic short-term plasticity (STP) electric pulse patterns, we applied paired voltage pulses to the PFM and recorded current spikes in accordance with pulsed stimulations. As shown, two continuous pulses of +2 or −2 V induce a current increase (ΔI = 8.9 nA), called a paired-pulse facilitation (PPF; Fig. 2A), or a signifi-

cant current decline (ΔI = −48.4 nA), called a paired-pulse depression (PPD; Fig. 2B), validating the capability of PFM in emulating the STP electric pulses. FEM simulation of ion dynamics under the same pulsed voltage waveforms reproduces the similar trends of current change (Fig. 2C), further demonstrating that STP electric pulses originated from time-dependent ion redistribution in PFM. The applied voltage drives the ion concentration polarization in the PimB layer that gives rise to the observed current spike. Upon removal of the external electric field (i.e., at the pulse interval), slow anion diffusion dynamics in the PimB layer would briefly hold the ion concentration polarization state owing to the strong interaction between Pim and anions. Hysteretic ion redistribution during the pulse interval continues to influence the anion enrichment or depletion in
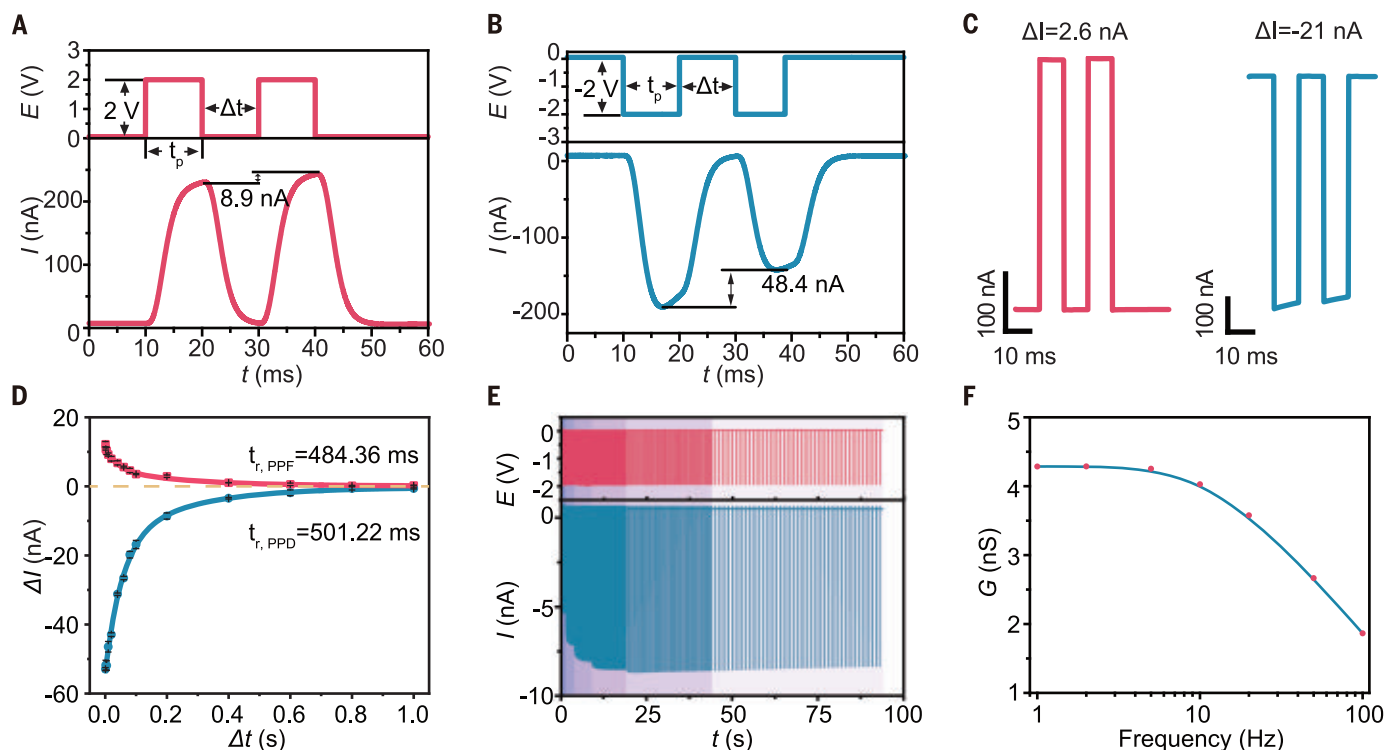
Fig. 2. STP electric pulses of PFM. PPF (**A**) and PPD (**B**) of PFM in 10 mM NaCl. The upper plots show voltage pulse waveforms. (**C**) The simulated I-t responses with FEM under the same voltage waveforms in (A) (red) and (B) (blue). (**D**) Plots of current changes (ΔI) with the paired pulse intervals (Δt) under positive ($V = +2V$, $t_p = 10$ ms, red) and negative ($V = -2V$, $t_p = 10$ ms, blue) bias voltages. Error bars present standard deviation of three measurements with the same device. (**E**) Current responses under voltage pulse train ($V = -2$ V, $t_p = 5$ ms) with varying frequency from 1 to 100 Hz. (**F**) Plot of conductivity versus the applied voltage pulse frequency.

the PimB layer when a voltage pulse was applied again, leading to the conductivity (or ion current) level up or down of the next spike, thus enabling the mimicking of STP electric pulses with the PFM. This conductivity change is strongly related to the pulse interval (Δt) following a biexponential relationship

$$\Delta I = A_1 e^{-\left(\frac{\Delta t}{\tau_1}\right)} + A_2 e^{-\left(\frac{\Delta t}{\tau_2}\right)} \quad (1)$$

where τ_1 and τ_2 are two time constants that might be related to the ion redistribution in the bulk and PimB layer, respectively; and A_1 and A_2 are the weights of these two dynamic processes. Shortening of the voltage pulse interval (Δt) leads to increased current change (ΔI), whereas a prolonged voltage pulse interval results in reduced ΔI. This decline dynamics emulates the change of synaptic weight in shaping biological STPs under repeated stimuli of varying frequencies (30). We then calculated the retention time (t_r) of PFM, defined as the pulse interval where ΔI drops to 5% of its maximum ($\Delta I_{\Delta t=t_r} = 5\% \Delta I_{\Delta t=0}$). For a certain voltage pulse stimulation (e.g., $V = \pm2$ V, $t_p = 10$ ms), t_r was calculated to be ~500 ms (Fig. 2D and table S1; $t_r = 484.36$ ms for facil-

itation and $t_r = 501.22$ ms for depression) in 10 mM NaCl aqueous solution. These values of PFM are comparable to those of STP in biological systems (table S1), where facilitation and depression of the synaptic weight occurs on a 10^2-ms scale (30).

We further validated the ability of the PFM to emulate dynamic filtering functions in sensory neurons. By applying a negative voltage pulse train with the pulse frequency ranging from 1 to 100 Hz ($V = -2$ V, $t_p = 5$ ms; Fig. 2E), frequency-dependent conductivity was obtained (Fig. 2F). The minor difference in the frequency of the voltage pulse train (e.g., 19, 20, or 21 Hz) could be differentiated by the conductivity differences with this filtering function (fig. S4). In addition, programming voltage pulses ($V_{set} = +2$ V, $V_{reset} = -0.6$ V) causes an analog ion conductivity switch among 100 continuous states. The device maintains good performance after 30,000 setreset tests (fig. S5), demonstrating the endurance of the PFM. Energy consumption (W) of the PFM was calculated on the basis of the integration of I-t responses under single voltage pulses with $W = \int VI dt$, which was closely related to the orifice size of the pipette and the applied voltage (fig. S6, A and B). For a 150-nm-

diameter nanopipette-based device, energy consumption under voltage stimulation of −100 mV ($t_p = \Delta t = 10$ ms) is 0.66 pJ per spike (fig. S6C), which is close to the biological voltage (−70 mV) and energy consumption (31). In contrast to most of the reported memristors that require high voltages, our PFM can operate at the voltage and energy consumption as low as those biological systems (table S2), demonstrating its potential for application in bioinspired sensorimotor implementation and neuroprosthetics.

Chemical-regulated STP electric pulses

Neurons work in a complex chemical environment wherein ions and molecules lay the foundations for all neuroactivities. Changes in the chemical environment fundamentally contribute to manifold behaviors of neurons, including synaptic scaling induced by N-methyl-D-aspartate (32) and enhanced transmission induced by neurotrophins (33). This chemical modulation effect was emulated with the PFM by tuning the Pim–anion interactions. The I-V curves collected in different electrolyte solution (NaCl, NaBF₄, or NaClO₄) illustrate the dependence of hysteresis loop area (S) on the species of anions (Fig. 3A). We then investigated
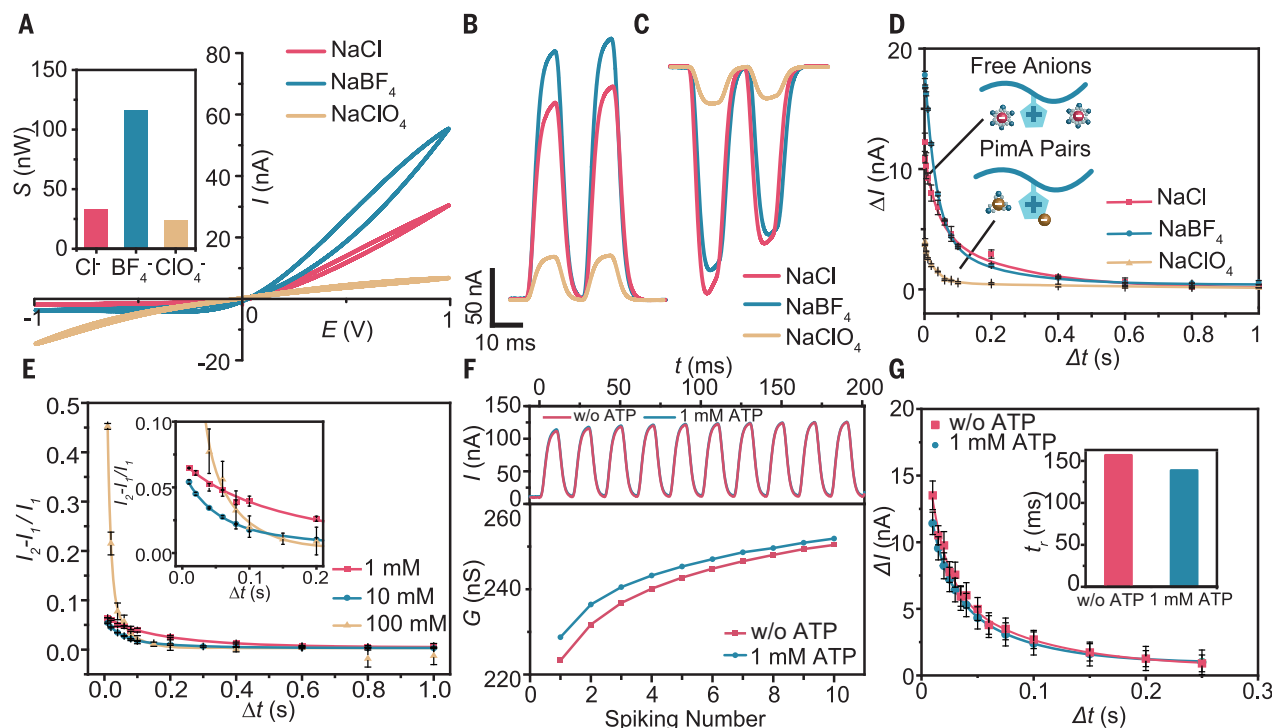
Fig. 3. Chemical-regulated STP electric pulses. (**A**) *I*-*V* curves of PFM in 10 mM NaCl, NaBF$_4$, or NaClO$_4$ solution with a scan rate of 50 mV/s. (Inset) The hysteresis loop area (*S*) from the *I*-*V* curves. (**B** and **C**) PPF (B) and PPD (C) of PFM in different electrolyte solutions. (**D**) Plots of current changes with pulse intervals in different electrolyte solution (*V* = −2 V, t_p = 10 ms). (Inset) Schematic illustration of free anions and PimA pairs. (**E**) Plots of normalized current changes with pulse intervals in KCl solutions with different concentrations (*V* = −2 V, t_p = 10 ms). (Inset) Zoom-in of the plot at short pulse intervals. (**F**) Current spikes (top) and conductivity changes (bottom) of PFM in phosphate-buffered saline (pH 7.4) with (blue) and without (red) 1 mM ATP under a 10-pulse train (*V* = +0.5 V, Δ*t* = t_p = 10 ms). (**G**) Plots of current changes (Δ*I* = I_{10} − I_1) under a 10-pulse train (*V* = +0.5 V, t_p = 10 ms) with pulse intervals. (Inset) Values of retention time with (blue) and without (red) 1 mM ATP in solution. Error bars in (D), (E), and (G) present standard deviation of three measurements with the same device.

the chemical regulation of STP by different anions (*V* = ±2 V, Δ*t* = t_p = 10 ms). Compared with that in NaCl aqueous solution (Fig. 3, B and C, red), the PFM in NaBF$_4$ solution exhibits stronger PPF and slightly attenuated PPD (Fig. 3, B and C, blue). Both effects were attenuated in NaClO$_4$ solution (Fig. 3, B and C, yellow). Moreover, t_r is related to the chemical environment, as revealed by the biexponential dynamic curve with different anion species (Fig. 3D and fig. S7A). The value of t_r decreases in the order of $t_{r,ClO_4^-} < t_{r,BF_4^-} < t_{r,Cl^-}$ both for positive and negative voltage pulse stimulation (table S1). In addition, the STP performance of the PFM could be regulated by the ionic strength. High-concentration electrolyte accelerates the disappearance of STP (the lower t_r) under either positive or negative voltage pulse stimulation (Fig. 3E, fig. S7B, and table S1).

To provide in-depth insights into the mechanism of this dependence between ion species or concentration and STP performance of the PFM, we used the Dukhin number at the pipette tip (Du$_0$) to evaluate the surface conductivity changes in the system. Larger Du$_0$ indicates that there are more anions partici-

pating in the ion redistribution to intensify memristive effect, and vice versa. The influence of Pim–anion interactions on Du$_0$ at steady state without bias voltages is described by the following equation

$$\text{Du}_0 = K C_A^{-1} \left(1 + \frac{k_2}{k_1} C_A \right)^{-1} \quad (2)$$

where, *K* is a structural constant of the PFM, C_A is the anion concentration of electrolyte, and k_1 and k_2 are the dissociation and association kinetic constants, respectively (see supplementary text). Here, the value of k_2/k_1 is closely related to the hydration energy of anions (*25*). For anions with a larger hydration energy, the value of k_2/k_1 would be lower, yielding a larger value of Du$_0$. The Cl$^-$ bears the highest hydration energy ($\Delta H^0_{Hyd,ClO_4^-} < \Delta H^0_{Hyd,BF_4^-} < \Delta H^0_{Hyd,Cl^-}$) and thus the largest value of Du$_0$. That is, more free Cl$^-$ counterions in the PimB layer participate in the redistribution process (Fig. 3D, inset, top), resulting in longer retention time ($t_{r,ClO_4^-} < t_{r,BF_4^-} < t_{r,Cl^-}$). For ions with lower hydration energy, such as BF$_4^-$ and ClO$_4^-$, the increased k_2/k_1 value results in a smaller Du$_0$. This means that more

BF$_4^-$ and ClO$_4^-$ counterions in the PimB layer exist in the form of imidazolium–anion (PimA) pairs than do Cl$^-$ counterions, resulting in a decrease of mobile anions participating in the ion redistribution in the PFM (Fig. 3D, inset, bottom, and supplementary text), and consequently the shorter retention time. Increasing the ion concentration also leads to the Du$_0$ decrease according to Eq. 2, explaining the change of retention time with ion strength. These chemical-regulated STP changes hold promise for the possibility of realizing neuromorphic functions with the synergism of multiple ion species, which is almost impossible for solid-state systems.

We further exploited bioactive molecules to modulate STP patterns in a complex environment stimulated by mild voltage pulses. In a physiological electrolyte (i.e., phosphate-buffered saline solution, pH 7.4), the PFM maintains its STP characteristic under the stimulation of 10 voltage pulses (*V* = +0.5 V, Δ*t* = t_p = 10 ms) (Fig. 3F, red), validating the PFM in biological environment. More importantly, when 1 mM adenosine triphosphate (ATP) was added into the solution, reduced conductivity changes were observed (Fig. 3F),
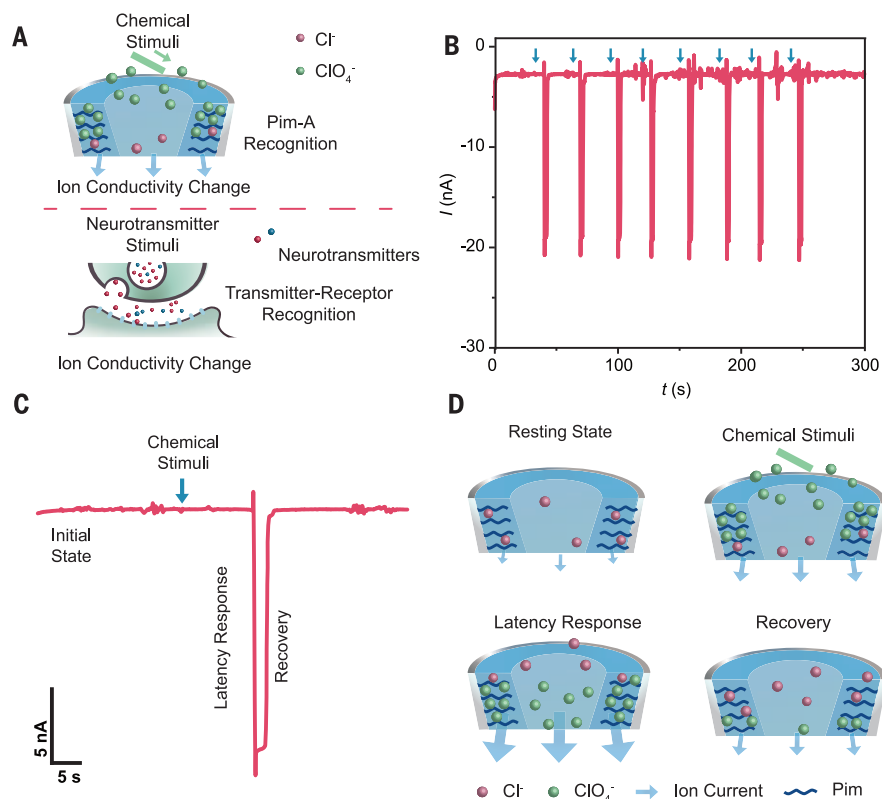
Fig. 4. Chemical-electric signal transduction of PFM. (**A**) Schematic illustration of the chemical-electric transduction of PFM (top) and biological synapses (bottom). (**B**) Electric pulse response of PFM under the stimulation of ClO_4^-. The blue arrows indicate the delivery of ClO_4^-. (**C**) Zoom-in of a single electric pulse. (**D**) Schematic illustration of the ion distribution changes in the PFM when chemical stimuli were delivered into the system.

comparison, no current spike occurs after injection of pure NaCl solution with the same stimulation time (fig. S8A). The PFM shows the capability of individually accomplishing transduction from chemical stimuli of certain species to electric pulse signals.

Moreover, the ion current pulses induced by chemical stimulation show typical spiking latency behavior. A time lapse was observed between the stimulation and the occurrence of neuromorphic spikes (Fig. 4, B and C). When stimulation intensity increases, the time lapse decreases accordingly (fig. S8, B and C). The spiking latency behavior in real neurons plays a key role in encoding input strength with spike timing (*36*), this result thus provides the possibility for encoding chemical stimulations based on PFM.

Discussion

In this work, we have experimentally demonstrated a fluidic memristor with neuromorphic functions by using polyelectrolyte-confined fluidic structure, which features the typical fingerprints of a memristor. The time-dependent ion redistribution controlled by Pim–anion interactions under spatial confinement contributes to the ion memory. The as-fabricated PFM features the powerful ability to mimic STP electric pulse patterns with retention time and energy consumption comparable to those of the ion channels in biological systems. More importantly, the fluidic-based ion redistribution dynamics can endow the PFMs with neuromorphic function versatility that is hardly achievable with solid-state devices, offering the opportunity to introduce specific chemical regulation pathways to neuromorphic functions. Even more impressively, the emulation of chemical-electric signal transduction can be accomplished with this device. Compared with neuromorphic devices based on other mechanisms, our fluidic-based device offers not only performances comparable to biological systems but also more advanced neuromorphic functionalities, especially chemical-related functions (table S2).

Although the as-presented PFM features a series of advantages—diversity in neuromorphic functions, the possibility of regulation and coexistence of multiple ion carriers, and convenient interfacing with biological systems—big challenges remain on the way toward realizing broader applications for PFMs. For example, realizing long-term plasticity functions is a key goal for fluidic-based systems, where the introduction of much stronger (even irreversible) interfacial recognition interactions (e.g., aptamers toward substrates) would be potentially helpful for prolonging ion memory. The scale-up of fluidic memristors for in-memory computing is another challenge, for which porous micro- or nanofluidic arrays might offer a solution.

along with a change in retention time from 156 ms to 138 ms (Fig. 3G). This phenomenon can also be well understood by Eq. 2 owing to the strong interaction of ATP with Pim (*34*). As indicated, the PFM may allow direct interfacing and communicating with biological systems, given that its neuroplastic behaviors are controllable by bioactive molecules.

Chemical-electric signal transduction with PFM

For biological systems, signal transduction at chemical synapses is mediated by the release and recognition of neurotransmitters (*35*) (Fig. 4A). Such a process is almost impossible to emulate with solid-state memristors, which hardly respond to external chemical stimulations. For fluidic-based devices with easily adaptable configurations, however, this chemical-electric signal transduction may be realized by tuning the behaviors of multiple ion species in the PimB-confined channel.

To achieve this target, a capillary controlled by a microinjector pump was inserted into the inner solution of the PFM, serving as the presynaptic neuron for the delivery of chemical stimuli. Herein, ClO_4^- was chosen as an "arti-

ficial neurotransmitter" for demonstration (Fig. 4A, top). When the chemical stimulus (ClO_4^-) was back-injected into the micropipette, a responsive electric pulse was observed (Fig. 4B), analogous to neural spikes induced by a neurotransmitter. Under a negative bias voltage (–1 V), the PFM holds at a low conductive state owing to the low anion concentration in the PimB layer, emulating the resting state of neurons. When the ClO_4^- anions were released from the capillary and transported to the sensitive tip region driven by electrophoresis and convective flow, formation of Pim-ClO_4^- pairs due to the stronger interaction between Pim and ClO_4^- would decrease the effective surface charge density, further hindering the depletion of anions in PimB layers, resulting in the increase of ion current under negative voltage (*25, 26*). This phenomenon is similar to the opening of postsynaptic ion channels activated by neurotransmitters. Then, electrophoresis and electroosmotic flow drive Cl^- ions moving toward the tip, and the subsequent dissociation of Pim-ClO_4^- pairs brings the current back to the initial state, emulating the clearance of transmitters (Fig. 4, C and D). In

REFERENCES AND NOTES

1. Z. Wang et al., Nat. Rev. Mater. 5, 173–195 (2020).
2. M. A. Zidan, J. P. Strachan, W. D. Lu, Nat. Electron. 1, 22–29 (2018).
3. Y. Lee et al., Sci. Adv. 4, eaat7387 (2018).
4. X. Zhang et al., Nat. Commun. 11, 51 (2020).
5. S. T. Keene et al., Nat. Mater. 19, 969–973 (2020).
6. T. Wang et al., Nat. Electron. 5, 586–595 (2022).
7. Y. Kim et al., Science 360, 998–1003 (2018).
8. S. Kim et al., Sci. Adv. 7, eabe3996 (2021).
9. D. B. Strukov, G. S. Snider, D. R. Stewart, R. S. Williams, Nature 453, 80–83 (2008).
10. Z. Wang et al., Nat. Mater. 16, 101–108 (2017).
11. Q. Xia, J. J. Yang, Nat. Mater. 18, 309–323 (2019).
12. Y. van de Burgt et al., Nat. Mater. 16, 414–418 (2017).
13. E. J. Fuller et al., Science 364, 570–574 (2019).
14. C. E. G. Hoskin, V. R. Schild, J. Vinals, H. Bayley, Nat. Chem. 14, 650–657 (2022).
15. C. Wei, A. J. Bard, S. W. Feldberg, Anal. Chem. 69, 4627–4633 (1997).
16. R. A. Lucas, C.-Y. Lin, L. A. Baker, Z. S. Siwy, Nat. Commun. 11, 1568 (2020).
17. M. R. Powell, L. Cleary, M. Davenport, K. J. Shea, Z. S. Siwy, Nat. Nanotechnol. 6, 798–802 (2011).
18. D. Wang et al., J. Am. Chem. Soc. 134, 3651–3654 (2012).
19. Q. Sheng, Y. Xie, J. Li, X. Wang, J. Xue, Chem. Commun. 53, 6125–6127 (2017).
20. J. S. Najem et al., ACS Nano 12, 4702–4711 (2018).
21. P. Zhang et al., Nano Lett. 19, 4279–4286 (2019).
22. P. Robin, N. Kavokine, L. Bocquet, Science 373, 687–691 (2021).
23. P. Robin et al., arXiv:2205.07653 [cond-mat.soft] (2022).
24. V. M. Ho, J.-A. Lee, K. C. Martin, Science 334, 623–628 (2011).
25. X. He et al., Angew. Chem. Int. Ed. 57, 4590–4593 (2018).
26. X. He et al., J. Am. Chem. Soc. 139, 1396–1399 (2017).
27. L. Chua, IEEE Trans. Circuit Theory 18, 507–519 (1971).
28. D. Wang et al., ChemElectroChem 5, 3089–3095 (2018).
29. L. Chua, G. Ch. Sirakoulis, A. Adamatzky, Eds., Handbook of Memristor Networks (Springer, 2019).
30. R. S. Zucker, W. G. Regehr, Annu. Rev. Physiol. 64, 355–405 (2002).
31. S. B. Laughlin, R. R. de Ruyter van Steveninck, J. C. Anderson, Nat. Neurosci. 1, 36–41 (1998).
32. D. Stellwagen, R. C. Malenka, Nature 440, 1054–1059 (2006).
33. H. Thoenen, Science 270, 593–598 (1995).
34. K. Zhang et al., Sci. China Chem. 63, 1004–1011 (2020).
35. A. E. Pereda, Nat. Rev. Neurosci. 15, 250–263 (2014).
36. E. M. Izhikevich, IEEE Trans. Neural Netw. 15, 1063–1070 (2004).
37. T. Xiong et al., Data for: Neuromorphic functions with a polyelectrolyte-confined fluidic memristor, Dryad (2022); https://doi.org/10.5061/dryad.d2547d85r.

NANOFLUIDICS

Long-term memory and synapse-like dynamics in two-dimensional nanofluidic channels

P. Robin[1]†, T. Emmerich[1]†, A. Ismail[2,3]†, A. Niguès[1], Y. You[2,3], G.-H. Nam[2,3], A. Keerthi[2,4], A. Siria[1], A. K. Geim[2,3], B. Radha[2,3]*, L. Bocquet[1]*

Fine-tuned ion transport across nanoscale pores is key to many biological processes, including neurotransmission. Recent advances have enabled the confinement of water and ions to two dimensions, unveiling transport properties inaccessible at larger scales and triggering hopes of reproducing the ionic machinery of biological systems. Here we report experiments demonstrating the emergence of memory in the transport of aqueous electrolytes across (sub)nanoscale channels. We unveil two types of nanofluidic memristors depending on channel material and confinement, with memory ranging from minutes to hours. We explain how large time scales could emerge from interfacial processes such as ionic self-assembly or surface adsorption. Such behavior allowed us to implement Hebbian learning with nanofluidic systems. This result lays the foundation for biomimetic computations on aqueous electrolytic chips.

Over the past decade, research in nanofluidics has shed light on many unconventional phenomena arising in the transport of water and ions through nanometric channels (1–12). The field has grown at a fast pace, driven by the discovery of previously unknown fundamental behaviors of aqueous transport at nanoscale, and also by potential applications, from water desalination to energy harvesting (2). Most notably, the recent development of two-dimensional (2D) channels, made by van der Waals assembly of various materials [graphite, hexagonal boron nitride, molybdenum disulfide (MoS_2), etc.], has enabled the study of ionic transport at the smallest scales, with unmatched versatility in terms of geometry or surface properties (13–16). Specifics of 2D interactions offer a new asset to fine-tune the properties of electrolytes, at odds with their bulk response. A recent, notable prediction is that 2D ionic self-assembly should be at the root of memory effects associated with conductance hysteresis under electrical forcing (17), a phenomenon known

as the memristor effect. This effect could allow the emulation of the brain's neuronal computation using ions in water as charge carriers, but artificial systems capable of mimicking this behavior have eluded experimental inquiry in aqueous electrolytes until now.

A memristor—short for memory resistor—is a resistor with an internal state that is susceptible to change depending on the history of voltage seen by the system, thereby modifying its conductance (18, 19). As this feature makes them the analogs of biological synapses, memristors have drawn considerable attention for their potential use as building blocks of bioinspired neuromorphic computers (20). However, most of the existing examples are based on solid-state devices (such as the metallic-insulator-metallic architecture) and function with coupled ion and electron dynamics (21). Although a handful of fluidic memristors were also designed (22–24), they require high voltage to operate, well above the water-splitting threshold (1.23 V with respect to a normal hydrogen electrode), use nonaqueous environments, or far exceed the nanoscale dimensions of biological systems. More generally, a challenge is to replicate the mechanism found in biological systems, where the transport and accumulation of solvated ions (notably calcium) in water are used for signalization, information processing, and the building of memory (25, 26). Developing such bioinspired memristors would enable the designing of

[1]Laboratoire de Physique de l'Ecole normale Supérieure, ENS, Université PSL, CNRS, Sorbonne Université, Université de Paris, Paris, France. [2]National Graphene Institute, The University of Manchester, Manchester, UK. [3]Department of Physics and Astronomy, The University of Manchester, Manchester, UK. [4]Department of Chemistry, The University of Manchester, Manchester, UK.
*Corresponding author. Email: lyderic.bocquet@ens.fr (L.B.); radha.boya@manchester.ac.uk (B.R.)
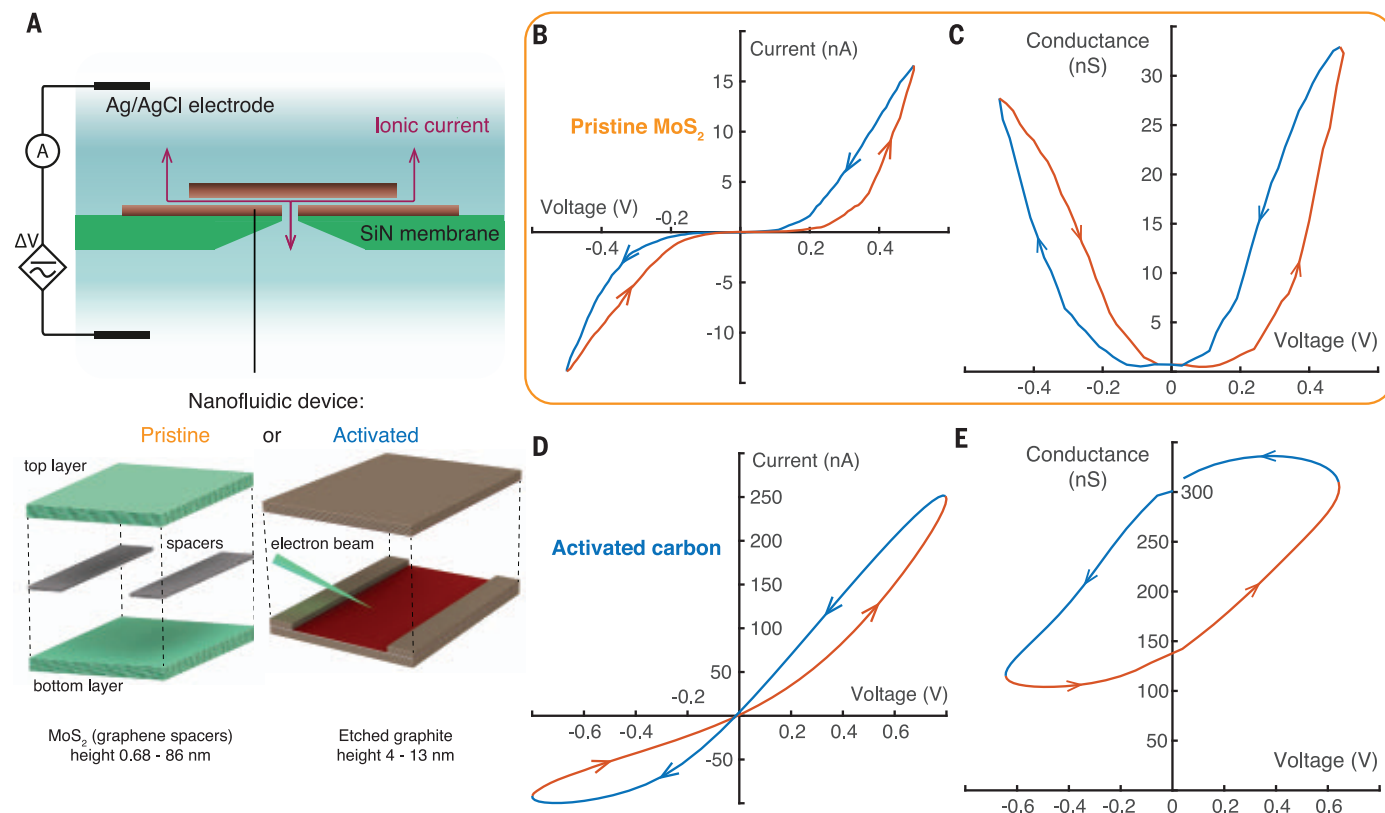†These authors contributed equally to this work.

Fig. 1. Experimental study of the memristor effect using two kinds of nanofluidic devices. (**A**) Sketch of the nanofluidic cell. A nanochannel was deposited on a membrane separating two reservoirs filled with an electrolytic solution. The red arrow indicates the path taken by water and ions across the system. We used two types of nanochannels: pristine MoS_2 channels (bottom left panel) and activated carbon channels (bottom right panel). (**B** and **C**) Typical examples of memristive current-voltage (*I-V*) and conductance-voltage (*G-V*) characteristics of a pristine MoS_2 channel (height h = 1 nm) under periodic voltage (triangular wave of frequency 8 mHz, using 3 M KCl). The *I-V* curve displays a loop that is pinched (but does not intersect) at the origin, and the *G-V* curve has a crossing point at zero voltage. (**D** and **E**) Typical examples of memristive current-voltage and conductance-voltage characteristics of an activated carbon channel (height h = 13 nm) under periodic voltage (sinusoidal wave of frequency 1 mHz, using 1 mM $CaCl_2$). Here, the *I-V* curve crosses itself at the origin, and the *G-V* curve takes the form of a simple loop. For all data, pH was not modified after salt dissolution in deionized water, resulting in a pH range of 5.1 to 5.5.

artificial nanofluidic chips for neuromorphic computation, the building of an interface between artificial nanofluidics and biological systems, and the exploration of possible gains in efficiency from using solvated ions as charge carriers. Here we report on a series of experiments demonstrating that 2D nanofluidic channels do open this avenue toward neuromorphic iontronics.

Experimental demonstration of nanofluidic memristors
Pristine MoS_2 channels versus activated carbon channels

In this work, we investigated two types of 2D nanochannels of similar geometry but different surface properties (Fig. 1A). "Pristine" channels, the first type, were made of two atomically smooth flakes of 2D material (here, MoS_2) separated by an array of multiple layers of graphene nanoribbons used as spacers. "Activated" carbon channels, the second type, consisted of two graphite flakes, in which a nanoscale trench was milled into the bottom flake using electron beam–induced etching (EBIE) (16). In both cases, the bottom wall of the channel was pierced and deposited on the aperture of a SiN_x membrane. Further details regarding the fabrication of activated and pristine channels can be found in (13) and (16), respectively, and are summarized in the supplementary materials (SM; figs. S1 and S2). Although similar in design, these channels differed on a few key properties. The height of pristine MoS_2 channels could be precisely controlled in increments of 0.34 nm and, here, down to 0.68 nm—the channel's depth corresponding to the spacers' thickness. Conversely, the depth of activated carbon channels was controlled by EBIE with a resolution limited to a few nanometers. As recently demonstrated by Emmerich *et al.* (16), the latter carries a much stronger surface charge compared with pristine walls, owing to the exposure of their bottom wall to the electron beam. We used activated carbon channels with a channel height of between 4 and 13 nm and pristine MoS_2 channels with a height of between 0.68 and 86 nm.

Once fabricated, the 2D channels were embedded in a fluidic cell connected to two reservoirs filled with an electrolyte (KCl, NaCl, LiCl, $CaCl_2$, $NiSO_4$, or $AlCl_3$). Salt concentrations between 1 mM and 3 M were tested. Unless stated otherwise, the solution's pH was not modified after salt dissolution in deionized water, resulting in a pH range of 5.1 to 5.5, depending on salt concentration. A patch-clamp amplifier (Keithley 2400 or 2600 Series) connected to Ag/AgCl electrodes allowed for ionic current measurements under imposed time-dependent voltage drop $V(t)$ of various frequencies (0.1 to 200 mHz), shapes (sinusoidal, triangular), and amplitudes (0.1 to 1 V). In each case, the channel's conductance $G(t)$ was determined from current measurements from an instantaneous Ohm's law $G(t) = I(t)/V(t)$. Further details regarding current measurements are reported in the SM. Typical
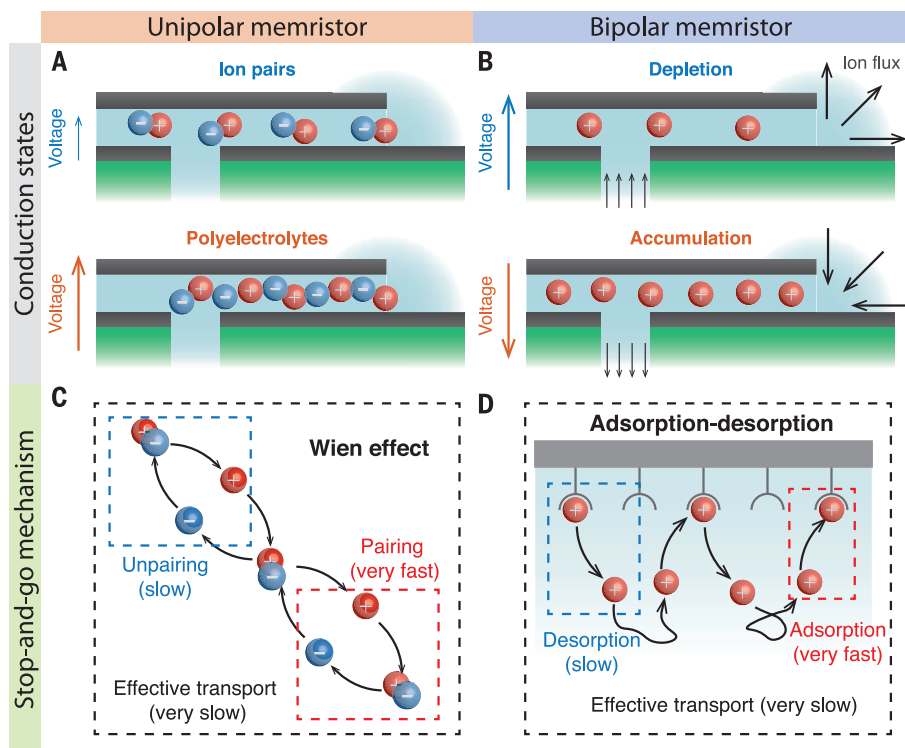
Fig. 2. Theory of nanofluidic memristors. (A and B) Description of the different conductance states explaining the memristor effect. (**A**) Wien effect as a source of the unipolar memristor effect. Under strong confinement, ions assemble into nonconducting Bjerrum pairs. Conduction can then occur through the breaking of pairs (Wien effect) or their clustering into conducting arcs (polyelectrolytic Wien effect), under the action of a strong electric field (regardless of sign). (**B**) Entry effects as a source of the bipolar memristor effect. The two mouths of the channel are asymmetric, resulting in ionic rectification depending on the side from which charges enter the system. If they enter from the side of low resistance, ions accumulate and conductance rises. Otherwise, the channel is depleted and conductance is lowered. As the channel's walls bear a strong negative charge, only positive ions are represented here. (**C** and **D**) Effective "stop-and-go" transport and long-term memory. In both mechanisms (Wien effect or geometrical asymmetry), the system's conductance state can be retained over large time scales if transport is governed by a stop-and-go motion, induced by repeated pairing-unpairing or adsorption-desorption events, respectively.

examples of experimental results for both types of systems are shown in Fig. 1.

Two types of memristors

Our central result is that 2D nanofluidic channels did exhibit a memristive effect (Fig. 1, B to E). When probed by a time-varying voltage, they displayed a nonlinear current-voltage (I-V) characteristic, which was pinched at zero voltage, associated with a conductance hysteresis. This pinched loop under periodic forcing is the hallmark of memristors (27). Such behavior was found in both types of channels—pristine and activated—for all tested electrolytes and at all salt concentrations (see SM for full results). The memristive effect was found to take place at frequencies between 0.1 and 200 mHz, well below frequencies where capacitive effects can introduce hysteresis. This result corresponds to dynamical time scales from seconds to hours. Moreover, the phenomenon was found to be robust and was ob-

served in a wide range of parameters—notably salt concentration, channel height, and pH (figs. S9 to S16). All tested salts displayed the same phenomenology. Specifically, we did not observe substantially different results with multivalent salts under the tested experimental conditions, suggesting that the materials used here (MoS_2 and activated carbon) are not subject to phenomena such as charge reversal that are commonly observed with divalent ions such as calcium (28). Our activated carbon channels typically displayed an overall conductance much higher than what could be expected from bulk estimates, owing to their high surface charge and hydrodynamic slippage (16).

Further, we could identify two types of memristors, depending on whether the current-voltage characteristics did or did not self-cross at the origin [compare Fig. 1B (pristine MoS_2 channel) and Fig. 1D (activated carbon channel)]. This fundamental difference is best illustrated by looking at the curve of conductance

as a function of voltage: It either displayed a twisted loop [with one crossing point (Fig. 1C)] or an open loop [no crossing point (Fig. 1E)]. Following the terminology introduced in (27), we classified our experimental data as follows: Systems that exhibited a self-crossing I-V curve (Fig. 1, D and E) were referred to as bipolar memristors. Conversely, those that instead displayed a self-crossing conductance-voltage (G-V) curve (Fig. 1, B and C) were referred to as unipolar memristors.

A key aspect of memristors is their ability to switch between different internal conductance states. We observed that bipolar memristors changed conductance state when the polarity of voltage was reversed, with, for example, maximum conductance at +1 V and minimum conductance at −1 V (Fig. 1E)—thus the name "bipolar." On the other hand, unipolar memristors generally exhibited symmetric I-V and G-V curves that were strongly nonlinear when the amplitude of voltage was increased. Their conductance only weakly depended on voltage polarity but could vary by up to two orders of magnitude between voltage $V = 0$ and $V = \pm 1$ V (Fig. 1C)—thus the name "unipolar." Together, these facts indicate that the possible internal states of unipolar and bipolar memristors were fundamentally different.

In addition, thinner pristine devices (with a channel height $h < 10$ nm) could display either kind of behavior, depending on salt concentration (with unipolar memristors at 0.1 M or higher). Thicker pristine MoS_2 channels, on the other hand, only displayed a weak bipolar memristor effect; however, the memory effect was not as notable as that observed in thinner channels, implying that confinement in a 2D geometry is essential for attaining memory effects. Lastly, the phenomenon was found to be weakened at acidic pH in both types of systems. All corresponding data are provided in the SM (figs. S9 to S16).

This comparison sheds light on a possible explanation. Bipolar memristors were observed for high surface charges (as found in activated carbon channels) and low salt concentration—in other words, for surface-dominated conduction. In contrast, unipolar memristors were observed for moderate surface charge (pristine MoS_2 channels), high salt concentration, and strong confinement; these results corresponded to a "confinement-dominated" regime. In both cases, a prerequisite for memory effects was the system's ability to display nonlinear ion transport. Accordingly, we next focus on the description of the system's various conductance states as a function of applied voltage.

Two sources of nonlinearity: Collective ionic transport and ionic rectification

The above observations suggested the existence of two distinct mechanisms behind the
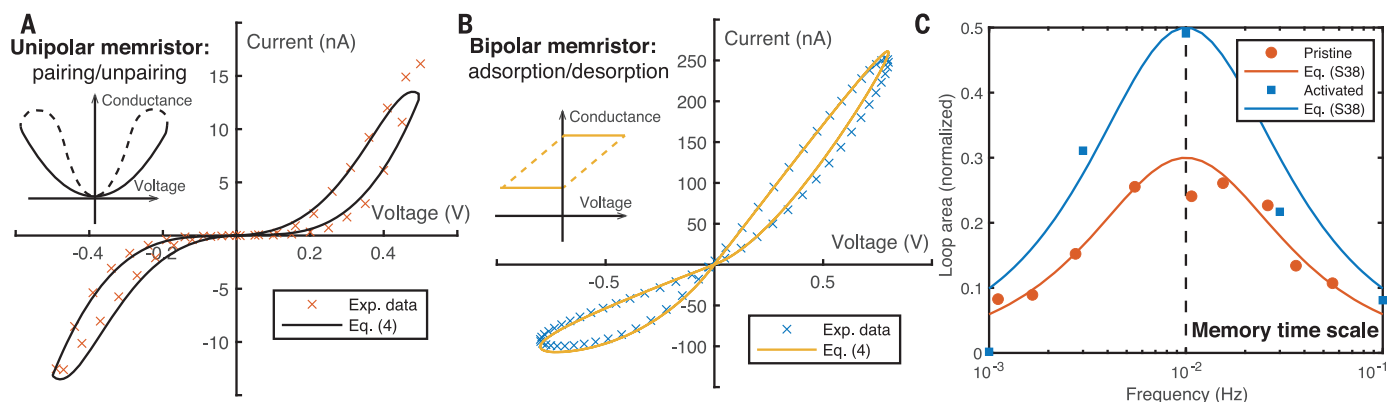
Fig. 3. Comparison of theoretical models and experimental results. (A and B) Fit of experimental *I-V* curves using the minimal model of the nanofluidic memristor. For unipolar memristors (**A**), the quasistatic conductance was taken to be a power law of applied voltage (here with exponent $\alpha = 2$), and a sign-dependent constant in the bipolar case (**B**) (see insets). The experimental curves were then fitted using the delay time τ as single free parameter (see Eq. 4). Datasets correspond to devices presented in Fig. 1, B to E: 3 M KCl in pristine MoS$_2$ channel (height $h = 1$ nm) or 1 mM CaCl$_2$ in activated carbon channel (height $h = 13$ nm). (**C**) Normalized area of the *I-V* loop as a function of voltage frequency. Data correspond to 100 mM CaCl$_2$ in 4 nm activated carbon channel and 1 M KCl in 0.68 nm pristine MoS$_2$ channel. The memory time scale τ_m could be extracted from experimental data by looking for the frequency where the loop was the largest. The curve of the loop area as a function of frequency was well described by that of the minimal model [see eq. S38 in the SM; solid lines]. See fig. S8 for the normalization process.

memristive behavior of nanofluidic channels. Unipolar memristors only existed in thin channels ($h < 10$ nm) and at high salt concentration ($c \geq 0.1$ M), and the corresponding experimental results directly echoed the theoretical mechanisms discussed in (*17*). In this picture, a nonlinear response can be accounted for by the formation of tightly bound Bjerrum pairs of ions if confinement is sufficiently strong (and the solution not too diluted), preventing conduction (Fig. 2A). The application of a sufficiently strong electric field can break these pairs or assemble them into an arc-like polyelectrolyte, allowing, in both cases, electrical current to flow, a process known as the (second) Wien effect. As a result, the system's conductance G is a strongly nonlinear function of voltage V that almost vanishes in the absence of voltage, behaving as

$$G(V) \propto |V|^{\alpha} \qquad (1)$$

with a predicted exponent $\alpha > 1$, and usually around 2 [see SM, section 3, and (*17*) for the derivation]. We can take into account the fact that not all ions may be paired up by adding a small constant term $G_0 = G(V = 0)$ into the above equation. This mechanism is independent of voltage sign and thus does correspond to a unipolar memristor. It also allows the conductance to vary continuously over a large range of values, accounting for experimental observations. In theory, this process can only take place in thinner channels—those less than 2 nm in thickness—as Bjerrum pairs only exist under strong confinement. In practice, the transition from unipolar to bipolar behavior was found to take place around a thickness of 10 nm. A possible explanation for this robustness is that ion pairs could still exist in the few water layers next to the channel's walls, even in slightly larger channels; in particular, the presence of a wall tends to lower the dielectric constant of the first water layers (*29*), and ions are thus expected to experience stronger electrostatic interactions near surfaces. If that is the case, then ionic pairing near solid surfaces could be relevant in other contexts, and their dynamics could be probed for with similar time-varying voltage.

On the other hand, bipolar devices changed state depending on the polarity of the applied voltage, and their memory should therefore stem from an internal asymmetry. However, in some experimental conditions, pristine MoS$_2$ channels did display this kind of hysteresis despite their internal surface being atomically smooth and controlled. Therefore, we attributed the source of asymmetry to entrance effects. By construction, the SiN$_x$ membrane was present on one side of the device only (Fig. 1A), and the two mouths of the channel did not have the same access resistance. Coupled with the exclusion of anions from the channel (due to its strong negative surface charge), this result is expected to result in ionic rectification (Fig. 2B and fig. S6). When cations flow from the side with lower access resistance, ions will accumulate inside the channel because entry is "easier" than exit, resulting in a conductance increase. If voltage is reversed, cations will flow from the side of higher resistance, the channel will instead be depleted, and conductance will drop. This mechanism is analogous to that of a p–n junction and results in a diode-like current-voltage characteristic (*30*) with two distinct possible values of conductance, defining a rectification factor β_{Rect}

$$\frac{G(V > 0)}{G(V < 0)} \simeq \beta_{Rect} \qquad (2)$$

Experimentally, we found $\beta_{Rect} = 1$ to 5, consistent with the above analysis in terms of entry effects (see SM, section 3). Because this type of nonlinearity depends on voltage sign, it corresponds to a bipolar memristor.

We stress that these two phenomena were not mutually exclusive; pristine MoS$_2$ channels could show signs of both mechanisms at the same time. In such cases, the *I-V* curve displayed two crossing points (rather than one or none). Further analysis and experimental data can be found in the SM (section 3.4 and fig. S17).

Although any system presenting a sufficiently strong nonlinearity associated with various internal conductance states could in theory display memristive behavior, it can only do so within a frequency range fixed by the time required to switch between the conducting and the insulating states. However, such time scales are normally too short to be accessible in nanofluidic systems, and this phenomenon requires peculiar transport processes to be observed.

Stop-and-go transport as a source of long-term memory

For both types of memristors, memory time scales were found to reach extremely large values, in the range of minutes to hours. Such long-term memory could be accounted for by taking ion pairing or surface adsorption into account in the dynamics of confined ions. In the theoretical framework of (*17*), the electrolyte is indeed predicted to retain its conductance state through the formation of ion clusters, which was estimated to typically take a few
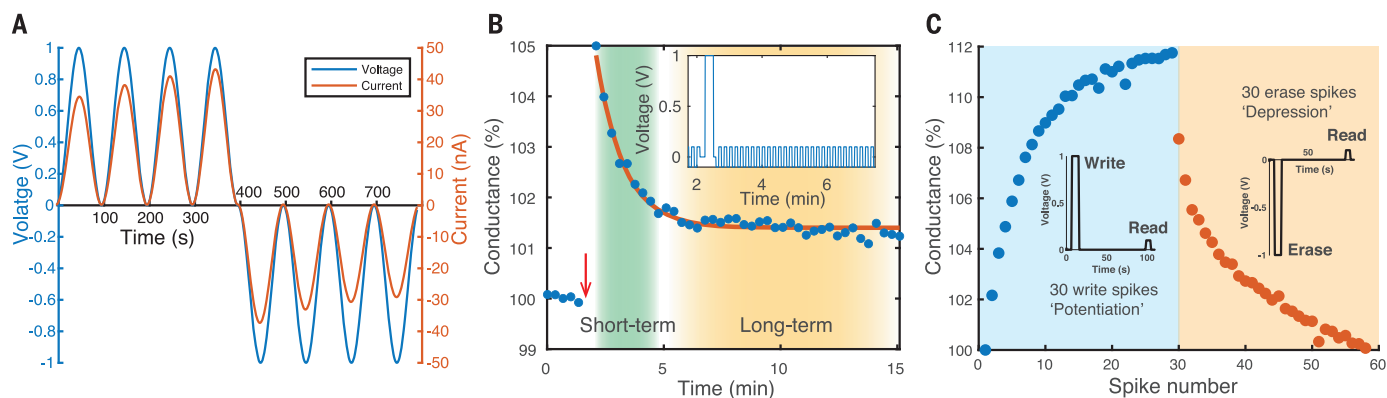
Fig. 4. Programming a nanochannel through reversible conductance strengthening. (**A**) Evolution of the ionic current (orange) under voltage pulses of constant polarity (blue). Successive positive (negative) pulses result in an increase (decrease) in conductance. (**B**) Conductance change, in percentage of the initial conductance, after a positive voltage pulse, exhibiting both short-term (<2 min) and long-term (>2 min) memory. The conductance was read by applying a weak square voltage wave that had no noticeable impact on the state of the system and modified through a strong voltage spike. Blue points are experimental data. The red solid line is a guide for the eye. (Inset) Applied voltage as a function of time. The red arrow indicates the beginning of the voltage spike. (**C**) Long-term modification of a nanochannel's conductance. Thirty write spikes (+1 V, 10 s) were applied, followed by 30 erase spikes (−1 V, 10 s), which brought the system back to its initial state. Between each spike, the conductance was allowed to stabilize for 2 min and was then measured with a read pulse (0.1 V, 5 s) (see fig. S3). All data correspond to activated carbon channels with height $h = 5$ nm filled with 1 mM $CaCl_2$.

milliseconds. More generally, one expects a nanofluidic channel to retain a conductance state (defined by the number of charge carriers present inside the channel) over a typical diffusion time scale, roughly L^2/D, where L is the channel length and D is a typical ionic diffusion coefficient in the channel. For channels with a length of ~10 μm, this result would yield a maximum memory time of 0.1 s, which is still orders of magnitude lower than experimental values. However, this picture changes if interfacial processes, rather than diffusion, govern ion transport. Consider a particle diffusing through a channel with chemically-active walls, such that it may adsorb on the surface (Fig. 2D). If the adsorption rate is much larger than the diffusion rate across the channel, then the particle will spend most of its time bound to the surface. As a result, the time it needs to escape the pore is the sum of the durations of all adsorption events. Let us define τ_{diff} as the time needed to escape through diffusion alone and τ_d as the time a particle bound to the surface takes to desorb. Then, if the particle is adsorbed every $\tau_a \ll \tau_{diff}$, there will be τ_{diff}/τ_a such events along the particle's trajectory as it crosses the channel. As a result, the system's memory time τ_m, given by the residence of the particle inside the pore, reads

$$\tau_m = \frac{\tau_{diff}}{\tau_a}\tau_d = \frac{\tau_d}{\tau_a}\tau_{diff} \gg \tau_{diff} \qquad (3)$$

In other words, the memory time of the system is the diffusion time scale multiplied by a ratio τ_d/τ_a measuring the strength of surface effects. At chemical equilibrium, this condition corresponds to the ratio of particle numbers on the surface and in the bulk of the channel, as quantified by the dimensionless Dukhin number Du = Σ/ehc, which compares the surface charge Σ with the charge density in the bulk of the electrolyte, ec. Expressed numerically, activated carbon channels typically have a Du of ~10^2 to 10^3, showing that surface effects strongly dominate the bulk effects. Equation 3 then predicts a memory time in the range of $\tau_m \sim$ Du × $\tau_{diff} \sim 100$ s. This estimation is in agreement with experimental values, which were found to be in the range of $\tau_m \sim 50$ to 400 s (figs. S12 and S14), and is consistent with previous reports of extremely slow diffusion of ions near a chemically active surface (31). Our prediction was found to generally underestimate experimental values: This can be attributed to the fact that our model assumes independent successive adsorption events, whereas, in reality, they tend to be correlated over long time scales (32). Moreover, this surface-driven mechanism could explain the disappearance of the phenomenon at low pH (fig. S16), which is known to greatly influence the channels' surface charge (16). The observed dependence of the memristor effect with the electrolyte could likewise result from a difference in chemical affinity between the various species of ions considered and surface defects (figs. S9 and S14)—however, this dependence is hard to analyze and would require further knowledge of the chemical nature of adsorption sites.

We note that this slow "stop-and-go" motion of ions near the channel's surface is not incompatible with the high conductance of activated carbon channels; although surface processes such as adsorption can slow down conductance changes, they do not modify the overall large number of ions present in the channel because of its strong surface charge.

We explain how to link conductance to surface charge in the SM (section 3.2). Similarly, we observe that the slowdown of the dynamics on the time scale of minutes emerges from microscopic processes (adsorbing events) with molecular time scales (say, 1 μs at best). This is, however, reminiscent of previous studies that showed how chemical or physical surface processes, involving the Stern layer, can result in hour-long phenomena when coupled to a water flow (33, 34).

A similar argument can be formulated for unipolar memristors. This time, the conduction state of the system is encoded in the number of ions that are not part of a tightly bound pair (and can therefore contribute to current)—according to the Wien effect. Similarly to surface adsorption, one expects that successive pairing-unpairing events will create a stop-and-go motion of ions through the system (Fig. 2C). The memory time is then, again, found to be given by diffusion multiplied by a ratio of pairing and unpairing times, potentially reaching minute- or even hour-long time scales.

Building on this qualitative picture, one may propose a minimal model, accounting for the memristor effect over minute-long times for both memory types, as detailed in the SM (fig. S7). We found that the system's conductance at time t was given by the convolution of its quasistatic conductance, as given by Eqs. 1 and 2, depending on memristor type, with an exponential memory kernel

$$G(t) = \int_0^\infty G_{qs}[V(t-s)]\frac{e^{-s/\tau}}{\tau}ds \qquad (4)$$

where G_{qs} is quasistatic (nonlinear) conductance, $V(t)$ the applied voltage, and τ a time scale of the order of the memory time τ_m. The
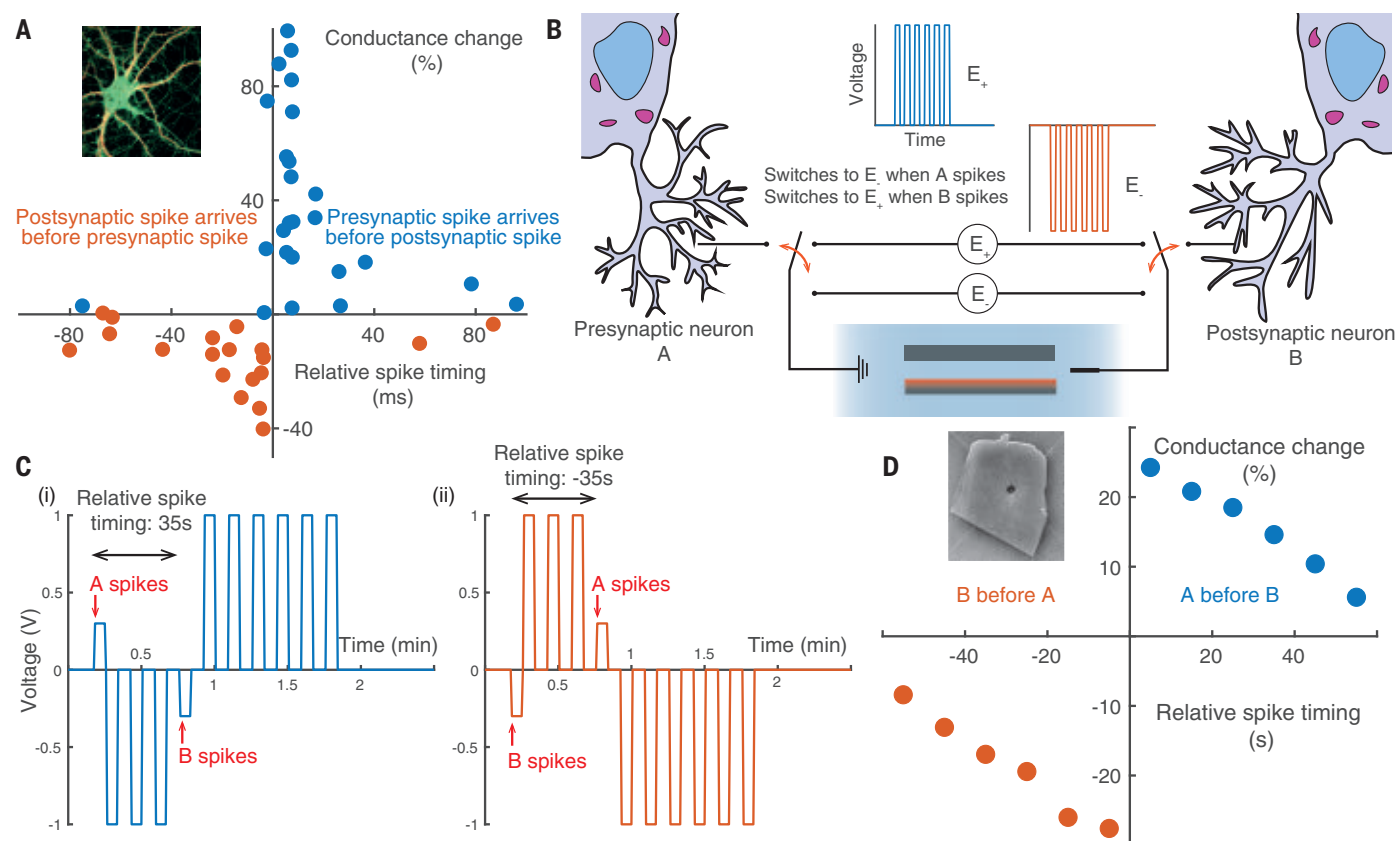
Fig. 5. Implementation of Hebb's law using activated carbon channels.
(**A**) Hebb's law in biological synapses: A synapse's conductance increases (decreases) when its presynaptic neuron fires just before (after) the postsynaptic one [adapted from (40)]. This process implements a form of causality detection known as spike timing–dependent plasticity (STDP). (Inset) Rat hippocampal neuron (ZEISS Microscopy from Germany, CC BY 2.0). (**B**) Hebb's law with nanofluidic memristors: Voltage spikes were applied to a nanochannel, mimicking the activation of two neurons A and B. After each spike from the presynaptic (postsynaptic) neuron, a series of erase (write) spikes was applied. (**C**) Example of voltage spike series depending on whether the presynaptic (i) or postsynaptic (ii) neuron activated first. (**D**) Conductance change after eight successive activations of the two neurons, in percentage of the initial conductance and as function of the relative activation timing of the neurons. Relative spike timing is measured from the onset of the first spike to the onset of the second. (Inset) Scanning electron microscopy image of an activated carbon nanochannel. Data correspond to an activated carbon channel with height h = 5 nm filled with 1 mM $CaCl_2$. See fig. S5 for additional data.

resulting prediction was in good agreement with experimental data (Fig. 3, A and B). According to this simple model, measuring the loop in the *I-V* curve allowed the characterization of the memristive effect (Fig. 3C). The curve of area as a function of voltage frequency exhibited a maximum when the frequency matched the intrinsic memory time τ_m, akin to a resonance. The comparison to the prediction of the model again showed good agreement and provided a direct measurement of τ_m (Fig. 3C).

Hebbian learning with nanofluidic memristors
Reversible modification of a nanochannel's conductance

This qualitative and quantitative rationalization of the ionic memristor effects paves the way for the implementation of learning algorithms using our nanofluidic devices. As a proof of concept, we show that these devices could be used to emulate some basic functionalities found in biological synapses. Because their memory was not lost when voltage was reset to zero, we only focused on bipolar memristors, as exhibited here with activated carbon channels. We first confirmed that their conductance could be increased or lowered through successive voltage sweeps of a given polarity (Fig. 4A). After a positive spike, the conductance was abruptly increased for a short period (~1 min) before relaxing to a long-term value above its initial state (Fig. 4B). This result shows that our device displayed both short- and long-term memory, similar to biological synapses (35).

These neural connections act as resistors whose conductance can be tuned during learning processes, with reversible modifications both on short (milliseconds to minutes) and long (minutes to hours or more) time scales (36, 37). The latter, known as long-term potentiation (or depression, when the conductance is lowered) enables the storage of information through the synapse's conductance state as a form of in-memory coding. Although the exact biological mechanisms are still debated, the transport and accumulation of calcium ions at specific places play a key role (26, 38). Taking inspiration from these features, we designed a protocol to implement in-memory computations with our nanofluidic channel (Fig. 4C). We incremented a nanochannel's conductance by applying a "write" voltage spike (+1 V for 10 s). It could then be accessed by a "read" pulse (+0.1 V for 5 s), which did not modify its value. It could also be reset to its original value with an "erase" spike (−1 V for 10 s). This setup allowed for a versatile and reversible modification and access to the stored value for computational applications. As a proof of concept, we show in Fig. 4C that the modification process was indeed fully reversible and allowed the storage of an analog variable over long time scales, by applying a series of 60 write and erase spikes. We thus demonstrated that nanoscale channels could be "programmed" through the tuning of their conductance, enabling the implementation of in-memory operations with ion-based nanofluidic systems.

Hebbian learning algorithm

Building on the similarities between our nanofluidic system and synapses, we next implemented a basic form of Hebbian learning. In biological neuron networks, this process consists of the modification of synaptic weights depending on the relative activation timings of two neurons connected by a given synapse (Fig. 5A). If the presynaptic neuron repeatedly emits an action potential shortly before the activation of the postsynaptic neuron, the synapse is strengthened (meaning its conductance is increased), as this result suggests a form of causality between the two activation events. Conversely, the synapse is weakened (i.e., its conductance is decreased) if the firing order is reversed, which would point at some anticausality relation. These modifications occur even if the presynaptic neuron only causes a mild response (when it is too weak to initiate an action potential by itself) of the postsynaptic one. Altogether, this process implements a form of principal components analysis of the inputs received by the network (39) and is believed to play a major role in learning.

To mimic this mechanism, we designed the experiment illustrated in Fig. 5B. A computer generated a voltage time series that emulated the behavior of two neurons. This time series was then applied to a nanofluidic channel. The activation of the presynaptic neuron A was modeled by a weak positive voltage pulse. Whenever it activated, a flip-flop mechanism was triggered, connecting the channel to a generator E_- that applied negative voltage spikes. This behavior lasted until the postsynaptic neuron B activated and the system was branched on another generator, E_+, applying positive spikes instead. The opposite chain of events occurred if neuron B activated first; in that case, the channel first received positive spikes from E_+, followed by negative spikes from E_- once neuron A activated. In both cases, the flip-flop reset if a given total amount of time passed since its activation, allowing the process to start over. Further details regarding the implementation are provided in the SM (fig. S4).

If neuron A activated just before neuron B, then the system received a few negative spikes, followed by many positive spikes (Fig. 5C, left panel). Its conductance was thus globally increased. Conversely, when the firing order was reversed, the system received more negative than positive spikes (Fig. 5C, right panel), and its conductance was therefore lowered.

We implemented this protocol in the experiments as follows: We first measured the system's conductance and ran the program, which consisted of eight successive activations of neurons A and B. Their relative spike timing—measured from the onset of the first spike to be triggered to the onset of the second—was used as a tunable parameter. Then, we measured the resulting change in conductance. The results are shown in Fig. 5D: When the presynaptic spike was followed (within a 40-s window) by a postsynaptic spike, conductance was increased, resulting in a strengthened connection between the two neurons. Otherwise, if the delay was too great or if the order was reversed, the connection was left unchanged or weakened, respectively. This phenomenology echoes the one observed in biological synapses, where the transient accumulation of certain ionic species triggers various mechanisms that ultimately result in the strengthening of neuron connections (38, 40); here, the accumulation of ions inside the nanochannel directly causes a conductance increase.

In this study, 2D nanochannels exhibited long-term memory, in the form of a memristor effect that could have two different physical origins—strong correlations between ions or entrance effects. In both cases, memory was retained over long time scales through interfacial processes that slowed down advection–diffusion across the channel. We fully characterized, experimentally and theoretically, both of these mechanisms. In particular, we showed that they may be harnessed for iontronics applications in a variety of contexts, as the memory effect was observed in all tested experimental conditions (salt concentration, electrolyte, pH). These systems reproduced the tunability of synapses, through an accumulation (or depletion) of ions, and could implement basic learning algorithms such as Hebb's rule within a simple nanofluidic architecture. More generally, our work illustrates how confinement-induced effects could be harnessed to build ionic machines inspired by biological systems. This work paves the way for the development of more complex iontronic devices on nanofluidic chips with advanced circuitry. Furthermore, the use of water and ions in the nanofluidic memristors, which is shared by biological systems, suggests the possibility to interface artificial channels with biological ones.

REFERENCES AND NOTES

1. N. Kavokine, R. R. Netz, L. Bocquet, *Annu. Rev. Fluid Mech.* **53**, 377–410 (2021).
2. L. Bocquet, *Nat. Mater.* **19**, 254–256 (2020).
3. M. Wang, Y. Hou, L. Yu, X. Hou, *Nano Lett.* **20**, 6937–6946 (2020).
4. K. Celebi et al., *Science* **344**, 289–292 (2014).
5. A. Marcotte, T. Mouterde, A. Niguès, A. Siria, L. Bocquet, *Nat. Mater.* **19**, 1057–1061 (2020).
6. S. Garaj et al., *Nature* **467**, 190–193 (2010).
7. C. A. Merchant et al., *Nano Lett.* **10**, 2915–2921 (2010).
8. G. F. Schneider et al., *Nano Lett.* **10**, 3163–3167 (2010).
9. J. Feng et al., *Nature* **536**, 197–200 (2016).
10. E. Secchi et al., *Nature* **537**, 210–213 (2016).
11. R. H. Tunuguntla et al., *Science* **357**, 792–796 (2017).
12. N. Kavokine, M.-L. Bocquet, L. Bocquet, *Nature* **602**, 84–90 (2022).
13. B. Radha et al., *Nature* **538**, 222–225 (2016).
14. A. Esfandiar et al., *Science* **358**, 511–513 (2017).
15. T. Mouterde et al., *Nature* **567**, 87–90 (2019).
16. T. Emmerich et al., *Nat. Mater.* **21**, 696–702 (2022).
17. P. Robin, N. Kavokine, L. Bocquet, *Science* **373**, 687–691 (2021).
18. L. Chua, *IEEE Trans. Circuit Theory* **18**, 507–519 (1971).
19. D. B. Strukov, G. S. Snider, D. R. Stewart, R. S. Williams, *Nature* **453**, 80–83 (2008).
20. A. Sebastian, M. Le Gallo, R. Khaddam-Aljameh, E. Eleftheriou, *Nat. Nanotechnol.* **15**, 529–544 (2020).
21. R. Ge et al., *Nano Lett.* **18**, 434–441 (2018).
22. Y. Bu, Z. Ahmed, L. Yobas, *Analyst* **144**, 7168–7172 (2019).
23. Q. Sheng, Y. Xie, J. Li, X. Wang, J. Xue, *Chem. Commun.* **53**, 6125–6127 (2017).
24. P. Zhang et al., *Nano Lett.* **19**, 4279–4286 (2019).
25. B. Hille, *Biophys. J.* **22**, 283–294 (1978).
26. W. Gerstner, W. M. Kistler, *Spiking Neuron Models: Single Neurons, Populations, Plasticity* (Cambridge Univ. Press, 2002).
27. Y. V. Pershin, M. Di Ventra, *Adv. Phys.* **60**, 145–227 (2011).
28. F. H. van der Heyden, D. Stein, K. Besteman, S. G. Lemay, C. Dekker, *Phys. Rev. Lett.* **96**, 224502 (2006).
29. L. Fumagalli et al., *Science* **360**, 1339–1342 (2018).
30. L. Bocquet, E. Charlaix, *Chem. Soc. Rev.* **39**, 1073–1095 (2010).
31. J. Comtet et al., *Nat. Nanotechnol.* **15**, 598–604 (2020).
32. S. Gravelle, R. R. Netz, L. Bocquet, *Nano Lett.* **19**, 7265–7272 (2019).
33. B. L. Werkhoven, J. C. Everts, S. Samin, R. van Roij, *Phys. Rev. Lett.* **120**, 264502 (2018).
34. P. Ober et al., *Nat. Commun.* **12**, 4102 (2021).
35. J.-X. Bao, E. R. Kandel, R. D. Hawkins, *Science* **275**, 969–973 (1997).
36. R. S. Zucker, W. G. Regehr, *Annu. Rev. Physiol.* **64**, 355–405 (2002).
37. M. Bear, B. Connors, M. A. Paradiso, *Neuroscience: Exploring the Brain, Enhanced Edition: Exploring the Brain* (Jones & Bartlett Learning, 2020).
38. T. V. P. Bliss, G. L. Collingridge, *Nature* **361**, 31–39 (1993).
39. W. Gerstner, W. M. Kistler, R. Naud, L. Paninski, *Neuronal Dynamics: From Single Neurons to Networks and Models of Cognition* (Cambridge Univ. Press, 2014).
40. G. Q. Bi, M. M. Poo, *J. Neurosci.* **18**, 10464–10472 (1998).
41. P. Robin et al., Experimental data for: Long-term memory and synapse-like dynamics in two-dimensional nanofluidic channels, version 1, Zenodo (2022); https://doi.org/10.5281/zenodo.7085645.

METALLURGY

Ductile 2-GPa steels with hierarchical substructure

Yunjie Li[1], Guo Yuan[1]*, Linlin Li[1]*, Jian Kang[1], Fengkai Yan[2], Pengju Du[3], Dierk Raabe[4]*, Guodong Wang[1]

Mechanically strong and ductile load–carrying materials are needed in all sectors, from transportation to lightweight design to safe infrastructure. Yet, a grand challenge is to unify both features in one material. We show that a plain medium-manganese steel can be processed to have a tensile strength >2.2 gigapascals at a uniform elongation >20%. This requires a combination of multiple transversal forging, cryogenic treatment, and tempering steps. A hierarchical microstructure that consists of laminated and twofold topologically aligned martensite with finely dispersed retained austenite simultaneously activates multiple micromechanisms to strengthen and ductilize the material. The dislocation slip in the well-organized martensite and the gradual deformation-stimulated phase transformation synergistically produce the high ductility. Our nanostructure design strategy produces 2 gigapascal–strength and yet ductile steels that have attractive composition and the potential to be produced at large industrial scales.

Bulk metallic materials with high strength and ductility, yet lean and sustainable chemical composition, are required for lightweight and safe transportation, construction, and infrastructure (1–3). However, in most metallic materials, an increase in strength comes at the expense of ductility, manifesting the strength-ductility trade-off (4, 5). This limits the workability and damage tolerance of high-strength alloys, a feature necessary for processing and application. The strength of maraging steels, a typical ultrahigh-strength alloy, reaches 2 GPa, which is almost the highest strength of all bulk-produced structural metals and alloys (6, 7). Maraging steels obtain their strength from the martensitic matrix and nanometer-sized fine intermetallic precipitates with small lattice misfit to the adjacent lattice, which strengthen the alloys without sacrificing ductility (8). In addition, metastable austenite can be introduced into a martensite matrix to exploit the transformation-induced plasticity (TRIP) effect for synchronously strengthening and ductilizing such high-strength steels (9, 10). The disadvantage of these approaches is the use of expensive and strategically limited alloying elements such as Co, Ni, Mo, or Ti (6, 8), which compromises the sustainability of these alloys so that the ductility increase remains limited.

Recently, in deformed and partitioned (D&P) steels, dislocations of high density in martensite have proven effective in increasing both the yield strength by dislocation forest hardening and the ductility through gliding of mobile dislocations (11). Also, chemical discontinuities inside the austenite acting as chemical boundaries in medium-Mn steels are effective for enhancing both strength and ductility (12) and even the steel's resistance to hydrogen embrittlement (13). The introduction of chemical boundaries creates submicrometer regions of variable austenite stability that force the martensite transformation into extremely fine martensite-austenite microstructures with an enhanced TRIP effect (12). With such dislocation and chemical boundary–based engineering strategies, steels can be produced with uniform elongation above 15% and tensile strength levels up to 2 GPa (11, 12); however, these steels show extensive Lüders bands or Portevin–Le Châtelier bands. These are serrated deformation patterns created by inhomogeneous plastic flow mechanisms, leading to undesired deformation inhomogeneity. In addition, the processing steps required to make these steels—including hot rolling, warm rolling, cold rolling, and fast heating, among others—are rather complex, rendering their production ineffective and costly. Thus, the quest for ductile, sustainable, and cost-effective 2-GPa steels presents itself as an unsolved problem.

Martensite is a dominant microstructure ingredient in all these ultrahigh-strength steels, usually topologically arranged in an unordered way—that is, without following any topological design or shape criteria (Fig. 1A). Its hierarchical organization and tetragonal distortion caused by the supersaturated interstitial carbon contribute to its high strength but also embrittle it (14). Yet, the topologically ordered alignment of martensite can help to turn brittleness into ductility. For example, in steels with laminated or prismatic martensite, strength, ductility, and toughness can be substantially improved by site-specific delamination along grain boundaries or phase boundaries (15, 16) (Fig. 1B). In particular, the interface alignment can play a critical role in ductilizing these types of microstructures (17, 18). Also, high interface

and bulk plasticity can be achieved in martensite with favorable orientation and topological alignment (19–21). Considering all of these structural advantages, we developed a simple and efficient forging route with subsequent deep cryogenic treatment and tempering (fig. S1) to realize these topological features in compositionally plain medium-Mn steel (22). The material's hierarchical architecture consists of a well-organized martensite structure and metastable austenite that formed in the refined prismatic parent austenite (Fig. 1C). The term "well-organized" refers to a twofold topologically aligned martensite (0° and 40 to 50°), as explained below. These hierarchical nanostructured steels exhibit tensile strength values of 2.0 to 2.4 GPa, uniform elongation of 18 to 25%, and total elongation of 24 to 30%.

Results

We designed a microalloyed medium-Mn steel with a composition of Fe-7.4Mn-0.34C-1Si-0.2V wt % , referred to as alloy A (fig. S2). The as-cast cuboidal sample (cross section 60 mm by 60 mm) was transversally forged multiple times at 650° to 800°C along two perpendicular directions with a total cross section reduction of 91%, and a prismatic parent austenitic microstructure was formed (Fig. 1D). The austenite assumed a rodlike shape along the longitudinal direction (LD) with a transversal size of 3.8 ± 1.4 µm and an aspect ratio of ~11.6 ± 4.5. After air cooling, most of the austenite transformed into martensite, with short-banded austenite retained at a volume fraction of 38.2%, forming a hierarchical structure (Fig. 1, E and F). The retained austenite bands mainly originated from the forging process instead of the Mn segregation (fig. S3). We then performed a cryogenic treatment in liquid nitrogen for 15 min to transform some (~19.5 vol %) of the retained austenite further into martensite, and later a tempering treatment at 300°C for 20 min to improve the austenite's stability (fig. S4, A and B). Eventually, 21.3 vol % austenite remained and the banded retained austenite had disappeared whereas the blocky retained austenite with a very fine size of ~0.61 ± 0.37 µm was uniformly distributed in the martensite matrix (Fig. 1G and fig. S4A). Notably, the carbon content inside the retained austenite increased by 0.11 wt % because of carbon partitioning during tempering (23) (fig. S4B). This improved the stability of the retained austenite, and the martensite-start temperature (M_s) was decreased from 77 to 37 K (24). The martensite with an average subblock size of ~0.62 ± 0.49 µm created a hierarchical substructure in each elongated region, inheriting directional features from the original rodlike parent austenite (Fig. 1H). The martensite exhibited two main morphology features, as shown in Fig. 1I and in fig. S4C at a larger field of view. The laths are mainly

[1]State Key Laboratory of Rolling and Automation, Northeastern University, Shenyang 110819, People's Republic of China. [2]Shenyang National Laboratory for Materials Science, Institute of Metal Research, Chinese Academy of Sciences, Shenyang 110016, People's Republic of China. [3]Jiangyin Xingcheng Special Steel Works Co., Ltd, Jiangyin 214400, People's Republic of China. [4]Max-Planck-Institut für Eisenforschung, 40237 Düsseldorf, Germany.
*Corresponding author. Email: yuanguo@ral.neu.edu.cn (G.Y.); lill@ral.neu.edu.cn (L.L.); d.raabe@mpie.de (D.R.)
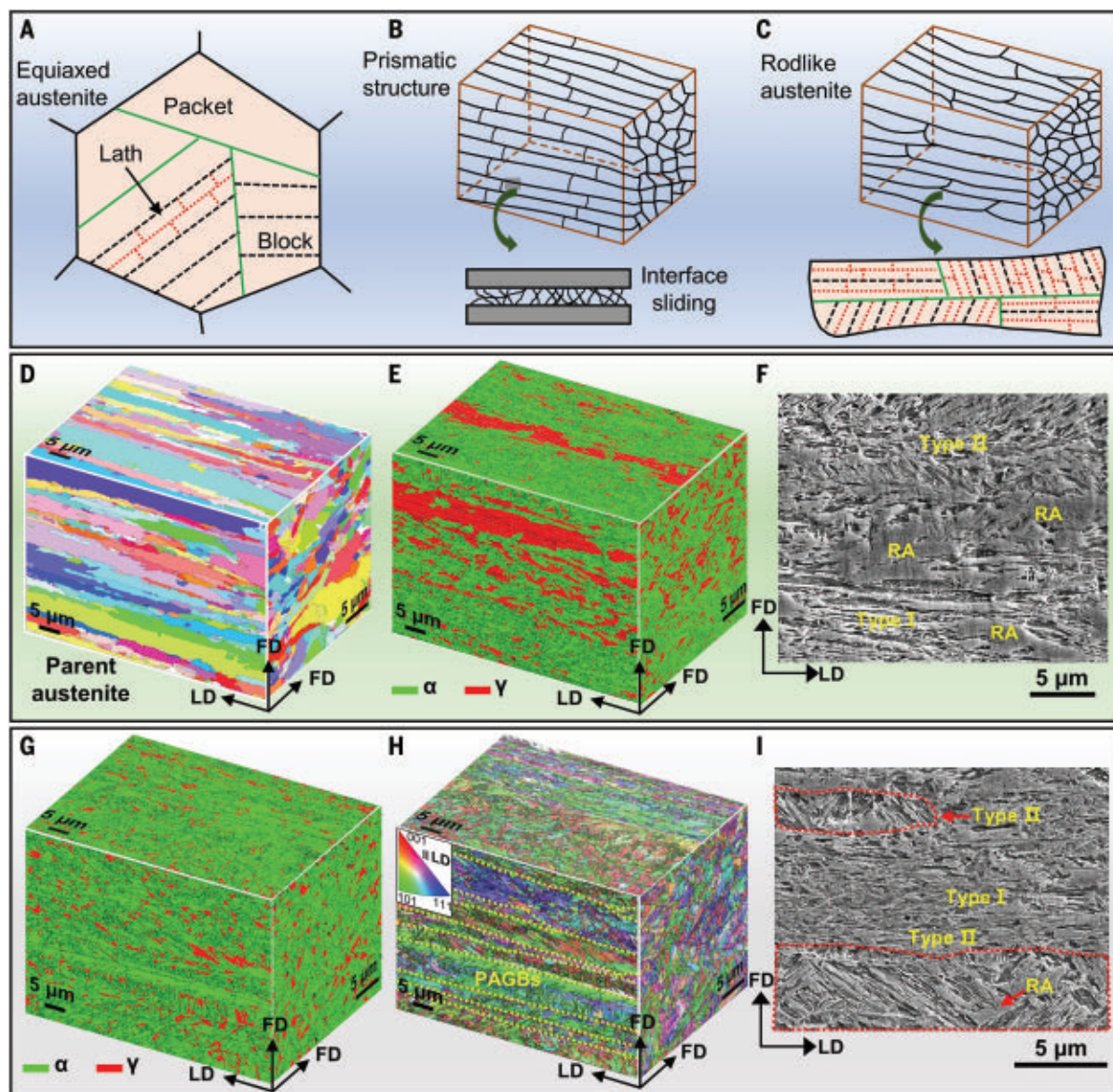
Fig. 1. The hierarchical microstructure evolution of the Fe-7.4Mn-0.34C-1Si-0.2V steel. (**A**) Conventional microstructure of martensite originated from equiaxed austenite. (**B**) Prismatic structure with interface features between layers. (**C**) Well-organized martensite transformed inside of the prismatic parent austenite, forming a hierarchical structure. (**D**) The mean crystallographic orientation map of the reconstructed parent austenite with rodlike shape, obtained with the MTEX Toolbox (*32*), (**E**) the EBSD phase map (α represents martensite; γ represents austenite), and (**F**) the SEM image showing the elongated martensite LD (type I) and inclined LD (type II) in the sample treated by forging and air-cooling to room temperature. LD indicates the longitudinal direction and FD indicates the forging direction. RA indicates the retained austenite. (**G**) The EBSD phase map, (**H**) the inverse pole figure (IPF) map of the martensite, and (**I**) the SEM image of the forged sample further treated by deep cryogenic treatment and subsequent tempering at 300°C for 20 min. The parent austenite grain boundaries (PAGBs) are marked as yellow dashed lines in (H).

aligned parallel to the LD in type I martensite, whereas most laths are inclined at a certain angle (40° to 50°) to LD in type II martensite. We refer to this configuration of the martensite microstructure as well-organized martensite, and its formation is attributed to the limited variant selection in fine, rodlike parent austenite (fig. S5). As a reference test, we conducted a similar experiment using hot rolling. When we replaced multiple-transversal forging with conventional hot rolling, an equiaxed

parent austenite morphology formed in the steel with an average size of 10 ± 2.4 μm (fig. S6). After successive cryogenic treatment and tempering at 300°C for 20 min to the hot-rolled sample, ~14.5 vol % austenite was retained, and the martensite laths and blocks were randomly arranged with an average sub-block size of ~0.65 ± 0.52 um (fig. S6).

Next, we performed transmission electron microscopy (TEM) characterization, which revealed that the lath martensite prevailed in

the forged steels after cryogenic treatment and tempering (fig. S7). The characteristic arrangement of the martensite (Fig. 2, A and B) is consistent with observations made with the scanning electron microscope (SEM) (Fig. 1I). The average lath thicknesses of type I and type II martensite were 126 ± 27 nm and 120 ± 32 nm, respectively. Each type of martensite developed in one packet, forming the hierarchically ordered structure shown in Fig. 1C. In the martensite matrix, the retained austenite

Fig. 2. The microstructure of Fe-7.4Mn-0.34C-1Si-0.2V steel.
(**A**) A local region of a parent austenite showing type I martensite paralleled to LD.
(**B**) A local region of a parent austenite showing type II martensite inclined 45° to LD.
(**C**) and (**D**) Dark-field imaging of the ultrafine retained austenite.
(**E**) 3D reconstructions of the tempered sample. (**F**) Three atomic percent isosurface of C and V. (**G**) One-dimensional compositional profiles along the axis of the 12 nm by 12 nm by 40 nm yellow cylinder in (F).
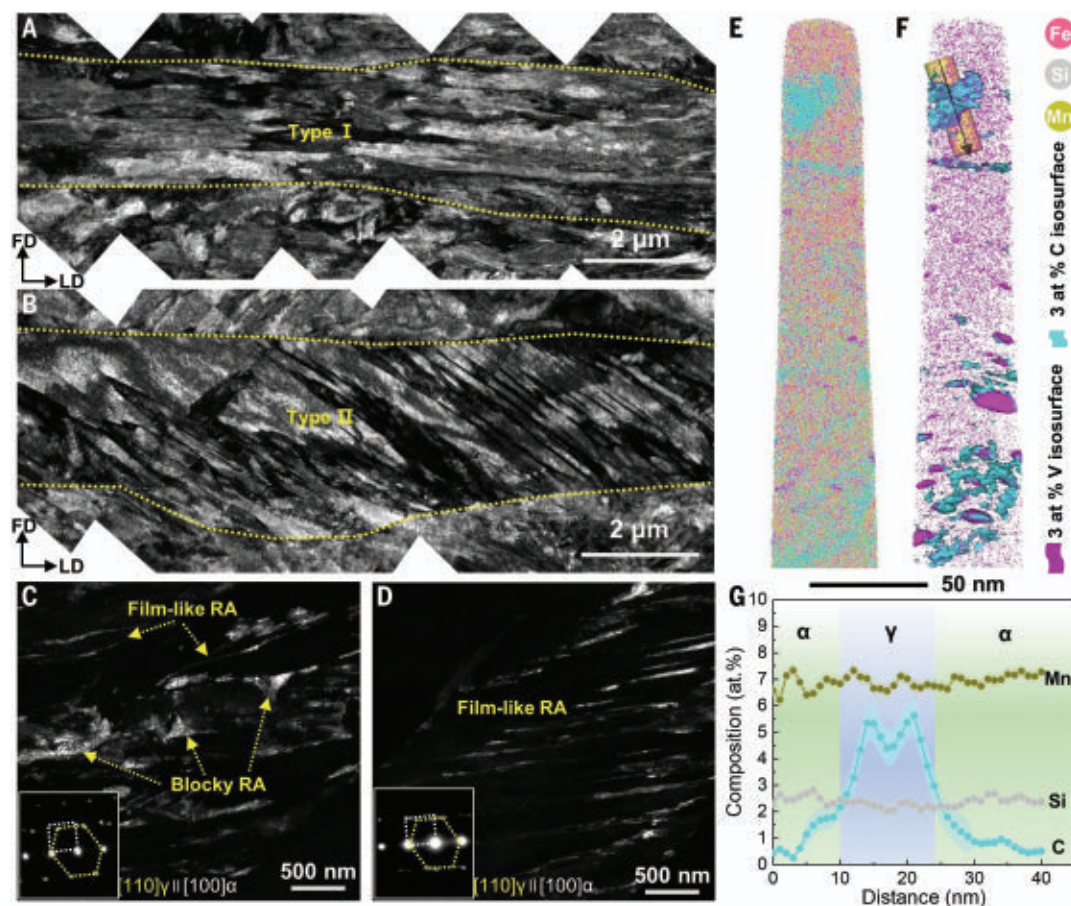
mainly assumed the form of thin films and small blocks. The blocky austenite prevailed at the block or packet boundaries with submicrometer sizes of ~300 nm (Fig. 2C), whereas the filmlike austenite was uniformly distributed between martensitic laths with average thickness of 27 ± 13 nm (Fig. 2D). Additionally, the severe multiple-transversal forging deformation promoted the dispersive distribution of nanoprecipitates in the matrix (fig. S8), whereas only coarse carbides formed in the unordered martensite of the hot-rolled sample (fig. S9). The dispersed nanoprecipitates were identified by TEM and atom probe tomography (APT) as ~5 nm–sized VC (vanadium carbide) (Fig. 2, E and F, and fig. S8). The APT results also showed that some carbon-rich regions correspond to retained austenite (Fig. 2, E to G), with the carbon concentration varying from 2 atomic percentage (at %) to 5 at %, or 0.4 wt % to 1.1 wt %. Yet, there was no segregation of the slowly diffusing Mn or Si, suggesting that only carbon diffused fast enough to partition into austenite from the adjacent martensite during tempering at 300°C (25).

The Fe-7.4Mn-0.34C-1Si-0.2V wt % steel we developed exhibits attractive tensile properties, combining a yield strength of 1822 ± 35 MPa, tensile strength of 2200 ± 20 MPa, and uniform

elongation of 18.0 ± 0.3% (Fig. 3A). Additionally, this sample possesses exceptionally high work-hardening rates up to a true strain of ~0.15 (Fig. 3A, inset), which equips the material with good formability. The present properties are substantially improved compared to those of conventional hot-rolled material (yield strength of 1266 ± 54 MPa, uniform elongation of 7.5 ± 0.8%). The higher yield strength of the forged steel primarily arose from the higher density of dislocations (3.4 × 10^{15} m^{-2}, two times higher than that of the hot-rolled sample) and more highly dispersed nanoprecipitates (table S1). Both of these important features result from the forging process. In particular, the cryogenic treatment refined the microstructure with extensive martensite transformation, and the tempering induced carbon partitioning, both of which efficiently increased the yield strength of the forged sample (fig. S10). A similar hierarchical structure with well-organized martensite also formed when we added slightly more carbon and vanadium (Fe-7.8Mn-0.39C-1Si-0.5V wt %, referred to as alloy B) (figs. S11 and S12). Alloy B displays attractive mechanical properties (Fig. 3A), showing the potential for further improvement of mechanical properties considering compositional adjustment, based on

the proposed processing route. We compared the tensile properties of both forged alloys A and B with other advanced ultrahigh-strength steels (Fig. 3B). The developed steels have a better strength-ductility synergy over other existing ultrahigh-strength steels. The product of tensile strength and uniform elongation (a measure of total energy absorption) exceeds 40 GPa·% (the dot-dash line in Fig. 3B), which is greater than that of existing 2-GPa steels.

Discussion

The mechanical properties—specifically, the excellent ductility—of the forged steels come from the synergistically acting deformation mechanisms. High-resolution digital image correlation (DIC) and electron backscattered diffraction (EBSD) results indicate that our forged steels deform more homogeneously than the hot-rolled reference materials (figs. S13 and S14). Large blocky austenite could deform and transform at an early deformation stage (fig. S13), thus equipping the material with constant strain hardening (26). According to the phase maps (Fig. 4, A and B) and x-ray diffraction (XRD) analyses (Fig. 4C), the retained austenite gradually transformed into martensite upon straining, until reaching a transformed volume fraction of 91% at
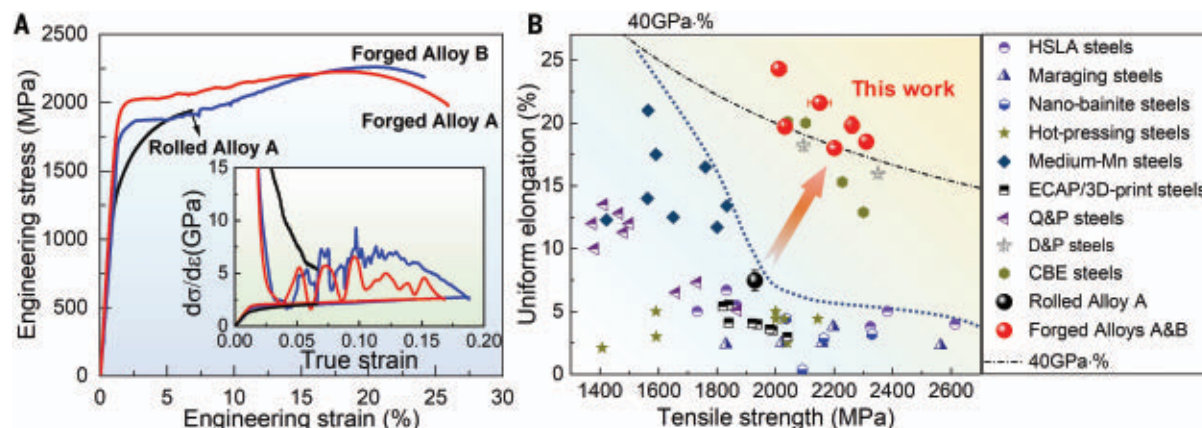
Fig. 3. Mechanical properties of the developed steels compared with other ultrahigh-strength steels. (**A**) Tensile stress–strain curves and corresponding strain-hardening curves of forged alloys A and B and hot-rolled alloy A. These samples were all processed by cryogenic treatment and tempering at 300°C for 20 min. (**B**) Tensile properties of both steels with well-organized martensite (forged alloys A and B) compared with those of other advanced ultrahigh strength steels, including high-strength low-alloy (HSLA) steels (*33–35*), maraging steels (*6, 8, 36*), nano-bainite steels (*37*), hot-pressing steels (*38–40*), medium-Mn steels (*41–45*), equal channel angular pressing (ECAP) or 3D-print steels (*46–48*), quenched and partitioned (Q&P) steels (*49–51*), D&P steels (*11*), and chemical boundary engineering (CBE) steels (*12*).

a tensile strain (ε) of 18.3%. The blocky retained austenite governed the TRIP effect during the early-to-middle deformation regimes and almost fully transformed at ε ≈ 8% (Fig. 4, A and B). With continued straining, the film-like thin retained austenite layers began to transform as well, even further reducing the volume fraction of the remaining metastable austenite (Fig. 4C). The latter thin austenite tends to transform at high stress and strain levels owing to its nanoscopic size and different partitioning, both of which translate to higher stability against athermal transformation (*27, 28*). This gradual and sufficient TRIP effect produces a high strain-hardening rate, improving both strength and ductility of the forged steels. By contrast, only 35% of the austenite was transformed at the point of fracture in the conventionally hot-rolled reference sample (fig. S15), thus contributing less to the strain hardening and the resulting uniform elongation.

In addition to the TRIP effect, well-organized martensite of the architected hierarchical structure also provides considerable ductility to the forged samples. The mechanical responses of type I and type II martensite were different (fig. S16) and strongly depend on the lath geometric and crystallographic orientations. Figure 4, D and E, shows the maximum Schmid factors and the primary slip systems of type II and I martensite, respectively. Most primary slip directions and slip planes are parallel to the lath or block boundaries for type II martensite, whereas they commonly intersect with these substructure boundaries for type I martensite. Hence, the strain localization zones were parallel to the lath interfaces of type II martensite with in-lath-plane slip and inclined

to that of type I martensite with out-of-lath-plane slip (Fig. 4, F and G, and fig. S16). Because of the slightly higher Schmid factors and preferentially activated in-lath-plane slip for type II martensite (*21, 29*), this material portion deformed slightly earlier than type I martensite (fig. S16). A high population of dislocations can glide parallel to the lath interface with a long-mean free path, thus increasing the ductility of this type II martensite (*21, 30*). In addition, interface plasticity assisted by thin films of retained austenite located between adjacent type II martensite laths also promoted the compound's plastic compliance (fig. S17) (*19, 20, 31*). Because of the crystallographic slip and interface sliding, type II martensite thus acts as a ductilizing element, lending this type of microstructure higher strain partitioning than type I martensite (Fig. 4H).

The lath structures and film-like retained austenite of type II martensite were clearly visible at a total tensile strain of 8% (Fig. 4I), yet most of them disappeared and extensive dislocation tangles formed at a strain of 12%, evidencing the activation of abundant out-of-lath-plane slip at higher deformation levels (Fig. 4J and fig. S17, J and K). Thus, the contribution of interface plasticity in type II martensite diminished gradually upon loading. The lath structure of type I martensite was still discernible at a strain of 12% (Fig. 4K) because of the smaller fraction of strain that had partitioned to it (Fig. 4H). The remaining film-like austenite in the type I martensite contributed some plastic compliance by means of the TRIP effect, as suggested by XRD detection (Fig. 4C). The dislocations mostly accumulated at the block boundaries as out-of-lath-plane slip was activated in type I martensite (Fig.

4K). These boundaries acted as effective barriers against dislocation slip, enhancing the local strength. That is, type I martensite contributed more to the strength, whereas type II contributed more to ductility, qualifying the forged steel as a kind of martensite-martensite composite (types I and II). Yet, there was good strain compatibility between type I and II martensite (figs. S13, S14, and S16) because of the higher volume fraction (> 60%) of type II martensite, the gradual TRIP effect, and the laminated martensitic arrangements, which can effectively alleviate stress concentrations at the boundaries between packets and grains. In comparison, the strain tended to localize at certain favorably oriented lath boundaries, inducing the early fracture of the hot-rolled reference material (figs. S13 and S14). At the final deformation stage (ε = 18.3%), multiple slip of numerous dislocations made the two types of martensite indistinguishable, and dislocation cell structures developed well (Fig. 4L), evidencing that dislocation slip in martensite prolonged the plastic deformation. By integrating the advantages of multiple strengthening and ductilizing mechanisms, the hierarchical structures of dually aligned martensite and retained austenite can sustain the uniform elongation as high as 20% at an ultrahigh strength level of 2.2 GPa.

Conclusions

Our work provides a topological structure design approach to achieving attractive ductility and ultrahigh strength in medium-Mn steels through tuning martensitic structures with moderate metastable austenite into a dual-aligned morphology. Aside from the gradual TRIP effect, the microstructure of the forged
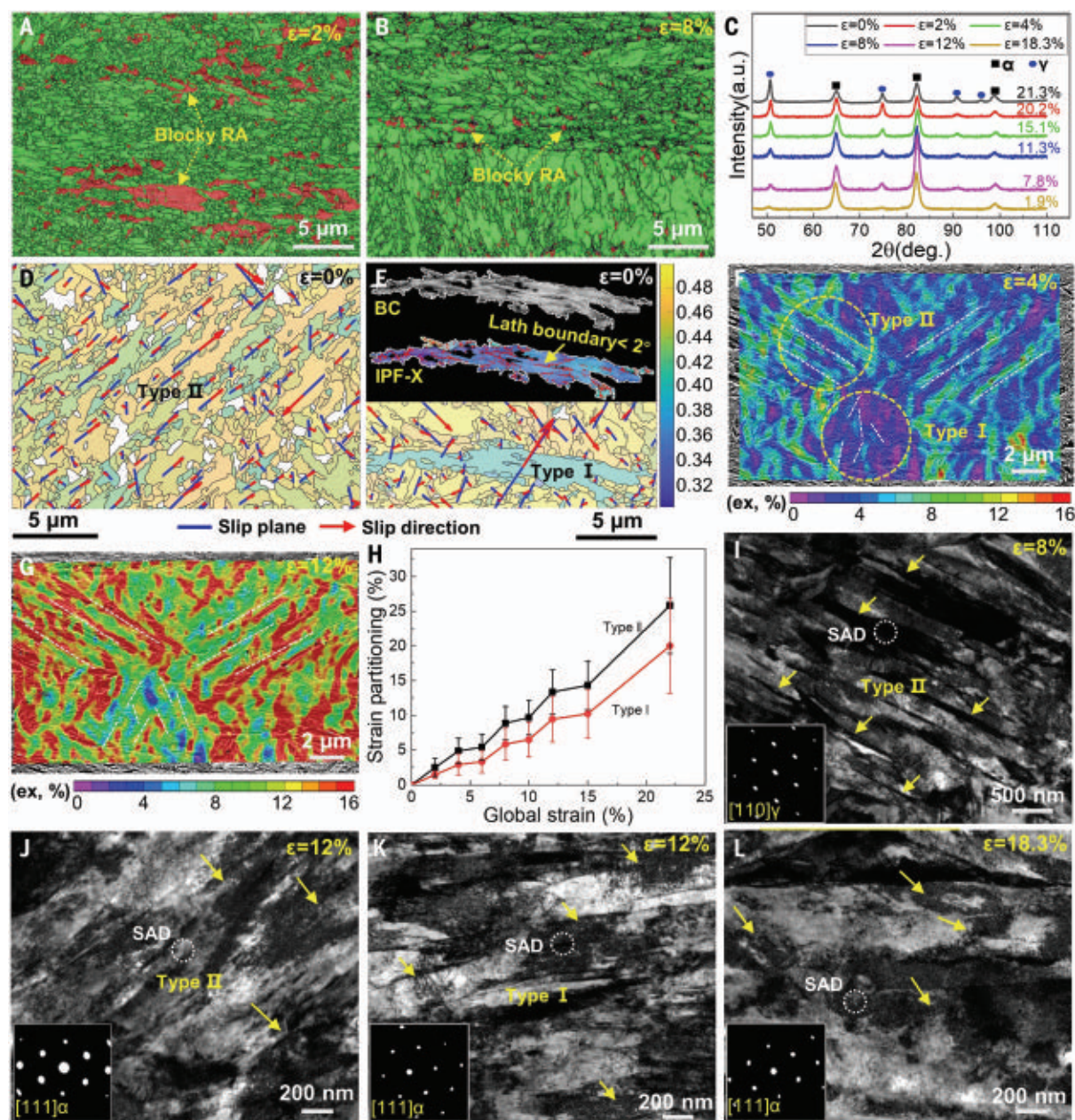
Fig. 4. The deformation microstructures of the present Fe-7.4Mn-0.34C-1Si-0.2V steel. The horizontal direction is the LD. (**A** and **B**) EBSD phase maps, showing that the volume fraction of blocky austenite decreased upon straining. (**C**) Variation in volume fraction of austenite with tensile strain probed by XRD. The distribution of the Schmid factors for the primary slip systems ({110} <111>) of (**D**) type II martensite and (**E**) type I martensite when loading in LD. The blue lines indicate slip plane traces, the red arrows indicate slip directions, and the white regions mark the retained austenite. (**F** and **G**) Strain distribution at a global tensile strain of 4 and 12%, respectively. The white dashed lines indicate the strain localization. (**H**) Strain partitioning between type I and type II martensite during tensile loading. The deformed structures of type II martensite at a tensile strain of (**I**) 8% and (**J**) 12%. (**K**) The deformed structures of type I martensite at a tensile strain of 12%. (**L**) Deformed structures at a tensile strain of 18.3%. The yellow arrows in (I) indicate the nanofilm-like retained austenite, and the yellow arrows in (J) to (L) show the dislocation structures.

steels also makes use of bulk and interface plasticity through the construction of ductile martensite of a large volume fraction, which substantially increases the material's overall ductility. The excellent tensile properties were obtained by a simple, cost-cutting, and emission-reduced thermomechanical treatment, which is compatible with existing industry processes. We believe that the mechanical properties can be further optimized by suitably tuning the processing methods and chemical compositions. This microstructural design concept could be extended and tailored to fit many other martensitic alloy classes, and it may work for large-scale processing with a wide range of possible applications in the vehicle, aerospace, and machinery sectors using standard forging equipment.

REFERENCES AND NOTES

1. D. Raabe, C. C. Tasan, E. A. Olivetti, *Nature* **575**, 64–74 (2019).
2. X. Li, K. Lu, *Nat. Mater.* **16**, 700–701 (2017).
3. X. Li, K. Lu, *Science* **364**, 733–734 (2019).
4. R. O. Ritchie, *Nat. Mater.* **10**, 817–822 (2011).

5. F. K. Yan, G. Z. Liu, N. R. Tao, K. Lu, *Acta Mater.* **60**, 1059–1071 (2012).
6. M. Niu *et al.*, *Acta Mater.* **179**, 296–307 (2019).
7. W. W. Sun, R. K. W. Marceau, M. J. Styles, D. Barbier, C. R. Hutchinson, *Acta Mater.* **130**, 28–46 (2017).
8. S. Jiang *et al.*, *Nature* **544**, 460–464 (2017).
9. D. Raabe, D. Ponge, O. Dmitrieva, B. Sander, *Scr. Mater.* **60**, 1141–1144 (2009).
10. S. Dehgahi, M. Sanjari, M. H. Ghoncheh, B. S. Amirkhiz, M. Mohammadi, *Addit. Manuf.* **39**, 101847 (2021).
11. B. B. He *et al.*, *Science* **357**, 1029–1032 (2017).
12. R. Ding *et al.*, *Sci. Adv.* **6**, eaay1430 (2020).
13. B. Sun *et al.*, *Nat. Mater.* **20**, 1629–1634 (2021).
14. G. Krauss, *Mater. Sci. Eng. A* **273-275**, 40–57 (1999).
15. L. Liu *et al.*, *Science* **368**, 1347–1352 (2020).
16. Y. Kimura, T. Inoue, F. Yin, K. Tsuzaki, *Science* **320**, 1057–1060 (2008).
17. Q. Cheng, L. Jiang, Z. Tang, *Acc. Chem. Res.* **47**, 1256–1266 (2014).
18. H. D. Espinosa, J. E. Rim, F. Barthelat, M. J. Buehler, *Prog. Mater. Sci.* **54**, 1059–1100 (2009).
19. C. Du, J. P. M. Hoefnagels, R. Vaes, M. G. D. Geers, *Scr. Mater.* **120**, 37–40 (2016).
20. L. Morsdorf *et al.*, *Acta Mater.* **121**, 202–214 (2016).
21. K. Kwak, Y. Mine, S. Morito, T. Ohmura, K. Takashima, *Mater. Sci. Eng. A* **856**, 144007 (2022).
22. Materials and methods are available as supplementary materials.
23. J. Speer, D. K. Matlock, B. C. De Cooman, J. G. Schroth, *Acta Mater.* **51**, 2611–2622 (2003).
24. S. M. C. van Bohemen, L. Morsdorf, *Acta Mater.* **125**, 401–415 (2017).
25. X. Tan *et al.*, *Acta Mater.* **165**, 561–576 (2019).
26. D. Raabe, Z. Li, D. Ponge, *MRS Bull.* **44**, 266–272 (2019).
27. M. M. Wang, C. C. Tasan, D. Ponge, A. C. Dippel, D. Raabe, *Acta Mater.* **85**, 216–228 (2015).
28. X. C. Xiong, B. Chen, M. X. Huang, J. F. Wang, L. Wang, *Scr. Mater.* **68**, 321–324 (2013).
29. Y. Mine, K. Hirashita, H. Takashima, M. Matsuda, K. Takashima, *Mater. Sci. Eng. A* **560**, 535–544 (2013).
30. D. Akama, T. Tsuchiyama, S. Takaki, *ISIJ Int.* **56**, 1675–1680 (2016).
31. F. Maresca, V. G. Kouznetsova, M. G. D. Geers, *Model. Simul. Mater. Sci. Eng.* **22**, 045011 (2014).
32. F. Niessen, T. Nyyssönen, A. A. Gazder, R. Hielscher, *J Appl Crystallogr* **55**, 180–194 (2022).
33. Y. Wang *et al.*, *Acta Mater.* **158**, 247–256 (2018).
34. Y. Kimura, T. Inoue, K. Tsuzaki, *J. Alloys Compd.* **577**, S538–S542 (2013).
35. B. Kim *et al.*, *Acta Mater.* **68**, 169–178 (2014).
36. Y. H. Gao *et al.*, *Mater. Sci. Eng. A* **759**, 298–302 (2019).
37. C. Garcia-Mateo *et al.*, *Mater. Sci. Technol.* **30**, 1071–1078 (2013).
38. Z. Y. Chang, Y. J. Li, D. Wu, *Mater. Sci. Eng. A* **784**, 139342 (2020).
39. T. Taylor, J. McCulloch, *Steel Res. Int.* **89**, 1700495 (2018).
40. O. Çavuşoğlu *et al.*, *J. Mater. Res. Technol.* **9**, 10901–10908 (2020).
41. P. Du, P. Chen, D. K. Misra, D. Wu, H. Yi, *Metals* **10**, 1343 (2020).
42. B. Hu *et al.*, *Acta Mater.* **174**, 131–141 (2019).
43. Z. R. Hou, T. Opitz, X. C. Xiong, X. M. Zhao, H. L. Yi, *Scr. Mater.* **162**, 492–496 (2019).
44. N. Yan, H. Di, R. D. K. Misra, H. Huang, Y. Li, *Mater. Sci. Eng. A* **753**, 11–21 (2019).
45. H. Lee *et al.*, *Acta Mater.* **147**, 247–260 (2018).
46. S. L. Gibbons *et al.*, *Mater. Sci. Eng. A* **725**, 57–64 (2018).
47. M. W. Vaughan *et al.*, *Scr. Mater.* **184**, 63–69 (2020).
48. J. Yan, H. Song, Y. Dong, W.-M. Quach, M. Yan, *Mater. Sci. Eng. A* **773**, 138845 (2020).
49. H. L. Cai *et al.*, *Scr. Mater.* **178**, 77–81 (2020).
50. E. J. Seo, L. Cho, Y. Estrin, B. C. De Cooman, *Acta Mater.* **113**, 124–139 (2016).
51. K. Zhang, P. Liu, W. Li, Z. Guo, Y. Rong, *Mater. Sci. Eng. A* **619**, 205–211 (2014).

SOLAR CELLS

Unveiling facet-dependent degradation and facet engineering for stable perovskite solar cells

Chunqing Ma,[1]† Felix T. Eickemeyer,[2]† Sun-Ho Lee,[1] Dong-Ho Kang,[1] Seok Joon Kwon,[3,4]* Michael Grätzel,[2,4]* Nam-Gyu Park[1,4]*

A myriad of studies and strategies have already been devoted to improving the stability of perovskite films; however, the role of the different perovskite crystal facets in stability is still unknown. Here, we reveal the underlying mechanisms of facet-dependent degradation of formamidinium lead iodide (FAPbI$_3$) films. We show that the (100) facet is substantially more vulnerable to moisture-induced degradation than the (111) facet. With combined experimental and theoretical studies, the degradation mechanisms are revealed; a strong water adhesion following an elongated lead-iodine (Pb-I) bond distance is observed, which leads to a δ-phase transition on the (100) facet. Through engineering, a higher surface fraction of the (111) facet can be achieved, and the (111)-dominated crystalline FAPbI$_3$ films show exceptional stability against moisture. Our findings elucidate unknown facet-dependent degradation mechanisms and kinetics.

S tability is one of the most pressing issues that hinders the commercialization of perovskite solar cells (PSCs), despite efficiencies greater than 25% (*1–3*). The degradation of hybrid perovskite thin films by moisture, thermal stress, and light is a complex process that involves changes in crystal structure, composition, film morphology, and optoelectronic properties (*4–9*). This is especially true for the most promising composition of formamidinium (FA)–based perovskite FAPbI$_3$, which shows a thermodynamically stable photoactive α-phase only at temperatures greater than 150°C and can rapidly transition to photoinactive δ-phase at room temperature (*10–13*). Although research on degradation has advanced considerably, a fundamental understanding of the role of the different crystal facets in the degradation process is missing (*14, 15*).

It is the perovskite surface with its various facets that is exposed to the environment (moisture, oxygen, etc.), and these facets are likely to degrade first (*16, 17*). Thus, understanding the overall stability of the perovskite thin film begins with understanding the stability and degradation behavior of the perovskite facets (*18*). Different crystal facets have different atomic arrangements and coordination, which lead to different atomic potential landscapes and, subsequently, to different electronic, physical, and/or chemical properties (*19–21*). Therefore, it is expected that the various facets suffer degradation with different kinetics and that a thermodynamically unstable facet is prone to degradation and drives overall degradation. Despite the critical importance of the facets to the degradation process, no attempt, to our knowledge, has yet been made to understand the stability and degradation behaviors of perovskite facets.

Here, we report direct observations of the degradation process of (100) and (111) facets within the FAPbI$_3$ perovskite thin film. We have found direct evidence that the (100) facet, which is predominant in perovskite thin films, limits the overall stability of the perovskite and exhibits a fast phase transition to δ-phase when exposed to moisture, whereas the (111) facet is much more stable to moisture-driven degradation. Based on the in situ characterization of an individual crystal with well-defined facets, ex situ measurements, and theoretical calculations, we show that a strong water adhesion after hydroxylation with an elongated Pb-I

[1]School of Chemical Engineering and Center for Antibonding Regulated Crystals, Sungkyunkwan University, Suwon 16419, Republic of Korea. [2]Laboratory of Photonics and Interfaces, École Polytechnique Fédérale de Lausanne (EPFL), 1015 Lausanne, Switzerland. [3]School of Chemical Engineering, Sungkyunkwan University, Suwon 16419, Republic of Korea. [4]SKKU Institute of Energy Science and Technology (SIEST), Sungkyunkwan University, Suwon 16419, Republic of Korea.
*Corresponding author. Email: sjoonkwon@skku.edu (S.J.K.); michael.graetzel@epfl.ch (M.G.); npark@skku.edu (N.-G.P.)
†These authors contributed equally to this work.

bond distance is responsible for the δ-phase transition. More importantly, the formed δ-phase substantially deteriorates the optoelectronic properties of the (100) facet. Because the (111) facet exhibits a high barrier to the phase transition, a facet engineering strategy in which ligands assist the preferred growth of the (111) facet is provided. The (111)-dominated film shows exceptional stability against thermal stress and moisture without any surface passivation.

Specific degradation on the (100) facet

To prepare perovskite thin films with well-defined (100) and (111) facets, piperidine additive was used (see methods) (22). X-ray diffraction (XRD) data in fig. S1 verify that the sample exhibits a high (100) peak and a low (111) peak located at 14.0° and 24.4°, respectively (23). Scanning electron microscopy (SEM) imaging confirms the well-defined polyhedral shapes (Fig. 1A). Most of the grains have a triangular facet in the center, corresponding to the (111) facet (22), and the (100) facets are in the lateral directions of the crystal surface (24). This observation suggests that the perovskite crystal is enclosed by (100) facets, with (111) facets at the truncated corners. A schematic model of the (100) and (111) facets on a perovskite cubic crystal and atomic arrangements are shown in Fig. 1B. The metal cations (Pb) or organic cations (FA) are connected to I anions on the (100) facet with Pb-I or FA-I layer terminations. The (111) facet is terminated by 3/8 FA cation and 3/2 I anion, and the unsaturated bond of the I anions can be balanced by either FA or Pb cations at the corresponding crystallographic sites. With the well-defined facets on the individual crystal, the degradation process of the (100) and (111) facets was studied. Atomic force microscopy (AFM) was used to examine changes in surface morphology and electronic properties during the course of facet degradation (25). The AFM image of the as-prepared (undegraded) sample in Fig. 1C shows smooth (100) and (111) facets, as confirmed by the SEM image. The sample was then exposed to ambient air with a relative humidity (RH) of 30 to 40% for 72 hours, and the AFM image of the degraded sample is shown in Fig. 1D. Interestingly, the triangular (111) facet shows a different degradation behavior compared with that of the lateral (100) facet. In particular, the (100) facets appear to degrade and reveal newly formed crystals that could be identified as small protuberances (marked by yellow rectangles), whereas the (111) facets are nearly intact against degradation. Further exposure to ambient air for 200 hours breaks the (100) facets into small pieces of crystals, whereas little degradation is observed for the (111) facets (Fig. 1E). The SEM image of the degraded sample (aged 72 hours) in fig. S2 also indicates that small crystals are formed on the (100) facet after exposure to air for 72 hours, and XRD data demonstrate that the newly formed crystals are δ-phase (fig. S3) (26). It was also observed that the (100) peak intensity is reduced after degradation, whereas the (111) peak in the film that was aged 72 hours exhibits a similar peak intensity to the as-prepared sample. To exclude the possibility that the selective (100) facet degradation could be caused by unevenly distributed methylammonium (MA) or bromine (Br) composition (27, 28), FAPbI₃ thin films without MA and Br were prepared. As shown in AFM images of the perovskite thin films with and without MAPbBr₃ additives (3 mol %; fig. S4), the crystal facet formation and distribution are not influenced by the small amount of MAPbBr₃ additives. The stability of these two facets was examined in various atmospheres at room temperature for 72 hours, including pure N_2, N_2 and O_2 mixed gas, low-humidity air (30 to 40% RH), and high-humidity air (60 to 70% RH). An AFM image of the sample (fig. S5C) after exposure to the low-humidity air reveals the phase transition to δ-phase on the (100) facet. The transition process to δ-phase is observed to be accelerated under high-humidity air (60 to 70% RH; fig. S5D). No δ-phases are detected in the samples that were exposed to pure N_2 and the N_2 and O_2 mixed gas, as shown in fig. S5, A and B. These results suggest that the (100) facets are intrinsically unstable and can easily suffer phase transition to δ-phase when exposed to moisture. It was reported that light and O_2 can also influence the stability of the perovskite thin film by inducing carrier accumulation and triggering ion diffusion, which suggests different degradation processes (5, 29). Based on the fast degradation of the (100) facet when exposed to moisture, it is assumed that the combined effects from moisture, O_2, and light can aggravate the degradation of the (100) facet, which needs further study.

Optoelectronic properties of the degraded facets

It is essential to examine how the optoelectronic properties are affected by the phase transited δ-phase on the (100) facet. We used photocurrent-AFM (pc-AFM) to study the optoelectronic properties of the (100) and (111) facets. Magnified AFM and pc-AFM images of the 72-hour-degraded sample in Fig. 2, A and B, show individual crystals with exposed (100) and (111) facets. A smooth surface and a uniform photocurrent are observed for the (111) facet, whereas the (100) facet exhibits high fluctuations in the current, where low-current regions (dark regions) correspond to
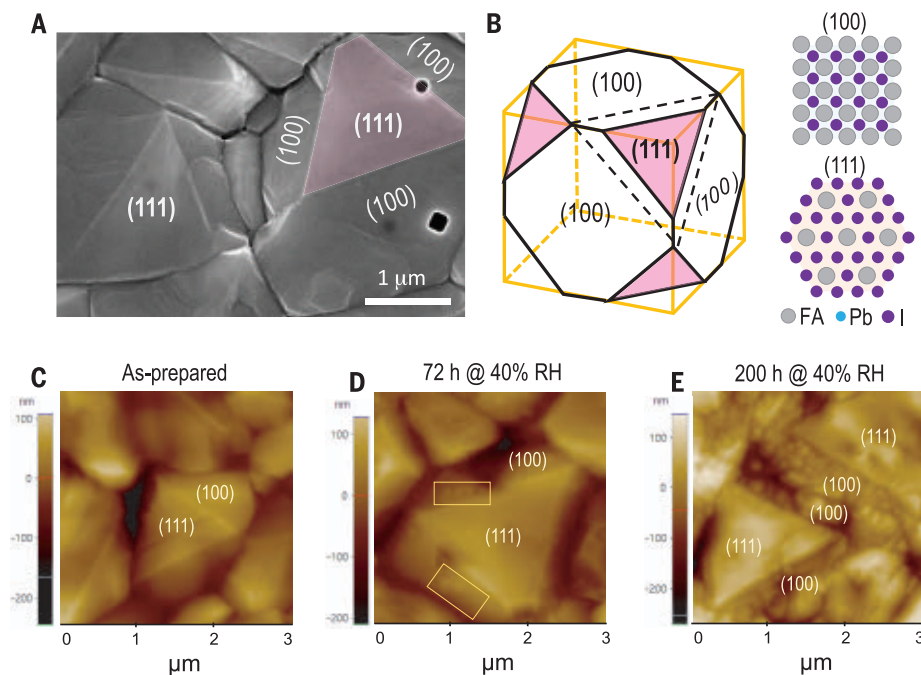

Fig. 1. Facet identification and facet-dependent degradation of FAPbI₃ perovskite thin films. (**A**) SEM image of the perovskite thin film showing the well-defined (100) and (111) facets. The samples were prepared on the SnO₂-coated FTO substrates. (**B**) Schematic model of the (100) and (111) facets on a perovskite cubic crystal (left) and atomic arrangements on the (100) and (111) facets (right). (**C** to **E**) AFM images of the as-prepared sample (C), the sample exposed to 30 to 40% RH for 72 hours (D), and the sample exposed to 30 to 40% RH for 200 hours (E). The (100) and (111) facets are marked on the images within a region of 3 μm by 3 μm. The yellow rectangles in (D) indicate the degraded parts on the (100) facet with protuberances.
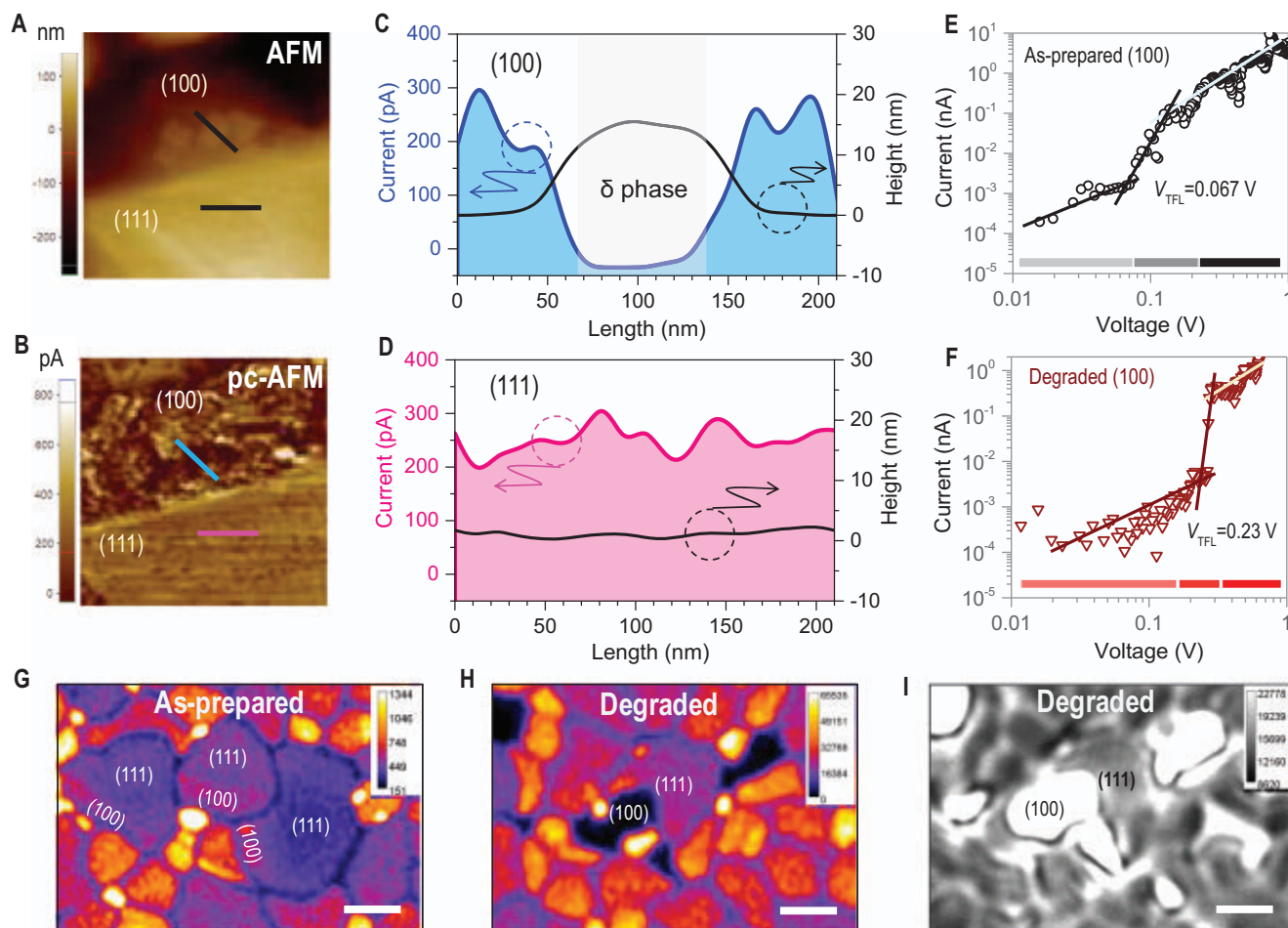
Fig. 2. Optoelectronic properties on the degraded (100) and (111) facets.
(**A** and **B**) AFM (A) and pc-AFM (B) images of the degraded (aged 72 hours) (100) and (111) facets within a region of 1 μm by 1 μm. (**C** and **D**) Current and height profiles extracted from the degraded (100) and (111) facets, respectively. The line scans are marked in (A) and (B). The dashed circles mark the current and the height levels. (**E** and **F**) Current-voltage curves measured from undegraded (E) and degraded (F) (100) facets using the AFM tip as an electrode. (**G**) Confocal PL mapping of the as-prepared sample. The inset legend indicates PL intensity. (**H** and **I**) Confocal PL (H) and transmission mapping (I) of the degraded sample. The triangular (111) and lateral (100) facets are marked on the images. In (G) to (I), scale bars are 1 μm.

the δ-phase that is consistent with the noticeable δ-phase peak in XRD in fig. S3. To demonstrate the heterogeneity on the (100) facet, height and photocurrent values were extracted by line scan (marked by solid lines in Fig. 2, A and B). As shown in the height profile (Fig. 2C), the δ-phase region on the (100) facet with a negligible photocurrent value is about 15 nm higher than the undegraded part, which shows a notable photocurrent value. The current profile exhibits a substantial reduction of the current from 300 to 0 pA on the δ-phase region, which is ascribed to the photoinactive character of the δ-phase. Conversely, photocurrent is continually generated on the (111) facet without changes in height (Fig. 2D), which indicates that the (111) facet is not affected by the degradation process. To identify any changes in the electronic property before and after degradation of the (100) facet, position-specific dark current-voltage curves were measured by using an AFM tip as a nanoelectrode (30, 31).

The current-voltage curves of the undegraded (100) parts and degraded (100) part are shown in Fig. 2, E and F, respectively. The trap state density of the undegraded and degraded (100) parts can be calculated from the trap-filled limit voltage V_{TFL} (see details in methods). The trap state density of the degraded (100) part is estimated to be 2.25×10^{15} cm^{-3}, which is about three times greater than that of the undegraded (100) part (0.65×10^{15} cm^{-3}) (32, 33). The deteriorated electronic property of the (100) facet after degradation is highly related to the formed δ-phase, which can act as trap states (15).

Next, we used confocal microscopy to differentiate the optoelectronic properties of the facets and to study the variations caused by the formed δ-phase on the (100) facet (34, 35). Figure 2G shows a confocal photoluminescence (PL) image of the as-prepared perovskite film. PL heterogeneity on the individual crystal is observed with a dim triangular region and a

bright lateral region, corresponding to the (111) and (100) facets, respectively. This is also confirmed by wide-field PL mapping in fig. S6. This suggests that the bright (100) facet has less nonradiative loss and, therefore, low trap state density, which is consistent with previous reports (21). Thus, we can exclude the possibility that the degradation of the (100) facet could be mainly attributed to surface defects. Figure 2H shows a confocal PL image and an overlaid transmission image (Fig. 2I) of a degraded perovskite film. A dark region on the (100) facet appears on the confocal PL image, which corresponds to the bright region in the transmission image. This implies that the dark regions that appear are photoinactive δ-phase associated with quenching centers, which is consistent with the pc-AFM results.

Mechanisms for facet-dependent degradation

The surface compositions of the (100) and (111) facets were analyzed by energy dispersive
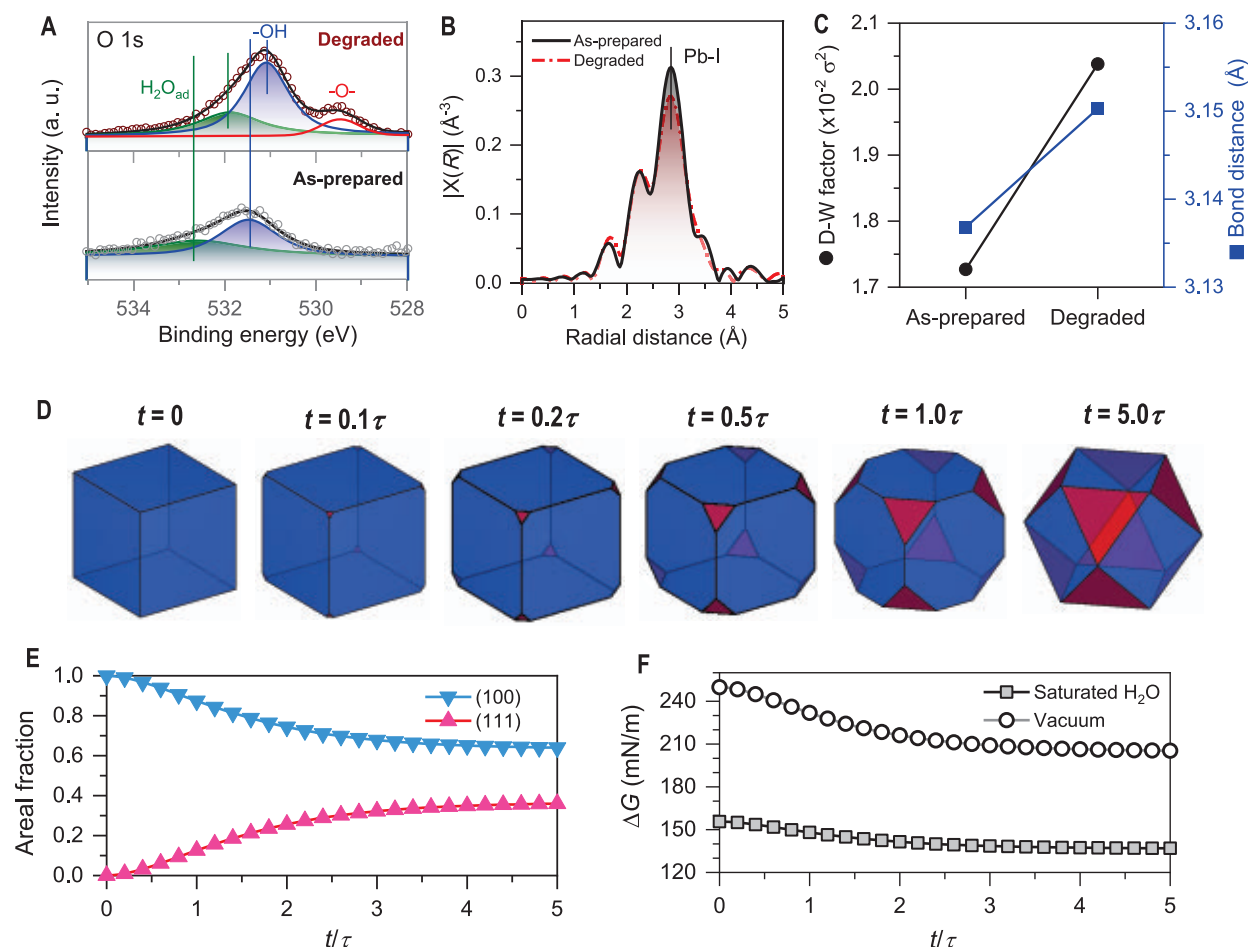
Fig. 3. Mechanisms for facet-dependent degradation. (**A**) O 1s XPS spectra of the as-prepared (bottom) and degraded (top) samples. Open circles and lines represent the measured data and the fitted results, respectively. a.u., arbitrary units. (**B**) Fourier-transformed radial distribution function of Pb K-edge EXAFS spectra for the as-prepared (black) and degraded (red) samples. (**C**) D-W factor and Pb-I bond distance of the as-prepared and degraded samples from the fit result of the EXAFS spectra. (**D**) Time-dependent morphological evolution of a unit cell (cube) of the single cubic crystalline α-FAPbI$_3$ [blue, (100) facets; red, (111) facets]. t, time; τ, the characteristic time scale for the degradation kinetic constant for (111) facet. (**E**) Time dependence of the areal fraction of two different facets in the unit cell. t/τ, the ratio of t to τ. (**F**) Time-dependent Gibbs free energy ΔG for the α-FAPbI$_3$ of the unit cell exposed to H$_2$O together with time-dependent ΔG in vacuum for comparison.

x-ray (EDX) spectroscopy to investigate the degradation process of the different facets. As shown in fig. S7, the N/Pb and I/Pb ratios from the (100) and (111) facets show similar values, which indicates that the compositional difference between these two facets is negligible. Thus, we exclude the possibility that the specific (100) degradation can be attributed to the different surface compositions or stoichiometries. To elucidate in detail the facet-dependent degradation induced by moisture, x-ray photoelectron spectroscopy (XPS) measurements were conducted. All peaks were calibrated using the C 1s peak at 284.6 eV (fig. S8A). As shown in Fig. 3A, the O 1s spectrum of the as-prepared sample is deconvoluted into two peaks at binding energies of 532.7 and 531.5 eV, which correspond to molecularly adsorbed H$_2$O (H$_2$O$_{ad}$) and –OH species attached to the perovskite surface via chemisorption,

respectively (*36*). After degradation, the O 1s XPS spectrum shows a substantial increase in the peak intensity of both the H$_2$O$_{ad}$ and –OH species. As shown in fig. S8B, the O/Pb ratio of the degraded sample is 0.8 and is much higher than that of the as-prepared sample (a ratio of 0.3). Concurrently, we observed peak shifts of ~0.8 and 0.4 eV to lower binding energies for the H$_2$O$_{ad}$ and –OH species, respectively. The increased O/Pb ratio, together with the peak shift for the degraded sample, is indicative of a large amount of water absorption and enhanced interaction between the water molecules and the perovskite surface (*37*). In addition, a small peak observed at a binding energy of 529.5 eV for the degraded sample (Fig. 3A) is assigned to –O– species, which is probably due to the further interaction between the perovskite surface and the oxygen in the –OH species (*38*). As shown in fig. S8C,

the N 1s XPS spectrum of the degraded sample shows an appearance of the –NH$_2$ shoulder owing to the deprotonation process, and the Pb 4f XPS spectrum of the degraded sample shows a small shift toward low binding energy (fig. S8D) (*39–41*). This can be explained by the bonding between the lead iodide framework and the organic cations in the perovskite crystal having been weakened upon moisture attack. To further confirm the degradation products, the samples stored under humid N$_2$ gas (N$_2$ and H$_2$O mixed gas, 30 to 40% RH) and dry O$_2$ gas (N$_2$ and O$_2$ mixed gas) for 72 hours were measured by XRD, and the sample stored under humid N$_2$ gas for 200 hours was also measured. As shown in fig. S9, δ-phase appears on the sample that was degraded under humid N$_2$ gas for 72 hours, which is enhanced for the longer exposure time of 200 hours. No δ-phase is detected on the

Fig. 4. (111) facet–dominated FAPbI$_3$ perovskite thin film has better stability. (**A** and **B**) XRD pattern (A) and SEM image (B) of the FAPbI$_3$ thin film prepared using CHA additive. A large triangular morphology of the (111) facet is distinct. (**C**) The areal ratio of the (111) facet calculated from five crystals of the control and (111)-dominated perovskite thin films. (**D** and **E**) XRD patterns (D) and PL spectra (E) of the control (bottom) and (111)-dominated (top) samples before (black dashed line) and after exposure to humidity for 1000 hours (red and green solid lines for the control and (111)-dominated samples, respectively). (**F**) Stability test of the unencapsulated devices for the (111)-dominated perovskite and the control sample stored under 30 to 40% RH in air atmosphere for 1938 hours.
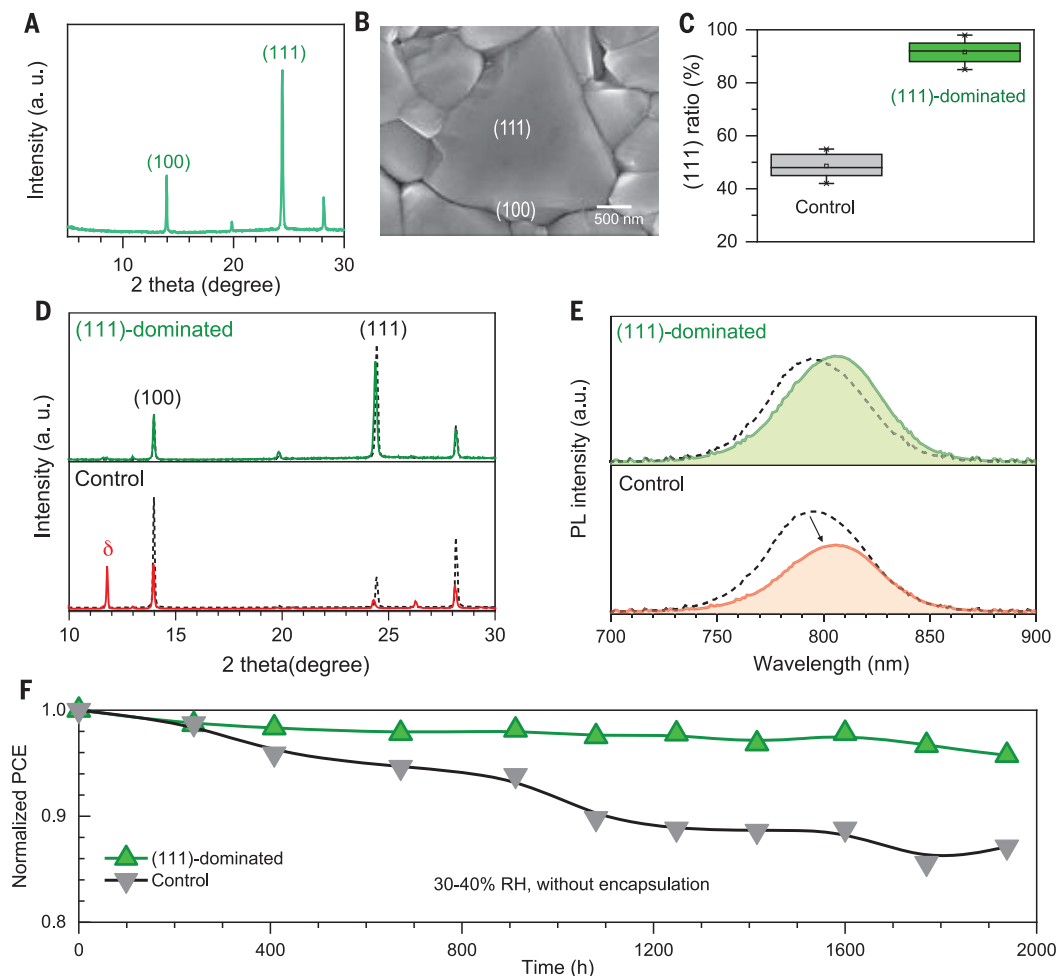
sample stored under dry O$_2$ gas. These results confirm that the degradation product of the FAPbI$_3$ thin film under moisture is δ-phase.

Extended x-ray absorption fine structure (EXAFS) was studied for the as-prepared and degraded samples to further understand local structural changes induced by the moisture (Fig. 3B and fig. S10) (*42*). Based on the Fourier-transformed spectra in Fig. 3B for the as-prepared and degraded samples, the Pb-I bond distance and Debye-Waller (D-W) factor were extracted (see methods for the more detailed fitting process). As shown in Fig. 3C, the degraded sample shows a higher D-W factor of 0.0204 than the as-prepared sample (0.0173), indicating a high structural distortion of the corner-sharing PbI$_6^{2-}$ octahedra. A relatively longer Pb-I bond distance (3.150 Å) is also observed for the degraded sample, which implies that the Pb-I bond is weakened by interaction with water molecules (*43*). Based on the XPS and EXAFS data, we conclude that the water molecules are adsorbed on the perovskite surface by forming –OH species, which results in structural distortion with a weak Pb-I bond. These processes with distorted and weakened

bonding can facilitate the δ-phase transition at room temperature.

A theoretical calculation was carried out to understand the degradation kinetics of cubic crystalline α-FAPbI$_3$ exposed to H$_2$O. First, we calculated the interaction energy of water molecules with (100) and (111) facets (see methods for details). From the calculation, we found that the adhesion (or wetting energy) of H$_2$O is 93.08 and 85.12 mN/m for the (100) and (111) facets, respectively. Thus, the (100) facet is energetically more favorable for H$_2$O adhesion than the (111) facet, which facilitates moisture-induced degradation of the (100) facet as compared with the (111) facet. Using the calculated interface energy of the different facets exposed to H$_2$O, we then made a simple mathematical model to describe the morphological evolution of single cubic crystalline α-FAPbI$_3$ driven by degradation dynamics. We used a simple cube model as the unit cell in which six (100) facets correspond to six faces of the cube with a unit length l at the initial state. Assuming a constant volume of the unit cell per the Wulff construction principle, the time dependences of areas of the facets were calculated (see details in methods) (*44*). As shown

in Fig. 3D, the unit cell is continuously evolving into a truncated cube where the areal fraction of the (111) facet (red face) is continuously increasing, whereas that of the (100) facet (blue face) is decreasing. As is apparent from Fig. 3E, the relative fraction of the (111) facet increases with time, whereas the (100) facet decreases because of the instability caused by moisture attack. The morphological evolution also provides evidence that the (111) facet is the facet that is thermodynamically more stable when the α-FAPbI$_3$ of the unit cell is exposed to H$_2$O. The total Gibbs free energy ΔG of the surfaces exposed to H$_2$O was also calculated. As shown in Fig. 3F, ΔG monotonically decreases with increasing time during the course of the H$_2$O-driven degradation of the unit cell. These results support that the (111) facet is more stable than the (100) facet when under moisture attack, in terms of thermodynamics and degradation kinetics.

Facet engineering of the (111)-dominated thin film to protect against degradation

Based on the degradation nature and dynamics of different facets, we provide a strategy to control the fraction of the (111) facet to reinforce

the film against moisture. Exploring this possibility eventually achieves the (111)-dominated perovskite film through "facet engineering." Cyclohexylamine (CHA) with a boiling point of 134°C is used as an additive to selectively induce (111) preferred growth. The XRD pattern of the perovskite with CHA additive in Fig. 4A confirms that the (111) phase dominates, with a relatively lower intensity (100) peak. The SEM image in Fig. 4B shows that the perovskite with CHA additive has a large triangular (111) facet with less lateral (100) facets on the individual crystal, whereas the control sample (shown in Fig. 1A) has a relatively smaller triangular (111) facet on the crystal surface with more lateral (100) structures.

The large triangular (111) facet shown in the SEM image is consistent with the dominant (111) phase of the XRD pattern. Larger-area SEM images of the control and (111)-dominated films are shown in fig. S11. Based on the exposed (111) and (100) facet area on the crystals, the exposed-area percentages of the (111) facets from five crystals are roughly calculated to be 85 to 98% and 40 to 55% for the (111)-dominated and control samples, respectively (Fig. 4C). Thus, we conclude that the perovskite with CHA additive exhibits an enlarged (111) facet with a reduced (100) facet where moisture-induced phase transition can occur. This enlarged (111) facet might be due to the preferred absorption of the CHA additive, which can reduce the surface energy of the (111) facet.

We examined the stability of the (100)- and (111)-dominated films by exposure to the 30 to 40% RH air atmosphere. After about 1000 hours, the bulk XRD pattern (Fig. 4D, top) of the degraded (111)-dominated film (green line) exhibits a negligible reduction of (100) and (111) peaks compared with the as-prepared film (black dashed line), consistent with the PL spectra that has only a slight peak shift (Fig. 4E, top). The slight PL peak shift might be due to the MA and FA phase segregation (45). However, the degraded control film that has relatively fewer (111) facets shows a substantial reduction in the (100) peak intensity to ~30% of that of the as-prepared film, with an enhanced δ-phase peak after exposure. The degradation of the control film also leads to a substantially reduced PL intensity, as shown in Fig. 4E, which is ascribed to the formed δ-phases on the (100) facet acting as nonradiative recombination centers.

To investigate the photovoltaic performance of PSCs, devices with the configuration of FTO/SnO$_2$ (~20 nm)/perovskite/spiro-MeOTAD (~300 nm)/Au (~80 nm) were prepared (FTO, fluorine-doped tin oxide; spiro-MeOTAD, 2,2′,7,7′-tetrakis[N,N-di(4-methoxyphenyl)amino]-9,9′-spirobifluorene). Figure S12 shows statistical data for the photovoltaic parameters based on 10 devices. For the best-performing devices

measured with a mask area of 0.125 cm^2, the control sample exhibits a power conversion efficiency (PCE) of 24.0% with a short-circuit current J_{sc} of 25.6 mA/cm^2, an open-circuit voltage V_{oc} of 1.12 V, and a fill factor FF of 0.84. The PCE for the (111)-dominated perovskite is 23.8% with a J_{sc} of 25.3 mA/cm^2, a V_{oc} of 1.15 V, and a FF of 0.82. The slightly lower J_{sc} for the (111)-dominated perovskite is due to a photocurrent generation capability that is a little lower than that of the (100) facet (22). It is anticipated that the performance of the (111)-dominated perovskite device can be further improved with surface passivation and optimization methods. In Fig. 4F, the humidity stability test of the devices without encapsulation reveals that the device with the (111)-dominated sample maintains 95% of initial PCE after ~2000 hours, which is notably better than the control device (87%). The average PCE degradation and standard errors (error bars) calculated from five devices are shown in fig. S13. Stability tests of the devices with encapsulation under 85% RH and 85°C were also conducted. As shown in fig. S14, the (111)-dominated sample maintains 85% of the initial PCE after 800 hours, whereas the PCE of the control device decreases to 75% of the initial value. The enhanced stability under high humidity and high temperature is highly related to the enlarged (111) facet on the perovskite surface.

Discussion

Moisture-induced degradation was found to depend on the crystal facet of the FAPbI$_3$ film. The (100) facet is specifically unstable under moisture, whereas the (111) facet is notably stable. Experimental and theoretical studies revealed that the α- to δ-phase transition is accelerated selectively on the (100) facet by moisture, whereas phase transition is considerably retarded on the (111) facet because of its thermodynamic stability against surface interaction with water molecules. A facet-engineered perovskite film with moisture-stable (111) facets was realized by controlling preferred growth using an organic ligand. Moisture and heat stability were substantially improved in the (111) facet–dominated perovskite thin film. Our findings describe distinct facet-dependent degradation, which provides an important insight into the design of stable PSCs using facet engineering.

REFERENCES AND NOTES

1. H. Min et al., Nature 598, 444–450 (2021).
2. Y. Rong et al., Science 361, eaat8235 (2018).
3. M. Kim et al., Science 375, 302–306 (2022).
4. X. Zheng et al., ACS Energy Lett. 1, 1014–1020 (2016).
5. W. Nie et al., Nat. Commun. 7, 11574 (2016).
6. A. M. A. Leguy et al., Chem. Mater. 27, 3397–3407 (2015).
7. H. Lu et al., Science 370, eabb8985 (2020).
8. S. Tan et al., Joule 4, 2426–2442 (2020).
9. D. P. McMeekin et al., Science 351, 151–155 (2016).
10. T. A. S. Doherty et al., Science 374, 1598–1605 (2021).
11. T. Chen et al., Sci. Adv. 2, e1601650 (2016).
12. J.-W. Lee, S. Tan, S. I. Seok, Y. Yang, N.-G. Park, Science 375, eabj1186 (2022).
13. G. E. Eperon et al., Energy Environ. Sci. 7, 982–988 (2014).
14. X. Li et al., Science 375, 434–437 (2022).
15. S. Macpherson et al., Nature 607, 294–300 (2022).
16. J. Chun-Ren Ke et al., Chem. Commun. 53, 5231–5234 (2017).
17. A. Jamshaid et al., Energy Environ. Sci. 14, 4541–4554 (2021).
18. C. Ma, M. Grätzel, N.-G. Park, ACS Energy Lett. 7, 3120–3128 (2022).
19. D. Luo, X. Li, A. Dumont, H. Yu, Z. H. Lu, Adv. Mater. 33, e2006004 (2021).
20. S. Y. Leblebici et al., Nat. Energy 1, 16093 (2016).
21. S. Dong et al., Adv. Mater. 34, e2204342 (2022).
22. C. Ma et al., Joule 6, 2626–2643 (2022).
23. X. Zheng et al., Nat. Energy 5, 131–140 (2020).
24. S. Sun, L. He, M. Yang, J. Cui, S. Liang, Adv. Funct. Mater. 32, 2106982 (2022).
25. J. M. Howard, R. Lahoti, M. S. Leite, Adv. Energy Mater. 10, 1903161 (2019).
26. S. Jiang et al., J. Am. Chem. Soc. 140, 13952–13957 (2018).
27. N. J. Jeon et al., Nature 517, 476–480 (2015).
28. J. W. Lee et al., Adv. Energy Mater. 5, 1501310 (2015).
29. N. Aristidou et al., Nat. Commun. 8, 15218 (2017).
30. R. Yang et al., J. Am. Chem. Soc. 128, 16532–16539 (2006).
31. O. G. Reid, K. Munechika, D. S. Ginger, Nano Lett. 8, 1602–1609 (2008).
32. D. W. deQuilettes et al., Science 348, 683–686 (2015).
33. J.-W. Lee et al., Chem 3, 290–302 (2017).
34. S. Sánchez et al., Energy Environ. Sci. 15, 3862–3876 (2022).
35. D. W. deQuilettes et al., ACS Nano 11, 11488–11496 (2017).
36. S. Yamamoto et al., J. Phys. Condens. Matter 20, 184025 (2008).
37. F. Orlando et al., Top. Catal. 59, 591–604 (2016).
38. S. Yamanaka et al., J. Appl. Phys. 123, 165501 (2018).
39. Q. Zhou et al., Adv. Energy Mater. 9, 1802595 (2019).
40. J. Zhao et al., Sci. Rep. 6, 21976 (2016).
41. Y.-H. Kye, C.-J. Yu, U.-G. Jong, Y. Chen, A. Walsh, J. Phys. Chem. Lett. 9, 2196–2201 (2018).
42. D.-H. Kang, Y.-J. Park, Y.-S. Jeon, N.-G. Park, J. Energy Chem. 67, 549–554 (2022).
43. C. Ma et al., ACS Appl. Mater. Interfaces 9, 14960–14966 (2017).
44. M. Laue, Z. Kristallogr. Cryst. Mater. 105, 124–133 (1943).
45. S. Chen et al., Adv. Energy Mater. 8, 1701543 (2018).

GENE EDITING

Ablation of CaMKIIδ oxidation by CRISPR-Cas9 base editing as a therapy for cardiac disease

Simon Lebek[1,2,3], Francesco Chemello[1,2], Xurde M. Caravia[1,2], Wei Tan[1,2], Hui Li[1,2], Kenian Chen[4], Lin Xu[4], Ning Liu[1,2], Rhonda Bassel-Duby[1,2], Eric N. Olson[1,2]*

CRISPR-Cas9 gene editing is emerging as a prospective therapy for genomic mutations. However, current editing approaches are directed primarily toward relatively small cohorts of patients with specific mutations. Here, we describe a cardioprotective strategy potentially applicable to a broad range of patients with heart disease. We used base editing to ablate the oxidative activation sites of CaMKIIδ, a primary driver of cardiac disease. We show in cardiomyocytes derived from human induced pluripotent stem cells that editing the *CaMKIIδ* gene to eliminate oxidation-sensitive methionine residues confers protection from ischemia/reperfusion (IR) injury. Moreover, *CaMKIIδ* editing in mice at the time of IR enables the heart to recover function from otherwise severe damage. *CaMKIIδ* gene editing may thus represent a permanent and advanced strategy for heart disease therapy.

CRISPR-Cas9 gene editing is being developed as a therapeutic approach to correct monogenic mutations causing hereditary diseases (1–6). However, most CRISPR-Cas9 editing strategies are focused on correction of specific genetic mutations that occur in a small subset of patients, limiting broader applications of the approach. We sought to design a CRISPR-Cas9 gene editing therapy potentially applicable to a broad range of adult patients with cardiovascular disease, the leading cause of worldwide morbidity and mortality (7). Ca^{2+}/calmodulin–dependent protein kinase IIδ (CaMKIIδ) is a central regulator of cardiac signaling and function (8). However, chronic overactivation of CaMKIIδ causes several cardiac diseases in humans and mice, including ischemia/reperfusion (IR) injury, heart failure, hypertrophy, and arrhythmias (9–16). Mechanistically, CaMKIIδ overactivation in the heart has been linked to disturbances in Ca^{2+} homeostasis, inflammation, apoptosis, and fibrosis, leading to cardiac dysfunction (9–13, 17). Oxidation of two methionine residues, Met281 and Met282, located in the regulatory domain of CaMKIIδ, promotes hyperactivation of the kinase by preventing association of the catalytic domain with the autoinhibitory region (18). Modification of these methionine residues to other amino acids prevents oxidation and overactivation of CaMKIIδ, thereby conferring cardioprotection as shown in knock-in mice, where both methionine residues were replaced with valines

in the germline (14, 18, 19). This genetic modification did not cause adverse effects. Both methionines are encoded by exon 11, which is not subject to alternative splicing, so targeting the oxidative activation sites would affect all CaMKIIδ splicing variants (for example CaMKIIδ$_B$, δ$_C$, and δ$_9$ as the major cardiac variants) (20).

Results

Design of a gene editing strategy to ablate the oxidative activation sites of CaMKIIδ

CRISPR-Cas9 adenine base editing (ABE) allows the precise conversion of adenine to guanine nucleotides without introducing double-stranded DNA breaks (1, 2, 21–23). We reasoned that ABE could potentially render CaMKIIδ insensitive to oxidative activation by converting ATG to GTG codons and thereby replacing the oxidation-sensitive methionines with valines (Fig. 1A). Instead of using CRISPR-Cas9 technology to correct genetic mutations, we used the technology to disrupt a pathological signaling pathway, offering a potential therapeutic approach for cardiac disease.

To identify optimal CRISPR-Cas9 base editing components, we used HEK293 cells to screen six different single guide RNAs (sgRNAs; table S1) that covered the genomic region encoding methionines 281 (adenine at nucleotide position c.841) and 282 (adenine at nucleotide position c.844). The sgRNAs were tested with two adenine base editors, ABEmax and ABE8e, in which the engineered deaminases were fused to either SpCas9 nickase or its variant SpRY nickase (3, 23, 24). Sanger sequencing revealed that sgRNA1 combined with ABE8e-SpCas9 had the highest efficiency for editing c.A841G (p.M281V), without editing c.A844 (p.M282). sgRNA6 combined with ABE8e-SpRY showed a broader editing window, editing c.A841G (p.M281V), c.A844G (p.M282V), and c.A848G (p.H283R; fig. S1 and table S2). We validated the sgRNA1 + ABE8e-SpCas9 and sgRNA6 +

ABE8e-SpRY editing strategies in human induced pluripotent stem cells (iPSCs) using nucleofection and observed the same editing pattern seen in HEK293 cells (Fig. 1, B to D). We picked several iPSC clones to test whether exposure to sgRNA6 + ABE8e-SpRY resulted in a heterozygous or homozygous genotype. Sanger sequencing revealed that 75, 17, and 8% of the clones were homozygous, heterozygous, and wildtype, respectively (fig. S2A).

Analysis of potential off-target editing in human iPSCs

The two oxidation-sensitive methionines of human CaMKIIδ are encoded by exon 11 of the *CaMKIIδ* gene, which shares 79% nucleotide homology with *CaMKIIα* and 76% nucleotide homology with *CaMKIIγ*. The sgRNA6 sequence shared 85% homology with *CaMKIIα* and *CaMKIIγ* (fig. S2B). We used deep amplicon sequencing to validate the specificity of ABE genomic editing of *CaMKIIδ* with sgRNA6 + ABE8e-SpRY. In human iPSCs, we observed no genomic changes of the *CaMKIIα* or *CaMKIIγ* genes (fig. S2, C and D, and table S3). However, sgRNA6 has sequence identity with the human *CaMKIIβ* gene, and sequencing analysis showed that the human *CaMKIIβ* gene was edited by sgRNA6. Fortunately, CaMKIIβ is not expressed in human cardiomyocytes, so genomic editing of the *CaMKIIβ* gene in the heart would be inconsequential (fig. S2, E and F) (12). To assess off-target editing, we used CRISPOR to identify the top eight potential off-target sites (table S4) (25). Sequencing analysis showed adenine to guanine editing only in the *DAZL* gene at the adenine base 13 nucleotides upstream from the protospacer adjacent motif (PAM; fig. S2G and tables S4 and S5). This edited site is located in an intronic region that is not expressed and therefore should not have deleterious consequences (25). All other adenines of the predicted top eight potential off-target sites showed adenine to guanine editing of <0.2%, which is considered unspecific background (26).

Functional analyses of CaMKIIδ-edited human iPSC-derived cardiomyocytes

To investigate the physiological consequences of both editing patterns, we generated three independent human homozygous iPSC lines with sgRNA1, sgRNA6, or no sgRNA (wildtype) and differentiated them into cardiomyocytes (iPSC-CMs) that were subjected to simulated IR injury using a hypoxia chamber. There was no difference in the amounts of CaMKII protein in wild-type (WT) or edited iPSC-CMs (fig. S3). After IR, WT iPSC-CMs showed an increase in CaMKII oxidation, as measured by Western blot with an antibody that specifically recognizes oxidized CaMKII, whereas CaMKII oxidation was strongly reduced in sgRNA1 iPSC-CMs and sgRNA6 iPSC-CMs (Fig. 1, E

[1]Department of Molecular Biology, University of Texas Southwestern Medical Center, Dallas, TX 75390, USA. [2]Hamon Center for Regenerative Science and Medicine, University of Texas Southwestern Medical Center, Dallas, TX 75390, USA. [3]Department of Internal Medicine II, University Hospital Regensburg, 93053 Regensburg, Germany. [4]Quantitative Biomedical Research Center, Department of Population and Data Sciences, University of Texas Southwestern Medical Center, Dallas, TX 75390, USA.
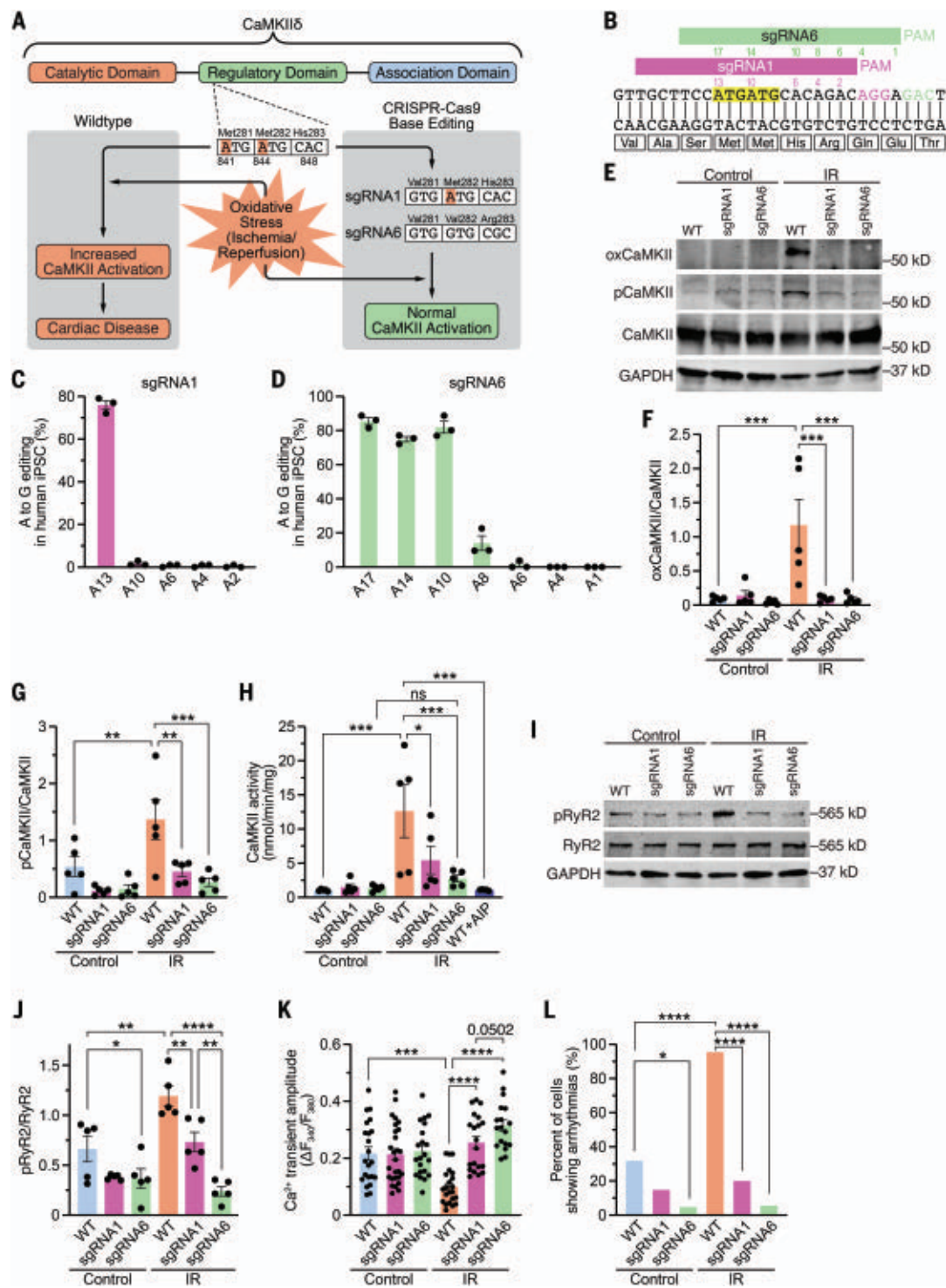*Corresponding author. Email: eric.olson@utsouthwestern.edu

Fig. 1. Genomic editing of *CaMKIIδ* in human iPSC-cardiomyocytes.
(**A**) Schematic of CaMKIIδ and its three domains. Both critical methionines (Met281 and Met282) are located in the regulatory domain. Upon oxidative stress, these methionines are oxidized, resulting in increased CaMKII activity and cardiac disease. Using CRISPR-Cas9 adenine base editing, we identified sgRNA1, which edited only c.A841G (p.M281V; sgRNA1), and sgRNA6, which edited c.A841G (p.M281V), c.A844G (p.M282V), and c.A848G (p.H283R; sgRNA6), thereby preventing CaMKII activation upon oxidative stress. (**B**) Sequence of a segment of exon 11 of *CaMKIIδ* genomic DNA encoding part of the regulatory domain of CaMKIIδ. Alignment of sgRNA1 and sgRNA6 with *CaMKIIδ*. PAM

sequences for sgRNA1 and sgRNA6 are in purple and green, respectively. Both ATGs encoding methionines are highlighted in yellow. Adenines within the sequences of sgRNA1 (purple) and sgRNA6 (green) are numbered (starting from the PAM). (**C**) Percentage of adenine (A) to guanine (G) editing in human iPSCs for each adenine in sgRNA1 after base editing with ABE8e and sgRNA1, as determined by Sanger sequencing. (**D**) Percentage of adenine (A) to guanine (G) editing in human iPSCs for each adenine in sgRNA6 after base editing with ABE8e and sgRNA6, as determined by deep amplicon sequencing. (**E**) Western blot analysis of oxidized CaMKII (specific antibody), autophosphorylated CaMKII (specific antibody), total CaMKII, and GAPDH in human WT, sgRNA1, and

sgRNA6 iPSC-CMs for control group and after simulated ischemia/reperfusion (IR). (**F**) Mean densitometric analysis for oxidized CaMKII normalized to total CaMKII in control and post-IR iPSC-CMs (*n* = 5 independent iPSC-CM differentiations). (**G**) Mean densitometric analysis for autophosphorylated CaMKII normalized to total CaMKII in control and post-IR iPSC-CMs (*n* = 5 independent iPSC-CM differentiations). (**H**) Scatter bar plot showing mean CaMKII activity in control and post-IR iPSC-CMs and in lysates of WT post-IR iPSC-CMs in presence of the CaMKII inhibitor AIP (*n* = 5 independent iPSC-CM differentiations). (**I**) Western blot analysis of ryanodine receptor type 2 (RyR2) phosphorylation at the CaMKII site (serine 2814), total RyR2, and GAPDH

in control and post-IR iPSC-CMs (*n* = 5 independent iPSC-CM differentiations). (**J**) Mean densitometric analysis for phosphorylated RyR2 normalized to total RyR2 in control and post-IR iPSC-CMs (*n* = 5 independent iPSC-CM differentiations). (**K**) Mean Ca²⁺ transient amplitude for each group (based on the number of cardiomyocytes). (**L**) Percentage of iPSC-CMs showing arrhythmias, as measured by epifluorescence microscopy. Statistical comparisons are based on one-way analysis of variance (ANOVA) post-hoc corrected by Holm-Sidak [(F) to (H)] and [(J) and (K)] and on Fisher's exact test (L). Data are presented either as individual data points with means ± SEM or as percent of cells (L).

and F, and fig. S3A). WT iPSC-CMs showed substantial increases in CaMKII autophosphorylation and activity post-IR, which were both reduced in sgRNA1- and sgRNA6-edited iPSC-CMs (Fig. 1, E, G, and H). In accordance with the changes in CaMKII activity, we observed increased CaMKII-dependent phosphorylation of ryanodine receptor type 2 (RyR2) at serine 2814 in WT but not in sgRNA1 or sgRNA6 iPSC-CMs post-IR (Fig. 1, I and J, and fig. S3). Function of iPSC-CMs was assessed by measuring cellular Ca²⁺ transients using epifluorescence microscopy. After IR, WT iPSC-CMs showed an increase in diastolic Ca²⁺ levels, a decrease in Ca²⁺ transient amplitude, and arrhythmias (Fig. 1, K and L, and fig. S4). By contrast, iPSC-CMs edited with sgRNA1 and sgRNA6 were protected from deleterious Ca²⁺ alterations post-IR.

CaMKIIδ editing in mice subjected to IR injury

Since editing with sgRNA6 conferred greater protection to iPSC-CMs than with sgRNA1, we used mouse-sgRNA6 (with 95% homology to human-sgRNA6) and ABE8e-SpRY for base editing to ablate the CaMKIIδ oxidative activation sites in vivo in 12-week-old male C57Bl6 mice (Fig. 2A and fig. S5). We packaged the ABE components in adeno-associated virus serotype-9 (AAV9) using a split-intein trans-splicing system to accommodate the large size of ABE8e and sgRNA6. AAV9 was chosen as the delivery system because it effectively infects the hearts of mice and large mammals (*2*, *4*). To ensure cardiac specificity, we used the cardiac troponin T (cTnT) promoter to drive ABE8e expression. After cardiac IR, AAV9 expressing sgRNA6 and ABE8e-SpRY (AAV-ABE-sgRNA6) was injected [7.5 × 10¹¹ viral genomes (vg) per kg bodyweight of each component] directly into the area of cardiac injury (Fig. 2A). Control mice were subjected to IR with either an injection of control AAV9 or no injection. Sham-treated mice were also subjected to 45-min open chest surgery. Before IR, all mice exhibited normal cardiac function and similar fractional shortening between groups, as measured by echocardiography (Fig. 2B and fig. S6). As expected, cardiac function decreased 24 hours after IR surgery to a similar extent in all groups (fig. S7). While cardiac function re-

mained stable for the first week (fig. S8), after 2 weeks mice that had been administered AAV-ABE-sgRNA6 began to functionally recover, as assessed by echocardiography (Fig. 2B and fig. S9). This recovery time is consistent with a previous study showing that genomic editing begins within 1 week after AAV9 delivery of CRISPR-Cas9 components in vivo (*5*). AAV-ABE-sgRNA6–edited mice showed further cardiac improvement 3 weeks post-IR and attained a level of fractional shortening comparable to that of the sham-treated mice (Fig. 2, B and C, and fig. S10). In addition, left ventricular end-diastolic dilation, a hallmark feature of heart failure, was observed after IR in control mice but was not seen post-IR in mice injected with AAV-ABE-sgRNA6 (Fig. 2D). Furthermore, cardiac magnetic resonance imaging, performed in a subgroup of mice at 4 weeks post-IR, showed impaired cardiac function in control mice and rescue of cardiac function in mice receiving AAV-ABE-sgRNA6 editing components, similar to the echocardiography findings (Fig. 2E, fig. S11, and movies S1 to S4).

Analysis of editing efficiency and potential off-target editing after in vivo ABE

Molecular analyses of heart tissue were performed at 5 weeks post-IR. Deep amplicon sequencing of DNA revealed an adenine to guanine editing efficiency of 7.6 ± 0.2% (c.A841G, p.M281V), 7.5 ± 0.2% (c.A844G, p.M282V), and 8.4 ± 0.2% (c.A848G, p.H283R) of the genomic DNA, and 46.1 ± 1.1% (c.A841G, p.M281V), 46.1 ± 1.1% (c.A844G, p.M282V), and 46.6 ± 1.0% (c.A848G, p.H283R) at the cDNA level (Fig. 3A and table S3). This difference can be explained because most cardiac CaMKIIδ is expressed in cardiomyocytes (*27*), which is the only cell type targeted by a troponin T-driven editing system. Notably, we detected a much higher editing efficiency at the anterior wall with 82.7 ± 1.2% (c.A841G, p.M281V), 85.7 ± 0.7% (c.A844G, p.M282V), and 85.8 ± 1.2% (c.A848G, p.H283R) at the cDNA level (Fig. 3B and C). This indicates that both critical methionines were ablated in almost all cardiomyocytes in the injured area of the heart. No off-target editing of the other *CaMKII* isoforms (α, β, γ) was seen in the hearts of mice injected with AAV-ABE-sgRNA6, as determined by deep amplicon sequencing

(fig. S12, A and B, and table S3). As expected, mouse hearts injected with control AAV9 showed no genomic editing in the *CaMKIIδ* gene. Since CaMKII is expressed in many different tissues (*27*), editing *CaMKII* in organs other than the heart may potentially cause severe adverse effects. Assessment of *CaMKII* editing in other tissues did not reveal genomic editing of any *CaMKII* isoforms in the brain, the tibialis anterior muscle, or the liver, validating the cardiac specificity of the cTnT promoter used in our AAV9 editing system (fig. S12). We also detected no increase in transcriptome-wide adenine to inosine editing in post-IR mice injected with AAV-ABE-sgRNA6 (Fig. 3D).

Protein analysis showed a 4.4-fold increase in the amount of oxidized CaMKII in control mice post-IR. The level of oxidized CaMKII post-IR was normalized in the hearts of mice injected with AAV-ABE-sgRNA6 (Fig. 3, E and F, and fig. S13). The residual signal of oxidized CaMKII in post-IR mice injected with AAV-ABE-sgRNA6 may either be unedited and oxidized CaMKIIδ, oxidized CaMKIIγ, or unspecific background. Consistent with the amount of oxidized CaMKII, CaMKII autophosphorylation and activity were increased in control mice post-IR but not in post-IR mice injected with AAV-ABE-sgRNA6 (Fig. 3, E, G, and H, and fig. S13). Moreover, we found CaMKII-dependent phosphorylation of RyR2 to be increased in control mice post-IR but not in *CaMKIIδ*-edited mice post-IR (Fig. 3, I and J, and fig. S13).

Mechanisms of cardioprotection and long-term effects conferred by CaMKIIδ editing in vivo

RNA sequencing of control and AAV-ABE-sgRNA6–edited hearts revealed three different types of transcriptomes by principal component analysis (fig. S14). Although the transcriptome changed after IR, no differences were detected between the two different control groups post-IR. However, hearts subjected to IR- and *CaMKIIδ*-editing had a transcriptome different from that of control WT mouse hearts and formed a third cluster. In total, we identified 211 genes that were differentially expressed in mice subjected to IR with injection of control AAV9 compared with sham-treated mice (fig. S14B). Gene ontology analysis of the 163 genes up-regulated

Fig. 2. CaMKIIδ base editing improves cardiac function in vivo post-IR. (**A**) Experimental design for subjecting mice to IR, injecting AAV-ABE-sgRNA6 for CaMKIIδ editing in vivo and monitoring heart function by echocardiography and cardiac magnetic resonance imaging (MRI). The AAV9 delivery system carrying the CRISPR-Cas9 base editing components with a split-intein trans-splicing system is shown. (**B**) Time course of fractional shortening for each group before IR as well as 24 hours, 1 week, 2 weeks, and 3 weeks post-IR (n = 8 mice for each group; x axis not shown to scale). (**C**) Representative M-mode recordings of hearts of a sham-treated mouse, a mouse subjected to IR, a mouse subjected to IR with intracardiac injection of a control virus, and a mouse subjected to IR with intracardiac injection of AAV-ABE-sgRNA6 (IR+Edit) at 3 weeks post-IR. (**D**) Mean left ventricular end-diastolic diameter 3 weeks post-IR (n = 8 mice for each group). (**E**) Mean left ventricular ejection fraction determined by cardiac MRI 4 weeks post-IR (n = 5 mice for each group). All replicates are individual mice. Statistical comparisons are based on two-way (B) and one-way [(D) and (E)] ANOVA post-hoc corrected by Holm-Sidak. Data are presented as means ± SEM.
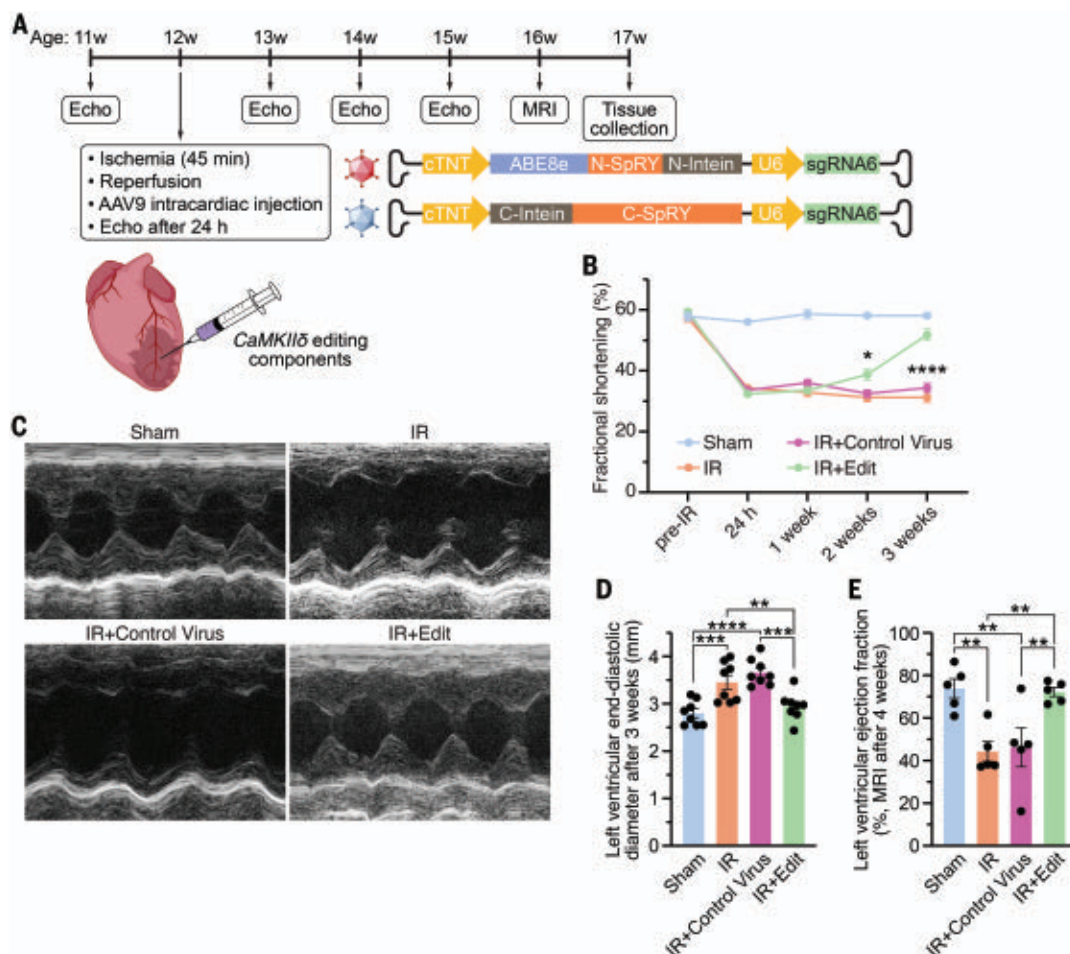
in IR (with control AAV9) revealed pathways related to cardiac disease whereas pathways associated with the 48 down-regulated genes were mainly related to cardiac function (fig. S14, C and D). Compared with mice treated with the control virus, we found 101 up-regulated and 108 down-regulated genes in mouse hearts with edited CaMKIIδ (Fig. 3K). Analysis of gene ontology terms revealed that pathways related to cardiac performance and disease—which were dysregulated in control AAV9 mice post-IR—were rescued in CaMKIIδ-edited mice post-IR (Fig. 3, L and M).

We found a substantial increase in the percentage of apoptotic cells in TUNEL-stained heart sections of mice post-IR compared with heart sections of sham-treated mice (Fig. 4, A and B). In contrast to the hearts of control mice post-IR, the percentage of apoptotic cells in CaMKIIδ-edited mice was comparable to the hearts of sham-treated mice. We also found a 2.7-fold increase in the area of fibrotic tissue in mice post-IR whereas the CaMKIIδ-edited mice were protected against fibrosis post-IR (Fig. 4, C and D, and figs. S15 and S16). We

observed an increase in myocardial infiltration of inflammatory cells in mice post-IR, but this was not seen in hearts of CaMKIIδ-edited mice (fig. S15).

To test for potential long-term adverse effects of CaMKIIδ editing, we analyzed mice 260 days after intraperitoneal injection of AAV-ABE-sgRNA6 at P5. Compared with noninjected littermates, we detected no difference in body-weight (fig. S17). Since oxidized CaMKII has previously been linked to exercise performance (especially in skeletal muscle), we challenged these mice with a treadmill exhaustion test (28). We observed no difference in exercise performance, and immediate echocardiography after exhaustion revealed normal cardiac function in mice subjected to cardiac-specific CaMKIIδ editing 260 days earlier (fig. S17).

Discussion

CaMKIIδ inhibition has previously been proposed as a therapy for cardiac disease, and several CaMKII inhibitors have been tested in preclinical studies (15–17). However, these CaMKII inhibitors face several challenges

(15), as some were reported to inhibit other ion channels (for example potassium channels) (29) and others showed few therapeutic benefits (15–17). Specific CaMKIIδ inhibitors that are ATP-competitive inhibitors also inhibit other kinases with potential deleterious effects, and other inhibitors are not bio-available or cell permeable (15, 16). Another challenge in using CaMKIIδ inhibitors is that CaMKIIδ is ubiquitously expressed and its global inhibition can have adverse effects in tissues other than the heart (27). Another clinical limitation of using CaMKIIδ inhibitors is the requirement for daily administration. Using the CRISPR-Cas9 ABE system to edit the genome provides a permanent change to the CaMKIIδ gene and overrides many of the above limitations. Incorporation of the cTnT promoter to restrict expression of the ABE components exclusively to the heart also prevents possible adverse consequences of CaMKIIδ inhibition in other tissues. Moreover, CRISPR-Cas9 gene editing is permanent, representing a "one and done" therapy (30).
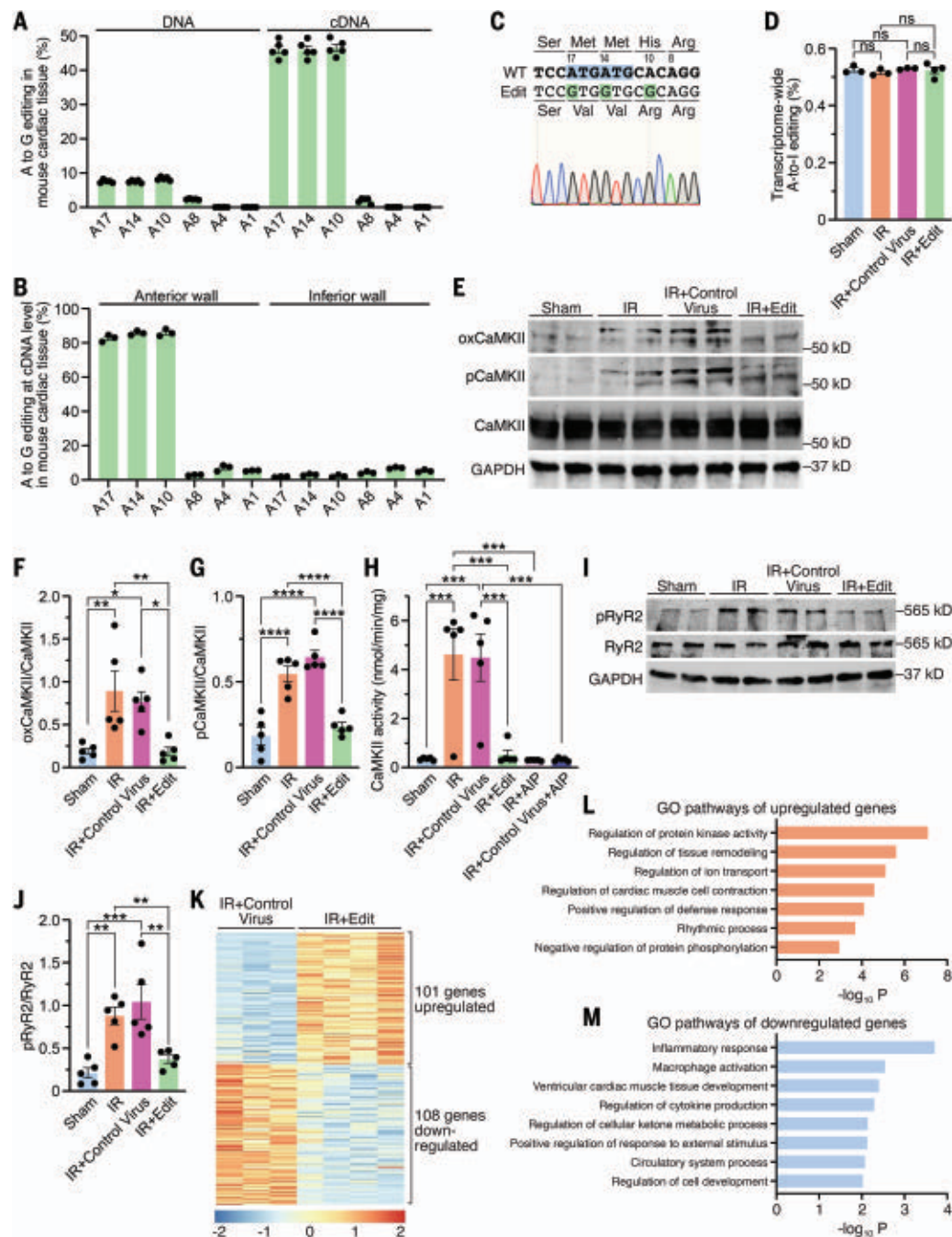
Fig. 3. Analysis of mouse hearts after *CaMKIIδ* in vivo genomic editing by administration of AAV-ABE-sgRNA6. (**A**) Percentage of adenine (A) to guanine (G) editing of DNA and cDNA for each adenine along sgRNA6 in the myocardium of mice treated with AAV-ABE-sgRNA6, as determined by deep amplicon sequencing. (**B**) Spatial analysis of adenine (A) to guanine (G) editing efficiency at the cDNA level for each adenine along sgRNA6 in the anterior and the inferior cardiac wall of mice injected with AAV-ABE-sgRNA6 in the anterior cardiac wall, as determined by Sanger sequencing. (**C**) Sequencing of a TOPO-TA clone shows in vivo editing of the *CaMKIIδ* gene at the cDNA level. (**D**) Percentage of transcriptome-wide adenine (A) to inosine (I) editing in the myocardium of sham-treated, IR, IR treated with a control virus, and IR-edited mice. (**E**) Western blot analysis of oxidized CaMKII, autophosphorylated CaMKII, total CaMKII, and GAPDH for all groups. (**F**) Mean densitometric analyses for oxidized CaMKII normalized to total CaMKII for sham-treated, IR, IR treated with a control virus, and IR-edited mice. (**G**) Mean densitometric analyses for autophosphorylated

CaMKII normalized to total CaMKII for all groups. (**H**) Mean CaMKII activity for all groups and for lysates of IR and IR+Control Virus mice, both in presence of the CaMKII inhibitor AIP. (**I**) Western blot analysis of ryanodine receptor type 2 (RyR2) phosphorylation at the CaMKII site (serine 2814), total RyR2, and GAPDH for all groups. (**J**) Mean densitometric analysis for phosphorylated RyR2 normalized to total RyR2 for all groups. (**K**) Heat map of 209 differentially expressed genes between mice subjected to IR and injected with either a control AAV9 ($n = 3$) or AAV-ABE-sgRNA6 for editing of the *CaMKIIδ* gene ($n = 4$). (**L**) Gene ontology terms associated with the 101 genes up-regulated in mouse hearts injected with AAV-ABE-sgRNA6 compared to mice receiving control AAV9. (**M**) Gene ontology terms associated with the 108 genes down-regulated in mouse hearts injected with AAV-ABE-sgRNA6 compared to mice injected with control AAV9. All replicates are individual mice. Statistical comparisons are based on one-way ANOVA post-hoc corrected by Holm-Sidak. Data are presented as individual data points with means ± SEM.
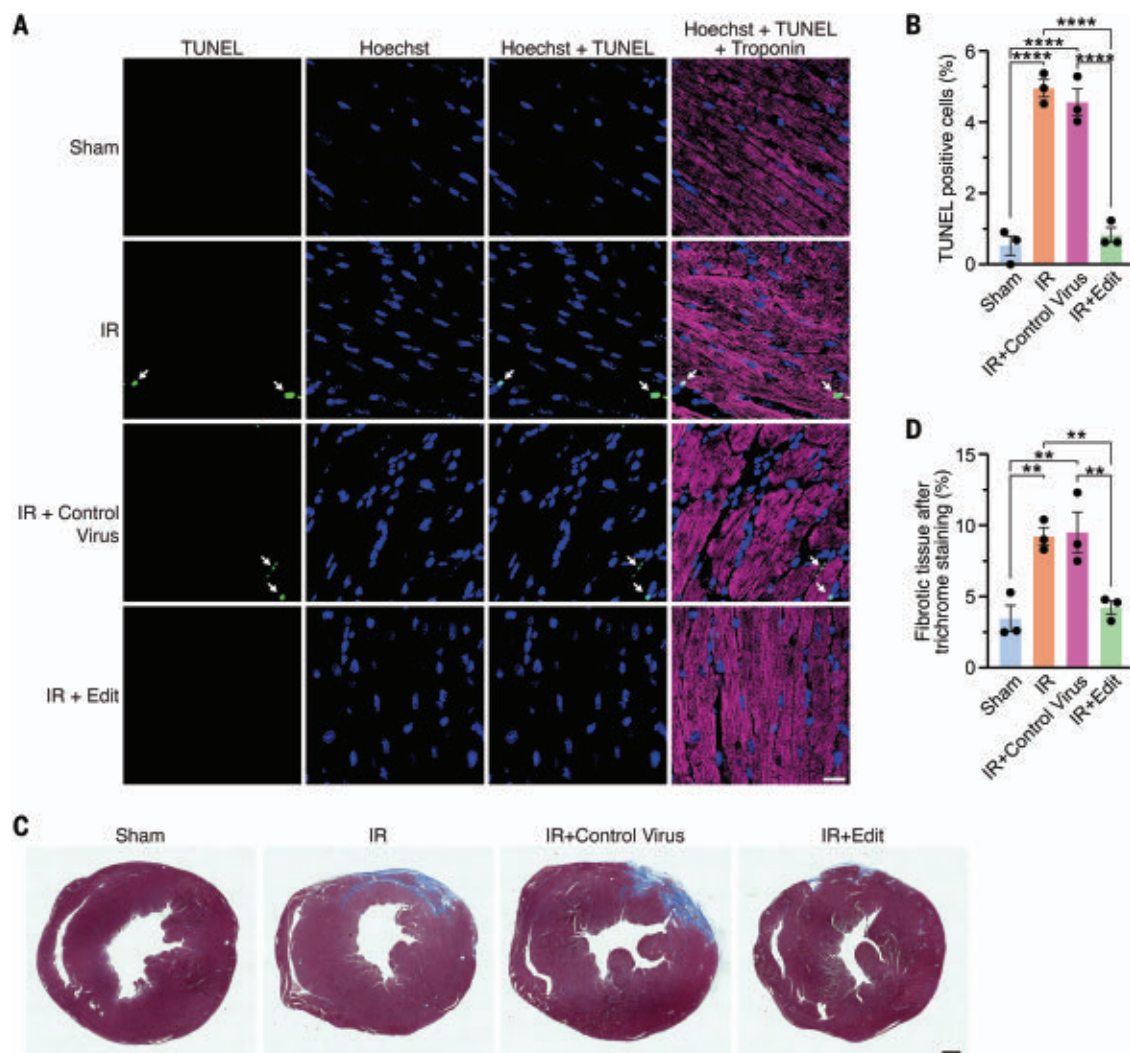
Fig. 4. Genomic editing of *CaMKIIδ* prevents cardiac cell death and fibrosis after IR. (**A**) Immunohistochemistry of TUNEL (green, arrows), Hoechst 33342 (blue, for all nuclei), and cardiac troponin (recolored in purple for colorblind accessibility) in representative heart sections of mice subjected to sham surgery, IR, IR treated with a control AAV9, and IR treated with AAV-ABE-sgRNA6 (IR+Edit; scale bar 20 μm). (**B**) Mean percentage of TUNEL-positive cells in each group. (**C**) Whole transverse cross-sections of trichrome stained hearts for each group (scale bar 500 μm). (**D**) Mean percentage of fibrotic cardiac tissue in each group. Replicates are individual mice. Statistical comparisons are based on one-way ANOVA post-hoc corrected by Holm-Sidak. Data are presented as individual data points with means ± SEM.

In patients, administration of *CaMKIIδ* editing components after a myocardial infarction could be achieved in conjunction with the standard of care in response to a heart attack. The first therapeutic step after a myocardial infarction is coronary angiography and revascularization of the infarct artery, which requires a catheter that could also be used to deliver *CaMKIIδ* editing components to the infarct artery or to the infarct area (*31*). Before starting initial human clinical trials, future studies are needed including more analyses of the pharmacological profile, optimization of the viral dosage, more studies regarding the toxicity and safety of the treatment (such as potential immunogenicity of the base editor), and assessment of animal long-term survival.

We analyzed the top eight predicted sites in the human genome for potential off-target editing, but a deeper analysis (*32*), especially after extended exposure to the base editor, will be required for formal regulatory review. It will also be necessary to analyze the interaction with other drugs and treatments as well as the effectiveness of *CaMKIIδ* editing compared to currently available heart failure medication. Further studies showing a benefit in larger animals such as pigs and nonhuman primates would also be an important step toward clinical advancement of this approach.

CRISPR-Cas9 gene editing technology is typically used to correct specific genetic mutations before disease onset (*1–6*). Since the total number of patients carrying one specific mutation is usually low, the offered treatment affects only a limited group of patients. CRISPR-Cas9 gene editing has already been used to knock down WT *PCSK9* gene in the liver as a strategy for hereditary familial hypercholesterolemia (*32*). Our strategy is designed to ablate a detrimental pathway in the adult heart and thereby provide therapeutic benefits for already-established heart disease. The concept of using CRISPR-Cas9 to block activation of deleterious pathways is also translatable to other signaling cascades in other human diseases.

REFERENCES AND NOTES

1. N. Liu, E. N. Olson, *Circ. Res.* **130**, 1827–1850 (2022).
2. F. Chemello *et al.*, *Sci. Adv.* **7**, eabg4910 (2021).

3. M. F. Richter *et al.*, *Nat. Biotechnol.* **38**, 883–891 (2020).
4. L. Amoasii *et al.*, *Science* **362**, 86–91 (2018).
5. L. Amoasii *et al.*, *Nat. Commun.* **10**, 4537 (2019).
6. L. W. Koblan *et al.*, *Nature* **589**, 608–614 (2021).
7. S. S. Virani *et al.*, *Circulation* **143**, e254–e743 (2021).
8. J. Beckendorf, M. M. G. van den Hoogenhof, J. Backs, *Basic Res. Cardiol.* **113**, 29 (2018).
9. S. Neef *et al.*, *Circ. Res.* **106**, 1134–1144 (2010).
10. J. Backs *et al.*, *Proc. Natl. Acad. Sci. U.S.A.* **106**, 2342–2347 (2009).
11. S. Lebek *et al.*, *Circ. Res.* **126**, 603–615 (2020).
12. T. Zhang, J. H. Brown, *Cardiovasc. Res.* **63**, 476–486 (2004).
13. H. Ling *et al.*, *Circ. Res.* **112**, 935–944 (2013).
14. M. Luo *et al.*, *J. Clin. Invest.* **123**, 1262–1274 (2013).
15. D. Nassal, D. Gratz, T. J. Hund, *Front. Pharmacol.* **11**, 35 (2020).
16. P. Pellicena, H. Schulman, *Front. Pharmacol.* **5**, 21 (2014).
17. S. Lebek *et al.*, *J. Mol. Cell. Cardiol.* **118**, 159–168 (2018).
18. J. R. Erickson *et al.*, *Cell* **133**, 462–474 (2008).
19. A. Purohit *et al.*, *Circulation* **128**, 1748–1757 (2013).
20. M. Zhang *et al.*, *Nat. Cell Biol.* **21**, 1152–1163 (2019).
21. N. M. Gaudelli *et al.*, *Nature* **551**, 464–471 (2017).
22. A. C. Komor, Y. B. Kim, M. S. Packer, J. A. Zuris, D. R. Liu, *Nature* **533**, 420–424 (2016).
23. L. W. Koblan *et al.*, *Nat. Biotechnol.* **36**, 843–846 (2018).
24. R. T. Walton, K. A. Christie, M. N. Whittaker, B. P. Kleinstiver, *Science* **368**, 290–296 (2020).
25. J. P. Concordet, M. Haeussler, *Nucleic Acids Res.* **46** (W1), W242–W245 (2018).
26. K. Clement *et al.*, *Nat. Biotechnol.* **37**, 224–226 (2019).
27. M. Uhlén *et al.*, *Science* **347**, 1260419 (2015).
28. Q. Wang *et al.*, *Nat. Commun.* **12**, 3175 (2021).
29. B. Hegyi *et al.*, *J. Mol. Cell. Cardiol.* **89** (Pt B), 173–176 (2015).
30. D. R. Karri *et al.*, *Mol. Ther. Nucleic Acids* **28**, 154–167 (2022).
31. J. S. Lawton *et al.*, *Circulation* **145**, e18–e114 (2022).
32. K. Musunuru *et al.*, *Nature* **593**, 429–434 (2021).

METABOLIC ADAPTATION

Loss of a gluconeogenic muscle enzyme contributed to adaptive metabolic traits in hummingbirds

Ekaterina Osipova[1,2,3,4,5,6], Rico Barsacchi[1], Tom Brown[1,3,7], Keren Sadanandan[8], Andrea H. Gaede[9,10], Amanda Monte[11], Julia Jarrells[1], Claudia Moebius[1], Martin Pippel[1,3], Douglas L. Altshuler[9], Sylke Winkler[1,7], Marc Bickle[12], Maude W. Baldwin[8], Michael Hiller[1,2,3,4,5,6]*

Hummingbirds possess distinct metabolic adaptations to fuel their energy-demanding hovering flight, but the underlying genomic changes are largely unknown. Here, we generated a chromosome-level genome assembly of the long-tailed hermit and screened for genes that have been specifically inactivated in the ancestral hummingbird lineage. We discovered that *FBP2* (fructose-bisphosphatase 2), which encodes a gluconeogenic muscle enzyme, was lost during a time period when hovering flight evolved. We show that *FBP2* knockdown in an avian muscle cell line up-regulates glycolysis and enhances mitochondrial respiration, coincident with an increased mitochondria number. Furthermore, genes involved in mitochondrial respiration and organization have up-regulated expression in hummingbird flight muscle. Together, these results suggest that *FBP2* loss was likely a key step in the evolution of metabolic muscle adaptations required for true hovering flight.

H ummingbirds are the only birds capable of true (sustained) hovering flight and exhibit exceptional maneuverability, including backward flight. These feats are enabled by shoulder girdle adaptations that produce lift both with the up- and down-stroke. Requiring rapid wingbeats, hovering flight is the most energy-demanding locomotion type, and hummingbirds have the highest mass-specific metabolic rate measured for vertebrates (*1, 2*). Hummingbirds fuel this energy-demanding activity largely with sugars, obtained by feeding on flower nectar. Within minutes after feeding, hummingbirds can fuel almost their entire metabolism with newly ingested sugars (*3, 4*).

These metabolic adaptations are facilitated by high sugar-uptake rates and increased rates of carbohydrate-metabolizing enzymes (*4–6*). Hummingbirds have the distinctive ability to directly metabolize dietary fructose as efficiently as glucose (*7, 8*), and their sweet taste perception evolved by co-option of an umami taste receptor (*9*). Sequence analyses revealed signatures of positive selection in hummingbird glycolytic enzymes (*10*). However, the genomic basis of metabolic muscle adaptations in hummingbirds is largely unknown.

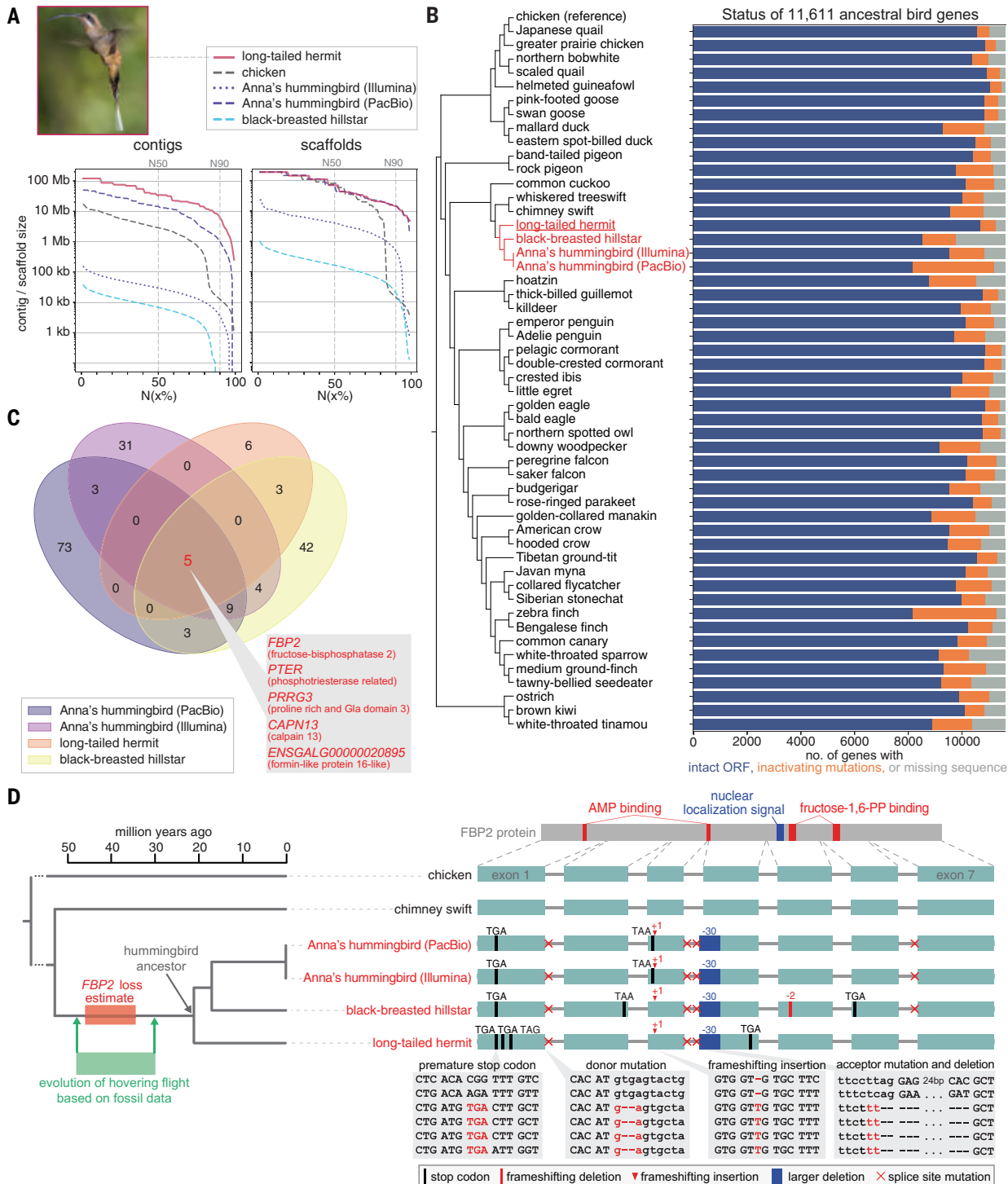### Assembly of the long-tailed hermit genome

True hovering flight and nectarivory are ancestral features of hummingbirds that evolved after the hummingbird and swift lineage split ~54 million years ago (Mya) and before the beginning of the hummingbird radiation ~22 Mya (*11, 12*). To reveal the genomic underpinnings of adaptations that evolved during that period, we generated PacBio continuous long reads, 10x genomics linked reads, Bionano optical maps, and chromosome conformation capture (Hi-C) read pairs to assemble a highly contiguous, chromosome-level genome of the long-tailed hermit (*Phaethornis superciliosus*), a representative of the hermit subfamily that is a sister clade to nearly all other hummingbirds (fig. S1A). Together with two other sequenced hummingbirds (*13–15*), this allowed us to infer ancestral hummingbird mutations on the basis

[1]Max Planck Institute of Molecular Cell Biology and Genetics, Pfotenhauerstr. 108, 01307 Dresden, Germany. [2]Max Planck Institute for the Physics of Complex Systems, Nöthnitzer Str. 38, 01187 Dresden, Germany. [3]Center for Systems Biology Dresden, Pfotenhauerstr. 108, 01307 Dresden, Germany. [4]LOEWE Centre for Translational Biodiversity Genomics, Senckenberganlage 25, 60325 Frankfurt, Germany. [5]Senckenberg Research Institute, Senckenberganlage 25, 60325 Frankfurt, Germany. [6]Goethe-University, Faculty of Biosciences, Max-von-Laue-Str. 9, 60438 Frankfurt, Germany. [7]DRESDEN concept Genome Center, Technische Universität Dresden, 01062 Dresden, Germany. [8]Evolution of Sensory Systems Research Group, Max Planck Institute for Ornithology, Seewiesen, Germany. [9]University of British Columbia, Vancouver, Vancouver, BC V6T 1Z4, Canada. [10]Structure and Motion Laboratory, Royal Veterinary College, University of London, London, UK. [11]Department of Behavioural Neurobiology, Max Planck Institute for Ornithology, Seewiesen, Germany. [12]Roche Institute for Translational Bioengineering, Grenzacherstrasse 124, 4070 Basel, Switzerland.
*Corresponding author. Email: michael.hiller@senckenberg.de

of parsimony (fig. S1B). Our hermit assembly has contig and scaffold N50 values of 35.2 and 72.7 Mb, respectively, and thus a higher contiguity than previous assemblies of two hummingbirds and even chicken (Fig. 1A). We estimated a high base accuracy with only about three remaining errors per 1 Mb [quality value (QV) 55.3].

To compare assembly quality, we used a previously developed approach (16) to determine how many of 11,611 ancestral bird genes have (i) an intact reading frame, (ii) gene-inactivating mutations (in-frame stop codons, frameshifting insertions and deletions, splice site mutations, and exon deletions), or (iii) missing sequence due to assembly incompleteness (tables S1 and S2).

Fig. 1. Loss of *FBP2* coincided with the evolution of hovering flight.
(**A**) Comparison of genome assembly contiguity. N(x%) graphs show contig (left) and scaffold (right) sizes on the *y* axis for which *x* percent of the assembly consists of contigs and scaffolds of at least that size. Photo: Mats Lindberg. (**B**) Status of 11,611 ancestral avian genes in 51 bird assemblies. (**C**) Overlap of gene losses identified in four assemblies of three hummingbird species. (**D**) Left: Timetree with the estimated time period of *FBP2* loss, which overlaps the period during which hovering flight evolved according to two dated fossils. Right: Visualization of the seven *FBP2* coding exons shows that hummingbirds share several inactivating mutations. Insets show the sequences of the six assemblies.

Considering genomes of 50 birds that cover major clades of the avian phylogeny (*11*), our long-tailed hermit assembly is among those with the highest number of intact genes (Fig. 1B). Compared with previous hummingbird assemblies, our hermit assembly has fewer genes with inactivating mutations (Fig. 1B and fig. S2). Together, this supports not only a high level of assembly completeness but also a high base accuracy.

Identification of hummingbird-specific gene losses

Loss of ancestral coding genes can be relevant for adaptation (*16–18*). To investigate whether gene losses may have contributed to hummingbird adaptations, we performed a genome-wide screen for genes that were specifically inactivated in the ancestral hummingbird lineage. We identified genes likely lost in all three sequenced hummingbird species and then excluded those genes that are also lost in swifts (the closest insectivorous sister lineage of hummingbirds) or any of 45 other birds (table S1). This screen identified five genes (Fig. 1C). Three of these five genes (*FBP2*, *PTER*, *CAPN13*) have inactivating mutations that are shared between the three hummingbird species, which parsimoniously suggests that these mutations, and thus the gene losses, occurred on the ancestral hummingbird branch (Fig. 1D and figs. S1B and S3).

FBP2 loss coincided with the evolution of hovering flight

Whereas four of these five genes have no known function related to metabolism and physiology, the fifth gene is *FBP2* (fructose-bisphosphatase 2) (table S3). This gene encodes a muscle FBPase enzyme that catalyzes a rate-limiting step in gluconeogenesis and converts fructose-1,6-bisphosphate to fructose-6-phosphate (*19*). *FBP2* exhibits numerous inactivating mutations, resulting in a nonfunctional protein. Six mutations are shared among assemblies of the three hummingbird species (Fig. 1D), which excludes the possibility of base errors.

To further investigate when the loss of *FBP2* happened on the ancestral hummingbird branch, we used a molecular dating approach that is based on the rate of nonsynonymous to synonymous substitutions and species divergence times (*11*, *12*). We estimated that *FBP2* inactivation happened 34 to 46 Mya (table S4). Two key fossils illuminate when hovering flight evolved in the hummingbird lineage. An insectivorous apodiform bird fossil (*Parargornis messelensis*) found in 48-million-year-old strata in Germany's Messel pit provides an upper bound (*20*). The oldest hummingbird-like fossil (*Eurotrochilus inexpectatus*), possessing key anatomical features for nectar feeding and hovering flight, dated 30 to 35 Mya (*21*). These fossils suggest that true hovering flight likely evolved between 48 and ~30 Mya, and our data indicate that *FBP2* loss coincided with this period (Fig. 1D).

Hummingbird muscle expresses no FBPases

In tetrapods, FBPase enzymes are encoded by two paralogous genes: *FBP1*, which is mostly expressed in the liver and kidneys, and *FBP2*, which is predominantly expressed in skeletal muscle (*22*). Because none of the investigated bird species, including hummingbirds, have lost *FBP1* (table S3), we tested whether hummingbird *FBP1* is expressed in muscle to compensate for *FBP2* loss. To this end, we performed RNA sequencing on biological triplicates of the major flight muscle (pectoralis) and liver tissue of Anna's hummingbird and the common swift. As in mammals, the common swift expressed *FBP1* in liver and *FBP2* in muscle (Fig. 2). In the hummingbird, no relevant exon expression of the *FBP2* remnant was detected (fig. S4), confirming its loss. Notably, the intact hummingbird *FBP1* gene is expressed in liver but not muscle (Fig. 2). This indicates that the consequences of *FBP2* loss are likely restricted to muscle, as

this tissue expresses no FBPase enzymes in hummingbirds.

FBP2 knockdown up-regulates glycolysis and mitochondrial respiration

Gluconeogenic FBPase enzymes oppose the action of phosphofructokinase, one of the rate-limiting enzymes in glycolysis (*23*). Thus, loss of the muscle enzyme encoded by *FBP2* may increase glycolytic flux. To test this experimentally, we used QM7 cells, a quail muscle (myoblast) cell line that expresses *FBP2* (fig. S5), and the CRISPR-Cas9 system to knock out *FBP2*. We designed four guide RNAs that specifically target intronic regions around exon 5 (Fig. 3A), which is required for substrate binding and encodes the nuclear localization signal required for FBP2's mitochondrial function (*24*, *25*). Although neither wild-type nor knockout QM7 cells survive in isolation, precluding the generation of a clonal knockout lineage, we achieved deletions of *FBP2* exon 5 in pools of cells (Fig. 3B and fig. S6). In these *FBP2* knockdown cells, we measured a 65% (P = 0.0007) reduction of *FBP2* expression without a compensatory up-regulation of *FBP1* and a 20% (P = 0.0025) lower FBPase activity (Fig. 3, B to D).

To test whether *FBP2* knockdown increases glycolytic flux, we used the Seahorse Glycolytic Rate Assay to measure in real time the glycolytic proton efflux rate, a direct readout of glycolytic flux. Both basal glycolysis and compensatory glycolysis, induced by mitochondrial inhibition, were significantly increased in *FBP2* knockdown cells in comparison with mock-treated wild-type cells (Fig. 3, E and F, and fig. S7).

Glycolysis produces pyruvate, which can be catabolized by mitochondrial oxidative phosphorylation (OXPHOS) under aerobic conditions. Analyzing the Seahorse real-time measurements of the oxygen consumption rate, a readout of OXPHOS, showed that *FBP2* knockdown significantly up-regulates mitochondrial respiration (Fig. 3, G and H), which we estimate to generate most adenosine 5´-triphosphate in QM7 cells
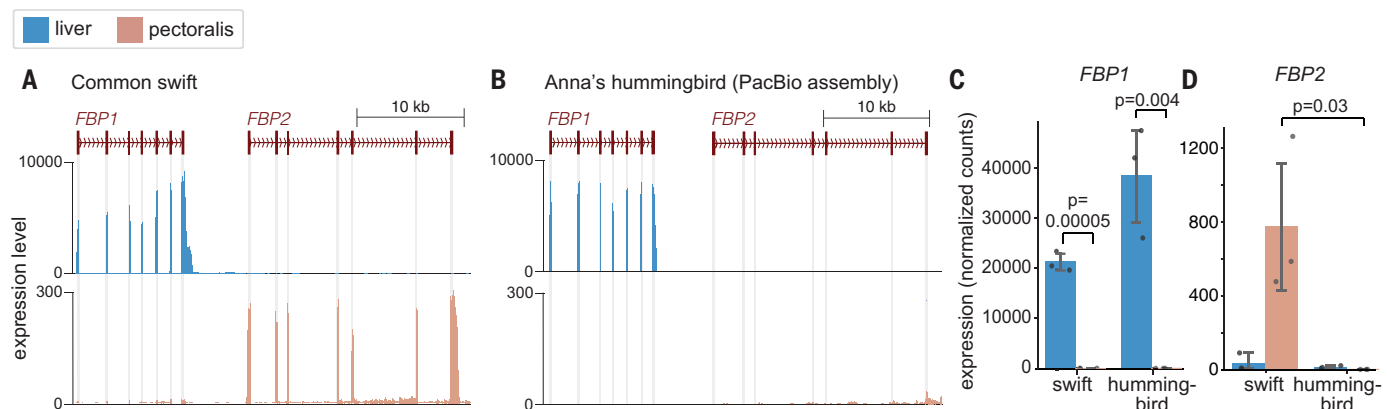

Fig. 2. Hummingbird muscle does not express FBPase enzymes. (**A** and **B**) UCSC Genome Browser screenshot showing the neighboring *FBP1* and *FBP2* genes in the common swift (A) and Anna's hummingbird (B) together with the expression level in liver (blue) and pectoralis muscle (red). (**C** and **D**) Quantification of *FBP1* (C) and *FBP2* (D) expression. A two-sided *t* test was used. Error bars represent standard deviation; *n* = 3 birds.
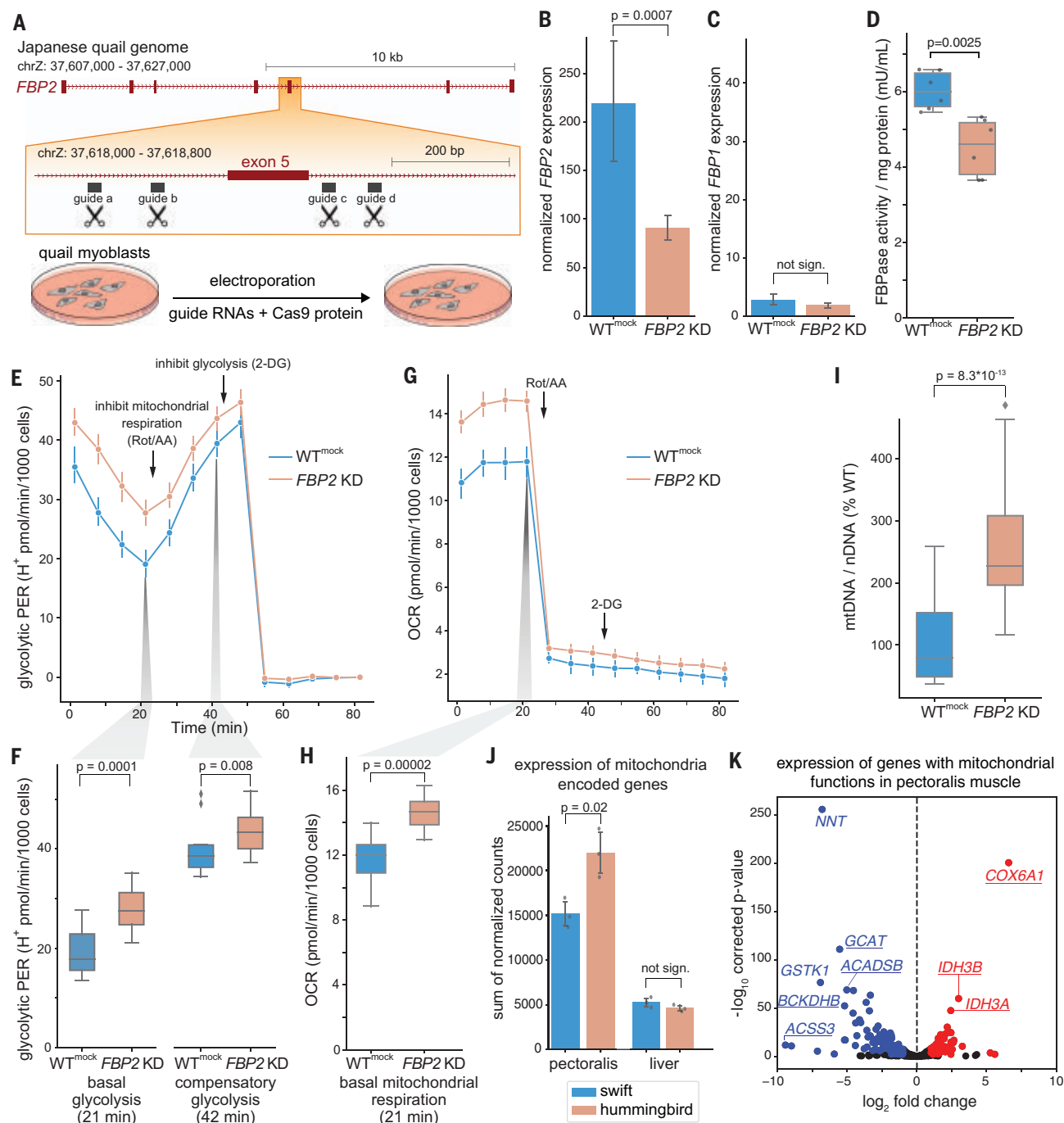
Fig. 3. *FBP2* knockdown up-regulates glycolysis and mitochondrial respiration.
(**A**) Positions of guide RNAs around exon 5 of the Japanese quail *FBP2*. *FBP2* knockdown in quail QM7 myoblast cells was achieved by electroporating the four guide RNAs with Cas9 protein. (**B** and **C**) Quantitative reverse transcription polymerase chain reaction (PCR) of *FBP2* and *FBP1* in mock-treated wild-type (WT^mock, electroporated with a negative control RNA) and *FBP2* knockdown (KD) cells; $n = 9$. (**D**) FBPase activity is reduced in *FBP2* KD compared to WT^mock cells. (**E**) Cell number–normalized glycolytic proton efflux rate (PER) values at different time points comparing *FBP2* KD with WT^mock cells. (**F**) Glycolytic PER values at two time points representing basal and compensatory glycolysis. Box plots show the first quartile, median, and third quartile with whiskers extending up to 1.5 times the interquartile distance; $n = 16$. (**G**) Cell number–normalized oxygen consumption rate (OCR) values comparing *FBP2* KD with WT^mock cells. The OCR drop after adding Rot/AA (rotenone and antimycin A) shows that mitochondrial

respiration is the main OCR contributor. (**H**) Box plots of OCR values before inhibiting mitochondrial respiration; $n = 16$. (**I**) Box plots of quantitative PCR measured ratios of mitochondrial to nuclear DNA indicate a higher number of mitochondria in *FBP2* KD cells; $n = 27$. (**J**) Sum of normalized expression values of mitochondria-encoded genes in pectoralis and liver of Anna's hummingbird and common swift; $n = 3$ birds. (**K**) Volcano plot shows the significance (y axis) versus the magnitude (x axis) of expression differences between hummingbird and swift muscle for 597 genes that function in mitochondria. Genes that are significantly up- or down-regulated (adjusted p value < 0.01 and >2-fold expression difference) are in red and blue, respectively. Genes mentioned in the text are underlined. A two-sided Mann-Whitney U-test was used in (C), (D), (F), (H), and (I); a two-sided t test was used in (D) and (J). Error bars in (C), (D), (E), and (G) represent the 95% confidence interval. Error bars in (J) represent the standard deviation.
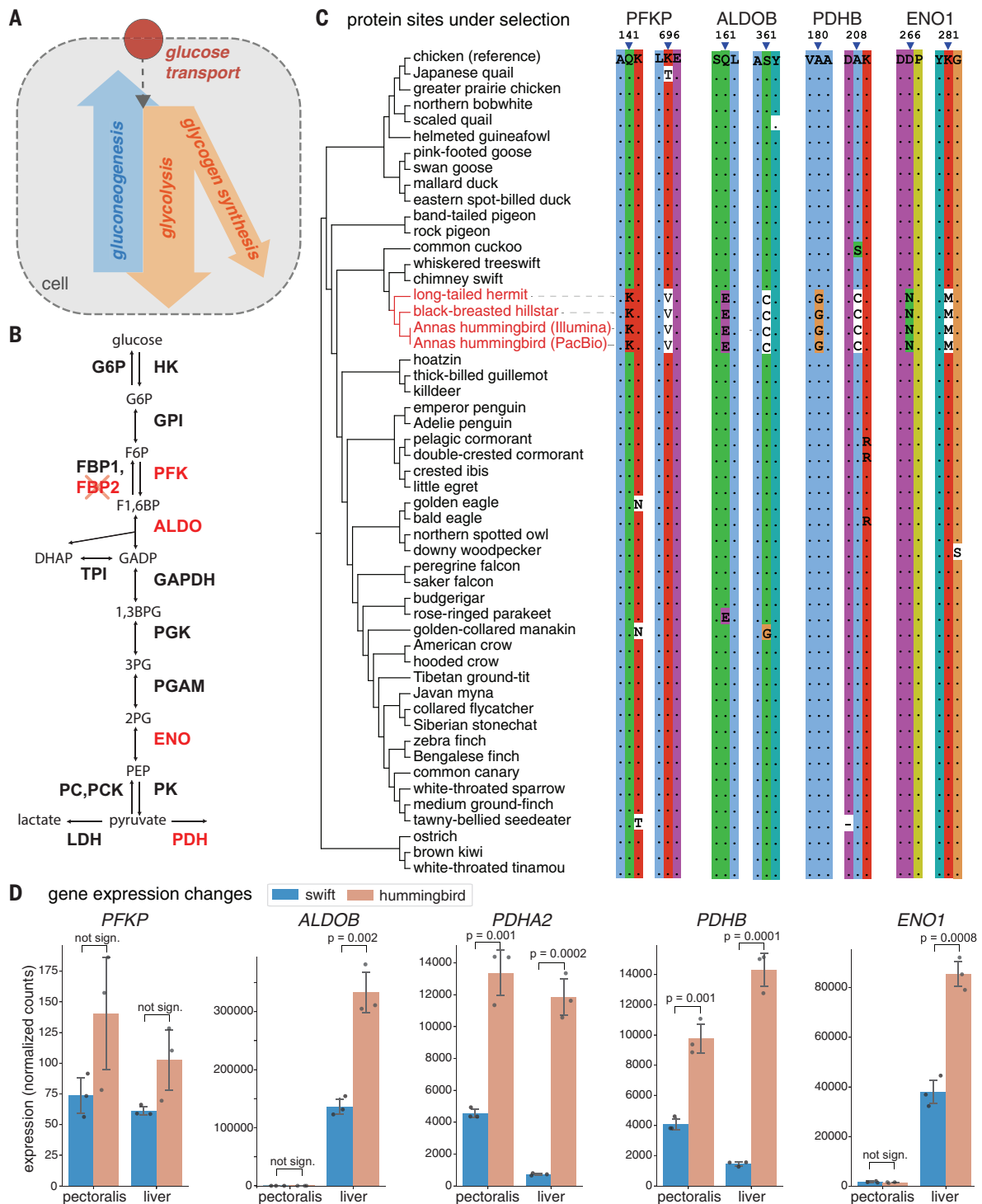
Fig. 4. Positive selection and expression up-regulation in glycolytic genes in hummingbirds. (**A**) Main glucose metabolism pathways. (**B**) Enzymes that catalyze reactions in the glycolysis and gluconeogenesis. Genes under significant positive selection [false discovery rate (FDR) < 0.05] in the ancestral hummingbird branch are in red. *ENO1* has an FDR just above the threshold (0.0505) and is also shown in red. (**C**) Protein alignments of PFKP, ALDOB, PDHB, and ENO1 show amino acid substitutions that likely evolved under positive selection in the ancestral hummingbird branch (Bayes empirical Bayes posterior probabilities >0.5). (**D**) Expression level of *PFKP*, *ALDOB*, *PDHA2*, *PDHB*, and *ENO1* in hummingbird tissues compared to swift. Error bars represent standard deviation; *n* = 3 birds.

(fig. S8). Together, this shows that *FBP2* knockdown increases both major energy-producing pathways in this avian myoblast cell line, potentially explaining the small but significant increase in lipid accumulation (fig. S9).

FBP2 knockdown increases mitochondria number
The observed increase in mitochondrial respiration could be due to increased mitochondrial biogenesis. Indeed, using the ratio of mitochondrial to nuclear DNA as a proxy for mitochondria number, we observed a ~50% higher ratio in *FBP2* knockdown compared with mock-treated wild-type cells (Fig. 3I and fig. S10). This indicates that *FBP2* down-regulation enhances mitochondrial biogenesis,

which is in line with observations that hummingbird flight muscles exhibit a high mitochondrial density (26).

Up-regulation of genes for mitochondrial biosynthesis and function

We next explored whether signatures of increased mitochondrial biogenesis and respiration are also evident in the transcriptomic data of hummingbirds that naturally lost *FBP2*. We first focused on mitochondria-encoded genes and found a ~30% increased expression in pectoralis muscle but not liver of Anna's hummingbird in comparison to the common swift (Fig. 3J and fig. S11). We next compared the expression of 597 nuclear-encoded genes that function in mitochondria. Genes significantly up- or down-regulated in hummingbird muscle showed distinct functional enrichments. Down-regulated genes are enriched for fatty acid and amino acid metabolism and include important enzymes such as *ACADSB*, *ACSS3*, *GCAT*, and *BCKDHB* (Fig. 3K and table S5). This is consistent with fatty acid and amino acid metabolism being less important for obligate nectarivores. By contrast, up-regulated genes are enriched for carbohydrate metabolism, the tricarboxylic acid (TCA) cycle, regulation of electron transport chain function, and the formation of inner mitochondrial membrane folds (cristae) (Fig. 3K and table S5). Up-regulated genes include *COX6A1*, which encodes a subunit of cytochrome c oxidase, and *IDH3A* and *IDH3B*, which encode two subunits of mitochondrial and nicotinamide adenine dinucleotide (NAD^+)–specific isocitrate dehydrogenase. IDH3 catalyzes a key reaction in the TCA cycle, and its up-regulation promotes a metabolic switch from glycolysis to OXPHOS (27). Overall, these expression differences are consistent with muscle-specific FBP2 negatively regulating mitochondria number and with previous observations that hummingbird flight muscles exhibit a high mitochondrial density and high levels of mitochondrial respiration (26).

Glycolytic genes evolved under positive selection

To investigate whether, in addition to the loss of *FBP2*, other genes involved in glucose metabolism exhibit changes in the ancestral hummingbird lineage, we screened for signatures of positive selection in 46 genes with roles in glycolysis and gluconeogenesis, glycogen synthesis, and monosaccharide uptake (Fig. 4, A and B, and table S6). We detected positive selection on the ancestral hummingbird branch for the less-characterized inositol (a sugar alcohol) transporter *SLC2A13* and five glycolytic genes (*PFKP*, *ALDOB*, *PDHA2*, *PDHB*, *ENO1*). *PFKP* encodes a phosphofructokinase enzyme that is expressed in many tissues, including muscle (22), and catalyzes the committed step in glycolysis. *ALDOB* encodes the liver-expressed aldolase, a key enzyme in both glycolysis and fructolysis, whose overexpression in cancer cells increases fructose metabolism (28). *PDHA2* and *PDHB* encode subunits of the pyruvate dehydrogenase enzyme complex that converts pyruvate to acetyl–coenzyme A, and thus connects glycolysis with the TCA cycle. *ENO1* encodes a ubiquitously expressed glycolytic enzyme whose up-regulation enhances glycolysis in tumors (29). Consistent with positive selection, we observed amino acid substitutions shared between all three hummingbird species, and some of them are potentially involved in regulating protein function or stability (Fig. 4C and fig. S12). Notably, *ALDOB* and *PDHB* also evolved under positive selection in nectar-feeding bats (10). Finally, compared to swift, expression of *ALDOB* and *ENO1* is significantly up-regulated in hummingbird liver and expression of *PDHA2* and *PDHB* is significantly up-regulated in hummingbird muscle and liver (Fig. 4D), indicating additional regulatory changes.

Discussion

Here, we discovered that the gluconeogenic muscle enzyme *FBP2* was inactivated in ancestral hummingbirds, coinciding with the time period during which energy-demanding hovering flight evolved. Experiments in an avian myoblast cell line showed that *FBP2* knockdown up-regulated glycolysis, mitochondrial biogenesis, and mitochondrial respiration, which concurs with characteristics of hummingbird flight muscles. The evolutionary loss of *FBP2* in hummingbirds provides interesting parallels to human cancer cells, in which down-regulation of *FBP2* (and *FBP1*) is frequently observed, because FBPases have tumor-suppressing functions (23, 25, 30). Consistent with our knockdown experiments in quail myoblast cells, down-regulation of *FBP1* or *FBP2* in cancer cells enhances glycolysis and contributes to the Warburg effect, which describes the preference of cancer cells for aerobic glycolysis to generate three-carbon precursors for rapid growth (25, 30). Furthermore, restoring *FBP2* expression in cancer cells inhibits mitochondrial biogenesis and respiration (25).

Whereas signatures of selection in more broadly expressed glycolytic enzymes, detected here and previously (10), highlight additional genomic changes with relevance for systemic metabolic adaptations in hummingbirds, metabolic shifts caused by losing the muscle-expressed *FBP2* gene were likely restricted to muscle tissue. Because down-regulation or inactivation of *FBP2* provides a mechanism to increase metabolic capacity in muscle by up-regulating sugar metabolism, the loss of the *FBP2* gene was likely beneficial for hummingbirds and could have been a key step in the coevolution of nectarivory and energy-demanding hovering flight.

REFERENCES AND NOTES

1. T. Weis-Fogh, *J. Exp. Biol.* **56**, 79–104 (1972).
2. R. K. Suarez, *Experientia* **48**, 565–570 (1992).
3. K. C. Welch Jr., B. H. Bakken, C. Martinez del Rio, R. K. Suarez, *Physiol. Biochem. Zool.* **79**, 1082–1087 (2006).
4. R. K. Suarez, K. C. Welch, *Nutrients* **9**, 743 (2017).
5. T. J. McWhorter, B. H. Bakken, W. H. Karasov, C. M. del Rio, *Biol. Lett.* **2**, 131–134 (2006).
6. J. E. Schondube, C. Martinez del Rio, *J. Comp. Physiol. B* **174**, 263–273 (2004).
7. C. C. W. W. Chen, K. C. Welch Jr., *Funct. Ecol.* **28**, 589–600 (2013).
8. A. M. Myrka, K. C. Welch Jr., *Comp. Biochem. Physiol. B Biochem. Mol. Biol.* **224**, 253–261 (2018).
9. M. W. Baldwin *et al.*, *Science* **345**, 929–933 (2014).
10. J. H. T. Potter *et al.*, *Curr. Biol.* **31**, 4667–4674.e6 (2021).
11. R. O. Prum *et al.*, *Nature* **526**, 569–573 (2015).
12. J. A. McGuire *et al.*, *Curr. Biol.* **24**, 910–916 (2014).
13. E. D. Jarvis *et al.*, *Science* **346**, 1320–1331 (2014).
14. A. Rhie *et al.*, *Nature* **592**, 737–746 (2021).
15. S. Feng *et al.*, *Nature* **587**, 252–257 (2020).
16. V. Sharma *et al.*, *Nat. Commun.* **9**, 1215 (2018).
17. R. Albalat, C. Cañestro, *Nat. Rev. Genet.* **17**, 379–391 (2016).
18. M. Blumer *et al.*, *Sci. Adv.* **8**, eabm6494 (2022).
19. F. Marcus, B. Gontero, P. B. Harrsch, J. Rittenhouse, *Biochem. Biophys. Res. Commun.* **135**, 374–381 (1986).
20. G. Mayr, *Ibis* **145**, 382–391 (2003).
21. G. Mayr, *Science* **304**, 861–864 (2004).
22. M. Uhlén *et al.*, *Science* **347**, 1260419 (2015).
23. L. B. Tanner *et al.*, *Cell Syst.* **7**, 49–62.e8 (2018).
24. A. Gizak, E. Maciaszczyk-Dziubinska, M. Jurowicz, D. Rakus, *Proteins* **77**, 262–267 (2009).
25. P. Huangyang *et al.*, *Cell Metab.* **31**, 174–188.e7 (2020).
26. R. K. Suarez, J. R. Lighton, G. S. Brown, O. Mathieu-Costello, *Proc. Natl. Acad. Sci. U.S.A.* **88**, 4870–4873 (1991).
27. D. Zhang *et al.*, *Cell Rep.* **10**, 1335–1348 (2015).
28. P. Bu *et al.*, *Cell Metab.* **27**, 1249–1262.e4 (2018).
29. T. Yang *et al.*, *Cell Death Dis.* **11**, 870 (2020).
30. C. Dong *et al.*, *Cancer Cell* **23**, 316–331 (2013).

SUPPLEMENTARY MATERIALS

Materials and Methods
Figs. S1 to S12
Notes S1 to S2
Tables S1 to S6
References (31–72)

CHEMICAL DYNAMICS

Stereodynamical control of the H + HD → H$_2$ + D reaction through HD reagent alignment

Yufeng Wang[1]†, Jiayu Huang[1]†, Wei Wang[1,2], Tianyu Du[1,2], Yurun Xie[1,3], Yuxin Ma[1,2], Chunlei Xiao[1,4]*, Zhaojun Zhang[1]*, Dong H. Zhang[1,3,4]*, Xueming Yang[1,3,4]*

Prealigning nonpolar reacting molecules leads to large stereodynamical effects because of their weak steering interaction en route to the reaction barrier. However, experimental limitations in preparing aligned molecules efficiently have hindered the investigation of steric effects in bimolecular reactions involving hydrogen. Here, we report a high-resolution crossed-beam study of the reaction H + HD(v = 1, j = 2) → H$_2$(v', j') + D at collision energies of 0.50, 1.20, and 2.07 electron volts in which the vibrationally excited hydrogen deuteride (HD) molecules were prepared in two collision configurations, with their bond preferentially aligned parallel and perpendicular to the relative velocity of collision partners. Notable stereodynamical effects in differential cross sections were observed. Quantum dynamics calculations revealed that strong constructive interference in the perpendicular configuration plays an important role in the stereodynamical effects observed.

T he fundamental goal for chemical reaction dynamics is to provide a detailed and quantitative understanding of the chemical reaction process and to provide new tools to control the outcome of a chemical event beyond the traditional ways, such as adding suitable catalysts and changing the temperature or pressure of a reaction mixture. One efficient way to control chemical reactions is to deposit some energy in the reaction coordinate of the reactant to make a desired molecular bond more easily cleaved (1–4). Numerous dynamical studies have been carried out to realize such an idea through vibrational excitation of reagent molecules, leading to the discovery and deep understanding of bond-selective or mode-specific chemistry (5–7). In addition to vibrational control, it is well established that the mutual orientation of the colliding partners also has a big effect on the chemical reaction outcome. Hence, by controlling colliding molecular orientation, it is possible to either promote or hinder the yield of products into specific final states or scattering angles (8–10).

For many years, steric control has been performed for inelastic and reactive systems mainly involving polar molecules (11–13). Many methods have been developed for aligning or orienting molecules in scattering experiments, including optical pumping (14), hexapole state selection (15), and brute force orientation (16). An elegant theoretical framework for the characterization of steric effects has been developed by Aldegunde et al. and Jambrina et al. (17, 18). Recently, Heid et al. investigated end-on and side-on collisions of Ar with oriented NO and demonstrated that the collision outcome could be controlled by varying the bond axis orientation (19). Wang et al. and Pan et al. carried out a series of experiments to probe the steric effect on the differential cross sections (DCSs) in the Cl + CHD$_3$ reaction (20–22). A strong steric effect was observed, which suggests that reorientation effects of CHD$_3$ en route to the reaction barrier are not strong in this system owing to the essentially nonpolar nature of CHD$_3$ (23).

Clearly, aligning nonpolar reacting molecules can have large steric effects because of their weak steering interaction en route to the reaction barrier. H$_2$ is undoubtedly the best candidate for the purpose because it is both the most widely studied molecule in dynamical experiments and the most tractable theoretically (24–27). However, until recently, it has been difficult to prepare sufficient concentrations of H$_2$ in specific quantum states for scattering experiments (28, 29). The development of the Stark-induced adiabatic Raman passage (SARP) technique not only opened the door to exciting a large concentration of H$_2$ and its isotopologues in specific quantum states to study collision dynamics for vibrationally excited H$_2$ molecules, but it also made it possible to align these molecules for steric dynamics experiments (30–32). Perreault et al. observed a strong stereodynamic preference of angular distributions in the inelastic scattering between aligned HD and D$_2$ molecules at temperatures down to 1 K (33), which indicates that the weak steering interaction can suppress the reorientation effects and expose more pronounced steric effects (34). They also created a quantum mechanical double-slit by preparing the rovibrationally excited D$_2$ molecule in a biaxial state with coherently coupled bond axis orientations and demonstrated that they act as the two slits of a double-slit interferometer manifesting interference as a strong modulation in the measured angular distribution when inelastic scattering with a He atom (35, 36). It would be highly desirable to see whether such striking steric effects can be observed in the simplest chemical reactions involving H$_2$ molecules and can be understood at the most fundamental level.

Experimental demonstration of stereodynamical control

We carried out a fully quantum state–resolved, crossed–molecular beam study for the H + HD → H$_2$ + D reaction, with HD molecules prepared in two preferentially aligned states using the stimulated Raman pumping (SRP) scheme. We found that the DCS of the reaction changed drastically with the direction of the HD bond axis, which indicated that we could effectively control the DCS of chemical reactions.

The experiment was conducted on a modified crossed-beam apparatus based on the Rydberg D atom time-of-flight (TOF) detection technique (37), as described in the supplementary materials. The HD beam was generated by supersonic expansion through a pulsed valve cooled by liquid nitrogen. The H beam was produced by ultraviolet laser photolysis of HI molecules in a pure HI beam at the nozzle tip of another pulsed valve. The HD beam and the H beam were collimated by skimmers and then entered the scattering chamber, where they collided at a crossing angle of 90º. The velocity of the HD beam was 1250 m/s. The speeds of H beam were 11,230, 17,470, and 22,949 m/s, corresponding to collision energies of 0.50, 1.20, and 2.07 eV, respectively. The HD molecules were excited from (v = 0, j = 0) to (v = 1, j = 2) (where v is the vibrational quantum number and j is the rotational quantum number) by SRP through the S(0) transition at the center of the scattering region of the two molecular beams. A single–longitudinal mode, optical parametric oscillator-amplifier produced the high-energy Stokes laser, which was the key for the high SRP excitation efficiency (38). After the reaction, the D atoms produced from the reaction were excited to a high-lying Rydberg state at the crossing region, then flew ~318 mm before reaching the MCP detector, where they were field-ionized by an electric field applied between the MCP and a metal mesh. The

ion signals were then amplified, discriminated, and recorded in the form of a TOF spectrum.

Figure 1 shows the schematic of the preparation of vibrationally excited HD in two different collision geometries, similar to the scheme used in (33). Linearly polarized pump and Stokes lasers with parallel directions of polarization were used, so the HD molecules were excited to the $(v = 1, j = 2, m = 0)$ state with quantization axis along the laser polarization direction. Because the HD bond axis in the $(v = 1, j = 2, m = 0)$ state was preferentially aligned parallel to the laser polarization direction, we were able to control the direction of the HD bond axis in scattering by changing the direction of the laser polarization. By setting the polarization direction of the pump and Stokes lasers parallel or perpendicular to the relative velocity of colliding partners, the bond axis of HD was preferentially aligned in parallel or perpendicular to the relative velocity. We named these two collision configurations parallel and perpendicular, respectively.

Figure 2, A to C, presents TOF spectra of the H + HD$(v = 1, j = 2)$ → H$_2$ + D reaction in the sideways direction with HD$(v = 1, j = 2)$ prepared in parallel and perpendicular configurations at collision energies of 0.50, 1.20, and 2.07 eV, respectively, measured on the scattering plane. Many sharp peaks were observed in the TOF spectra. Based on the conservation of momentum and energy, they could be assigned to various rovibrational states of H$_2$ products. It was obvious that TOF spectra obtained with parallel and perpendicular configurations were quite different.

By measuring TOF spectra at different scattering angles on the scattering plane, DCSs of the reaction on the plane were obtained. It should be noted that in the perpendicular configuration, the alignment of the HD molecular bond on the x axis breaks the scattering symmetry about the z axis. As a result, the measured DCS on the scattering plane differs from the conventional DCS, whose integration over the scattering angle θ gives the integral cross section. Figure 3, A and C, shows DCSs of H + HD$(v = 1, j = 2)$ → H$_2$ + D obtained at the collision energy of 0.50 eV for parallel and perpendicular configurations, respectively. Even casual inspection reveals that the DCSs for these two configurations were different. For the parallel configuration, the H$_2$ products were predominantly backward scattered, with some small peaks for the products with low translational energy in the sideways direction. For the perpendicular configuration, the DCS showed pronounced sideways scattered peaks, in particular for the products with low translational energy. Evident differences between the two DCSs indicated the existence of strong stereodynamical effects in this reaction.

The difference in the DCSs for these two configurations at the collision energy of 1.20 eV was even more obvious. For the parallel configuration, the H$_2$ products remained predominantly backward scattered, whereas the sideway peaks became higher and some forward components showed up (Fig. 3E). In strong contrast, the angular distribution for the perpendicular configuration was dominated by sideways peaks (Fig. 3G) with backward-scattered amplitude suppressed substantially, underscoring strong stereodynamical effects in the reaction.

With a further increase of collision energy to 2.07 eV, the angular distributions for both the parallel and perpendicular configurations looked quite similar—dominated by sideways peaks with more or less the same scattering angles and the same translational energies (Fig. 3, I and K). However, the relative intensities for large-angle scattering and for forward scattering were much stronger for the parallel configuration.

Figure 3 also shows the change of relative reactivity for these two configurations. At low collision energies, the parallel configuration that leads to end-on collisions is predominant because of a narrow cone of acceptance and small impact parameters. As the collision energy increases, the side-on configurations become increasingly prevalent and sideways or forward scattering takes over with the broadening of the acceptance cone and the increasing of the impact parameters.

Quantum dynamical simulation of stereodynamical effect

To understand the strong stereodynamical effects in the reaction, we carried out nonadiabatic time-dependent wave packet calculations on the diabatic potential energy surface we constructed for this reaction (39). Details of the theoretical calculation can be found in
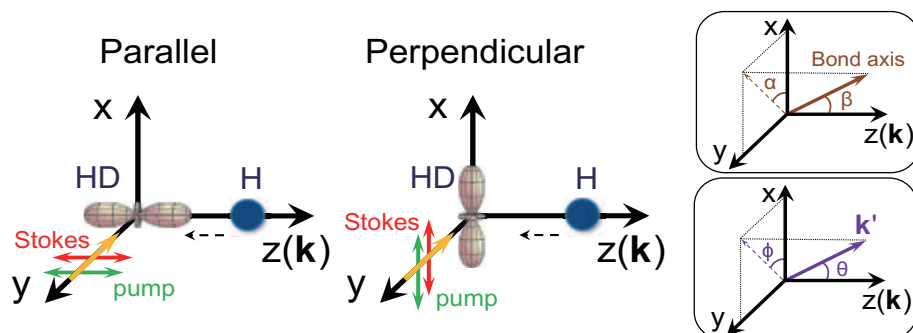

Fig. 2. TOF spectra of the D atom product from the H + HD($v = 1, j = 2$) → H$_2$(v, j) + D reaction. (**A** to **C**) They were obtained at three collision energies: 0.50 eV (A), 1.20 eV (B), and 2.07 eV (C) in parallel (blue solid line) and perpendicular (red solid line) configurations in the sideways direction, at laboratory angles of 25° (A), 28° (B), and 29° (C), respectively. The sharp peaks can be assigned to various rovibrational states of the H$_2$ product, as indicated in the figure.

Fig. 1. The schematic of two collision geometries prepared by SRP. The scattering frame is defined so that the z axis is parallel to the reactant relative velocity, and xz is the detection plane (or scattering plane). The alignment of the molecular bond axis was controlled using the polarized pump and Stokes laser pulses, as indicated by the green and red double arrows, respectively. The preferential direction of the HD molecular bond axis in the scattering frame is specified by the polar and azimuthal angle (β, α). In theory, the direction of k' is described by the polar and azimuthal angle (θ, ϕ). In the present experiment, $\phi = 0$.
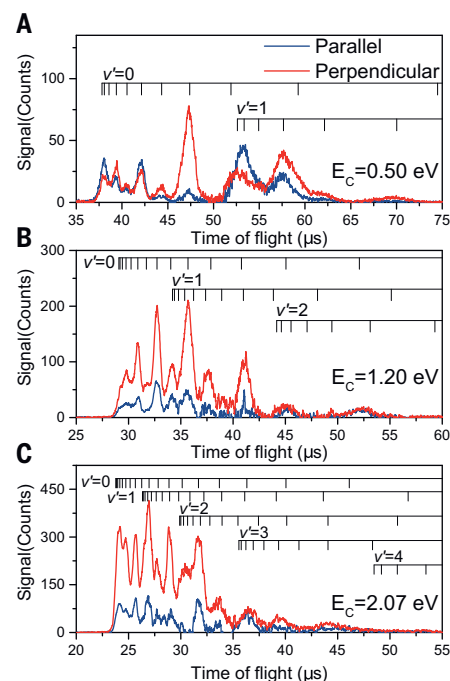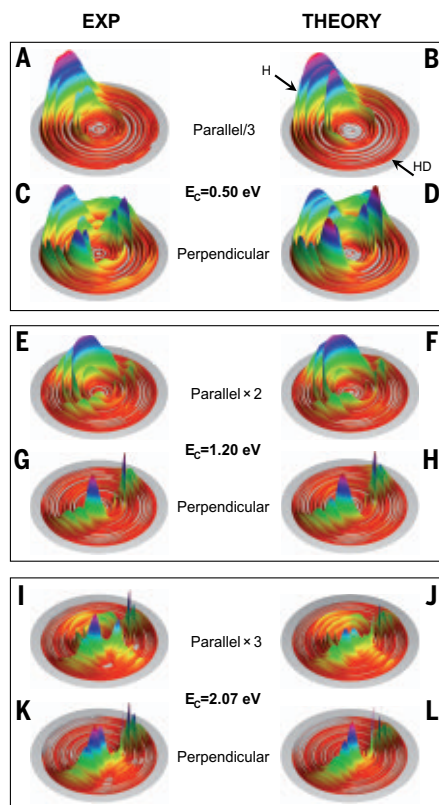
Fig. 3. Three-dimensional scattering H₂ product contour plots on the scattering plane. (A to **L)** Product contour plots are shown in the center-of-mass frame for experimental measurements (left column) and quantum dynamics calculations (right column) at collision energies of 0.50 eV [(A) to (D)], 1.20 eV [(E) to (H)], and 2.07 eV [(I) to (L)], with parallel [(A), (B), (E), (F), (I), and (J)] and perpendicular [(C), (D), (G), (H), (K), and (L)] configurations, respectively.

the supplementary materials. For the parallel configuration, the state of HD prepared by SRP is $|v = 1, j = 2, m = 0\rangle$, and for the perpendicular configuration, the state of HD prepared is

$$
\begin{aligned}
&|v = 1, j = 2, m_x = 0\rangle \\
&= \sqrt{\frac{3}{8}}|v = 1, j = 2, m = +2\rangle \\
&\quad - \frac{1}{2}|v = 1, j = 2, m = 0\rangle \\
&\quad + \sqrt{\frac{3}{8}}|v = 1, j = 2, m = -2\rangle \quad (1)
\end{aligned}
$$

where m denotes the projection of angular momentum along the quantization axis z at the direction of relative velocity, and m_x denotes the component along the x axis. The DCS for the parallel configuration for an outgoing channel with specific quantum state $(v'j'm')$ has a cylindrical symmetry with re-

spect to the z axis and can be evaluated easily as

$$
\begin{aligned}
&\frac{d\sigma(v = 1, j = 2, m_z = 0 \to v'j'm')}{d\Omega} \\
&= |f(v = 1, j = 2, m = 0 \to v'j'm')|^2 \equiv |f_0|^2 \\
&\qquad\qquad\qquad\qquad\qquad\qquad\qquad (2)
\end{aligned}
$$

where $f(v = 1, j = 2, m = 0 \to v'j'm')$ represents the state-to-state scattering amplitude within a solid angle $d\Omega$ along the direction (θ, ϕ) defined with respect to the quantization z axis, which is abbreviated as f_0 with the under script 0 denoting $m = 0$ and other index omitted. For the perpendicular configuration, the DCS results from the interference of the scattering amplitudes associated with the three input channels as follows

$$
\begin{aligned}
&\frac{d\sigma(v = 1, j = 2, m_x = 0 \to v'j'm')}{d\Omega} = \\
&\left| \sqrt{\frac{3}{8}} f(m = +2) - \frac{1}{2} f(m = 0) \right. \\
&\left. + \sqrt{\frac{3}{8}} f(m = -2) \right|^2 = \frac{3}{8}|f_{+2}|^2 + \frac{1}{4}|f_0|^2 \\
&\quad + \frac{3}{8}|f_{-2}|^2 + Re\left[\frac{3}{4} f_{+2} f_{-2}{}^* \right. \\
&\left. - \sqrt{\frac{3}{8}} f_{+2} f_0{}^* - \sqrt{\frac{3}{8}} f_{-2} f_0{}^* \right] \quad (3)
\end{aligned}
$$

In Fig. 3, the theoretical DCSs at each collision energy and for the internuclear axis preparations are also shown. The excellent agreement between experiment and theory demonstrates the high accuracy of the quantum calculations.

Influence of quantum interference on stereodynamical effect

Given that the quantum dynamical simulation was capable of accurately reproducing the observed DCSs, we were confident of using theory to determine the physical origin of the strong stereodynamical effects. At the collision energy of 0.50 eV, the DCS for the parallel configuration was determined by single input channel with $m = 0$ and manifested a predominated backward feature, as shown in Fig. 4A, as a result of head-on collision dynamics. By contrast, the DCSs for $m = \pm 2$, which are the main input channels for the perpendicular configuration, peak at $\theta = 100°$, indicative of peripheral dynamics with large impact-parameter collisions as can been seen from the opacity functions shown in fig. S12 and the dependence of DCS on the total angular momentum shown in figs. S13 to S15. The direct combination of the $m = 0$ and $m = \pm 2$ DCSs with ¼ and ¾ weights without the

interference term shown in Eq. 3 gave rise to an essentially straight line with a small bump at $\theta = 90°$. However, the actual DCS for perpendicular configuration showed an evident peak around $\theta = 90°$, with a height considerably higher than the direct combination result, apparently as a result of the constructive interference between the $m = 0$ and $m = \pm 2$ channels. Therefore, the pronounced sideways peaks for the perpendicular configuration shown in Fig. 3C came from the constructive interference between the $m = 0$ and $m = \pm 2$ channels. It is worthwhile to point out that the interference term at the forward and backward directions is zero, as explained in the supplementary materials.

Figure 4B shows the angular distribution at the collision energy of 1.2 eV. Although the DCS for the parallel configuration was still backward dominated, it extended all the way up to the forward direction with a substantial amplitude. The DCS for $m = \pm 2$ channels
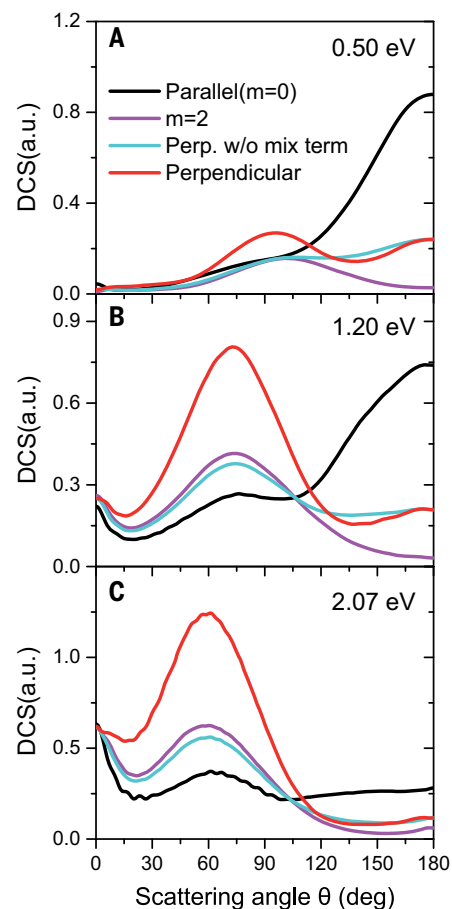

Fig. 4. Calculated DCSs on the scattering plane. (A to **C)** All final states of the H₂ product from the H + HD($v = 1, j = 2$) → H₂ + D reaction are included at collision energies of 0.50 eV (A), 1.20 eV (B), and 2.07 eV (C), respectively. The results of $m = -2$ are equal to that of $m = 2$, so only $m = 2$ is shown. a.u., arbitrary units.

resembled that at the collision energy of 0.5 eV as a broad peak, but the peak position moved forward to θ = 70°. The direct combination of the $m = 0$ and $m = \pm2$ DCSs without the interference terms resulted in a rather uniform distribution with a small but broad peak at θ = 70°. In strong contrast, the actual DCS had a pronounced peak also at θ = 70° with the amplitude doubled as compared with that without the interference terms because of the constructive interference between the $m = 0$ and $m = \pm2$ channels—obviously higher than the backward scattering.

With the further increase of the collision energy to 2.07 eV, the DCS for $m = \pm2$ channels resembled those at low collision energies as a broad peak but with the peak position moving forward further to θ = 60°. The DCS for the parallel configuration changed substantially and became rather uniform, with a broad peak at θ = 60° and another narrower peak in the forward direction, apparently as a result of a broader cone of acceptance and larger impact parameters. The direct combination of the $m = 0$ and $m = \pm2$ DCSs without the interference terms looked close to $m = \pm2$ with one peak in the forward direction and another at θ = 60° with the same heights. The interference between the $m = 0$ and $m = \pm2$ channels substantially increased the peak intensity at θ = 60° and doubled the peak height, but it had no effect on the forward peak intensity, making the relative intensity of the forward-scattering peak considerably suppressed.

To verify this strong interference behavior, we show in Fig. 5, A and B, the comparison between experimental and theoretical DCSs for the product $H_2(v' = 0, j' = 1)$ and $H_2(v' = 1, j = 3)$ states, respectively, at the collision energy of 0.50 eV. As seen, the theory agreed with experiment well on the DCSs for both product states. The DCS for the $H_2(v' = 0, j' = 1)$ state exhibited two clear peaks at θ = 125° and 180°, respectively, whereas the direct combination without the interference terms only showed a tiny bump at θ = 120°. The DCS for the $H_2(v' = 1, j = 3)$ state exhibited two peaks with a pronounced one at θ = 90°; by contrast, the direct combination without the interference terms only had one broad peak. The interference effects were obvious for the perpendicular configuration.

The concept of intrinsic polarization-dependent differential cross sections (PDDCSs) has been widely used to study the stereodynamical effects in chemical reactions (17). Because the quantum dynamical simulation reproduces the observed DCSs very well, as shown in Fig. 3 (as well as the total DCSs, as shown in figs. S6 to S8), we can use the theoretical PDDCSs to analyze the observed stereodynamical effects. As shown in figs. S9 to S11,
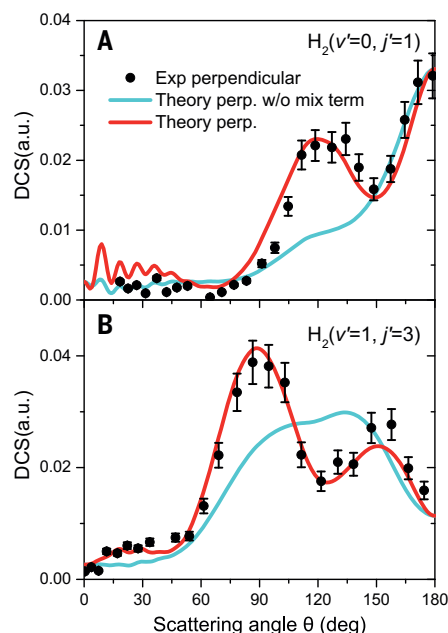

Fig. 5. Comparisons between experiment and theory on product state–resolved DCSs. (**A** and **B**) Comparisons are made on the scattering plane at the collision energy of 0.50 eV for the H_2 product in the ($v' = 0, j' = 1$) (A) and ($v' = 1, j' = 3$) (B) states. In this experiment, TOF spectra at different laboratory angles were acquired by scanning the laboratory angle back and forth 36 times. By analyzing the summed TOF signals for the above H_2 product states at each laboratory angle in these scans, the error bars of one standard deviation (1σ) in the experimental DCS shown in this figure were estimated to be ~10%. Analysis of experimental data and evaluation of error bars are also discussed in the supplementary materials.

the $S_0^{(2)}(\theta)$ and $S_0^{(4)}(\theta)$ moments are responsible for the effects in the parallel configuration as found in many theoretical studies (12, 17, 19), whereas the feature of stereodynamical effects in the sideways direction in the perpendicular configuration are mainly originated from the $S_{\pm2}^{(2)}(\theta)$ and $S_{\pm4}^{(4)}(\theta)$ moments.

Therefore, the $m = 0$ and $m = \pm2$ channels for the $HD(v = 1, j = 2)$ state had different angular distributions, with one backward dominated and the other peaked in a mostly sideways direction. For the perpendicular configuration, the angular distribution on the scattering plane is determined by Eq. 3, with the interference term between the $m = 0$ and $m = \pm2$ channels. Notably, strong constructive interference occurred in the sideways direction, substantially enhancing the peak height in the sideways direction particularly at the collision energies of 1.20 and 2.07 eV. As a result, the measured angular distributions for the perpendicular configuration were markedly different

from the parallel configuration, manifesting strong stereodynamical effects.

REFERENCES AND NOTES

1. R. N. Zare, *Science* **279**, 1875–1879 (1998).
2. F. F. Crim, *Acc. Chem. Res.* **32**, 877–884 (1999).
3. F. F. Crim, *Proc. Natl. Acad. Sci. U.S.A.* **105**, 12654–12661 (2008).
4. P. M. Hundt, B. Jiang, M. E. van Reijzen, H. Guo, R. D. Beck, *Science* **344**, 504–507 (2014).
5. B. R. Strazisar, C. Lin, H. F. Davis, *Science* **290**, 958–961 (2000).
6. H. Guo, B. Jiang, *Acc. Chem. Res.* **47**, 3679–3685 (2014).
7. G. Czakó, J. M. Bowman, *Science* **334**, 343–346 (2011).
8. K. Liu, *Annu. Rev. Phys. Chem.* **67**, 91–111 (2016).
9. B. L. Yoder, R. Bisson, R. D. Beck, *Science* **329**, 553–556 (2010).
10. R. B. Bernstein, D. R. Herschbach, R. D. Levine, *J. Phys. Chem.* **91**, 5365–5377 (1987).
11. D. H. Parker, R. B. Bernstein, *Annu. Rev. Phys. Chem.* **40**, 561–595 (1989).
12. F. J. Aoiz *et al.*, *Phys. Chem. Chem. Phys.* **17**, 30210–30228 (2015).
13. H. J. Loesch, *Annu. Rev. Phys. Chem.* **46**, 555–594 (1995).
14. Z. Karny, R. C. Estler, R. N. Zare, *J. Chem. Phys.* **69**, 5199–5201 (1978).
15. D. H. Parker, H. Jalink, S. Stolte, *J. Phys. Chem.* **91**, 5427–5437 (1987).
16. H. J. Loesch, A. Remscheid, *J. Chem. Phys.* **93**, 4779–4790 (1990).
17. J. Aldegunde *et al.*, *J. Phys. Chem. A* **109**, 6200–6217 (2005).
18. P. G. Jambrina, M. Morita, J. F. E. Croft, F. J. Aoiz, N. Balakrishnan, *J. Phys. Chem. Lett.* **13**, 4064–4072 (2022).
19. C. G. Heid, V. Walpole, M. Brouard, P. G. Jambrina, F. J. Aoiz, *Nat. Chem.* **11**, 662–668 (2019).
20. F. Wang, J. S. Lin, K. Liu, *Science* **331**, 900–903 (2011).
21. F. Wang, K. Liu, T. P. Rakitzis, *Nat. Chem.* **4**, 636–641 (2012).
22. H. Pan, F. Wang, G. Czakó, K. Liu, *Nat. Chem.* **9**, 1175–1180 (2017).
23. K. Liu, *J. Chem. Phys.* **142**, 080901 (2015).
24. G. C. Schatz, A. Kuppermann, *J. Chem. Phys.* **59**, 964–965 (1973).
25. J. Z. H. Zhang, S.-I. Chu, W. H. Miller, *J. Chem. Phys.* **88**, 6233–6239 (1988).
26. J. Jankunas *et al.*, *Proc. Natl. Acad. Sci. U.S.A.* **111**, 15–20 (2014).
27. Y. Xie *et al.*, *Science* **368**, 767–771 (2020).
28. T. Wang *et al.*, *Science* **342**, 1499–1502 (2013).
29. T. Yang *et al.*, *Science* **347**, 60–63 (2015).
30. T. Wang, T. Yang, C. Xiao, D. Dai, X. Yang, *J. Phys. Chem. Lett.* **4**, 368–371 (2013).
31. N. Mukherjee, R. N. Zare, *J. Chem. Phys.* **135**, 024201 (2011).
32. N. Mukherjee, W. Dong, R. N. Zare, *J. Chem. Phys.* **140**, 074201 (2014).
33. W. E. Perreault, N. Mukherjee, R. N. Zare, *Science* **358**, 356–359 (2017).
34. W. E. Perreault, N. Mukherjee, R. N. Zare, *Nat. Chem.* **10**, 561–567 (2018).
35. H. Zhou, W. E. Perreault, N. Mukherjee, R. N. Zare, *Science* **374**, 960–964 (2021).
36. X. Wang, X. Yang, *Science* **374**, 938–939 (2021).
37. M. Qiu *et al.*, *Rev. Sci. Instrum.* **76**, 083107 (2005).
38. Y. Wang *et al.*, *Rev. Sci. Instrum.* **91**, 053001 (2020).
39. D. Yuan *et al.*, *Science* **362**, 1289–1293 (2018).
40. Y. Wang *et al.*, Stereodynamical Control of the H+HD→H₂+D Reaction through HD Reagent Alignment, dataset, Dryad (2022); https://doi.org/10.5061/dryad.x0k6djhpk.

ENZYME DESIGN

Combinatorial assembly and design of enzymes

R. Lipsh-Sokolik[1], O. Khersonsky[1], S. P. Schröder[2], C. de Boer[2]†, S.-Y. Hoch[1], G. J. Davies[3], H. S. Overkleeft[2], S. J. Fleishman[1]*

The design of structurally diverse enzymes is constrained by long-range interactions that are necessary for accurate folding. We introduce an atomistic and machine learning strategy for the combinatorial assembly and design of enzymes (CADENZ) to design fragments that combine with one another to generate diverse, low-energy structures with stable catalytic constellations. We applied CADENZ to endoxylanases and used activity-based protein profiling to recover thousands of structurally diverse enzymes. Functional designs exhibit high active-site preorganization and more stable and compact packing outside the active site. Implementing these lessons into CADENZ led to a 10-fold improved hit rate and more than 10,000 recovered enzymes. This design-test-learn loop can be applied, in principle, to any modular protein family, yielding huge diversity and general lessons on protein design principles.

I nnovation in many areas of engineering relies on the combination of preexisting modular parts (1). For example, in electrical engineering, standard modular parts, such as transistors or processing units, are combined to assemble devices (2). Similarly, in a hypothetical and entirely modular protein, fragments could be combined to generate stable, well-folded, and potentially functional domains (3). However, in practice, protein domains exhibit a high density of conserved molecular interactions that are necessary for accurate native-state folding. Furthermore, mutations may be epistatic such that they can only be incorporated against the background of other mutations, severely limiting options for fragment combination (4, 5). Recombination is an important source of protein diversity in natural and laboratory evolution (6–8) and the design of de novo backbones (9); however, because of epistasis, evolution is typically restricted to recombining fragments from only a few high-homology proteins (6).

Despite these challenges, immune system antibodies present a notable example in which modularity enables extremely rapid and effective innovation through the combination of a small set of genetic fragments [V, (D), and J genes] (10). The result of this process is an enormous diversity of binding proteins that can, in principle, counter any pathogen. Nature has no equivalent strategy to generate structural and functional diversity in enzymes, but some protein folds, such as TIM barrels, β propellers, and repeat proteins, have evolved through the duplication, recombination, and mutation of modular fragments and are therefore prominent candidates for fragment combination. Moreover, these folds constitute some of the most structurally and functionally versatile enzymes and binding proteins in nature (11).

In this study, we ask whether enzymes could be generated from combinable fragments. We develop a method called CADENZ (combinatorial assembly and design of enzymes) to design and select protein fragments that, when freely combined, give rise to vast repertoires of low-energy proteins that exhibit high sequence and structural diversity. Isolating active enzymes in such vast protein libraries requires high-throughput screening methods (12, 13) but can be readily and accurately achieved by using activity-based protein profiling (ABPP). ABPP uses mechanism-based covalent and irreversible inhibitors composed of a chemical scaffold that emulates structural features of the target substrate with an enzyme active site electrophile and a fluorophore or affinity tag. To exploit ABPP, we focused on glycoside hydrolase family 10 (GH10) xylanases (Enzyme Classification: 3.2.1.8) (14–16) as a model sys-

tem and a dedicated GH10 xylanase–specific activity-based probe (ABP) as the principal enzyme activity readout. We found that CADENZ generated thousands of functional enzymes with more than 700 diverse backbones. We then trained a machine learning model to rank designs on the basis of their structure and energy features. Applying the learned model, we designed a second-generation library that demonstrated an order of magnitude increase in the success rate of obtaining functional enzymes.

Design of modular and combinable protein fragments

For a protein fold to be a candidate for modular assembly and design, its secondary-structure elements should be conserved among homologs, but loop regions should exhibit diverse conformations, including insertions and deletions (17–19). In such cases, the secondary-structure elements typically provide robustness, whereas the loop regions encode functional differences. The TIM-barrel fold is a prime example of such modularity in which eight β/α segments comprise an inner β barrel surrounded by α helices (20, 21). The catalytic pocket is located at the top of the barrel with critical contributions from all β/α loops. Evolutionary analysis indicates that TIM-barrel proteins arose through dual duplication of an ancestral β/α–β/α segment, suggesting that modern TIM-barrel enzymes can be segmented into four parts (Fig. 1A) (22–24). Nevertheless, during evolution, each protein accumulated mutations to adapt their intersegment interactions for specific functional and stability requirements. Therefore, recombining fragments from existing proteins mostly produces unstable and dysfunctional proteins that require further mutational optimization to become stable and active (25). To address this problem, the CADENZ design objective is to compute a spanning set of backbone fragments that produce folded and active proteins when freely combined and without requiring further optimization. The primary challenge CADENZ addresses is designing mutually compatible (modular) fragments among which epistasis is minimal.

The first step of CADENZ is the alignment of homologous but structurally diverse enzymes (in the case of this study, 81 structures of GH10 xylanases) and fragmenting them along points that are structurally highly conserved (within

[1]Department of Biomolecular Sciences, Weizmann Institute of Science, 7610001 Rehovot, Israel. [2]Leiden Institute of Chemistry, Leiden University, Einsteinweg 55, 2300 RA Leiden, Netherlands. [3]York Structural Biology Laboratory, Department of Chemistry, The University of York, Heslington, York YO10 5DD, UK.
*Corresponding author. Email: sarel@weizmann.ac.il
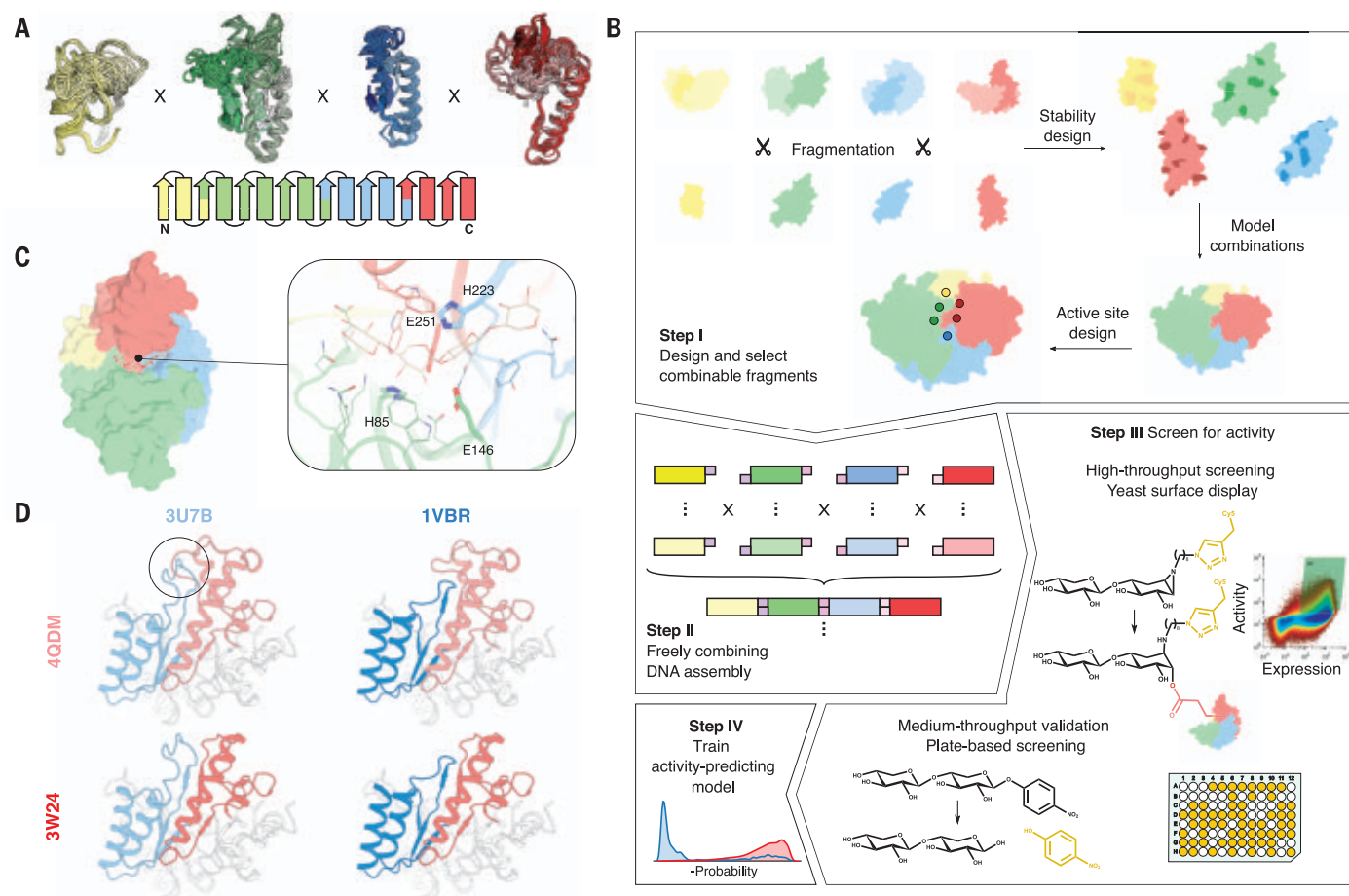†Present address: DSM Nutritional Products Ltd, Wurmisweg 576, 4303 Kaiseraugst, Switzerland.

Fig. 1. Key steps in the CADENZ workflow. (**A**) (Top) Cartoon representation of selected fragments. (Bottom) Segmentation scheme for GH10 xylanases (color scheme is consistent in all structural figures). (**B**) The design pipeline. Step I: Design maximizes internal stability and compatibility with other fragments and diversifies active site positions that are not directly involved in the catalytic step. Step II: DNA oligos encoding fragments are freely ligated with Golden Gate Assembly (*32*) to generate DNA molecules encoding the full-length designs. Step III: Designs are sorted with a xylobiose-emulating activity-based probe (*34*) that labels the nucleophilic Glu (red lines) of yeast-displayed functional enzymes. Activity is confirmed on a subset of the selected enzymes in a plate-based chromogenic assay. Step IV: An activity predictor is trained on the basis of features that distinguish presumed active and inactive designs. (**C**) Four catalytic residues are restrained throughout design calculations (in sticks, numbering correspond to PDB entry: 3W24). (**D**) Fragments can assemble into low- or high-energy structures depending on other fragments. (Top left) Segments 3 (blue) and 4 (red) are incompatible (overlap marked by black circle), resulting in extremely high energy (+1,529 REU). The other designs exhibit low energies (≤ 950 REU).

the core β segments) (see Fig. 1B for a visual guide to the algorithm) (*18*, *26*). Next, the fragments are designed to increase stability while holding the active site fixed. All design calculations take place within a single arbitrarily chosen template [Protein Data Bank (PDB) entry 3W24 (*27*)] to provide a realistic structural context and to promote compatibility between fragments. In practice, each fragment replaces the corresponding one in the template structure, and we used the PROSS stability-design algorithm (*28*) to implement stabilizing mutations within the fragment (8 to 42 mutations in each fragment; up to 28%) (fig. S1A). In GH10 xylanases, the active site interacts with the xylan substrate through more than a dozen residues from all β/α loops (*29*, *30*), posing a challenge for modular design

(Fig. 1C). To maintain catalytic activity, in all design calculations the side chains of four key catalytic amino acids are restrained to their crystallographically observed conformations. At the end of this process, we obtained a set of fragments that are internally stabilized within a common template and designed to support the catalytically competent constellation of active site residues.

However, because of epistasis, combining the designed fragments would likely result in mostly high-energy structures that are unlikely to fold into their intended conformation or support the catalytic constellation (Fig. 1D). To address this problem, we enumerated all possible combinations of designed fragments and ranked them by Rosetta all-atom energy (Fig. 1B, step I). This process yields hundreds

of thousands of distinct structures, most of which exhibit unfavorable energies, as expected. To find mutually compatible (modular) fragments, we present a machine learning–based approach called EpiNNet (Epistasis Neural Network), which ranks fragments according to their probability of forming low-energy full-length structures (Fig. 2A). EpiNNet is trained to predict whether a combination of fragments exhibits favorable Rosetta energy on the basis of its constituent fragments. The trained network weights are then used to nominate fragments to generate the enzyme library. For the next design steps, we used the top six to seven fragments from each segment, which assembled into 1764 structures.

To add active site diversity and increase the chances of favorable fragment combination,
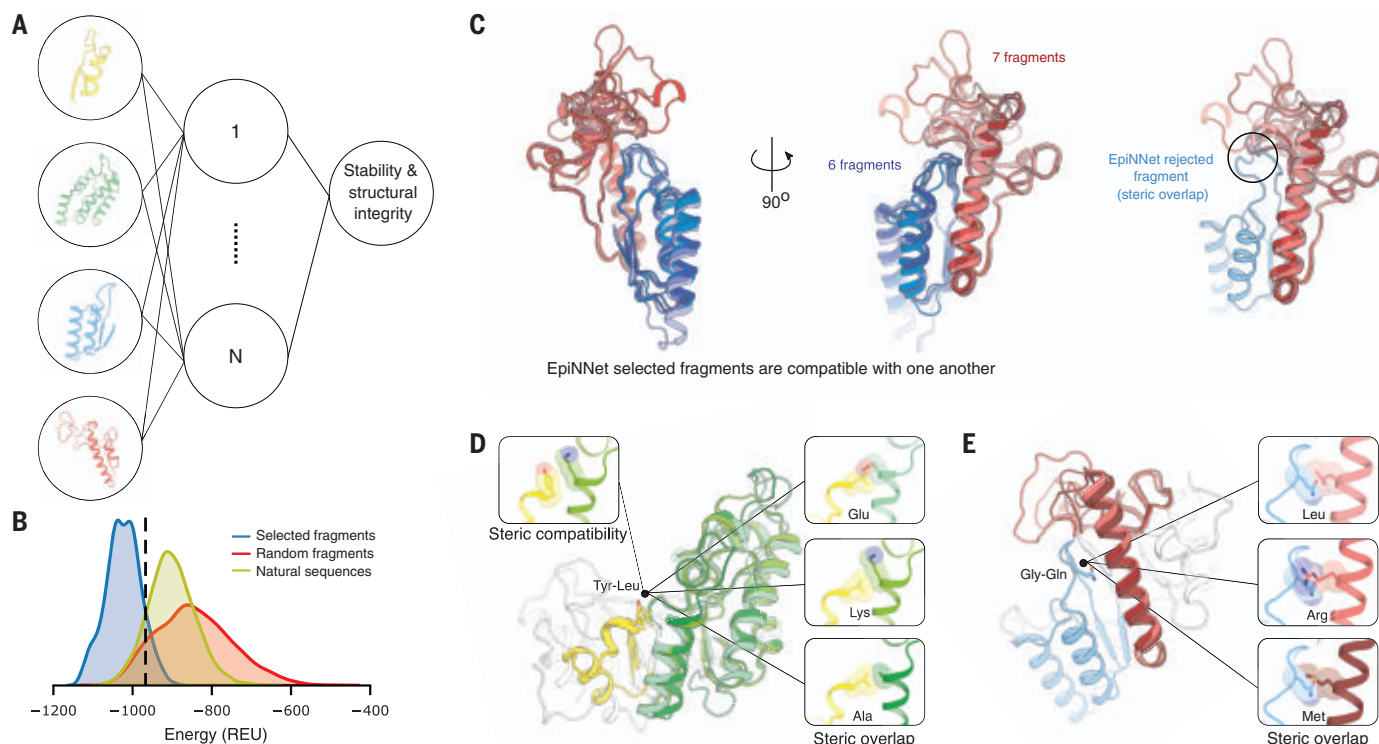
Fig. 2. EpiNNet selects fragments that assemble to low-energy structures.
(**A**) Schematic representation of the EpiNNet architecture. (**B**) Most
(89%) of the EpiNNet-selected designs exhibit low energy (< -967 REU,
dashed line) (see materials and methods) relative to proteins generated
by assembling randomly selected or natural fragments. (**C**) EpiNNet removes
incompatible fragments. (Left) All fragments selected for segment 3
(blue) and 4 (red). (Right) Discarded fragment with a β/α loop that is
incompatible with the other fragments. (**D** and **E**) Examples of mutations
selected by EpiNNet (taken from the second-generation library).
(D) Segment 1 from PDB entry 3W24 (27) (yellow) faces segment 2 (green).
EpiNNet prioritizes tyrosine (Tyr) over leucine (Leu) which cannot be
accommodated with neighboring fragments. (E) Segment 3 from PDB entry
1VBR (55) (blue) faces segment 4 (red). EpiNNet prioritizes the small Gly
over the large Gln.

we designed several sequence variants for each of the backbone fragments. We used the FuncLib design method (31) to generate low-energy amino acid constellations at positions in the active site and in the interfaces between β/α fragments while fixing the conformations of the key catalytic residues as observed in experimentally determined structures (Fig. 1C). We then used EpiNNet again, this time to find the single-point mutations that are most likely to form low-energy full-length proteins in combination with other mutations (fig. S2A).

The CADENZ strategy does not necessarily select the lowest-energy fragment combinations, but rather mitigates the risk of combining incompatible ones. The consequences of intersegment epistasis are notable: Whereas the energies in the fully enumerated set of designed GH10s can be as high as +2500 Rosetta energy units (REU), after EpiNNet fragment selection, the energies are < −890 REU (Fig. 2B). As a reference, we also generated the distribution of energies obtained by combining the sequence of the fragments selected by EpiNNet before any of the design steps. This reference simulates the recombination
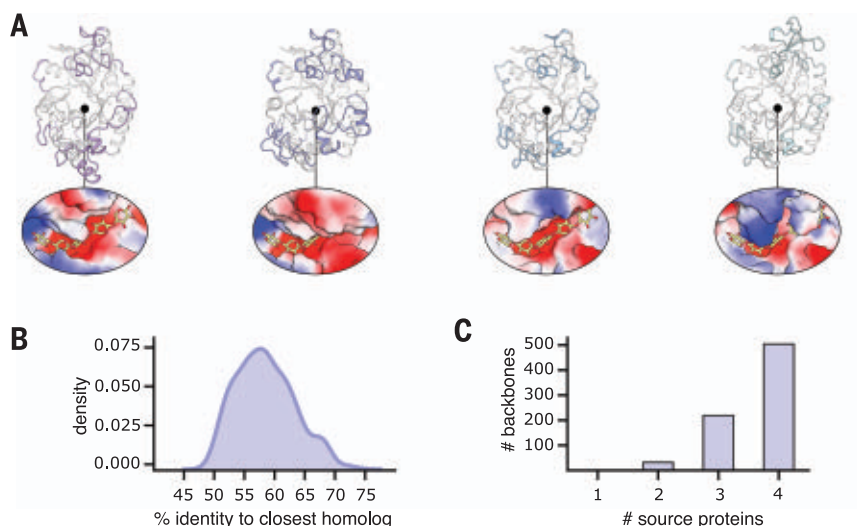

Fig. 3. CADENZ generates functional enzymes with high structure and sequence diversity.
(**A**) Representative model structures of recovered enzymes designed by CADENZ. Regions that vary among the four designs are highlighted in colors (top). Active-site electrostatic potential surfaces of the representative designs exhibit marked differences (putative ligand-bound conformation marked in yellow sticks on the basis of PDB entry 4PUD) (bottom). (**B**) Distribution of sequence identity to nearest natural homologs of recovered designs. (**C**) The number of distinct structures from which fragments are sourced. Most recovered designs incorporate fragments from four different sources.

of natural GH10 genes and exhibits a less favorable energy distribution than the combination of PROSS-stabilized fragments (> 100 REU difference, on average), underscoring the impact of the design process (Fig. 2B and fig. S1B). Furthermore, EpiNNet alleviates intersegment epistasis by discarding backbone fragments and designed single-point mutations that are incompatible with neighboring segments (Fig. 2, C to E). This analysis highlights the challenge that epistasis poses for effective fragment combination while underscoring the strengths of the EpiNNet selection strategy. Although EpiNNet eliminates more than 60% of the fragments, the designed library exhibits high diversity and includes a total of 952,000 sequences adopting 1764 different backbones.

CADENZ generates thousands of structurally diverse and active enzymes

We used Golden Gate Assembly to combine designed fragments into full-length genes (Fig. 1B, step II) (32) and transformed the library into yeast cells for functional screening with cell-surface display (Fig. 1B, step III) (see materials and methods) (33). To probe enzyme activity, we incubated the library with a xylobiose ABP (34), which reacts within the enzyme active site to form a covalent and irreversible ester linkage with the glutamic acid nucleophile (35). We then used fluorescence-activated cell sorting (FACS) to collect the population of yeast cells expressing active designs (fig. S3A). ABP labeling depends on the nucleophilicity of the catalytic glutamic acid (Glu), the ability of the active site catalytic acid-base residue to enhance the electrophilicity of the ABP epoxide by protonation, and the integrity of the xylan molecular recognition elements within the active-site pocket. Therefore, ABP labeling acts as a sensitive probe for design accuracy in the active site (which comprises elements from all β/α units). Retaining glycosidase ABPs report on the first steps of substrate processing, namely ligand binding to the active site and subsequent nucleophilic attack. To confirm that selected proteins exhibit the complete catalytic cycle (36), we transformed *Escherichia coli* cells with DNA from the sorted population and randomly selected 186 colonies for screening in 96-well plates with the chromogenic substrate 4-nitrophenyl β-xylobioside (O-PNPX₂) (37). Of the selected enzymes, 58% processed the substrate (fig. S3B), indicating that most designs selected by the ABP exhibited catalytic activity for this reaction.

We next applied single-molecule real-time (SMRT) long-read sequencing (38) to the sorted population. Encouragingly, sequencing showed that the sorted population included a large number of structurally diverse designs: specifically, 3114 distinct designs based on 756 dif-
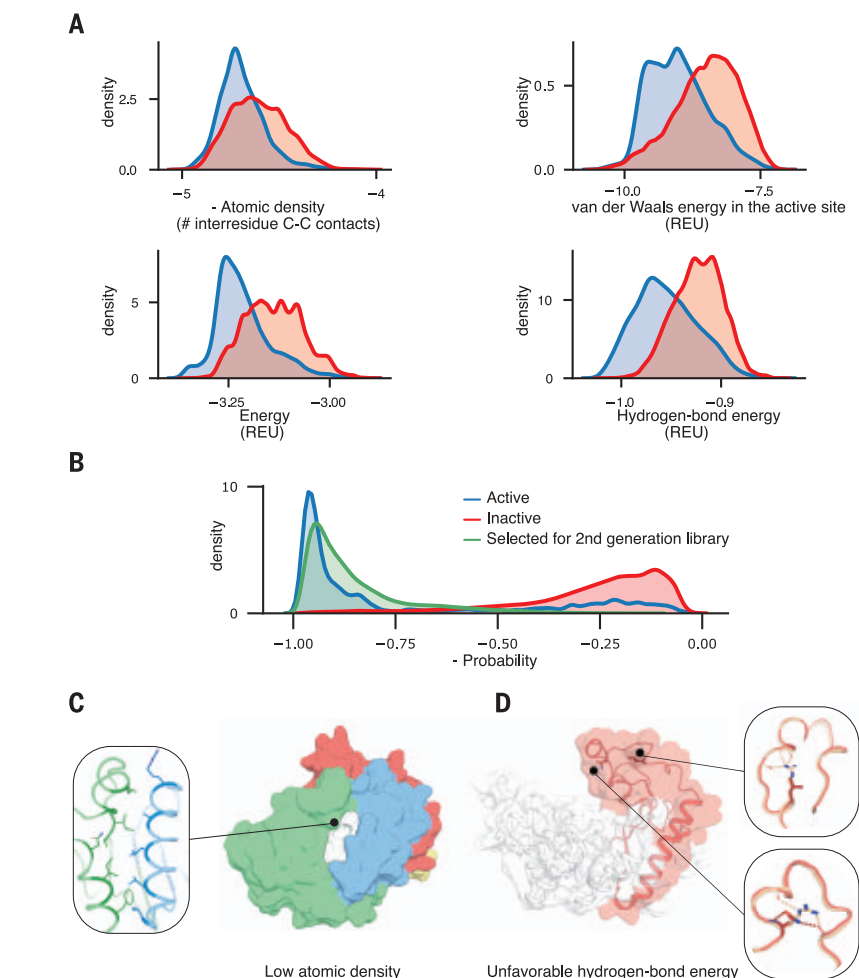

Fig. 4. Energy and structure features discriminate between active and inactive designs.
(**A**) Representative features included in the activity predictor. The features show a statistically significant difference between presumed active and inactive designs with an independent two-sample *t* test, but no feature is individually an effective discriminator. All features are normalized by protein length. Low values are favorable. (**B**) Separation of designs recovered by ABPP versus other designs on the basis of a logistic regression model. In green, probability distribution for designs assembled by the fragments selected for the second-generation library. (**C** and **D**) Examples of backbone fragments eliminated by the activity predictor in the second-generation library. Fragment color scheme as in Fig. 1. (C) 2WYS in segment 2 (green) was selected for the first-generation library but discarded in the second because of low atomic density. The interface with segment 3 (blue) is poorly packed, leaving a gap between the segments (white). (D) 1UQZ in segment 4 (red) was selected for the first-generation library but discarded in the second because of unfavorable hydrogen bond energy. Close inspection revealed two mutations introduced during sequence design, Arg²⁸²→Asn and Arg²⁸⁹→Leu [residue numbering refers to PDB entry: 1UQZ (56)], eliminating hydrogen bonds that are crucial for β/α loop backbone stabilization. Mutations in red.

ferent backbones (Fig. 3A), compared with only 376 GH10 xylanase entries in the UniProt database (39). The recovered designs exhibited many insertions and deletions relative to one another, with sequence lengths varying from 317 to 395 amino acids and 62% sequence identity to one another on average. In all models, residues responsible for the catalytic steps are held in place by construction, but the active-site pocket exhibits high geometric and electrostatic differences (Fig. 3A, bottom) because of loop conformation diversity. The designs

exhibit as many as 169 mutations and 48 to 73% sequence identity (Fig. 3B) to their nearest natural homolog [in the nonredundant (nr) sequence database (40)], and most designs source fragments from four different structures (Fig. 3C).

Recovered designs are compact and preorganized for activity

The deep sequencing analysis provides a valuable dataset for improving enzyme design methodology. For each design, we computed
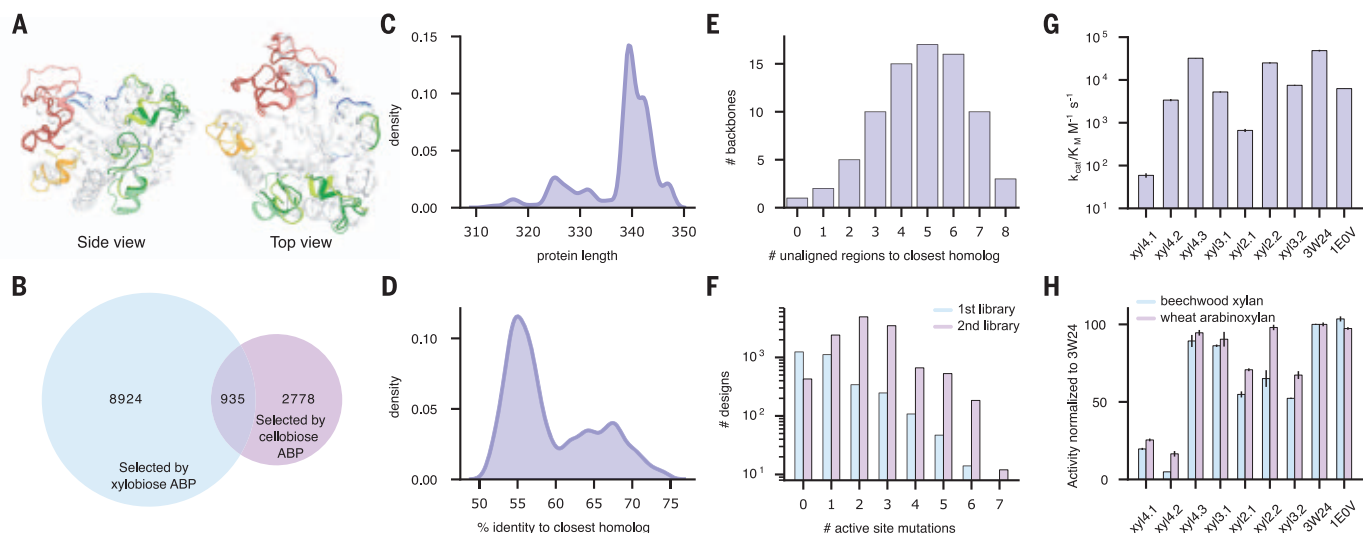
Fig. 5. Activity predictor significantly increases design success rate.
(**A**) Backbone fragments selected for the second-generation library (colors as in Fig. 1, low diversity regions in white). (**B**) Number of sequences in the population selected by the xylobiose and cellobiose ABPs (blue and purple, respectively). In the overlap region, designs selected by both ABPs. (**C**) Protein sequence length of recovered designs in the second-generation library. (**D**) Distribution of sequence identity to nearest natural homolog of recovered designs in the second-generation library. (**E**) Number of unaligned regions to nearest natural homolog of recovered designs in the second-generation library.

(**F**) Designs recovered in the second-generation library incorporate more active site mutations than in the first-generation library. (**G**) Catalytic efficiency of seven xylanases from the small-set design and two representative natural ones [right, names correspond to PDB entry. 3W24 (*27*) is a xylanase from the thermophilic organism *Thermoanaerobacterium saccharolyticum*]. The first number in the design name indicates the number of different proteins from which the fragments were sourced. (**H**) Normalized activity with wheat arabinoxylan and beechwood xylan. Data are the means ± standard deviation of duplicate measurements.

85 structure and energy metrics, some relating to the entire protein, and others restricted to the active site. We avoided using the designed mutations or fragment identities as features for learning so that we might infer general lessons that apply to other enzymes. We tested the differences between the presumed active and inactive sets using an independent two-sample *t* test, finding that 63 metrics exhibited *P* values less than 10^{-10}. To select the most meaningful metrics, we visually inspected their distributions and focused on 10 (Fig. 4A and fig. S4) that were not significantly correlated (see materials and methods). We then trained a logistic regression model based on these 10 metrics to predict whether an enzyme is active (Fig. 4B and tables S1 to S3).

The 10 dominant predictive metrics relate to essential aspects of enzyme catalysis. The most dominant feature is atomic density, which gauges protein compactness and correlates with stable packing. Another dominant feature is the compatibility of the amino acid identity and the local backbone conformation, a key determinant of protein foldability (*41*). By contrast, this feature is disfavored within the active-site pocket, presumably because active-site residues are selected for their impact on activity rather than stability. We also find that hydrogen-bond energies are highly discriminating, reflecting the prevalence of buried long-range hydrogen bond networks in large proteins of a complex fold such as TIM

barrels (fig. S5) (*42*, *43*). However, Rosetta system energy makes a small contribution to predicting activity, presumably because all designs exhibit low energy by construction (Fig. 2B).

Within the active site, the model assigns almost equal importance to atomic density and van der Waals energy, two features that promote precise catalytic residue placement but penalize overly packed constellations, respectively. The resulting dense yet relaxed packing arrangements are likely to be key in promoting active site preorganization. Focusing on the four catalytic residues only, the model includes a feature that penalizes high repulsive energy, further emphasizing the importance of a relaxed and preorganized active site. Our analysis highlights prerequisites of catalytic activity that were not observed in previous high-throughput studies of design methods, which focused on the kinetic stability of designed miniproteins and binders (*44*, *45*). Additionally, the design objective function is substantially different within the active site versus the remainder of the protein.

Recently, the AlphaFold2 ab initio structure prediction method (*46*) has been shown to discriminate correctly from incorrectly folded de novo–designed binders (*47*). However, when AlphaFold2 was applied to our set, no discernable difference was found between presumed active and inactive designs in either the root-mean-square deviation (RMSD) between pre-

dicted and designed models, or in the AlphaFold2 confidence scores (pLDDT) (fig. S6). This result suggests that despite the high mutational load and the sequence and structure diversity in the designs, CADENZ generates sequences with native-like characteristics.

Order-of-magnitude increase in design success in second-generation library

We next asked whether the lessons we learned from the first-generation library could improve design success rate. We used the same set of combinatorial designs from the first library, but instead of ranking them on the basis of Rosetta energies, we ranked them according to the activity predictor (Fig. 4B and fig. S2B). We then applied EpiNNet to nominate fragments that are likely to be mutually compatible. As in the first library, we designed several sequence variants for each backbone fragment, holding sidechain conformations of the core catalytic residues fixed in all design calculations. This second-generation library included three backbone fragments for each of the four segments and up to 11 sequence variants per fragment (for a total of 100 designed fragments), resulting in 334,125 designed full-length xylanases with 81 different backbones. To gain insight into the molecular features that are disfavored by the activity predictor, we analyzed which backbone fragments were chosen in the first library but discarded in the second. We found, for example,

that atomic density (Fig. 4C) and hydrogen-bond energy (Fig. 4D) were unfavorable in many discarded fragments.

We synthesized and screened the second-generation library as we did with the first-generation library (fig. S7). Notably, sequencing confirmed 9859 active designs, an order-of-magnitude increase in the rate of positive hits compared with that of the first library (Fig. 5A). In addition to the xylobiose screen, we also screened the library with an ABP that is based on cellobiose (Fig. 5B), the disaccharide repeat moiety in cellulose rather than in xylan (48). We found 2778 designs that reacted with the cellobiose ABP but were not sequenced in the library sorted with the xylan ABP, for a total of more than 12,637 active designs (3.8% of the design population). To verify that the ABP-selected designs exhibited the full catalytic cycle, we used plate-based validation with O-PNPX₂ and cellPNP (to detect cellulase activity) confirming 85 and 60% of active clones in the xylobiose- and cellobiose-labeled populations, respectively (fig. S7, C and D).

Ranking designs on the basis of the activity predictor resulted in a more focused library that included 79 of the 81 designed backbones and sequence lengths ranging from 312 to 347 amino acids (Fig. 5C). Although the activity predictor was blind to the identities of the designed fragments and mutations, we were concerned that it might have focused the second library on a set of fragments identified in functional enzymes in the first library. We analyzed the source of the active designs in the second-generation library, finding that 75% of these designs incorporated backbone fragments that were not encoded in the first library, and verifying that the learned energy and structure features generalized to fragments not included in the training data. Moreover, the active designs are as divergent from natural GH10 enzymes as they were in the first library, exhibiting 50 to 73% sequence identity to the most similar sequences in the nr database (40) (Fig. 5D) as well as up to 140 mutations and eight unaligned regions (Fig. 5E). Furthermore, the second-generation library incorporates more active site mutations (Fig. 5F), increasing the potential for altered substrate specificities. We also analyzed the distribution of energy and structure metrics among active and inactive designs in the second-generation library. The discrimination that we observed, however, was lower than in the first-generation library, suggesting that the specific learning process we implemented converged.

As an independent test, we applied the learned activity predictor to select a small set of individually designed GH10 enzymes (18). On the basis of the AbDesign strategy (26), we used Rosetta atomistic modeling to enumerate all fragment combinations and design their sequences as full-length enzymes, fol-lowed by selection with the activity predictor. This strategy encodes more stabilizing inter-segment interactions than when the fragments are designed independently, and the designs are therefore more likely to be stable and fold-able. Thus, in this implementation, the design and selection process does not favor modular-ity but rather optimal structure and energy properties. The activity predictor selected 27 designs for experimental characterization with up to 143 mutations and 51 to 74% sequence identity to their nearest natural homologs. Although these designs were generated by a different process than the one used to train the activity predictor, notably, 25 (93%) of the designs were active in hydrolyzing O-PNPX₂ (table S4), compared with less than 50% in a previous application of AbDesign to GH10 enzymes (18). We further characterized the kinetics of the seven most promising designs with various substrates (table S5). Among these designs, several exhibited catalytic efficiencies (k_{cat}/K_M) comparable to those of natural GH10 xylanases from thermophiles, including against natural wood and wheat xylan (Fig. 5, G and H), despite incorporating over 80 mutations from any known natural protein sequence. These results are a marked improvement in the success of backbone design in enzymes and underscore that the lessons we learned from high-throughput screening can be applied to generate a diverse and highly active set of designs, for either high- or low-throughput screening.

Discussion

Modularity is a prerequisite for innovation in numerous engineering disciplines, but protein domains exhibit high epistasis, severely hampering the ability to combine fragments into stable and active structures. CADENZ addresses this conflict by designing a spanning set of low-energy and mutually compatible protein fragments that can be assembled into thousands of diverse and functional proteins. We have also begun to investigate how EpiNNet can be implemented to design large repertoires of active site sequence variants (49). Our approach increases the number and diversity of functional enzymes that can be interrogated relative to the natural diversity, providing an alternative to metagenomic libraries (12). Current methods for optimizing and diversifying proteins rely on sequence statistics (50, 51) or cycles of mutation, recombination, and screening (52). Because of high epistasis, these methods explore a small fraction of sequence and structure space, whereas we show in this system that CADENZ can generate 10^6 structurally diverse designs of which >10,000 are recovered on the basis of activity.

Our results also show that ABPP is an effective strategy for high-throughput isolation of successful CADENZ designs and could be extended to other substrates (53), either natural or engineered. The combined strategy of CADENZ and ABPP enabled us to implement effective design-test-learn cycles on many enzyme designs that have previously led to deeper understanding of the design principles for de novo–designed miniproteins (44, 45). The rules we learned increased the design success rate by an order of magnitude and were directly transferable to automated small-scale design. Such functional data from many homologous yet structurally diverse enzymes may guide future improvements in macromolecular energy functions and advance efforts to develop AI-based enzyme design methods.

REFERENCES AND NOTES

1. M. E. Csete, J. C. Doyle, *Science* **295**, 1664–1669 (2002).
2. Y. Lazebnik, *Cancer Cell* **2**, 179–182 (2002).
3. M. Parter, N. Kashtan, U. Alon, *PLOS Comput. Biol.* **4**, e1000206 (2008).
4. D. M. Weinreich, R. A. Watson, L. Chao, *Evolution* **59**, 1165–1174 (2005).
5. D. A. Kondrashov, F. A. Kondrashov, *Trends Genet.* **31**, 24–33 (2015).
6. C. A. Voigt, C. Martinez, Z.-G. Wang, S. L. Mayo, F. H. Arnold, *Nat. Struct. Biol.* **9**, 553–558 (2002).
7. S. Nepomnyachiy, N. Ben-Tal, R. Kolodny, *Proc. Natl. Acad. Sci. U.S.A.* **111**, 11691–11696 (2014).
8. N. Ferruz et al., *J. Mol. Biol.* **432**, 3898–3914 (2020).
9. T. M. Jacobs et al., *Science* **352**, 687–690 (2016).
10. K. Murphy, C. Weaver, *Janeway's Immunobiology* (Garland Science, 2016).
11. E. Dellus-Gur, A. Toth-Petroczy, M. Elias, D. S. Tawfik, *J. Mol. Biol.* **425**, 2609–2621 (2013).
12. P.-Y. Colin et al., *Nat. Commun.* **6**, 10008 (2015).
13. P. Kast, M. Asif-Ullah, N. Jiang, D. Hilvert, *Proc. Natl. Acad. Sci. U.S.A.* **93**, 5043–5048 (1996).
14. S. G. Withers et al., *Biochem. Biophys. Res. Commun.* **139**, 487–494 (1986).
15. E. Drula et al., *Nucleic Acids Res.* **50** (D1), D571–D577 (2022).
16. CAZypedia Consortium, *Glycobiology* **28**, 3–8 (2018).
17. A. Tóth-Petróczy, D. S. Tawfik, *Curr. Opin. Struct. Biol.* **26**, 131–138 (2014).
18. G. Lapidoth et al., *Nat. Commun.* **9**, 2780 (2018).
19. R. Netzer et al., *Nat. Commun.* **9**, 5286 (2018).
20. N. Nagano, C. A. Orengo, J. M. Thornton, *J. Mol. Biol.* **321**, 741–765 (2002).
21. R. Sterner, B. Höcker, *Chem. Rev.* **105**, 4038–4055 (2005).
22. B. Höcker, J. Claren, R. Sterner, *Proc. Natl. Acad. Sci. U.S.A.* **101**, 16448–16453 (2004).
23. B. Höcker, S. Beismann-Driemeyer, S. Hettwer, A. Lustig, R. Sterner, *Nat. Struct. Biol.* **8**, 32–36 (2001).
24. M. Richter et al., *J. Mol. Biol.* **398**, 763–773 (2010).
25. D. L. Trudeau, M. A. Smith, F. H. Arnold, *Curr. Opin. Chem. Biol.* **17**, 902–909 (2013).
26. R. Lipsh-Sokolik, D. Listov, S. J. Fleishman, *Protein Sci.* **30**, 151–159 (2021).
27. X. Han et al., *Proteins* **81**, 1256–1265 (2013).
28. A. Goldenzweig et al., *Mol. Cell* **63**, 337–346 (2016).
29. S. R. Andrews et al., *J. Biol. Chem.* **275**, 23027–23033 (2000).
30. B. Henrissat et al., *Proc. Natl. Acad. Sci. U.S.A.* **92**, 7090–7094 (1995).
31. O. Khersonsky et al., *Mol. Cell* **72**, 178–186.e5 (2018).
32. C. Engler, R. Kandzia, S. Marillonnet, *PLOS ONE* **3**, e3647 (2008).
33. G. Chao et al., *Nat. Protoc.* **1**, 755–768 (2006).
34. S. P. Schröder et al., *ACS Cent. Sci.* **5**, 1067–1078 (2019).
35. D. Tull et al., *J. Biol. Chem.* **266**, 15621–15625 (1991).
36. D. Tull, S. G. Withers, *Biochemistry* **33**, 6363–6370 (1994).
37. H. Taguchi, T. Hamasaki, T. Akamatsu, H. Okada, *Biosci. Biotechnol. Biochem.* **60**, 983–985 (1996).
38. A. Rhoads, K. F. Au, *Genomics Proteomics Bioinformatics* **13**, 278–289 (2015).

39. A. Bateman *et al.*, *Nucleic Acids Res.* **49**, D480–D489 (2021).
40. E. W. Sayers *et al.*, *Nucleic Acids Res.* **50** (D1), D20–D26 (2022).
41. A. Goldenzweig, S. J. Fleishman, *Annu. Rev. Biochem.* **87**, 105–129 (2018).
42. O. Khersonsky, S. J. Fleishman, *BioDesign Research* 2022, 1–11 (2022).
43. D. Baran *et al.*, *Proc. Natl. Acad. Sci. U.S.A.* **114**, 10900–10905 (2017).
44. G. J. Rocklin *et al.*, *Science* **357**, 168–175 (2017).
45. L. Cao *et al.*, *Nature* **605**, 551–560 (2022).
46. J. Jumper *et al.*, *Nature* **596**, 583–589 (2021).
47. N. Bennett *et al.*, *bioRxiv* (2022), p. 2022.06.15.495993.
48. C. de Boer *et al.*, *RSC Chem. Biol.* **1**, 148–155 (2020).
49. J. Y. Weinstein *et al.*, *bioRxiv* 2022.10.11.511732 [Preprint] (2022). https://doi.org/10.1101/2022.10.11.511732.
50. W. P. Russ *et al.*, *Science* **369**, 440–445 (2020).
51. N. Ferruz, S. Schmidt, B. Höcker, *Nat. Commun.* **13**, 4348 (2022).
52. S. L. Lovelock *et al.*, *Nature* **606**, 49–58 (2022).
53. L. Wu *et al.*, *Curr. Opin. Chem. Biol.* **53**, 25–36 (2019).
54. R. Lipsh-Sokolik *et al.*, Data for: Combinatorial assembly and design of enzymes (2022); http://dx.doi.org/10.5281/zenodo.7382421.
55. T. Ihsanawati *et al.*, *Proteins* **61**, 999–1009 (2005).

NEURODEVELOPMENT

Excessive mechanotransduction in sensory neurons causes joint contractures

Shang Ma[1], Adrienne E. Dubin[1], Luis O. Romero[2,3], Meaghan Loud[1], Alexandra Salazar[1], Sarah Chu[4], Nikola Klier[4], Sameer Masri[4], Yunxiao Zhang[1], Yu Wang[1], Alex T. Chesler[5,6], Katherine A. Wilkinson[4], Valeria Vásquez[2], Kara L. Marshall[7], Ardem Patapoutian[1]*

Distal arthrogryposis (DA) is a collection of rare disorders that are characterized by congenital joint contractures. Most DA mutations are in muscle- and joint-related genes, and the anatomical defects originate cell-autonomously within the musculoskeletal system. However, gain-of-function mutations in PIEZO2, a principal mechanosensor in somatosensation, cause DA subtype 5 (DA5) through unknown mechanisms. We show that expression of a gain-of-function PIEZO2 mutation in proprioceptive sensory neurons that mainly innervate muscle spindles and tendons is sufficient to induce DA5-like phenotypes in mice. Overactive PIEZO2 causes anatomical defects through increased activity within the peripheral nervous system during postnatal development. Furthermore, botulinum toxin (Botox) and a dietary fatty acid that modulates PIEZO2 activity reduce DA5-like deficits. This reveals a role for somatosensory neurons: Excessive mechanosensation within these neurons disrupts musculoskeletal development.

D istal arthrogryposis (DA) is a rare disorder with congenital contractures primarily affecting joints. It is estimated to afflict ~1 in 3000 individuals worldwide and usually requires invasive surgeries to alleviate the symptoms (1, 2). Various mutations have been identified in patients with DA in genes important for musculoskeletal function (3). DA subtype 5 (DA5) is an autosomal dominant disorder with distinct clinical features, including ophthalmoplegia and restrictive lung disease, in addition to contractures in distal joints (4). Gain-of-function (GOF) mutations in PIEZO2, a mechanically activated ion channel, have been found in patients with DA5 (5). PIEZO2 is the principal mechanosensor in somatosensory neurons and underlies touch sensation (6) and proprioception (the sense of where one's limbs are in space) (7), as well as mechanosensory processes in internal organs such as lung, aorta, and bladder (8–10). However, a direct role for this ion channel in muscles or tendons has not been described.

Overactive PIEZO2 increases mechanosensitivity of sensory neurons

We engineered mice that conditionally express a GOF *Piezo2* mutant to study the disease mechanism for DA5. One such human GOF mutation, E2727del, is in the C terminus of PIEZO2 and it causes slower channel inactiva-

tion (5). We designed a knock-in strategy that allows Cre recombinase–dependent replacement of a wild-type C-terminal exon of PIEZO2 with one that harbors the human-equivalent mouse GOF variant E2799del (Fig. 1A). We generated constitutive GOF *Piezo2* mice (GOF$^{const.}$) by breeding mice homozygous for the GOF allele into *Cmv*^{Cre} driver that expresses Cre recombinase ubiquitously (11). We used whole-cell patch clamp to record PIEZO2-dependent mechanically activated currents from dorsal root ganglion (DRG) neurons of homozygous GOF *Piezo2* mice and wild-type littermates (Fig. 1B and fig. S1A). We initially tested homozygous instead of heterozygous mice to avoid diluting the effects of the GOF allele by a wild-type allele. Although most homozygotes died perinatally for unknown reasons, we were able to obtain DRGs from viable mice for recording. DRG neurons from homozygous GOF$^{const.}$ mice showed a slower inactivation and a remaining current at the end of the stimulus (as a percentage of the peak current at the strongest stimulus applied) compared with wild type (Fig. 1B and fig. S1B). As expected, there was no detectable difference in I_{max} (maximal current) and apparent threshold between wild-type and GOF neurons (fig. S1C). We also compared mechanically activated currents in DRG neurons of heterozygous mice with those of wild-type mice to reflect the human condition. To enrich the recorded population for PIEZO2-dependent rapidly inactivating neurons, we crossed mice carrying the GOF *Piezo2* allele into *Pvalb*^{Cre}/Ai9, which express Cre recombinase and the Ai9 tandem dimer Tomato (tdTomato) reporter protein in proprioceptive neurons (7, 12). We observed robust differences in the kinetics of mechanically activated currents between heterozygous GOF and wild-type DRGs (Fig. 1, C and D). These results validate that the engineered mice express a functional GOF PIEZO2 channel with similar kinetics of inactivation as human GOF

[1]Howard Hughes Medical Institute, Department of Neuroscience, Dorris Neuroscience Center, Scripps Research, La Jolla, CA 92037, USA. [2]Department of Physiology, College of Medicine, University of Tennessee Health Science Center, Memphis, TN, USA. [3]Integrated Biomedical Sciences Graduate Program, College of Graduate Health Sciences, University of Tennessee Health Science Center, Memphis, TN, USA. [4]Department of Biological Sciences, San Jose State University, San Jose, CA, USA. [5]National Institute of Neurological Disorders and Stroke, National Institutes of Health, Bethesda, MD, USA. [6]National Center for Complementary and Integrative Health, National Institutes of Health, Bethesda, MD, USA. [7]Department of Neuroscience, Baylor College of Medicine, Houston, TX, USA.
*Corresponding author. Email: ardem@scripps.edu

mutations analyzed in a heterologous system (5). They also demonstrate that heterozygosity of GOF PIEZO2 is sufficient to increase mechanosensitivity in sensory neurons.

Overactive PIEZO2 causes limb defects in mice

The constitutive heterozygous GOF mice had normal body weight at different ages (fig. S2A), suggesting that overactive PIEZO2 is unlikely to affect overall growth. In addition, food intake and metabolic rate of these transgenic mice were comparable to those of wild-type littermates over a period of 8 days (fig. S2, B and C), suggesting normal eating behavior and metabolism.

We observed that hindlimbs of the transgenic mice had contractures compared with wild-type littermates (Fig. 2A). Direct visualization as well as micro–computed tomography (CT) images showed that the angles between major hindlimb joints were smaller in GOF^const. mice than in wild type (Fig. 2A, upper panel). We measured the angle between the phalange and metacarpal, the two major bones of hindlimbs (quantitatively studying forelimbs is challenging because of their small size), and found that phalange-metacarpal angles in hindlimbs of GOF^const. mice were significantly decreased compared with those of wild-type mice (Fig. 2A, bar graph). Patients with DA5 have weak or absent tendon reflexes, which suggests that defective tendon development might be associated with joint contractures (5). To evaluate tendon phenotypes, we dissected the intact tendons from hindlimbs (Fig. 2B), and we observed

that the average length of tendons was significantly reduced in GOF^const. mice compared with those of wild type (Fig. 2B). It is therefore possible that the DA5-like contractures are caused by shortened tendons.

Anatomical deformities cause limited joint movements and affect motor functions in patients with DA. To test whether GOF PIEZO2 affects limb functionality in mice, we performed two behavioral tests. First, we used a hanging-wire assay (13). The test is based on the latency of a mouse to fall off from a metal wire (Fig. 2C). We found that wild-type mice were able to remain on the wire for at least 30 s, whereas GOF^const. mice fell off significantly earlier (Fig. 2C). Second, we performed the inverted-screen test (14), which measures the time until a mouse falls off a square screen after it is turned upside down (Fig. 2D and materials and methods). All wild-type mice were able to hold on for at least 90 s. By contrast, the average success rate for GOF^const. mice was <10% (Fig. 2D). Thus, these results suggest that limb functionality was compromised in GOF^const. mice, consistent with the anatomical defects.

We also measured the gait of GOF *Piezo2* mice (Fig. 2E). The length of the stride during locomotion was similar to that of wild type (Fig. 2F). By contrast, the width of their stride was decreased compared with that of wild type (Fig. 2G). This is expected, given the anatomical deficits, and is reminiscent of the limited range of limb motion observed in human patients

with DA5 (5). Despite these defects, GOF *Piezo2* mice had normal daily activity patterns in an open-field arena over 8 days (fig. S2D), which suggests that overactive PIEZO2 is not completely debilitating.

Somatosensory PIEZO2 overactivity causes limb defects

To investigate which cell types are involved in the DA5 etiology, we expressed GOF *Piezo2* allele in various tissues. We induced GOF PIEZO2 expression in all mesenchymal cells, including skeletal muscles, cartilages, and tendons, using *Prrx1*^Cre (15, 16). This Cre line induces robust recombinase activity in mouse limb mesenchyme that starts from early embryogenesis. These GOF *Piezo2* mice had normal phalange-metacarpal angles and tendon lengths in their hindlimbs (Fig. 3, A and B). Consistently, these mice performed comparably to wild-type mice on behavioral assays (Fig. 3, C and D). By contrast, we found that expression of GOF PIEZO2 in proprioceptive sensory neurons (by using *Pvalb*^Cre knock-in mice) that mainly innervate muscle spindles and tendon organs (7, 17) was sufficient to cause joint contractures, shortened tendons, and poor performance on behavioral assays (Fig. 3, A to D). These data suggest that overactive PIEZO2 in sensory neurons, but not in mesenchyme, is sufficient to induce DA5-like phenotypes in vivo.

Because DA is a developmental disorder that presumably originates during fetal stages (2), we used our mouse model to determine the
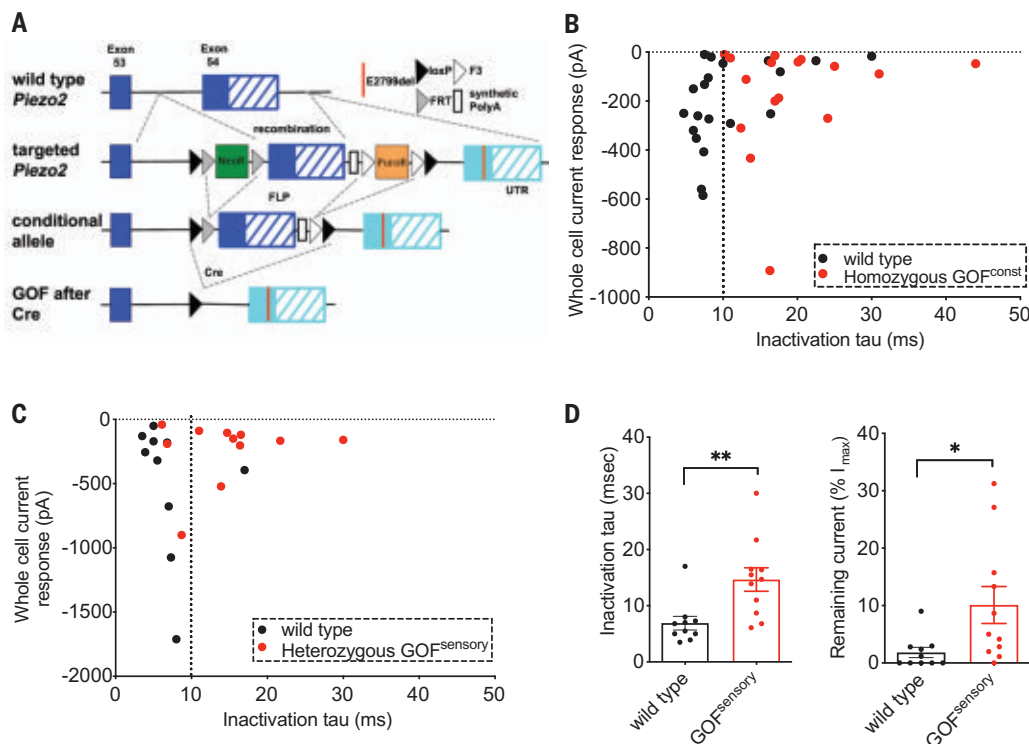

Fig. 1. Gain-of-function (GOF) PIEZO2 increases mechanosensitivity of sensory neurons. (**A**) Conditional GOF *Piezo2* mouse model. Cre-dependent replacement of wild-type exon (blue) by GOF-carrying exon (cyan). UTR, untranslated region; E2799del, deletion of glutamic acid at position 2799; FRT, flippase recognition target site; FLP, flippase-mediated recombination. (**B**) Mechanically activated currents and inactivation time constant (tau) in DRG sensory neurons from wild-type (black) and constitutively homozygous GOF *Piezo2* mice (red). Eighty-seven percent of wild-type and 70% of GOF neurons were responsive to the stimulus. (**C**) Mechanically activated currents and inactivation time constant in Tdtomato+ neurons from *Pvalb*^Cre/*Ai9* (wild type, black) and GOF *Piezo2; Pvalb*^Cre/*Ai9* mice (red). (**D**) Bar graphs representing inactivation time constant (ms) and remaining current at the end of the stimulus (percentage of I_{max} value) in DRG sensory neurons. Each data point represents a single DRG neuron. *$P < 0.05$, **$P < 0.01$, ***$P < 0.001$ (Student's t test).

timing of PIEZO2 activity in sensory neurons that affects musculoskeletal development. We used an inducible sensory neuron–specific GOF *Piezo2* mouse by crossing the GOF allele into *Advillin*[Cre-ERT2] driver mice (*18*). Advillin is expressed in most DRG neurons, but not central nervous system or non-neuronal cell types, starting in early embryogenesis (*19*, *20*). We induced GOF PIEZO2 expression in sensory neurons at various developmental stages by tamoxifen injection (Fig. 3E). When induced at embryonic day 12.5 (E12.5) or postnatal day 7 (P7) to P10, these mice showed significantly decreased phalange-metacarpal joint angles (Fig. 3F), suggesting that the phenotype is mainly dependent on the expression of PIEZO2 sometime after P7. However, induction of GOF PIEZO2 expression in sensory neurons after P21 or during adulthood

(>1 month old) did not cause joint defects in mice (Fig. 3F). Consistent with anatomical phenotypes, mice expressing GOF PIEZO2 in sensory neurons during the embryonic (E12.5) and early postnatal stage (P7 to P10), but not after early adulthood (>P21), performed poorly on behavioral tests (Fig. 3, G and H). These results confirm our earlier findings using *Pvalb*[Cre] that overactive PIEZO2 in sensory neurons causes DA5-like defects (Fig. 3, A to D). In addition, they suggest a critical postnatal developmental period between days 7 and 21 during which excessive mechanotransduction in somatosensory neurons causes limb malformation.

To ensure that the anatomical deficits are not an indirect consequence of compromised proprioceptive neuronal development, we examined proprioceptive nerve endings of muscle

spindles and Golgi tendon organs (fig. S3). We did not observe overt anomalies in these proprioceptive endings (fig. S3A). In addition, we quantified the size of proprioceptors innervating muscle spindles and observed no difference between GOF *Piezo2* and wild-type mice (fig. S3B). Furthermore, we did not find significant changes in extrafusal and intrafusal muscle fiber diameters in GOF *Piezo2* mice (fig. S3C), suggesting that overactive PIEZO2 in sensory neurons does not appear to have strong effects on muscle development.

Overactive PIEZO2 causes defects mediated by efferent pathways

We also used a pharmacological approach to further test whether anatomical defects of GOF *Piezo2* mice are attributed to hyperactivation of sensory neurons. We performed intramuscular
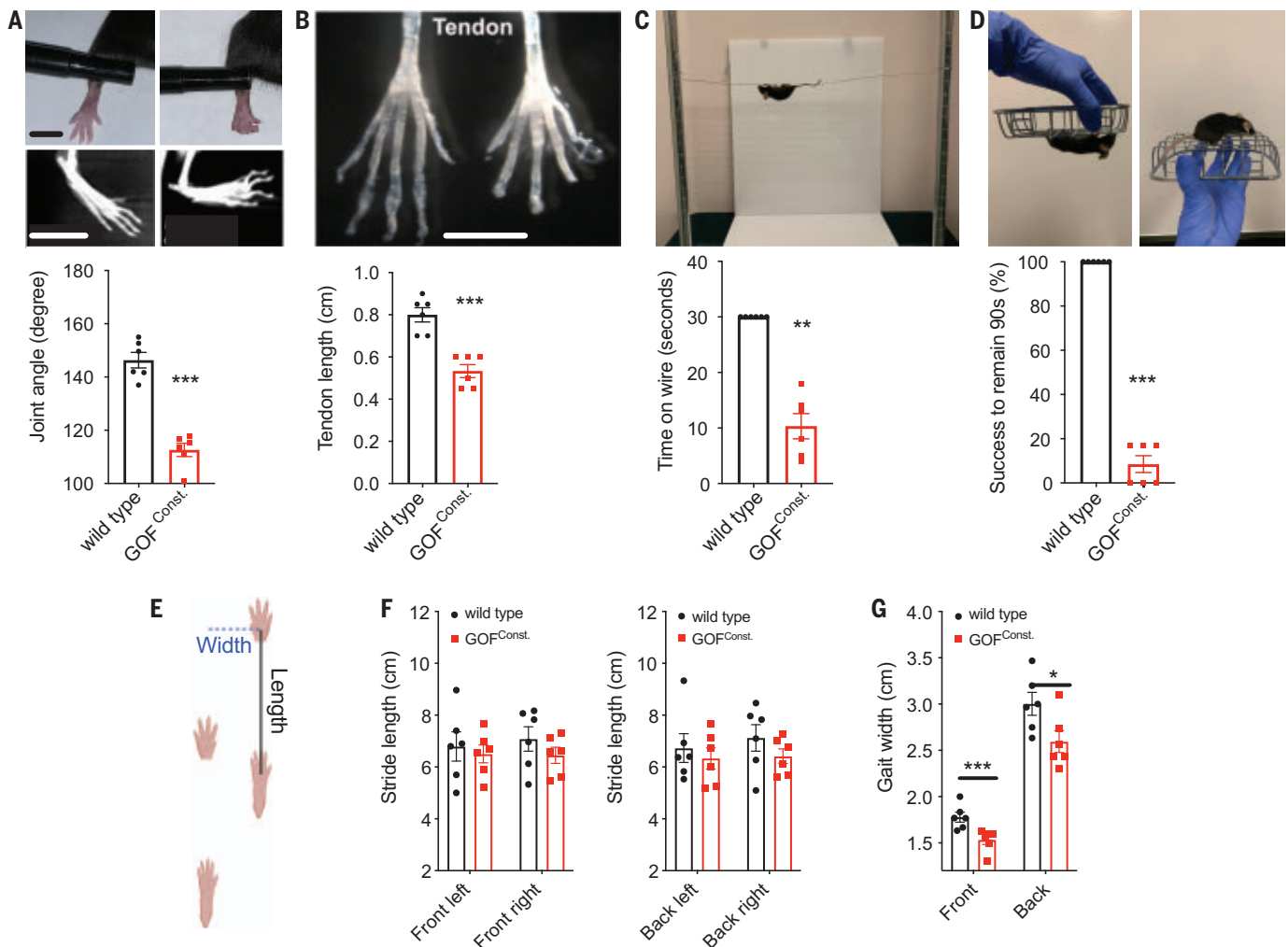

Fig. 2. GOF *Piezo2* mice develop limb defects. (**A**) Joint morphology of live animals and CT scan (upper images) and phalange-metacarpal joint angles (lower graph) in the hindlimb. Left, wild type; right, GOF mice. Scale bars, 0.5 cm. (**B**) Intact tendon (upper) and tendon length (lower) from hindlimbs. Scale bar, 0.5 cm. (**C**) Hanging-wire test (upper) and time (s) that animals remained on the metal wire, with 30 s as cutoff (lower). (**D**) Inverted-screen test (upper)

and quantification as percentage of animals successfully remaining on the rotating screen for 90 s (lower). (**E**) Gait assay: the stride length measures forelimb-hindlimb distance in the first (front) and second (back) stride. Gait width is the distance between forelimbs (front) or between hindlimbs (back). (**F** and **G**) Quantifications for (E). Each data point represents a single animal. *P < 0.05, **P < 0.01, ***P < 0.001 (Student's *t* test).

injection of botulinum toxin (Botox) into the hindlimb of mice at P7 to P10 (Fig. 4A), at the beginning of the critical period. The contralateral hindlimb received vehicle injection as an internal control. Botox blocks neural transmission from both sensory and motor neurons by inhibiting exocytosis (21). Four weeks after a single dose of injection, we observed that Botox did not affect joint morphology and tendon length in wild-type mice (Fig. 4A). Meanwhile, it rescued joint and tendon defects in the hindlimb that received the treatment in GOF *Piezo2* mice compared with hindlimb injected with vehicle control (Fig. 4A). Furthermore, if administered on both sides of hindlimbs, Botox improved performances on the behavioral assays for GOF *Piezo2* mice (Fig. 4B). However, it failed to completely restore the behavioral outcomes, probably owing to deficits in forelimbs that did not receive Botox treatment. This result suggests that GOF PIEZO2–dependent neuronal activity is responsible for joint defects.

Mechanical activation of proprioceptive nerve endings has two consequences: (i) It causes local Ca^{2+}-dependent signaling within the peripheral proprioceptive endings, culminating in exocytosis (22); and (ii) it induces an afferent signal by initiating firing of proprioceptive neurons, which activates downstream motor neurons that innervate the same peripheral muscle to counteract the stretch (23). Botulinum toxin would block both these processes. To test whether the results we observed using Botox resulted from blocking motor neuron output, we injected α-bungarotoxin, which blocks neural transmission from motor neurons to muscles (24), into hindlimbs of GOF *Piezo2* mice at P7 to P10. This treatment did not alleviate anatomical defects in these mice (Fig. 4C). It is possible that a single dose of α-bungarotoxin is insufficient to inhibit motor transmission throughout the critical developmental period because it has a shorter pharmacological window than Botox (25). To assess this possibility, we injected α-bungarotoxin into the hindlimbs for 5 consecutive days. This treatment was sufficient to severely affect motor neuron function, as it compromised motor behavior (Fig. 4D), but it still failed to rescue anatomical defects in GOF *Piezo2* mice (Fig. 4E). This implies that motor activity does not play a major role in DA5-like deficits. Together, our pharmacological experiments suggest that GOF PIEZO2 causes musculoskeletal abnormalities through ectopic efferent activity in afferent peripheral mechanosensory neuronal endings, likely involving increased levels of exocytosis.

We also tested whether the GOF PIEZO2 allele caused increased proprioceptive firing (afferent function) during development. To measure muscle spindle firing, we evaluated proprioceptor mechanotransduction ex vivo. In this assay, we mechanically stretched the extensor digitorum longus muscle and recorded from the innervating proprioceptors (muscle spindles) to assess stretch-induced neuronal activity (fig. S4A) (7, 26). We found that muscle spindle afferent activity in response to stretch is not significantly different between wild-type and GOF *Piezo2* mice at P7 postnatal stage (fig. S4, B and C). Therefore, we observe increased PIEZO2 current in cell culture assays, but no increased neuronal firing ex vivo. It is possible that somatosensory neurons have compensatory mechanisms for
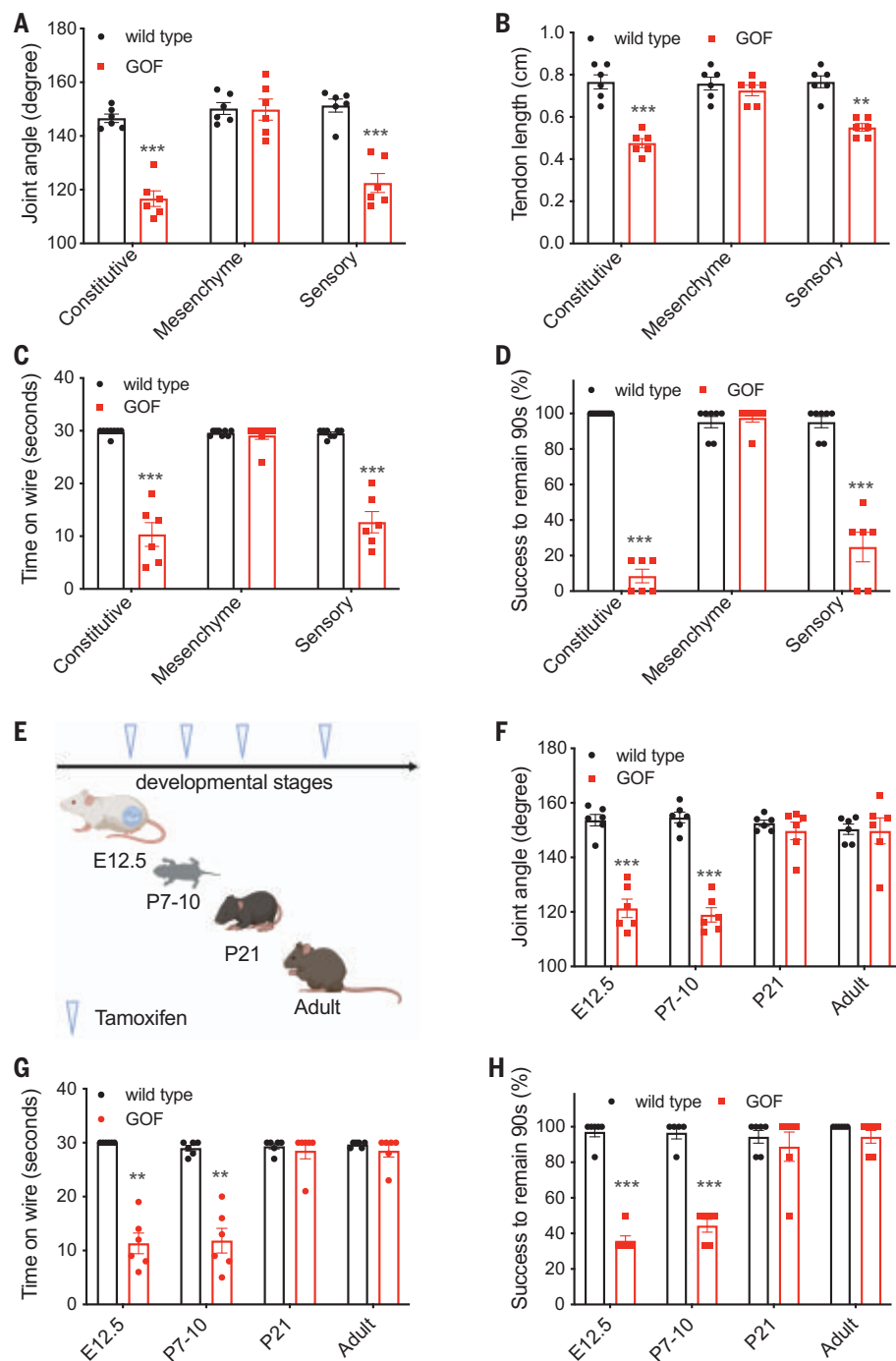

Fig. 3. GOF PIEZO2 in sensory neurons causes limb defects. (**A**) Phalange-metacarpal joint angle of the hindlimbs in wild-type and tissue-specific GOF mice (black, wild type; red, GOF *Piezo2*). (**B**) Tendon length of hindlimbs. (**C**) Quantification of hanging-wire test results. (**D**) Quantification of inverted-screen test results. (**E**) Tamoxifen induction of GOF PIEZO2 in sensory neurons by *Advillin^{Cre-ERT2}* at various developmental stages. (**F**) Phalange-metacarpal joint angle of the hindlimbs in (E). (**G**) Quantification of hanging-wire test results in (E). (**H**) Quantification of inverted-screen test in (E). Each data point represents a single animal. *$P < 0.05$, **$P < 0.01$, ***$P < 0.001$ (one-way analysis of variance followed by Tukey's multiple comparison).
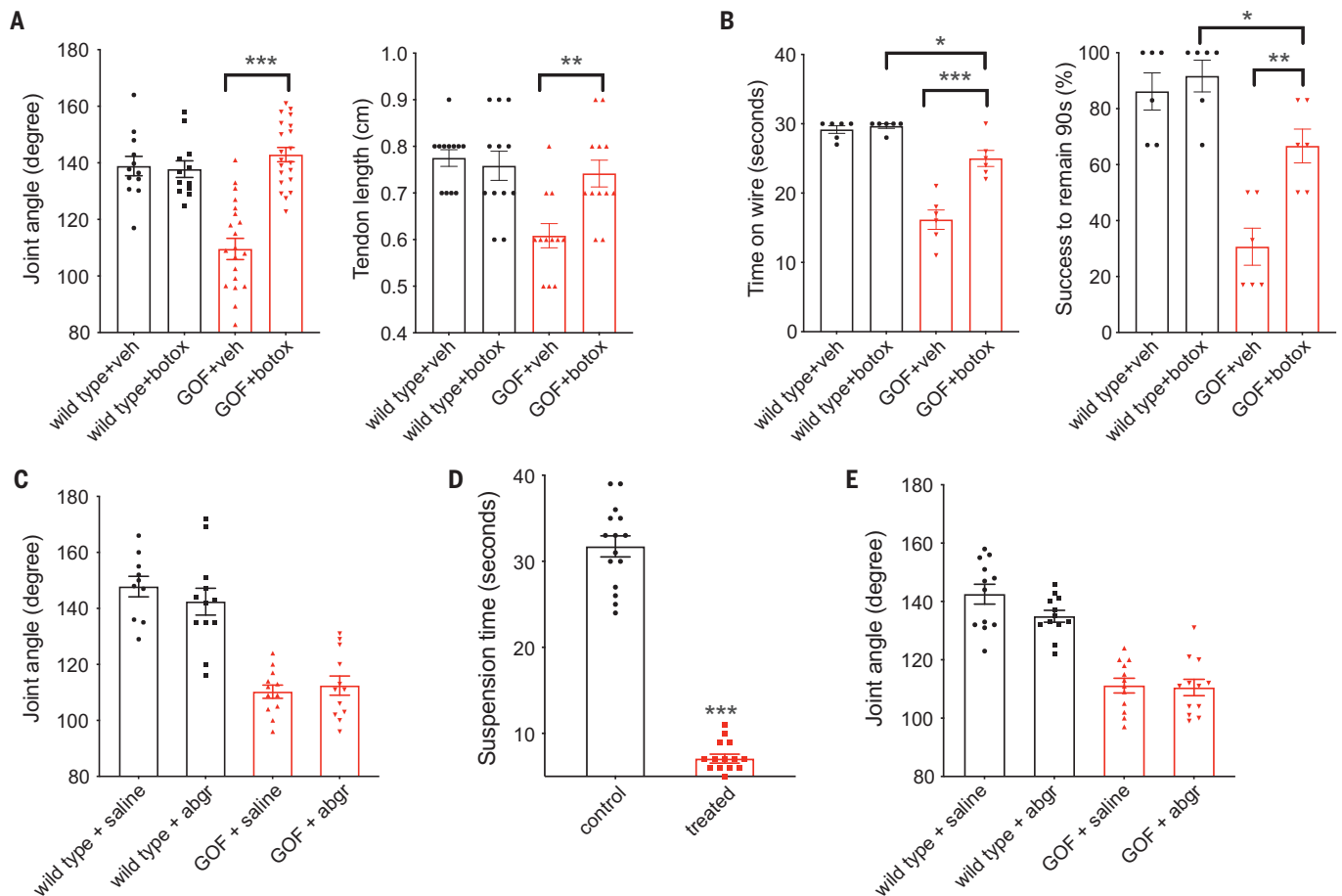
Fig. 4. Pharmacological effects on limb phenotypes in GOF mice.
(**A**) Phalange-metacarpal joint angle and tendon length of the hindlimbs in young adult wild-type and GOF *Piezo2*; *Pvalb^Cre^* mice that received botulinum toxin (Botox) at P7 to P10. veh, vehicle. (**B**) Quantification of behavioral tests in mice treated with Botox. (**C**) Phalange-metacarpal joint angle of the hindlimbs in young adult mice receiving a single dose of alpha-bungarotoxin (abgr) at P7 to P10. (**D**) Quantification for motor defects (in a modified hanging-wire assay) in young adult mice receiving 5-day abgr treatment at P7 to P10. (**E**) Phalange-metacarpal joint angle of the hindlimbs in young adult mice receiving daily abgr treatment from P5 to P10 in (D).

controlling overactive transduction responses. Thus, these recordings are consistent with the idea that local efferent action of afferent proprioceptive neurons caused by overactive PIEZO2 is responsible for the developmental deficits.

Eicosapentaenoic acid diet alleviates defects in GOF mice

Our data suggest that manipulations that would decrease overall PIEZO2 activity during a critical development time could potentially rescue the DA5-like phenotype. The ω-3 polyunsaturated fatty acid (PUFA) eicosapentaenoic acid (EPA), a membrane lipid component, significantly decreases the inactivation time of wild-type and GOF PIEZO1 channels, a close relative of PIEZO2 (*27, 28*). Because EPA is commonly found in fish and widely used as a dietary supplement, we tested whether a diet enriched in ω-3 PUFAs has therapeutic potential.

We first showed that overnight incubation with EPA (200 μM) reduced wild-type as well as GOF mutant PIEZO2 inactivation time constant in a heterologous expression system (Fig. 5, A and B). This suggests that EPA has the potential to modulate disease-causing mutations in PIEZO2. We then fed female mice a diet enriched in EPA during pregnancy and nursing. The sensory neurons of their offspring were later assessed for PIEZO2-dependent mechanosensitivity (fig. S5A). We found that EPA-enriched diet intake significantly reduced the inactivation time constant of mechanically stimulated currents in sensory neurons but had no effect on the current intensity and apparent threshold (fig. S5A). Next, we determined the effect of this diet on the anatomical defects in GOF *Piezo2* mice. Liquid chromatography–mass spectrometry showed that the feeding protocol successfully incorporated EPA into the plasma membrane of sensory neurons that carry the GOF *Piezo2* mutation (fig. S5B). Last, we observed that dietary EPA partially prevented joint malformations (Fig. 5C) and improved the performances on

the hanging-wire and inverted-screen tests (Fig. 5D) in GOF *Piezo2* mice.

Our study has identified a critical postnatal period during development when relatively small excess PIEZO2 activity in somatosensory neurons can cause tendon deficits and severe joint contractures. Previous work has shown that loss of PIEZO2 in proprioceptive neurons causes skeletal abnormalities manifested as spine malalignment in mice (*15*), indicating a requirement of proprioceptive feedback for proper vertebral development. We hypothesize that overactive PIEZO2 causes anatomical abnormalities in joints through increased exocytosis from sensory neuron endings without involving motor circuitry. Indeed, it is known that sensory neurons secrete a variety of factors in response to neuronal stimulation, including glutamate release from proprioceptive endings (*22*). Although the role of secreted factors such as calcitonin gene–related peptide (CGRP) from nociceptors in mediating pain and inflammation is well documented
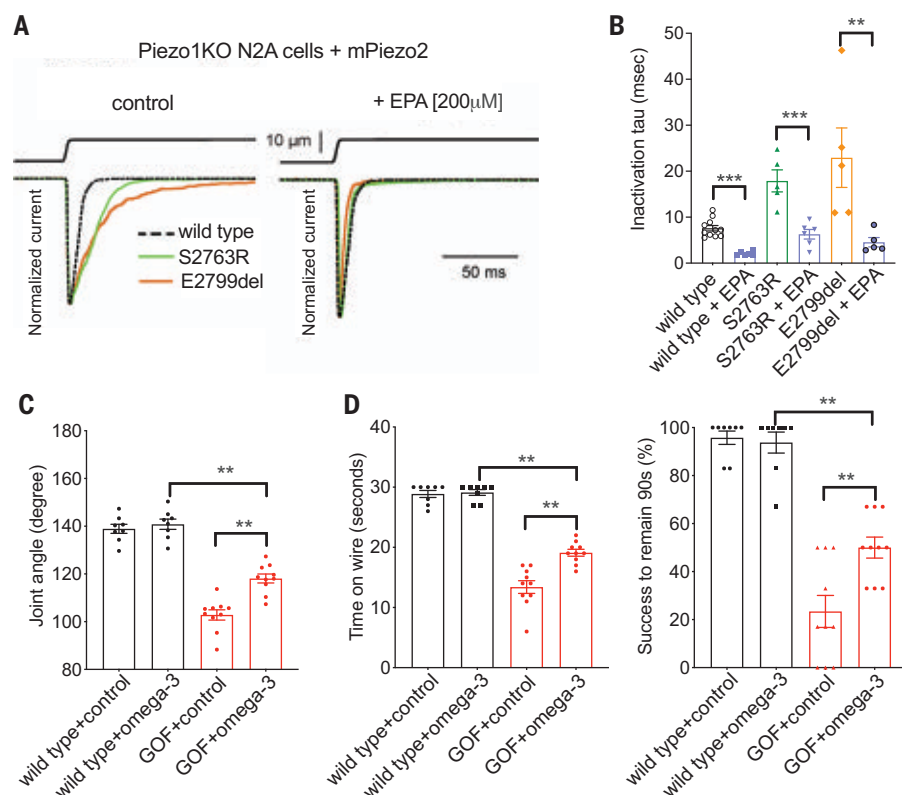
Fig. 5. EPA diet rescues joint defects in GOF mice. (**A**) Mechanically activated currents in N2A*Piezo1*$^{-/-}$ cells heterologously expressing mouse PIEZO2 wild type (stippled) and GOF mutants S2763R (green), substitution of serine at amino acid position 2763 with arginine and E2799del (brown), deletion of glutamic acid at position 2799. (**B**) Quantification of the inactivation time constant results in (A). (**C**) Phalange-metacarpal joint angle of the hindlimbs in young adult wild-type and GOF *Piezo2*; *Pvalb*^{Cre} mice that received an EPA-enriched diet. Control: sunflower oil–based food, which has a similar level of fat content and energy. (**D**) Quantification of hanging-wire and inverted-screen test results in (C). *$P < 0.05$, **$P < 0.01$, ***$P < 0.001$ (two-way analysis of variance followed by Tukey honestly significance test).

(*29*), relatively little is known about the importance and identity of such efferent signaling molecules in other sensory neurons, including proprioceptors.

We also present proof of concept that Botox injection or dietary treatment can counteract the effect of overactive PIEZO2 function to evade DA-like phenotypes in mice when applied during a developmental critical period. These approaches might have clinical applications. Beyond this, our findings call attention to the importance of considering sensory mech-anotransduction when diagnosing and treating other musculoskeletal disorders.

REFERENCES AND NOTES

1. M. Bamshad, A. E. Van Heest, D. Pleasure, *J. Bone Joint Surg. Am.* **91** (suppl. 4), 40–46 (2009).
2. B. Kowalczyk, J. Feluś, *Arch. Med. Sci.* **12**, 10–24 (2016).
3. H. Tajsharghi *et al.*, *Arch. Neurol.* **65**, 1083–1090 (2008).
4. R. K. Beals, R. G. Weleber, *Am. J. Med. Genet. A.* **131**, 67–70 (2004).
5. B. Coste *et al.*, *Proc. Natl. Acad. Sci. U.S.A.* **110**, 4667–4672 (2013).
6. S. S. Ranade *et al.*, *Nature* **516**, 121–125 (2014).
7. S.-H. Woo *et al.*, *Nat. Neurosci.* **18**, 1756–1762 (2015).
8. K. Nonomura *et al.*, *Nature* **541**, 176–181 (2017).
9. W.-Z. Zeng *et al.*, *Science* **362**, 464–467 (2018).
10. K. L. Marshall *et al.*, *Nature* **588**, 290–295 (2020).
11. F. Schwenk, U. Baron, K. Rajewsky, *Nucleic Acids Res.* **23**, 5080–5081 (1995).
12. L. Madisen *et al.*, *Nat. Neurosci.* **13**, 133–140 (2010).
13. D. C. Rogers *et al.*, *Mamm. Genome* **8**, 711–713 (1997).
14. R. M. J. Deacon, *J. Vis. Exp.* **2013**, 2610 (2013).
15. E. Assaraf *et al.*, *Nat. Commun.* **11**, 3168 (2020).
16. M. Logan *et al.*, *Genesis* **33**, 77–80 (2002).
17. S. Hippenmeyer *et al.*, *PLOS Biol.* **3**, e159 (2005).
18. J. Lau *et al.*, *Mol. Pain* **7**, 1744-8069-7-100 (2011).
19. A. N. Akopian, J. N. Wood, *J. Biol. Chem.* **270**, 21264–21270 (1995).
20. L. L. Orefice *et al.*, *Cell* **178**, 867–886.e24 (2019).
21. B. Davletov, M. Bajjohrs, T. Binz, *Trends Neurosci.* **28**, 446–452 (2005).
22. G. S. Bewick, B. Reid, C. Richardson, R. W. Banks, *J. Physiol.* **562**, 381–394 (2005).
23. H.-H. Chen, S. Hippenmeyer, S. Arber, E. Frank, *Curr. Opin. Neurobiol.* **13**, 96–102 (2003).
24. P. T. Wilson, E. Hawrot, T. L. Lentz, *Mol. Pharmacol.* **34**, 643–650 (1988).
25. H. C. Fertuck, W. Woodward, M. M. Salpeter, *J. Cell Biol.* **66**, 209–213 (1975).
26. K. A. Wilkinson, H. E. Kloefkorn, S. Hochman, *PLOS ONE* **7**, e39140 (2012).
27. J. F. Cordero-Morales, V. Vásquez, *Curr. Opin. Struct. Biol.* **51**, 92–98 (2018).
28. L. O. Romero *et al.*, *Nat. Commun.* **10**, 1200 (2019).
29. S. Iyengar, M. H. Ossipov, K. W. Johnson, *Pain* **158**, 543–559 (2017).

HPLC Solvent Monitor

The Solvent Line Monitor from TESTA Analytical Solutions is a true plug-and-play addition to any HPLC system designed to detect when one or more of its pump solvent reservoirs are empty and automatically shut off the system. Running out of solvent when running an HPLC or any other liquid chromatography system is a problem most separation scientists will have encountered. Your chromatograph running out of solvent can lead to loss of data, need to reprime the pump, and system downtime, often necessitating revalidation to make sure the obtained results are within expected limits. The Solvent Line Monitor runs independently and is fully compatible with almost any liquid chromatograph. It continuously monitors the fill status of tubing carrying solvent to up to two liquid chromatography pumps.

TESTA Analytical Solutions
For info: +49-30-864-24076
www.custom-chromatography.com/technologies.html

Automated Cell Density and Cell Viability Analysis

Nova Biomedical announces the launch of Bio Profile FAST CDV, a high-throughput, fully automated viable cell density and viability analyzer capable of producing results in under 70 sec with just 100 uL of sample volume. In addition, it performs all sample dilutions internally, enabling cell culture samples up to $140e^6$ c/mL to be analyzed without any external sample dilution. Cell culture samples can be analyzed via the external 36-position load-and-go tray or via an innovative 96-well plate option. All aspects of the software and networking capabilities are 21 CFR Part 11 compliant. FAST CDV utilizes trypan blue dye exclusion methodology for determination of live and dead cells and uses the industry's highest resolution camera and optics coupled with the most advanced algorithms to provide the most accurate cell density and cell viability measurements.

Nova Biomedical
For info: +1-800-822-0911
www.novabiomedical.com

Photochemical Reactor System

Asynt introduces the LightSyn Lighthouse—a photochemical reactor system in their LightSyn range, developed in response to customer demand for higher reaction yields, ease of use, high operational safety, and competitive pricing. The LightSyn Lighthouse uses new technology to channel light through a quartz rod directly into the reaction medium, maximizing power intensity while keeping photon flux even throughout. Easily adapted to suit different-sized tubes/vials, and round bottom flasks, the LightSyn Lighthouse is an effective and versatile system for scaling your experiments. Initially available in single or up to three position configurations, this benchtop photochemical reactor provides heating and agitation via any magnetic hotplate stirrer and is suitable for temperatures from ambient to +80 ºC (or down to -30ºC with an optional cooling ring).

Asynt
For info: +44-1638-781709
www.asynt.com/product/lightsyn-lighthouse

Motorized XYZ Deck

Prior Scientific introduces the H189 Motorized XYZ Deck. This deck is purposely designed to match the increased size and versatility of the latest generation of 2P/3P/Multiphoton/Confocal microscopy systems, giving researchers the flexibility to utilize all the potential of the added sample space and microscope power of these new microscopes. The XYZ Deck incorporates two removable shelves with a 25 kg load-lifting capacity. Its removable shelf feature facilitates sample preparation when working with larger specimens or preparing complex experiments. Oversized breadboard deck plates make the XYZ Deck the optimal solution for a large range of sample types from whole animal in vivo to slides and petri dishes. Compatible with Queensgate Piezo models, the XYZ Deck is compatible with most imaging software and ideal for use with manipulators, probes, or other sensory devices. With 50 mm of motorized in XY and Z travel and a sample height adjustable from 79.5 mm to 410 mm, the XYZ Deck will prove to be a valuable addition to your system configuration.

Prior Scientific
For info: +44- (0)-1223-881711
www.prior.com/product/high-precision-motorized-xyz-deck

Aptamers for Cancer Therapy and Diagnosis

AMS Biotechnology (AMSBIO) offers an extensive range of aptamers targeting many human proteins linked to cancer. Aptamers bind to target molecules with the same affinity and specificity as antibodies but offer significant advantages, in particular a lack of immunogenicity, which makes them an ideal tool for cancer therapy and diagnosis. There are two major applications for aptamers in cancer therapy. Aptamers can be used as antagonists by targeting and inhibiting cancer-specific molecules. They can also be used as delivery vehicles for therapeutics by specifically targeting cell membrane receptors on cancer cells. In this application, aptamer–drug conjugates bind to and are internalized by cancer cells while avoiding damage to healthy cells. Aptamers also have enormous potential for use in cancer diagnostics. They can be used to identify cancer cells and recognize cancer biomarkers, cancer metabolites, and differentiating cells as well as molecules that affect tumor behavior.

AMS Biotechnology
For info: +1-617-945-5033
www.amsbio.com/aptamers-for-cancer

Liquid Handling Platforms

DISPENDIX, a BICO company, announces the I.DOT HT Non-contact Dispenser and the L.DROP Liquid Handler. The I.DOT HT builds on the core technology of the I.DOT, expanding the source well layout to a 384 format to support the management of compound libraries at large pharmaceutical and smaller biotechnology companies. The L.DROP Liquid Handler couples sensor technology and a web-based architecture to provide a more dynamic instrument that is capable of scaling protocols across instruments and even laboratories without tedious optimization. Both can be fully integrated into the "lab of the future" that is data-driven and optimizes researchers time spent on scientific discovery.

DISPENDIX
For info: +1-(833)-235-5465
www.dispendix.com

Electronically submit your new product description or product literature information! Go to www.science.org/about/new-products-section for more information.

Newly offered instrumentation, apparatus, and laboratory materials of interest to researchers in all disciplines in academic, industrial, and governmental organizations are featured in this space. Emphasis is given to purpose, chief characteristics, and availability of products and materials. Endorsement by *Science* or AAAS of any products or materials mentioned is not implied. Additional information may be obtained from the manufacturer or supplier.

myIDP:
A career plan customized for you, by you.

For your career in science, there's only one **Science**

Features in myIDP include:

- Exercises to help you examine your skills, interests, and values.

- A list of 20 scientific career paths with a prediction of which ones best fit your skills and interests.

- A tool for setting strategic goals for the coming year, with optional reminders to keep you on track.

- Articles and resources to guide you through the process.

- Options to save materials online and print them for further review and discussion.

- Ability to select which portion of your IDP you wish to share with advisors, mentors, or others.

- A certificate of completion for users that finish myIDP.

myIDP

Visit the website and start planning today!
myIDP.sciencecareers.org

Science Careers In partnership with:
AAAS

FASEB
Federation of American Societies for Experimental Biology

University of Massachusetts Medical School
UMASS

UCSF
University of California San Francisco

UIC
BURROUGHS WELLCOME FUND

By **Stephen Peters-Collaer**

Stay curious

"Hot dog! Looks like you've got a *Mahonia repens*," Sherel exclaimed in his rural Utah twang. I crouched and gently touched the plant with yellow flowers by my feet. "This one here? How can you tell it's a *Mahonia*?" Sherel carefully bent down and adjusted his camo hat to block the Sun. The 75-year-old botanist and leader of our field crew paused briefly to admire the plant before launching into an energetic description of its defining features. That evening, watching the Sun fade behind the mountains, I texted my childhood friend. "Day 1 was actually kind of fun," I started, "but we'll see how long it takes before I get bored from just identifying plants in the field all day."

Up to that point, I had avoided fieldwork. To an undergraduate studying ecology, bending over plants for 10 hours a day seemed a lot less interesting than identifying big-picture trends in large data sets. But I knew potential graduate schools would likely view my lack of field experience as a hole in my resume, and my mother thought I should work for a few years to explore my interests before pursuing further education. So, I applied to field-based summer positions after graduation and landed a job assessing sage grouse habitat in Utah. It felt like a necessary evil before I could move on to bigger, more "intellectual" things.

But as the weeks of fieldwork rolled by, the boredom I expected never arrived. I came home from the sagebrush each night with sore legs and a sunburned neck, invigorated by the day's finds. By picking Sherel's brain about pronghorn antelopes, aspen groves, and every species of sagebrush, I discovered field days are about much more than rote identification. Each day is an opportunity to learn a little bit more.

When the summer was over, I found myself in another field job, this time surveying forest in Michigan's Upper Peninsula. One frozen morning a few weeks in, I came across a strange wasp probing the bark of a decaying beech with what looked like an enormous stinger, 10 centimeters long. Our official duties didn't extend to insects, but my curiosity was piqued. "Hey, come check this out!" I called to the rest of our field crew, instinctively channeling Sherel's tireless enthusiasm. Despite the cold, we watched transfixed by this otherworldly insect, which my colleague identified as a giant wasp laying eggs, until it slowly pulled back its ovipositor, stretched, and flew off. As we dispersed back to our tasks, I noticed migrating sandhill cranes flying overhead and thought of their cousins in northern Utah. I sent silent thanks to Sherel for teaching me to approach fieldwork with a sense of wonder—excited to learn, even when my hands are numb.

"Each day is an opportunity to learn a little bit more."

I'm now a third-year Ph.D. student in forest ecology, and the time I spend leading research crews in the woods of New Hampshire every summer is one of my favorite parts of the year. Our crews typically don't have previous field experience, and I try to bring Sherel's excitement to our work. By answering questions with enthusiasm, sharing interesting tidbits, and providing the intellectual context behind our efforts, I hope to show that working in the field can be fascinating and fun.

My younger self would have been surprised: It's when I'm not in the field that it can sometimes be difficult to remain energized about my work. It's not just being immersed in nature that I miss. Fieldwork may be buggy, wet, and physically taxing, but collaborating with others helps keep spirits high, and the physical activity helps me stay sharp. Much of my Ph.D. work, on the other hand, is solo and sedentary. So I've tried to bring aspects of fieldwork to my day-to-day routine. I take breaks to talk to other graduate students to escape intellectual ruts, and I try to get up from my desk and move for a minute or two throughout the day.

I also try to recapture fieldwork's spirit of discovery by reading a journal article that excites me, regardless of the topic, every Monday. If I'm bogged down by the repetition of analyzing another data set, this helps restore my curiosity and enthusiasm for my work. And when I remember that gleam in Sherel's eye as he responded to my seemingly mundane, random questions, I remind myself that any task can present an opportunity to learn—as long as I am open to it. ∎

Stephen Peters-Collaer is a Ph.D. student at the University of Vermont. Send your career story to SciCareerEditor@aaas.org.

TRILLIONS OF MICROBES

ONE ESSAY

The NOSTER *Science* Microbiome Prize is an international prize that rewards innovative research by investigators who have completed their terminal degree in the last 10 years and are working on the functional attributes of microbiota. The research can include any organism with the potential to contribute to our understanding of human or veterinary health and disease, or to guide therapeutic interventions. The winner and finalists will be chosen by a committee of independent scientists chaired by a senior editor of *Science*. The top prize includes a complimentary membership to AAAS, an online subscription to *Science*, and USD 25,000. Submit your research essay today.

Jennifer Hill, Ph.D.
2022 Winner

NOSTER | Science
MICROBIOME
PRIZE

Apply by 24 January 2023 at www.science.org/noster

Sponsored by Noster, Inc

Discover inspiring stories from the life-science community

How do human connections drive science forward? Find out how relationships with friends, colleagues, peers, and mentors have influenced some of the world's leading scientists.

Find the stories here
abcam.me/together

progress happens together
abcam